

UC Berkeley

UC Berkeley Electronic Theses and Dissertations

Title

Transport and Thermodynamics in Polymer Blends and Electrolytes

Permalink

<https://escholarship.org/uc/item/91p6d0nf>

Author

Gao, Kevin

Publication Date

2022

Peer reviewed|Thesis/dissertation

Transport and Thermodynamics in Polymer Blends and Electrolytes

By

Kevin Wu Gao

A dissertation submitted in partial satisfaction of the
requirements for the degree of

Doctor of Philosophy

in

Chemical Engineering

in the

Graduate Division

of the

University of California, Berkeley

Committee in charge:

Professor Nitash P. Balsara, Chair

Professor Bryan D. McCloskey

Professor Mary C. Scott

Summer 2022

Transport and Thermodynamics in Polymer Blends and Electrolytes

© Copyright 2022

Kevin Wu Gao

All rights reserved

Abstract

Transport and Thermodynamics in Polymer Blends and Electrolytes

By

Kevin Wu Gao

Doctor of Philosophy in Chemical Engineering

University of California, Berkeley

Professor Nitash P. Balsara, Chair

The widespread use of variable and intermittent renewable energy sources will require robust energy storage systems. Rechargeable batteries have the potential to meet this need. The lithium-ion battery is the one of the most popular rechargeable batteries, consisting of a graphite anode, a liquid organic electrolyte, and a metal oxide cathode. Unfortunately, the energy density in commercial lithium-ion batteries is approaching the theoretical limit for lithium-ion technology, and improvements are necessary to enable large scale grid energy storage applications. Safety is also an important criterion for energy storage applications, necessitating a fundamental improvement in the highly flammable lithium-ion batteries. Replacing the graphite anode with pure lithium metal can enable higher energy densities and replacing the flammable organic liquid solvent with a nonvolatile polymer electrolyte can improve safety. We are interested in polymer electrolytes because of their improved safety conditions and their compatibility with lithium metal anodes. However, ion transport and thermodynamics in polymer electrolytes is fundamentally different than in traditional liquid electrolytes. This thesis focuses on understanding ion transport and thermodynamics in polymer electrolytes.

Ion transport of polymer electrolyte systems is characterized under the framework of Newman's concentrated solution theory. We explicitly define the cation transference number, which describes the fraction of current carried by the cation. Two experimental approaches (Hittorf and Bruce-Vincent) for measuring the cation transference number are described. We illustrate the importance of the cation transference number and its dependence on reference frames, and compare values for commonly reported transference numbers in PEO electrolyte systems. We also provide a comprehensive description of the electrochemical properties of poly(ethylene oxide) (PEO) electrolytes that accounts for error propagation and uncertainty. Data from 64 independent PEO electrolyte samples, with PEO molecular weights ranging from 5 kg mol⁻¹ to 275 kg mol⁻¹, are compiled and analyzed to demonstrate that ion transport properties remain constant above the entanglement threshold. A preliminary investigation into the possibility of a salt diffusion coefficient dependence on molecular weight in PEO electrolytes and a discussion of its implications is presented.

PEO has been the most extensively studied polymer for lithium battery applications, yet its use as an electrolyte is limited by its poor ionic conductivity and low cation transference number with respect to solvent velocity. Two strategies for developing superior ion transport properties are presented. (1) Moving beyond homopolymer electrolytes (*i.e.* single polymer and salt) to block

copolymer systems. The ion transport and thermodynamics of the hybrid inorganic-organic block copolymer poly(ethylene oxide)-*b*-polyhedral oligomeric silsesquioxane (PEO-POSS) are reported. We find that PEO-POSS electrolytes self-assembles into a variety of morphologies ranging from lamellar to disorder, and these morphologies affect ion transport. Decreasing the length of the alkyl chain substituent on the POSS monomer is found to improve ion transport. (2) Mixing two chemically distinct polymers with lithium salt to create miscible polymer blend electrolytes. We use small angle neutron scattering (SANS) as an unambiguous method for determining the phase behavior of polymer blend systems with and without salt. We demonstrate that PEO and poly(1,3,5-trioxocane) (P(2EO-MO)) are miscible in the presence of lithium salt. Miscibility, or homogeneity, is governed by the thermodynamics of the polymer blend system. We apply the Random Phase Approximation to homogeneous PEO/P(2EO-MO) electrolyte systems to calculate the Flory-Huggins parameter, which describes the enthalpic interaction between two different polymers. We also show that PEO and poly(1,3,-dioxolane) (P(EO-MO)) follow the same miscibility trend as PEO/P(2EO-MO) blends, but that P(2EO-MO)/P(EO-MO) blends are only miscible in the salt-free state.

The Flory-Huggins interaction parameter is also relevant beyond battery applications to topics such as separation where uptake in polymer membranes is dictated by thermodynamics, *e.g.* Donnan equilibrium. We have developed a set of equations describing the thermodynamics of univalent and multivalent charged polymer networks in electrolytic solution. In effect, we have modified the classical Donnan equilibrium model to account for both enthalpic interactions and the elasticity of the gel. We model experimental data obtained in a block copolymer membrane soaked in a traditional liquid electrolyte. We also compare experimental data from literature with our model results.

This thesis provides a thorough description for the measurement and analysis of ion transport in polymer electrolytes. It is a good starting point for further studies into thermodynamics of polymer blend electrolytes and polymer membranes.

Table of Contents

Abstract	1
List of Figures.....	v
List of Tables	ix
Acknowledgements	xi
1 Introduction	1
1.1 Motivation	1
1.2 Polymer Electrolytes	1
1.3 Electrochemical Characterization of Polymer Electrolytes.....	2
1.4 Outline of Dissertation	3
2 The Transference Number.....	5
2.1 Introduction	5
2.2 Experimental Methods: Hittorf Cell and Symmetric Cell.....	6
2.3 Poly(ethylene oxide) Electrolytes	9
2.4 Conclusions	10
2.5 Acknowledgements	11
2.6 Nomenclature.....	11
3 Electrochemical Properties of Poly(ethylene oxide) Electrolytes Above the Entanglement Threshold.....	13
3.1 Introduction	13
3.2 Experimental Methods	15
3.2.1 Electrochemical Characterization.....	15
3.2.2 Error Propagation.....	16
3.3 Results and Discussion.....	16
3.4 Conclusions	21
3.5 Acknowledgements	22
3.6 Supporting Information	22
3.7 Nomenclature.....	23
4 Dependence of the Salt Diffusion Coefficient on Molecular Weight.....	24
4.1 Introduction	24
Experimental Methods.....	25
4.2 Results and Discussion.....	27

4.3	Conclusions	29
4.4	Acknowledgements	30
4.5	Nomenclature.....	30
5	Optimizing the Monomer Structure of Polyhedral Oligomeric Silsesquioxane for Ion Transport in Hybrid Organic-Inorganic Block Copolymers	31
5.1	Introduction	31
5.2	Experimental Methods	32
5.2.1	Synthesis.....	32
5.2.2	Small Angle X-ray Scattering (SAXS)	33
5.2.3	Electrochemical Measurements	34
5.2.4	Rheology	35
5.2.5	Transmission Electron Microscopy Imaging	35
5.3	Results and Discussion.....	35
5.4	Conclusions	42
5.5	Acknowledgements	42
5.6	Supporting Information	43
5.6.1	Synthesis of PEO-POSS Block Copolymer.	43
5.6.2	Differential Scanning Calorimetry (DSC).....	48
5.6.3	Absolute SAXS Data	51
5.6.4	Impedance Spectroscopy.....	51
5.6.5	Density Measurements and Volume Fraction Calculations	52
5.7	Nomenclature.....	54
6	Miscible Polyether/Poly(ether-acetal) Electrolyte Blends	56
6.1	Introduction	56
6.2	Experimental Methods	58
6.2.1	Synthesis of 1,3,6-trioxocane, (2EO-MO)	58
6.2.2	Synthesis of Poly(1,3,6-trioxocane), P(2EO-MO)	58
6.2.3	Polymer Blend Electrolyte Preparation and Composition	58
6.2.4	DSC Sample Preparation and Experiments.....	61
6.2.5	Small Angle Neutron Scattering (SANS) Sample Preparation and Experiments ...	61
6.2.6	Electrochemical Sample Preparation and Experiments	61
6.3	Results and Discussion.....	61
6.4	Conclusions	73

6.5	Acknowledgements	73
6.6	Supporting Information	74
6.6.1	General Synthetic Considerations.....	74
6.6.2	Instrumentation.....	74
6.6.3	Polymer Characterization.....	75
6.6.4	NMR Spectra	77
6.6.5	AC Impedance Spectroscopy	79
6.6.6	Disclaimer	80
6.7	Nomenclature.....	80
7	Relationship between Ion Transport and Phase Behavior in Polymer Blend Electrolytes Studied by Electrochemical Characterization and Neutron Scattering	82
7.1	Introduction	82
7.2	Materials and Methods.....	84
7.2.1	Polymer Blend Electrolyte Preparation and Composition	84
7.2.2	SANS Sample Preparation and Experiment.....	84
7.2.3	Electrochemical Sample Preparation and Experiments	85
7.3	Results and Discussion.....	86
7.4	Conclusions	94
7.5	Acknowledgements.....	95
7.6	Supporting Information.....	95
7.6.1	General Synthetic Considerations.....	95
7.6.2	Instrumentation.....	96
7.6.3	Synthetic Procedures.....	96
7.6.4	NMR Spectra	98
7.6.5	Additional SANS Data.....	100
7.7	Nomenclature.....	101
8	Increased Donnan Exclusion in Charged Polymer Networks at High Salt Concentrations.	103
8.1	Introduction	103
8.2	Theory	106
8.3	Results and Discussion.....	109
8.4	Conclusions	118
8.5	Acknowledgements.....	118
8.6	Supporting Information.....	119

8.6.1	Materials.....	119
8.6.2	Measurement of Electrolyte Uptake and Salt Partitioning.....	119
8.6.3	Flory-Huggins Interaction Parameter	119
8.6.4	Volume Fraction of Bound Negative Ions in the Gel Phase	120
8.6.5	Comparing Experimental Donnan Exclusion Data and Theoretical Predictions. .	122
8.7	Nomenclature.....	124
9	Conclusions and Outlook	126
10	References.....	128
11	Appendices.....	151
11.1	Additional Discussion on Electrochemical Experiments and Data Analysis.....	151
11.1.1	Resistance Measurements and Fitting.....	151
11.1.2	Restricted Diffusion Measurements and Analysis.....	155

List of Figures

Figure 2.1. Schematics of cells used to measure the transference number.	7
Figure 2.2. Plots of the current fraction and transference numbers with respect to the solvent and mass average velocities versus concentration for PEO/LiTFSI at 90 °C.	9
Figure 2.3. Schematic of a battery with a composite anode and cathode.....	10
Figure 3.1. Molecular weight dependence of PEO/LiTFSI electrolytes at representative salt concentrations at 90 °C	17
Figure 3.2. Electrochemical measurements of PEO/LiTFSI electrolytes at 90 °C for different salt concentrations and molecular weights	19
Figure 3.3. PEO/LiTFSI electrolyte properties at 90 °C	21
Figure 4.1. Example PEO (35 kg mol ⁻¹) electrolyte data showing potential response to applied current density and open circuit relaxation.	26
Figure 4.2. Salt diffusion coefficient and ionic conductivity calculated under different applied current densities, for a range of PEO molecular weights.	27
Figure 4.3. Dependence of salt diffusion coefficient on molecular weight of PEO.	28
Figure 4.4. Effect of salt diffusion coefficient and molecular weight on the cation transference number in PEO.....	29
Figure 5.1. Chemical structure of PEO-POSS polymers synthesized.....	33
Figure 5.2. Scattering intensity at 70 °C of the three PEO-POSS polymers with various salt concentrations, plotted as a function of the magnitude of the scattering vector, q.....	36
Figure 5.3. Lorentzian fits of the scattering around the primary peak.	37
Figure 5.4. PEO-POSS scattering peak location, full-width-half-max, and volume fraction of more ordered phase.	38
Figure 5.5. TEM micrographs of PEO-POSS.....	39
Figure 5.6. Morphology of phases on a salt concentration, r , versus POSS silica cage alkyl substituent plot.....	40
Figure 5.7. Electrochemical data for PEO-POSS.	41
Figure 5.8. Storage and loss moduli as a function of frequency for PEO-POSS.....	42
Figure 5.9. ¹ H-NMR spectra of PEO-POSS-ethyl.	44
Figure 5.10. ¹ H-NMR spectra of PEO-POSS-isobutyl.....	45
Figure 5.11. ¹ H-NMR spectra of PEO-POSS-isooctyl.....	46
Figure 5.12. GPC data for PEO-POSS block copolymers and PEO-based macroalkoxyamine starting material.	47
Figure 5.13. TGA data for PEO-POSS-ethyl plotting weight percent versus temperature.....	47
Figure 5.14. TGA data for PEO-POSS-isobutyl plotting weight percent versus temperature.	48
Figure 5.15. TGA data for PEO-POSS-isooctyl plotting weight percent versus temperature.	48
Figure 5.16. DSC curves of PEO-POSS-ethyl from $r = 0$ to $r = 0.30$ upon second heating cycle.	49
Figure 5.17. DSC curves of PEO-POSS-isobutyl from $r = 0$ to $r = 0.30$ upon second heating cycle.	49
Figure 5.18. DSC curves of PEO-POSS-isooctyl from $r = 0$ to $r = 0.30$ upon second heating cycle.	50

Figure 5.19. Glass transition temperature, T_g , as a function of salt concentration, r , for the three PEO-POSS(5-1) polymers.....	50
Figure 5.20. Absolute scattering intensities for PEO-POSS(5-1) (a) ethyl (b) isobutyl (c) iso-octyl.	51
Figure 5.21. Nyquist plots at 90 °C for (a) blocking electrode conductivity cell for an isobutyl $r = 0.12$ sample and (b) lithium symmetric cell for an isobutyl $r = 0.12$ sample.....	52
Figure 5.22. Volume fraction of the EO/LiTFSI-rich phase, $\phi_{\text{EO/LiTFSI}}$, as a function of r	53
Figure 6.1. Chemical structure of poly(ethylene oxide) (PEO), poly(1,3,6-trioxocane) (P(2EO-MO)), and lithium bis(trifluoromethanesulfonyl)imide (LiTFSI).	57
Figure 6.2. Sample DSC data and glass transition data for blends.	62
Figure 6.3. Measured absolute SANS intensity, $I(q)$, vs scattering vector, q , at 90 °C for blends.	63
Figure 6.4. SANS intensities, $I_{\text{coh}}(q)$, plotted as a function of the magnitude of the scattering vector, q , at 90 °C for the dPEO/P(2EO-MO)/LiTFSI (P(2EO-MO) $M_n = 26.7 \text{ kg}\cdot\text{mol}^{-1}$) blends at the miscible salt concentrations.	65
Figure 6.5. RPA fits (solid black lines) for a dPEO/P(2EO-MO)/LiTFSI (P(2EO-MO) $M_n = 26.7 \text{ kg}\cdot\text{mol}^{-1}$) blend with $r = 0.08$ at different temperatures.....	67
Figure 6.6. Effective Flory-Huggins interaction parameter, χ_{eff} , as a function of inverse temperature, $1/T$, for the dPEO/P(2EO-MO)/LiTFSI blends.	69
Figure 6.7. Effective Flory-Huggins interaction parameter, χ_{eff} , for the dPEO/P(2EO-MO)/LiTFSI (P(2EO-MO) $M_n = 26.7 \text{ kg}\cdot\text{mol}^{-1}$) blends as a function of salt concentration, r , at three different temperatures.....	70
Figure 6.8. Electrochemical characterization of the PEO/P(2EO-MO)/LiTFSI blend as a function of salt concentration, r , compared with conventional PEO/LiTFSI ($M_n = 35.0 \text{ kg}\cdot\text{mol}^{-1}$) and P(2EO-MO)/LiTFSI ($M_n = 55.2 \text{ kg}\cdot\text{mol}^{-1}$) polymer electrolyte systems.....	71
Figure 6.9. GPC traces of P(2EO-MO).	75
Figure 6.10. Representative thermogravimetric analysis of poly(1,3,6-trioxocane).	76
Figure 6.11. 1,3,6-trioxocane (2EO-MO) ^1H NMR Spectrum (500 MHz, CDCl_3).....	77
Figure 6.12. 1,3,6-trioxocane (2EO-MO) ^{13}C NMR Spectrum (125 MHz, CDCl_3).....	78
Figure 6.13. Poly(1,3,6-trioxocane) (P(2EO-MO)) ^1H NMR Spectrum (500 MHz, CDCl_3).....	78
Figure 6.14. Poly(1,3,6-trioxocane) (P(2EO-MO)) ^{13}C NMR Spectrum (125 MHz, CDCl_3).....	79
Figure 6.15. Nyquist plots at 90 °C for lithium symmetric cells of PEO/P(2EO-MO)/LiTFSI blends.	79
Figure 7.1. Chemical structure of poly(ethylene oxide) (PEO), poly(1,3,6-trioxocane) (P(2EO-MO)), poly(1,3-dioxolane) (P(EO-MO)), and lithium bis(trifluoromethanesulfonyl)imide (LiTFSI).....	83
Figure 7.2. Electrochemical characterization of the PEO/P(EO-MO)/LiTFSI and P(EO-MO)/P(2EO-MO)/LiTFSI blend electrolytes as a function of LiTFSI concentration.	86
Figure 7.3. Measured absolute SANS intensity ($I(q)$) versus the magnitude of scattering vector (q) at 90 °C for (a) dPEO/P(EO-MO)/LiTFSI and (b) dP(EO-MO)/P(2EO-MO)/LiTFSI polymer blend electrolytes at different salt concentration (r).	87
Figure 7.4. Coherent SANS intensity profiles $I_{\text{coh}}(q)$ (open symbols) and corresponding RPA fits (solid curves) for miscible blends at 90 °C.....	89

Figure 7.5. Effective Flory-Huggins interaction parameter χ_{eff} as a function of inverse temperature ($1/T$) for the one-phase (a) dPEO/P(EO-MO)/LiTFSI polymer blend electrolytes and (b) dP(EO-MO)/P(2EO-MO) polymer blends.	91
Figure 7.6. Effective Flory-Huggins interaction parameter χ_{eff} as a function of salt concentration, r , for the (a) dPEO/P(EO-MO)/LiTFSI, and (b) dP(EO-MO)/P(2EO-MO)/LiTFSI polymer blends at different temperatures.	92
Figure 7.7. Efficacy, $\kappa\rho_+$, of PEO/P(EO-MO)/LiTFSI and P(EO-MO)/P(2EO-MO)/LiTFSI polymer blend electrolytes as a function of r compared with each homopolymer/LiTFSI) at 90 °C.	93
Figure 7.8. Summary of phase behavior and ion transport efficacy, $\kappa\rho_+$, of polymer blend electrolytes with added LiTFSI salt at 90 °C.	95
Figure 7.9. ^1H NMR spectrum of <i>d</i> EO-MO.	98
Figure 7.10. ^{13}C NMR spectrum of <i>d</i> EO-MO.	99
Figure 7.11. ^1H NMR spectrum of <i>d</i> P(EO-MO).	99
Figure 7.12. ^{13}C NMR spectrum of <i>d</i> P(EO-MO).	100
Figure 7.13. Absolute SANS scattering intensity of deuterated homopolymers.	100
Figure 7.14. Coherent SANS scattering intensity of salt free polymer blends.	101
Figure 8.1. Schematic of a crosslinked polymer phase with negative charges covalently bound to the polymer chains in contact with a reservoir containing an electrolytic solution.	104
Figure 8.2. Experimental data for the swelling and salt partitioning between a PSLiTFSI- <i>b</i> -PE- <i>b</i> -PSLiTFSI triblock copolymer membrane and external solutions of LiTFSI in an EC/DMC mixture.	105
Figure 8.3. Polymer volume fraction in the gel phase and ion exclusion dependence on volume fraction of anions in the external solution for $z_+ = -z_-$, $N = 10$, and $\chi = 1$, various f	110
Figure 8.4. Polymer volume fraction in the gel phase and ion exclusion dependence on volume fraction of anions in the external solution for $z_+ = -z_-$, $N = 50$, and $\chi = 1$, various f	111
Figure 8.5. Polymer volume fraction in the gel phase and ion exclusion dependence on volume fraction of anions in the external solution for $z_+ = -z_-$, $N = 200$, and $\chi = 1$, various f	111
Figure 8.6. Polymer volume fraction in the gel phase and ion exclusion dependence on volume fraction of anions in the external solution for $z_+ = -z_-$, $N = 200$, and $f = 0.3$, various χ	112
Figure 8.7. Polymer volume fraction in the gel phase and ion exclusion dependence on volume fraction of anions in the external solution for $\chi = 1$, $N = 200$, and $f = 0.3$, various $z_+ = -z_-$	113
Figure 8.8. Comparing present theory with the classical Donnan prediction.	114
Figure 8.9. Experimental data for the swelling and salt partitioning between a PSLiTFSI- <i>b</i> -PE- <i>b</i> -PSLiTFSI triblock copolymer membrane and external solutions of LiTFSI in an EC/DMC mixture.	116
Figure 8.10. Comparing experimental data with theoretical predictions.	118
Figure 8.11. Dependence of the volume fraction of bound negative ions in the gel phase, $\phi_{-,b}$, on the volume fraction of anions in the external solution, ϕ_-^c for $z_+ = -z_-$, $N = 10$, $\chi = 1$, various f	120
Figure 8.12. Dependence of the volume fraction of bound negative ions in the gel phase, $\phi_{-,b}$, on the volume fraction of anions in the external solution, ϕ_-^c for $z_+ = -z_-$, $N = 50$, $\chi = 1$, various f	121

Figure 8.13. Dependence of the volume fraction of bound negative ions in the gel phase, $\phi_{-,b}$, on the volume fraction of anions in the external solution, $\phi_{-,e}$ for $z_+ = -z_-$, $N = 200$, $\chi = 1$, various f	121
Figure 8.14. Dependence of the volume fraction of bound negative ions in the gel phase, $\phi_{-,b}$, on the volume fraction of anions in the external solution, $\phi_{-,e}$ for $z_+ = -z_-$, $N = 50$, $f = 0.3$, various χ	122
Figure 8.15. Dependence of the volume fraction of bound negative ions in the gel phase, $\phi_{-,b}$, on the volume fraction of anions in the external solution, $\phi_{-,e}$ for $N = 50$, $\chi = 1$, $f = 0.3$, various z_+ and z_-	122
Figure 8.16. Experimental data for the swelling and salt partitioning between a PSLiTFSI- <i>b</i> -PE- <i>b</i> -PSLiTFSI triblock copolymer membrane and external solutions of LiTFSI in an EC/DMC mixture.	123
Figure 8.17. Comparing experimental data with theoretical predictions.	124
Figure 11.1. Equivalent circuits for (a) blocking electrode and (b) non-blocking electrode setups.	151
Figure 11.2. Example concentration profiles showing relaxation of concentration profiles, c , over time, t , in a lithium-electrolyte-lithium symmetric cell.	155
Figure 11.3. Initial concentration profiles across the electrolyte and the resulting change in concentration difference across the electrolyte over dimensionless time.	157
Figure 11.4. Qualitatively comparing the linearity of $\ln(\Delta c)$ vs. dimensionless time after fitting from long time of $\alpha = 0.01$, 0.03 , and 0.05	157
Figure 11.5. The residuals for the linear fit, R^2 , plotted against the different “long time” values of α at which the data is first fit to a linear relationship, for different initial steady-state concentration profiles (red: step, black: cosine, blue: linear, green: cosine reflected) relaxing in restricted diffusion.	158
Figure 11.6. Potential over time showing relaxation of concentration gradient in a lithium-electrolyte-lithium cell.	159

List of Tables

Table 2.1. List of symbols and abbreviations.	11
Table 3.1. PEO molecular weights in PEO/LiTFSI electrolytes.....	16
Table 3.2. List of symbols and abbreviations.	23
Table 4.1. List of symbols and abbreviations.	30
Table 5.1. Summary of PEO-POSS(5-1) characteristics	33
Table 5.2. List of symbols and abbreviations.	54
Table 6.1. Molar masses and dispersities of PEO and P(2EO-MO) homopolymers used.	59
Table 6.2. Polymer components of blends used in each experiment.	59
Table 6.3. Volume fractions, ϕ_i , and α values used in RPA fits of dPEO/P(2EO-MO)/LiTFSI blends.	66
Table 6.4. A and B constants for dPEO/P(2EO-MO)/LiTFSI blends at various salt concentrations, r , and their linear fit R^2 values.	68
Table 6.5. List of symbols and abbreviations.	80
Table 7.1. Molar masses and dispersities of homopolymers, and type of experiments used in this study.	84
Table 7.2. Component volume fractions ϕ_i and α values of miscible blends.	90
Table 7.3. A and B values for dPEO/P(EO-MO)/LiTFSI and dP(EO-MO)/P(2EO-MO) blends at various r	92
Table 7.4. List of symbols and abbreviations.	101
Table 8.1. List of symbols and abbreviations.	124

This thesis is dedicated to my family.
Thank you all.

Acknowledgements

The work and research reflected in this dissertation was only possible with the support of countless people, and certainly many were missed here. Thank you all.

I am fortunate to have had the most kind and supportive advisor in Nitash Balsara. He encouraged me to pursue my endeavors both inside and outside the lab. Nitash provided me with just the right amount of guidance and support while still allowing me the freedom to become an independent researcher. As a result, I have been able to pursue research ideas that have branched out in many different yet interesting directions. Nitash's enthusiasm and energy for science is unmatched and truly infectious, yet it is his understanding and thoughtfulness that stands out to me. I have always felt that Nitash has my best interests at heart and that is something I will always be thankful for. This kind of personality fosters a great culture, and I am so grateful he took the chance accepting me into the lab.

Joining the Balsara Lab was the best decision of my graduate school career. I had no prior research experience in polymers or batteries yet my transition into the field was smooth thanks to wonderful students and postdocs in the lab. I owe much of my training and education to them. Not only that, but the lab culture when I joined was really welcoming, and I made many close friends here.

Many colleagues I only had the pleasure of knowing for a short time. However, I am thankful for all they have shared with me in that small amount of time, either directly or indirectly. Dr. Irune Villaluenga helped me get started on another project when my initial first year project was going nowhere, and Chapter 5 is a direct result of her mentorship. Danielle Pesko, Ksenia Timachova, and Rita Wang were role models to look up to, and much of my research has built up on their prior work. Dr. Kim Mongcopa was always helpful and I still have a copy of her notes on neutron scattering sample preparation in my lab notebook. Professor Hee Jeung Oh was the epitome of a driven scientist, yet still kind and fun to be around – if there was anybody I would do a postdoc with, it would be her.

The students two years above me left a big impact on me. Deep Shah was probably my first friend in the group. I miss the times we would chat in 33, our daily workouts, and your safety leadership. I learned a lot from talking science with you. I also learned a lot from Jackie Maslyn. The way she does science is incredibly meticulous and we should all strive to reach her level of care. I miss our Insanity morning workouts and funny conversations. Whitney Loo taught me everything I know about neutron scattering. Her helpful mentorship was critical for my development as a researcher and her future students will be lucky to have her as an advisor. I miss the yoga sessions she would lead and her strong leadership within the lab, but look forward to hearing about the interesting results coming out of the Loo Lab.

Dr. Youngwoo Choo got me started on the blends work. His selfless attitude enabled me to take on this project. Dr. Louise Frenek has a wealth of electrochemical knowledge, but it is her kind and outgoing personality that stands out to me. Her baking, social outing organization, and bright personality are already missed in the lab, but I look forward to working together with her soon. Dr. Saheli Chakraborty is very helpful with all the synthesis questions I have, and her warm presence in 33 is always felt. Dr. David Halat is an insightful and funny researcher – I have no doubt that he will become a future professor. Dr. Xiaopeng Yu is always helpful towards me with all things related to Donnan and synthesis, and I am sad that I am not able to collaborate more with him. Dr.

Xi Jiang is my go-to for anything microscopy related, and I am thankful for his instrumental help in my first publication. Dr. Jaeyong Lee is both my neighbor, close collaborator, and good friend. He is a really funny guy and a diligent researcher, and the future of blends work in the group is in good hands with him.

I learned a tremendous amount from the students directly above me. Gumi Sethi helped me learn organic-inorganic block copolymer synthesis, small angle x-ray scattering, and many more experimental techniques, and was instrumental in my first publication. Her friendliness extends beyond research and I am excited to work with her again. Mike Galluzzo was my de facto mentor, teaching me everything about experimental electrochemistry. I still make pouch cells the way he taught me in my first year. Mike is an incredibly resourceful, intelligent and hard working scientist. I still think he should be a professor someday. I miss our workouts, ski trips, science discussions, and the way we could talk about anything together.

I am grateful to have joined the lab alongside Lorena Grundy. I am always amazed at her scientific achievements, ranging from her initial work on NMR to her latest work on electrochemistry. Lorena is kind and helpful, and I am sure she will improve the field of scientific pedagogy in the future. Alec Ho, Zach Hoffman, and Neel Shah are three students below me that I have had the pleasure of working with. Alec always impresses me with his research breadth and depth, though he sometimes mixes up short talks with long talks. He is someone I would want on my team, whether that is in academia, industry, or life. I will miss our snowboarding hikes, pool games, and car dialogues, but not shoveling roadways of snow. Zach is a hard worker and selfless leader, someone that every organization needs. I am thankful for our discussions both academic and social, and I will miss running together and partnering up in the defense for intramurals. Neel has taken on scattering experiments adequately, and I am excited to see the interesting neutron science he will publish on.

To the younger students, I am thankful for the short time I have gotten to know you and learned about your budding research. Morgan Seidler and Darby Hickson are both productive researchers and taking more and more leadership in the lab. Karim Aruta and Vivaan Patel both show exceptional initiative and work ethic. Emily Abdo, Michael Bowen, and Lily Gido are all eager to learn and I am sure they will go on to do great things. Please carry on the welcoming disciplined and fun spirit that powers the scientific excellence that is the Balsara Lab.

Outside of the Balsara Lab I have had the pleasure of collaborating with numerous researchers. Dr. Rachel Snyder, Professor Brooks Abel, Dr. Cheol Kang, and Professor Geoffrey Coates were amazing collaborators who synthesized many of the materials in my blends work. I learned so much about both science and scientific presentation from them. Dr. Susana Teixeira helped train me on the NIST neutron scattering beamline and was a vital part of the blends work presented in this dissertation. When the beamlines at NIST shut down, Dr. Lilin He was instrumental in helping me run neutron scattering experiments at ORNL. Joseph Nolan and Carlet Altamirano provided adequate administrative support during my time at Berkeley. I would also like to acknowledge two undergrads that I worked with, Michael Yi and Andrew Lee, both of whom have gone on to graduate school. I also need to thank my qualifying exam committee: Professor Jeff Long, Professor Bryan McCloskey, Professor Rui Wang, and Professor Mary Scott. I am grateful that Bryan and Mary have served on my thesis committee as well.

Outside of graduate school, I have had an amazing support system. Paul Kim and Eric Qiao, it was nice eating lunch once a week together. Kwasi Amofa and the rest of “Your GSI,” we will win that

shirt someday. Andy Rico was an unlikely but good friend I made at pickup soccer through Colinsfooty. The members of the “Goon Lagoon,” Evren Gokcen, Pedro Ojeda, and Valentin Skoutnev, we will always have another adventure to go on. My “non-dota” playing friends, Calvin Luo, Yiding Jiang, and Dave Luo kept me sane at the beginning of 2020 and beyond. Michael Malek, wherever you are, we need to meet up and cold approach. Lorenzo Venneri, we have several trips that we need to go on and startup ideas to develop still. Lilly Luo, thanks for the referral, we need to bake together again. Tristan Nee, you are an inspiration, and as such I must admit I do take a few ideas from you, but it has been so fun; sorry for not being a bro on our Asia trip. I am glad to have known the sunshine that is Yu Hu.

Finally, and most importantly, I must thank my family. To my mother, Ruilian, who has taken care of the entire family, I have had priceless and immeasurable support. There are no words to describe her sacrifice and commitment to us. My father, Xiaoming, laid the foundations of my scientific mind. I am more and more appreciative of his mindset with every passing day. My older sister, Connie, was always the role model to look up to and provides advice and guidance whenever I need it. She really paved the road for my academic journey and none of this would have been possible without her. I am sure my younger brother, David, will be in graduate school someday too, and I hope we can play soccer together more often. My little sister, Jennie, is just beginning her academic journey, but regardless, I am sure she will have a bright future. Thank you all.

FUNDING ACKNOWLEDGEMENT

This work was intellectually led by the Joint Center for Energy Storage Research (JCESR), an Energy Innovation Hub funded by the U.S. Department of Energy, Office of Science, Office of Basic Energy Science, under Contract No. DE-AC02-06CH11357. Work at the Donner Lab, the Molecular Foundry, and the Advanced Light Source, which is a DOE Office of Science User Facility, was supported by Contract No. DE-AC02-05CH11231. Work at the Stanford Synchrotron Radiation Light Source, a user facility at SLAC National Accelerator Laboratory, was supported by the U.S. Department of Energy, Office of Science, Office of Basic Energy Science under Contract No. DE-AC02-76SF00515. We acknowledge the support of the National Institute of Standards and Technology, U.S. Department of Commerce, and Oak Ridge National Laboratory, U.S. Department of Energy, in providing the neutron facilities used in this work. K.W.G. acknowledges funding from a National Defense and Science Engineering Graduate Fellowship.

1 Introduction

1.1 Motivation

Renewable energy is one of the fastest-growing energy sources, with worldwide electricity generation from solar, wind, and hydro expected to overtake fossil fuels by 2050.¹ The variable nature of these renewable energy sources necessitates a means of energy storage to balance variable demand and supply. Rechargeable batteries are a promising technology to meet this need. The most popular rechargeable battery is the lithium-ion battery, which is used almost everywhere today, from portable electronics to electric vehicles. However, numerous improvements are required for the lithium-ion battery to be implemented for large scale grid energy storage: the energy density, lifetime, charge time, cost, and safety must all be improved.^{2,3}

A standard lithium-ion battery consists of a graphite anode, a metal oxide cathode, and an organic liquid electrolyte contained within an inert separator. During charging, current is passed to the battery: lithium in the cathode undergoes an oxidation reaction, becoming lithium ions that move across the electrolyte toward the anode, where it undergoes a reduction reaction. This entire process effectively converts electrical energy into stored chemical potential energy. During discharge, the stored chemical potential energy is converted to electrical energy: the anode releases the lithium ions it had gained from charging in an oxidation reaction, and these ions move through the electrolyte toward the cathode, where it undergoes a reduction reaction to return into the cathode.

The importance of the electrolyte cannot be understated. It must solvate lithium ions, have good electrochemical and thermal stability, support large currents, meet safety metrics, and most importantly, facilitate the movement of ions.²⁻⁵ Understanding ion transport in the electrolyte is of fundamental importance for improving battery technology. This thesis presents electrolyte research to meet two primary challenges facing lithium ion batteries. (1) Energy density, as commercial lithium ion batteries have nearly reached their theoretical energy density of 385 Wh kg⁻¹.⁶ (2) Safety, as the organic liquid electrolytes found in lithium ion batteries (typically a mixture of carbonates) are highly flammable due to their volatility.

Substituting the graphite anode with pure lithium metal can enable higher energy densities as lithium metal has a specific capacity about ten times higher than that of graphite.^{7,8} However, lithium metal is not stable with traditional organic liquid electrolytes.^{7,9} One solution is to replace the liquid electrolyte with a polymer electrolyte, as polymers can be stable against lithium metal and are also inherently nonvolatile materials.^{10,11} Unfortunately, there are several issues discouraging the use of polymer electrolytes in lithium batteries with the main problem being slow transport of ions. The ionic conductivity, which provides a measure of the motion of ions, is orders of magnitude lower in polymer electrolytes than in traditional liquid electrolytes.¹² Hence, a major goal is to improve upon the ion transport in polymer electrolytes.

1.2 Polymer Electrolytes

The field of polymer electrolytes began in 1973 when Fenton, Wright, and Parker discovered that alkali metal salts were soluble in poly(ethylene oxide) (PEO).¹³ Since then, there has been significant interest in polymer electrolytes for battery applications.^{12,14-19} Still, the most widely studied polymer electrolyte remains mixtures of PEO with a lithium salt due to its nonvolatility,

electrochemical stability, and compatibility with lithium salts such as lithium bis(trifluoromethanesulfonyl)imide (LiTFSI).^{12,17} The strong ability of PEO to solvate lithium salts is due to the presence of oxygen-containing ether linkages.

The ionic conductivity of PEO/LiTFSI is around 10^{-3} S cm⁻¹ at elevated temperatures (>70 °C) above its crystalline melting point.²⁰ This is an order of magnitude below competitive ionic conductivity values for standard lithium ion batteries.⁴ Improvement upon this metric remains a longstanding goal in the field of polymer electrolytes. Several strategies have been pursued such as additives (ionic liquids, nanoparticles, plasticizers), block copolymers, and blending.^{21–26} This thesis focuses on polymer electrolytes consisting of homopolymer electrolytes and heterogeneous electrolytes such as block copolymers and polymer blends.

Heterogeneous electrolytes such as block copolymer and polymer blends have interesting thermodynamic properties. Block copolymers such as polystyrene-*b*-poly(ethylene oxide) consist of two different polymer units chemically connected by a covalent bond. Polymer blends consist of mixtures of two distinct polymers. The favorability of mixing between two different polymers is governed by the Gibbs free energy of mixing, which is composed of the entropy gain of mixing and enthalpy of mixing. The enthalpy of mixing depends on the Flory-Huggins interaction parameter, which describes how much two different polymers like or dislike each other. The addition of salt can affect the Flory-Huggins interaction parameter and numerous other factors such as polymer chain length, volume fraction, and temperature can also affect the thermodynamics of these heterogeneous systems.^{26–31} This concept can be extended beyond polymer electrolytes for battery applications to topics such as membrane desalination where ion uptake in polymeric networks is dictated by thermodynamics, *e.g.* Donnan equilibrium.³²

Block copolymers can self-assemble into different morphologies, ranging from lamellar to hexagonally packed cylinders, and the different types of morphologies are known to affect ion transport.^{23,33} Polymer blends, because they are not chemically bonded, can either be immiscible or phase separated like mixtures of oil and water, or they can form miscible, single phase mixtures. The relationship between ion transport and miscibility is not well understood.

1.3 Electrochemical Characterization of Polymer Electrolytes

While ionic conductivity provides a simple measure for the motion of ions, full electrochemical characterization is necessary to fully understand transport in an electrolyte. For example, differences in the movement of the cation and anion during charging or discharging of a battery can lead to the development of concentration gradients within the electrolyte. Such concentration gradients can result in concentration overpotentials, reducing the usable current. In the case of very steep concentration gradients, the ion concentration within the electrolyte can be completely depleted, leading to battery failure.^{34–36}

A complete description of ion transport in electrolytic mixtures was first developed by Onsager, who recognized the importance of three independent transport parameters that are now known as Onsager coefficients.³⁷ These coefficients quantify the frictional interactions between cation and solvent, anion and solvent, and anion and cation. Measuring these transport coefficients is quite challenging.

Newman formulated concentrated solution theory based on the Onsager approach, recasting ion transport in terms of three different but related transport coefficients: ionic conductivity, salt diffusion coefficient, and cation transference number with respect to the solvent velocity.^{38,39} In addition, it is necessary to measure the thermodynamic factor, which quantifies the dependence of the mean molal activity coefficient of the electrolyte on salt concentration, *i.e.* a measurement of the ideality of the electrolyte. These four parameters can all be determined from a set of well-defined experiments.⁴⁰ While this thesis focuses on Newman's approach for characterizing ion transport, there are many other frameworks proposed in the literature.^{41–50}

Newman's concentrated solution theory enables full-scale modeling of concentration gradients in the electrolyte during battery operation. Furthermore, this approach applies to any mixture of charged species in a neutral solvent, as it is not just limited to polymer electrolytes. Thus, fully characterizing an electrolyte can allow for battery performance optimization.

A longstanding goal is to gain a fundamental understanding of the molecular underpinnings for the transport observed in these polymer systems. The advantage of studying polymer electrolytes is the wide variable space that can be tuned *i.e.* size, chemical structure, identity, salt loading, additive. Our research focuses on observing these systems in this variable space using a wide variety of experimental techniques.

1.4 Outline of Dissertation

This work focuses on the thermodynamics and ion transport of polymer blends and electrolytes.

Chapter 2 discusses the importance of the cation transference number and its dependence on reference frames. Two experimental approaches (Hittorf and Bruce-Vincent) for measuring the cation transference number are described, and experimental data for a PEO/LiTFSI system is shown. Chapter 3 covers the ion transport properties of PEO/LiTFSI in great depth in the framework of Newman's concentrated solution theory, paying special attention to uncertainty analysis and error propagation. Data from 64 independent PEO/LiTFSI samples, with PEO molecular weights ranging from 5 kg mol⁻¹ to 275 kg mol⁻¹, are compiled and analyzed to demonstrate that ion transport properties are constant above the entanglement threshold. Chapter 4 investigates the possibility of a salt diffusion coefficient dependence on molecular weight in PEO/LiTFSI and discusses its potential implications.

In Chapter 5, we extend beyond homopolymer electrolytes to study a hybrid organic-inorganic block copolymer with the organic conducting block based on PEO. Changing the chemical structure of the inorganic monomer resulted in differences in both thermodynamics and surprisingly, ion transport. Morphology is characterized using small angle x-ray scattering, and transmission electron microscopy. In Chapter 6 we use a different approach, blending PEO with a poly(ether-acetal) and LiTFSI to form a polymer blend electrolyte. We find that in the presence of enough salt, miscible blend is obtained, an important result that demonstrates it is possible to obtain homogeneous mixtures of two chemically distinct polymers with a lithium salt for electrolytic applications. Small angle neutron scattering is used as an unambiguous method for determining miscibility. Chapter 7 is a continuation on polymer blends work, investigating the relationship between phase behavior and ion transport in two new polymer blend electrolyte systems, including one that does not include PEO as a component.

Chapter 8 broaches the thermodynamics of univalent and multivalent charged polymer networks in electrolytic solutions. We present a new set of equations for describing Donnan equilibrium, the partitioning of ions between a charged gel and an electrolytic solution, that accounts for the elasticity of the gel and enthalpic interactions. Our model is compared to experimental data from literature.

Chapter 9 provides a summary of the work and outlook for future experiments. This thesis provides a comprehensive description for the measurement and analysis of ion transport in polymer electrolytes. It is also a starting point for further studies into thermodynamics of polymer blend electrolytes as well as Donnan equilibrium. It is my hope that the work presented here can help enable the development of better batteries and improved energy storage.

2 The Transference Number[†]

Abstract

The performance of rechargeable batteries and other electrochemical systems depends on the rate at which the working ion (often a cation) is transported from one electrode to the other. The cation transference number is an important transport parameter that affects this rate. The purpose of this perspective is to distinguish between approximate and rigorous methods used in the literature to measure the transference number. We emphasize the fact that this parameter is dependent on the reference frame used in the analysis; care must be taken when comparing values obtained from different sources to account for differences in reference frames.

2.1 Introduction

Virtually all batteries contain electrolytes dissolved in solvents. The alkaline battery contains KOH, the lead-acid battery contains H₂SO₄, and the lithium-ion battery contains LiPF₆. The presence of two dissociated ions makes them three-species, two-component systems. Electrolytes comprising a lithium salt dissolved in a polymer such as poly(ethylene oxide) are similar to conventional electrolytes except for the fact that the solvent is a chain-like molecule. Describing transport in three-species systems requires three transport coefficients, which are often taken to be conductivity, κ , salt diffusion coefficient, D , and t_+^0 , the cation transference number with respect to the solvent velocity.^{38,51,52}

The passage of current through these systems causes a gradient in the concentration of the electrolyte. At early times, the gradients are localized near the electrode surface, where there is a change in the transference number of the current carrying species. These gradients propagate into the solution as time progresses. These processes are quantified in concentrated solution theory,³⁸ wherein the time-dependence of electrolyte molarity, c , in the presence of ionic current is given by the following material-balance equation:

$$\frac{\partial c}{\partial t} + \nabla \cdot (c\mathbf{v}_0) = \nabla \cdot \left[D \left(1 - \frac{d \ln c_0}{d \ln c} \right) \nabla c \right] - \frac{\mathbf{i} \cdot \nabla t_+^0}{F z_+ \nu_+}, \quad (2.1)$$

where \mathbf{v}_0 is the spatially dependent solvent velocity, c_0 is the solvent molarity, \mathbf{i} is the current density, F is the Faraday constant, z_+ is the charge number of cation, and ν_+ is the moles of cations obtained by dissociating a mole of the electrolyte. An expression that is equivalent to equation 2.1 can be derived in terms of the mass fraction of the electrolyte, ω_e .³⁸

$$\rho \frac{\partial \omega_e}{\partial t} + \rho \mathbf{v} \cdot \nabla \omega_e = \nabla \cdot (\rho D \nabla \omega_e) - \frac{M_e \mathbf{i} \cdot \nabla t_+^M}{F z_+ \nu_+}, \quad (2.2)$$

where ρ is the density of the electrolytic solution, \mathbf{v} is the mass averaged velocity, M_e is the molar mass of the electrolyte, and t_+^M is the cation transference number with respect to the mass average velocity.

[†] This chapter was reported in *Energy & Environmental Materials*, **2022**, 5 (2), 366-369.

The transference number is defined as the fraction of ionic current carried by the cation in an electrolyte of uniform composition. The cation current is given by

$$\mathbf{i}_+ = Fc_+z_+\mathbf{v}_+, \quad (2.3)$$

where \mathbf{v}_+ is the velocity of the cation. A frame of reference is necessary for defining any velocity and thus a frame of reference is also necessary to define the transference number. It has long been recognized that the solvent velocity is a convenient frame of reference for quantifying the cation current.^{38,51–54} We note in passing that the total current \mathbf{i} is independent of the frame of reference due to charge neutrality.

2.2 Experimental Methods: Hittorf Cell and Symmetric Cell

Recognition of the importance of the transference number dates back to Hittorf.^{53,54} Figure 2.1 shows one version of the Hittorf cell which comprises two chambers connected by a tube. Initially, the electrolyte concentration is uniform through the cell; we refer to this concentration as c_{av} . A constant current, I , is passed through the cell using two electrodes placed in the two chambers. For simplicity, we assume that the electrodes are metal foils that can undergo the redox reactions shown in Figure 2.1. As current flows, cations M^{z+} enter the anodic chamber, which requires the transport of anions X^{z-} from the tube into the anodic chamber to maintain charge neutrality. This will result in depletion of anions from the cathodic chamber. We assume that the measurements are conducted at early times so that the concentration within the tube can be approximated as c_{av} . This also implies that the electrolyte concentrations in the two chambers near the ends of the tube are also c_{av} , as shown schematically in Figure 2.1. At time t , the chambers are isolated, perhaps by closing valves located at the ends of the tube, and the final electrolyte concentration in the anodic chamber, c_{final} , is measured.

The accumulation of M^{z+} ions in the anodic chamber can be written as:

$$(c_{final} - c_{av})V_{chamber} = \text{input} - \text{output} = \frac{1}{z_+v_+F}(It - It_+), \quad (2.4)$$

where $V_{chamber}$ is the volume of the anodic chamber, and t_+ is the fraction of current carried by the cation at the concentration c_{av} . The moles of M^{z+} entering the anodic chamber (input) is proportional to It , and the moles of M^{z+} ions exiting the chamber through the tube (output) is proportional to Itt_+ . The prefactor on the right side of equation 2.4 converts coulombs into moles. Rearranging equation 2.4 gives:

$$t_+ = 1 - z_+v_+F \frac{(c_{final} - c_{av})V_{chamber}}{It}. \quad (2.5)$$

Data from the Hittorf cell can be used to determine t_+ if all other parameters on the right side of equation 2.5 are measured.

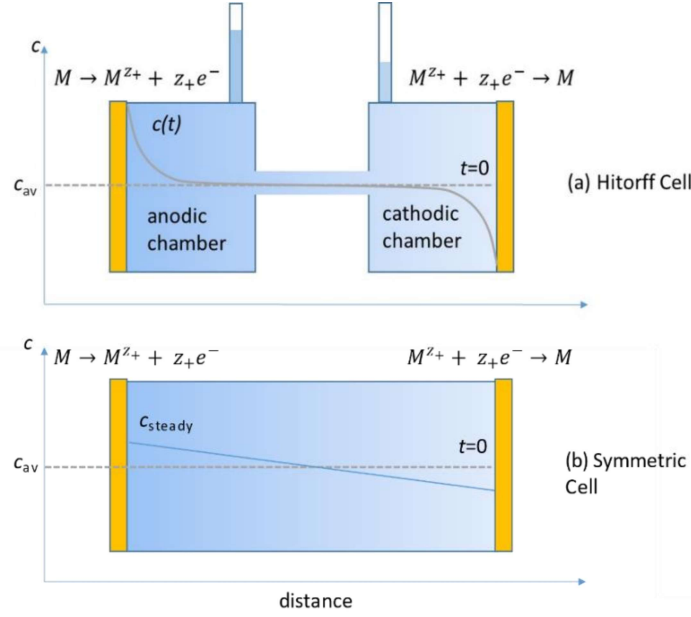


Figure 2.1. Schematics of cells used to measure the transference number. The electrolyte that is initially of concentration c_{av} is placed between two electrodes. The final electrolyte concentrations are shown by curves and shading. Ionic current is drawn from left to right by polarizing the nonblocking metal electrodes (M). Salt concentration (c) profiles after ionic current is drawn are also shown. For the lower drawing, sufficient time has passed to yield a steady profile.

Equation 2.5 assumes zero solvent motion in the passage between the two chambers in the Hittorf cell. It has been experimentally confirmed that the motion of solvent molecules between the chambers is nonnegligible (see Figure 2.1). A more detailed analysis of solvent transport in the Hittorf cell based on concentrated solution theory^{38,55-57} gives the following expression for the transference number:⁵⁸

$$t_+^0 = 1 - z_+ \nu_+ F \frac{(c_{\text{final}} - c_{av})V_{\text{chamber}}}{It(1 - \bar{V}_e c_{av})}, \quad (2.6)$$

where \bar{V}_e is the partial molar volume of the electrolyte and t_+ in equation 2.5 is replaced by t_+^0 .

If the transference number in one reference frame is measured, it can readily be determined in another reference frame.³⁸ For example:

$$t_+^M = t_+^0 \omega_0 + \omega_-, \quad (2.7)$$

where ω_0 and ω_- are the solvent and anion mass fractions.

Even though the transference number is defined for a solution of uniform composition, it is a property that can be used to quantify transport in electrolytes which are not of uniform composition; see equations 2.1 and 2.2. Any attempt to pass current through an electrolyte results in an electrolyte of nonuniform composition, and experiments that are used to determine the transference number must account for this complication, as done by Hittorf. In some cases, the nonuniformity may be restricted to narrow regions near the electrodes (e.g., Figure 2.1). The transference number in equation 2.5 is one that applies to an infinitely dilute electrolyte. Even in this case, a reference

frame is needed for the definition; one would not want to develop separate equations for cells at rest and cells located on a moving vehicle. In the dilute limit, the mass average and solvent velocities are identical.

Bruce et al. and Watanabe et al. proposed an approximate method for measuring the transference number.⁵⁹⁻⁶¹ In this experiment, a fixed potential is applied to a symmetric cell with electrodes similar to those used in the Hittorf cell, and the current is measured as a function of time (Figure 2.1b). It was shown that if the electrolyte is infinitely dilute then the transference number is given by:⁶²

$$\frac{i_{ss}}{i_0} = t_+, \quad (2.8)$$

where i_0 is the initial current density measured before concentration polarization sets in and i_{ss} is the current density obtained at steady state. Experiments are seldom done on infinitely dilute electrolytes, partly because the need to maximize the charge carrier concentration forces us to use concentrated electrolytes in practical applications. In concentrated electrolytes, the current ratio i_{ss}/i_0 , which we call ρ_+ , is given by:

$$\frac{i_{ss}}{i_0} = \rho_+ = \frac{1}{1 + Ne}, \quad (2.9)$$

where Ne , a dimensionless quantity that we call the Newman number, is given by

$$Ne = \frac{v}{(v_+z_+)^2} \frac{\kappa RT(1 - t_+^0)^2}{F^2 Dc} \left(1 + \frac{d \ln \gamma_{\pm}}{d \ln m} \right), \quad (2.10)$$

where v is total moles of cations and anions produced by dissociating a mole of the electrolyte, R is the gas constant, T is the temperature, γ_{+-} is the mean molal activity coefficient of the electrolyte, and m is molality. t_+^0 can thus be measured rigorously using symmetric cells if the other parameters in equation 2.10 are known.⁶³ κ can be measured by ac impedance, D can be measured by the restricted diffusion method, and the dependence of γ_{+-} on m can be measured in concentration cells, as reported by Ma et al.⁴⁰

In a Hittorf cell, the net influx of cations into the anodic chamber via the electrode is It/z_+v_+F . When an electrolyte with positive t_+^0 is examined in a Hittorf cell, the net accumulation of cations in the anodic chamber is less than this influx, indicating that cations leave the anodic chamber and enter the tube. On the other hand, when an electrolyte with negative t_+^0 is examined in a Hittorf cell, the net accumulation of cations in the anodic chamber is greater than this influx. In other words, cations enter the tube from the cathodic chamber, travel through the tube, and enter the anodic chamber. There are two possible microscopic reasons for this: (1) the cations are present in negatively charged clusters that are drawn to the positive electrode, or (2) the solvent molecules are drawn toward the anodic chamber, and cations are complexed with them. Similar scenarios exist for t_+^M , but solvent motion is likely to play a smaller role in determining its value. Computer simulations are well-suited to examine the molecular origins of the measured transference number.^{49,64,65}

2.3 Poly(ethylene oxide) Electrolytes

In Figure 2.2, we show the dependence of t_+^0 , t_+^M , and ρ_+ on c for a well-studied electrolyte: a mixture of poly(ethylene oxide) and lithium bis(trifluoromethanesulfonyl)imide (PEO/LiTFSI).^{20,35,63,66} The plot, which is taken from ref²⁰, is based on data obtained from 64 independent electrolyte samples. Thus, the quantity measured directly, ρ_+ , has relatively narrow error bars. However, t_+^0 is obtained by combining several experimentally measured quantities (see equation 2.10), and this results in much larger error bars. ρ_+ , t_+^0 , and t_+^M must be equal in the dilute limit. All the measured data in Figure 2.2 appear to be well outside this limit.

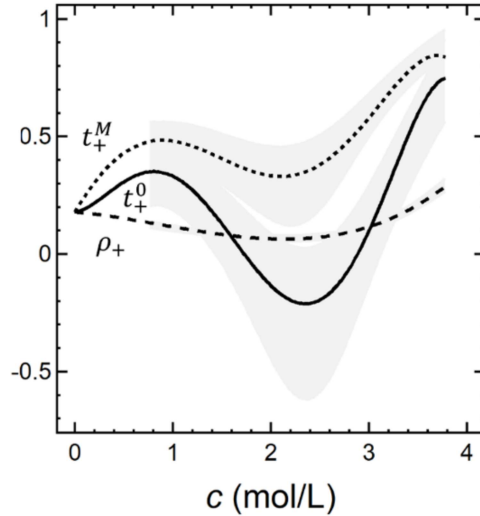


Figure 2.2. Plots of the current fraction and transference numbers with respect to the solvent and mass average velocities versus concentration for PEO/LiTFSI at 90 °C. The shaded areas reflect 95% confidence intervals for t_+^0 and t_+^M . The same confidence interval for ρ_+ is commensurate with the thickness of the curve. These curves are fits to experimentally measured data points for $0.77 < c < 3.77$ and an extrapolated $c = 0$ value of $\rho_+ = t_+^0 = t_+^M = 0.1783$ in the dilute limit where we fit $\rho_+ = 0.0155c^3 - 0.0412c^2 - 0.0368c + 0.1783$. The curves for t_+^0 and t_+^M are given by the following polynomial fits: $t_+^0 = -0.0532c^5 + 0.4612c^4 - 1.2179c^3 + 0.9141c^2 + 0.0488c + 0.1783$ and $t_+^M = -0.0189c^5 + 0.1336c^4 - 0.1886c^3 - 0.3108c^2 + 0.6869c + 0.1783$. Note that ρ_+ is not a good approximation for either transference number.

The concentration-dependence of the three parameters is very different. ρ_+ is positive at all concentrations, as required by the second law of thermodynamics (see equations 2.9 and 2.10), and has a shallow minimum at $c = 2.2$ mol/L. t_+^M is also positive at all concentrations but has a deeper minimum at roughly the same concentration. The deepest minimum is seen in t_+^0 ; at $c = 2.4$ mol/L, $t_+^0 = -0.2$. t_+^0 is negative at concentrations between 1.8 and 2.9 mol/L. The importance of specifying the frame of reference is clear from Figure 2.2. ρ_+ is not a good approximation for the transference number in any frame of reference.

2.4 Conclusions

The overall objective of measurements of the transference number and other transport properties is to determine the performance of batteries as they are charged or discharged. Figure 2.3 shows a schematic of a battery. Two examples of salt concentration profiles in the battery when current is drawn through it are given in Figure 2.3. For a given battery, the magnitude of the concentration gradients obtained at the same state-of-charge increases with increasing current. At low current density (e.g., i_1), the salt concentration is finite throughout the battery and the entire electrodes can participate in redox reactions. At sufficiently high current density, however, (e.g., i_2) the local salt concentration is zero at some locations in the electrodes (e.g., $x > L_{\text{limit}}$ in Figure 2.3), and active particles in these regions cannot participate in redox reactions. This will lead to limited utilization of the capacity of the battery and other complications such as irreversible side reactions in the $x > L_{\text{limit}}$ region.

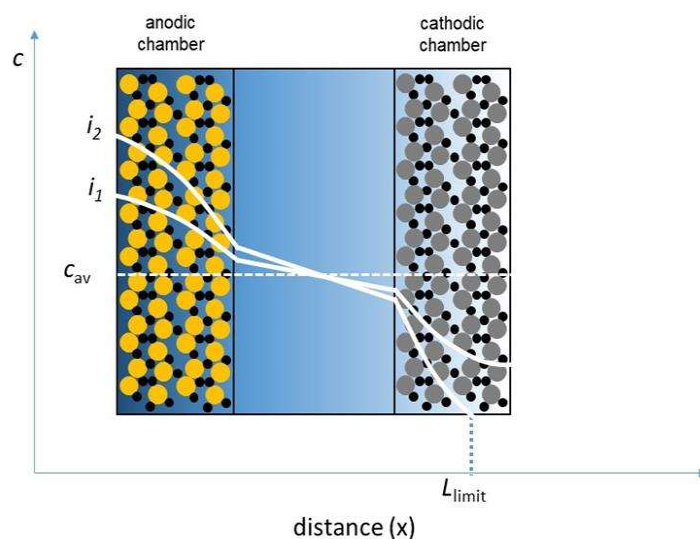


Figure 2.3. Schematic of a battery with a composite anode and cathode. Active particles are shown in different colors with electron-conducting carbon particles shown in black are in intimate contact with the electrolyte. An inert porous separator (not shown explicitly) flooded with the electrolyte separates the cathodic and anodic chambers. The battery contains an electrolyte that is initially of concentration c_{av} . The salt concentration profile at two applied current densities ($i_2 > i_1$) are shown. At the lower current density, all of the active particles participate in the redox reaction. At the higher current density, the cathode particles in the region $x > L_{\text{limit}}$ do not participate in the redox reaction. The shading of the electrolytic phase reflects salt concentration. Predicting the concentration profiles as a function of current density requires knowledge of the concentration dependence of the transference number.

Equation 2.1 (or equivalent equations such as equation 2.2) lies at the heart of computer programs used to predict electrolyte concentration profiles in functioning battery.⁶⁷ The concentration dependence of the transference number (not the absolute magnitude but the magnitude of the gradient of the curve in Figure 2.2) is an important parameter that is needed for such calculations.

In conclusion, we have discussed the transference number in the context of the Hittorf cell, symmetric cells, and batteries. We stress the importance of specifying the frame of reference when

defining the transference number. The large error bars associated with transference numbers are unavoidable if they are determined by combining the results of four separate experiments as is routine in current literature.^{40,63,68} Emerging methods such as electrophoretic NMR may enable higher precision measurements of the transference number.^{69–71}

2.5 Acknowledgements

This work was intellectually led by the Joint Center for Energy Storage Research (JCESR), an Energy Innovation Hub funded by the U.S. Department of Energy, Office of Science, Office of Basic Energy Science, under Contract No. DE-AC02-06CH11357. K.W.G. acknowledges funding from a National Defense and Science Engineering Graduate Fellowship.

2.6 Nomenclature

Table 2.1. List of symbols and abbreviations.

Symbol	Meaning
KOH	Potassium hydroxide
H ₂ SO ₄	Sulfuric acid
LiPF ₆	Lithium hexafluorophosphate
κ	Ionic conductivity
D	Salt diffusion coefficient
t_+^0	Cation transference number with respect to solvent velocity
c	Electrolyte concentration in molarity
t	Time
\mathbf{v}_0	Spatially dependent solvent velocity
c_0	Solvent molarity
\mathbf{i}	Current density
F	Faraday constant
z_+	Cation charge number
ν_+	Moles of cation obtained by dissociating a mole of electrolyte
ω_e	Mass fraction of electrolyte
ρ	Density of electrolyte
\mathbf{v}	Mass averaged velocity
M_e	Molar mass of electrolyte
t_+^M	Cation transference number with respect to the mass average velocity
\mathbf{i}_+	Cation current
c_0	Solvent concentration in molarity
c_+	Cation concentration in molarity
\mathbf{v}_+	Cation velocity
V_{chamber}	Volume of anodic chamber
t_+	Fraction of current carried by the cation
c_{av}	Average concentration in molarity
c_{final}	Final concentration in molarity
V_e	Partial molar volume of electrolyte

ω_0	Solvent mass fraction
ω_-	Anion mass fraction
i_0	Initial current
i_{ss}	Current at steady states
ρ_+	Current fraction
Ne	Dimensionless Newman number
ν	Total moles of cations and anions produced by dissociating a mole of electrolyte
R	Gas constant
T	Temperature
γ_{+-}	Mean molal activity coefficient of the electrolyte
m	Molality
PEO	Poly(ethylene) oxide
LiTFSI	Lithium bis(trifluoromethanesulfonyl)imide

3 Electrochemical Properties of Poly(ethylene oxide) Electrolytes Above the Entanglement Threshold[†]

Abstract

Ion transport in electrolytes depends on three transport coefficients, conductivity (κ), salt diffusion coefficient (D), and the cation transference number with respect to the solvent velocity (t_+^0), and the thermodynamic factor (T_f). Current methods for determining these parameters involve four separate experiments, and the coupled nature of the equations used to determine them generally results in large experimental uncertainty. We present data obtained from 64 independent polymer electrolytes comprising poly(ethylene oxide) (PEO) and lithium bis(trifluoromethanesulfonyl)imide (LiTFSI) salt. The molecular weights of PEO ranged from 5 to 275 kg mol⁻¹; these samples are all above the entanglement threshold. We minimize the experimental uncertainty in transport and thermodynamic measurements by exploiting the fact that ion transport in entangled polymer electrolytes should be independent of molecular weight. The dependence of κ , D , t_+^0 , and T_f as a function of salt concentration in the range $0.035 \leq r \leq 0.30$ are presented with a 95% confidence interval, where r is the molar ratio of lithium ions to ethylene oxide monomer units. While κ , D , and T_f are all positive as required by thermodynamic constraints, there is no constraint on the sign of t_+^0 . We find that t_+^0 is negative in the salt concentration range of $0.093 \leq r \leq 0.189$.

3.1 Introduction

A complete description of ion transport in electrolytic mixtures was first provided by Onsager, who recognized the importance of three independent transport parameters that we refer today as Onsager coefficients.³⁷ These coefficients quantify frictional interactions between the cation and solvent, anion and solvent, and anion and cation. Measuring these transport coefficients is, however, nontrivial and beyond the scope of Onsager's original work. Newman developed concentrated solution theory based on the Onsager approach and recast ion transport in terms of three different but related transport coefficients: ionic conductivity (κ), salt diffusion coefficient (D), and cation transference number with respect to the solvent velocity (t_+^0).³⁸ In addition, it is necessary to measure the thermodynamic factor (T_f) which quantifies the dependence of the mean molal activity coefficient of the electrolyte, γ_{\pm} , on salt concentration ($\frac{d \ln \gamma_{\pm}}{d \ln(m)}$), where m is the molality. Newman's approach is powerful because each of the four parameters κ , D , t_+^0 , and T_f can be determined from a set of well-defined experiments.⁴⁰

While we focus on Newman's approach for characterizing ion transport, it is one of many frameworks proposed in the literature.⁴¹⁻⁵⁰ Some of these approaches employ different definitions for diffusion coefficients and transference numbers. For completeness, we clarify the definitions of these two parameters that are used in this paper, as specified in ref. ³⁸. (1) The salt diffusion coefficient, D , is the proportionality factor that relates the flux density of salt to the

[†] This chapter was reported in *Solid State Ionics*, **2021**, 364, 115609.

concentration gradient. (2) The cation transference number with respect to the solvent velocity, t_+^0 , is the fraction of ionic current carried by the cation relative to the solvent velocity in an electrolyte of uniform composition, *i.e.*, the cation velocity needed to calculate ionic current is determined using the solvent velocity as the reference. Even though t_+^0 is defined for a solution of uniform composition, it is a property that can be used to quantify transport in electrolytes which are not of uniform composition, but it no longer represents the fraction of the current carried by the cation.³⁸ There is no ambiguity in the definitions of either conductivity, κ , or the mean molal activity coefficient of the electrolyte, γ_{\pm} .

The Onsager-Newman approach applies to any mixture of charged species in a neutral solvent such as a low molecular weight liquid or a high molecular weight polymer. An example of an electrolyte of interest for rechargeable lithium batteries is a mixture of a lithium salt such as lithium hexafluorophosphate (LiPF₆) dissolved in a suitable organic solvent such as propylene carbonate (PC); commercial batteries employ a mixture of carbonate solvents.^{5,72,73}

The passage of current through a battery results in the formation of concentration gradients within the electrolytic phase. The rate at which batteries can be charged and discharged is limited by the magnitude of these gradients. The limiting current is typically defined as the current at which the ion concentration at the cathode (we assume that the working ion is a cation) approaches zero. Operating a battery at currents that exceed this value can result in rapid degradation and, in some cases, catastrophic failure. Similar problems arise if the salt concentration at the anode exceeds the solubility limit.^{36,74} Concentration gradients in a battery electrolyte can only be predicted if κ , D , t_+^0 , and T_f are known functions of salt concentration.^{35,36,75}

The Newman approach for measuring transport coefficients involves four separate experiments.⁴⁰ Conductivity, κ , is obtained from a relatively straightforward experiment via ac impedance measurements using blocking electrodes. For the case of 1 M LiPF₆/PC electrolytes at 25 °C, κ is consistently reported^{58,76–80} to lie between 5.9×10^{-3} to 6.4×10^{-3} S cm⁻¹. Measuring the other transport parameters for lithium battery electrolytes requires the construction of lithium/electrolyte/lithium symmetric cells. The data obtained from these cells is inherently more complex due to the extreme reactivity of lithium, formation of the solid electrolyte interphase between lithium metal and all known electrolytes, and the instability of the lithium/electrolyte interface during electrochemical plating.^{7,8,81} Of the remaining parameters, the salt diffusion coefficient, D , is most straightforward to measure because it is obtained directly from restricted diffusion experiments. In spite of this, the reported^{58,79,80} value of the salt diffusion coefficient, D , in 1 M LiPF₆/PC electrolytes at 25 °C varies significantly, from 1.8×10^{-6} to 4.0×10^{-6} cm² s⁻¹. Determining t_+^0 and T_f is further complicated because they are determined by combining results from two separate experiments, one involving a symmetric cell and the other involving a concentration cell where two electrolytes at different salt concentrations are coupled together between lithium electrodes.⁴⁰ The symmetric cell is used to obtain the steady-state current fraction, ρ_+ , the ratio of current obtained under steady dc polarization to that obtained in the absence of concentration polarization.⁸² The concentration cell is used to measure the dependence of the open circuit potential, U , on salt concentration ($\frac{dU}{d\ln(m)}$). If we combine the values of D given above for 1 M LiPF₆/PC with typical values^{58,76–80,83,84} for κ (6.1×10^{-3} S cm⁻¹), ρ_+ (0.33), and $\frac{dU}{d\ln(m)}$ (-90 mV ln(m)⁻¹), the estimated values of t_+^0 are 0.36 and -0.43. In other words, the uncertainty in salt

diffusion coefficient, which by itself seems reasonable, is so large that even the sign of t_+^0 cannot be determined.

While there are many reports of κ , D , t_+^0 , and T_f in the literature, a detailed analysis of the uncertainty in the reported values is seldom mentioned. In this paper, we report the values of these parameters obtained in a standard polymer electrolyte, a mixture of poly(ethylene oxide) (PEO) and lithium bis(trifluoromethanesulfonyl)imide (LiTFSI) salt. We present data obtained at 90 °C from polymers with molecular weights ranging from 5 to 275 kg mol⁻¹. We define a salt concentration r as the molar ratio of lithium ions to ethylene oxide repeat units. Our study covers salt concentrations in the range $0.005 \leq r \leq 0.3$. In these electrolytes, the PEO chains are entangled; the critical molecular weight for entanglement in these polymer chains is 2 kg mol⁻¹.^{85,86} The importance of chain entanglement in polymer electrolytes was first recognized by Shi and Vincent.⁸⁷ A previous study⁸⁸ showed that κ of PEO/LiTFSI at a fixed salt concentration was independent of polymer molecular weight above the entanglement threshold, an experimental observation corroborated by molecular dynamics simulations.⁸⁹ In this paper, we show that this is more or less true at all salt concentrations. In addition, D , ρ_+ , $\frac{dU}{d \ln(m)}$, t_+^0 , and T_f are also more or less independent of molecular weight above the entanglement threshold at all salt concentrations. An important but rarely mentioned advantage of polymer electrolytes, then, is the capability to measure electrolyte properties using experiments that cover a wide range of molecular weights above the entanglement threshold, and average the data obtained from the different electrolytes, thereby reducing experimental uncertainty. In contrast, in the case of liquid electrolytes such as 1 M LiPF₆/PC, properties can only be measured at a single solvent molecular weight.

3.2 Experimental Methods

3.2.1 Electrochemical Characterization

κ is determined by ac impedance spectroscopy of electrolytes with blocking electrodes. Measuring D and ρ_+ require lithium/electrolyte/lithium symmetric cells: D is measured by restricted diffusion⁹⁰ and ρ_+ via the Bruce-Vincent^{60,91} method. U is measured by monitoring the open circuit potential of a concentration cell in which an electrolyte of salt concentration m is contacted together with a reference electrolyte of $r = 0.06$ or $m = 1.38$ kg mol⁻¹. $\frac{dU}{d \ln(m)}$ can be obtained from the slope of a plot of U with respect to the natural logarithm of m .

The thermodynamic factor, T_f , is given by the following equation:

$$T_f = \frac{\kappa}{2RTDc \left(\frac{1}{\rho_+} - 1 \right)} \left(\frac{dU}{d \ln(m)} \right)^2 \quad (3.1)$$

where R is the gas constant, T is the temperature, and c is the molarity. The cation transference number is given by the following equation:

$$t_+^0 = 1 - t_-^0 = 1 - \frac{FDc}{\kappa \left(\frac{dU}{d \ln(m)} \right)} \left(1 - \frac{1}{\rho_+} \right) \quad (3.2)$$

where t_-^0 is the anion transference number and F is the Faraday constant.

Data was taken from previously published results which also include more detailed experimental procedures for measuring each transport parameter (see Table 3.1).^{35,63,75,92–94} Data used in this report, and their units of measurement, is provided in the Supporting Information (SI).

Table 3.1. PEO molecular weights in PEO/LiTFSI electrolytes

Molecular Weight (kg mol ⁻¹)	Reference(s)
5	Pesko et al. Chintapalli et al.
10	Hoffman et al.
35	Gribble et al.
100	Zheng et al.
275	Pesko et al.

3.2.2 Error Propagation

The electrochemical data shown at each specific molecular weight and salt concentration is the average of at least three measurements in as many different samples. The error bars are the standard deviation of the measured values among the samples. We use standard error propagation for t_+^0 , assuming independent variables and neglecting correlations.⁹⁵ The error for t_+^0 , then, is given by a simplified expression:

$$\delta t_+^0 = |t_-^0| \sqrt{\left(\frac{\delta\kappa}{\kappa}\right)^2 + \left(\frac{\delta D}{D}\right)^2 + \left(\frac{\delta\rho_+}{\rho_+}\right)^2 + \left(\frac{\frac{\delta dU}{d\ln(m)}}{\frac{dU}{d\ln(m)}}\right)^2} \quad (3.3)$$

where $|t_-^0|$ is the magnitude of the anion transference number and the standard deviations for each electrochemical measurement are given by $\delta\kappa$, δD , $\delta\rho_+$, and $\delta\frac{dU}{d\ln(m)}$. Note that the first term of the right side of Equation 3.3 is the magnitude of the anion transference number, and we also include error from the concentration cell data, facts that were missed in ref⁶³. $\delta\kappa$, δD , and $\delta\rho_+$ are experimental standard deviations while $\delta\frac{dU}{d\ln(m)}$ is approximated from the fit of the experimental concentration cell data by using each fit coefficient's standard deviation and applying standard error propagation.⁹⁵

3.3 Results and Discussion

Figure 3.1 plots the electrochemical properties κ , D , ρ_+ , and U of PEO/LiTFSI electrolytes as a function of PEO molecular weight. Five representative salt concentrations are shown ($r = 0.02$,

0.08, 0.14, 0.2, and 0.3). As expected, none of the properties shown in Figure 3.1 exhibit discernible and systematic dependence on molecular weight.

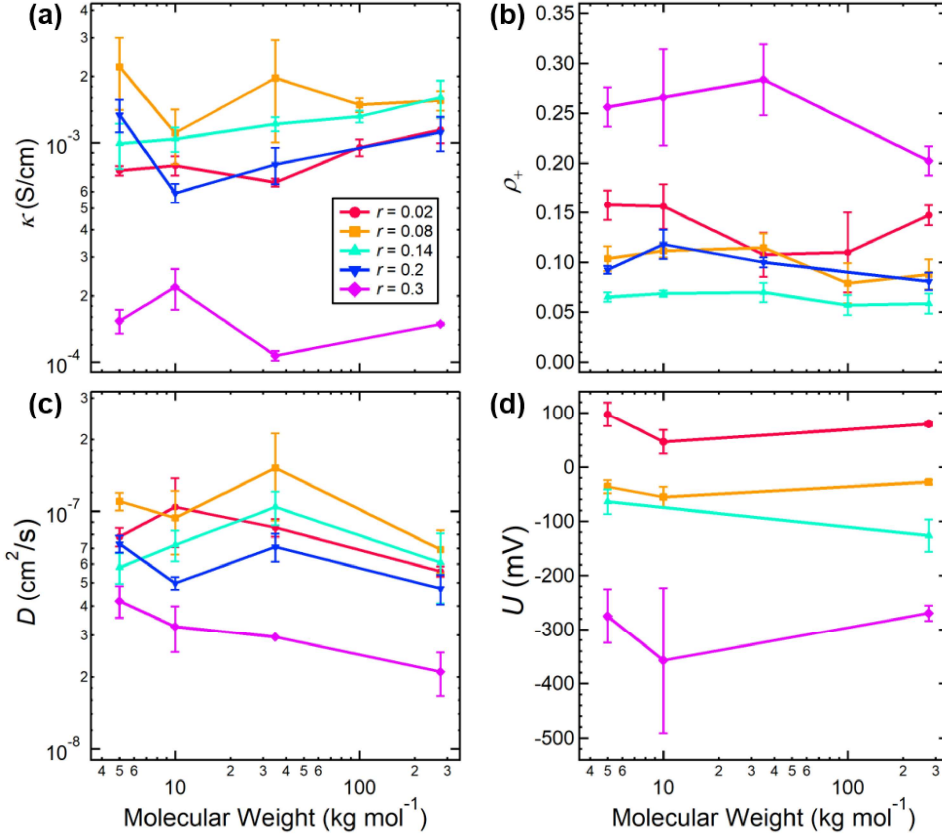


Figure 3.1. Molecular weight dependence of PEO/LiTFSI electrolytes at representative salt concentrations at 90 °C (circles/ $r = 0.02$; squares/ $r = 0.08$; triangles/ $r = 0.14$; inverted triangles/ $r = 0.2$; diamonds/ $r = 0.3$) for (a) ionic conductivity, κ , (b) current fraction, ρ_+ , (c) salt diffusion coefficient, D , and (d) open circuit potential from concentration cells, U . Each data point in (a) – (d) represents the average of at least 3 independent samples and the error bars correspond to the standard deviation.

Figure 3.2a shows κ of PEO/LiTFSI electrolytes as a function of salt concentration. The curve was obtained by fitting an expression for conductivity proposed by Mongcopa et al.⁹⁶ through the entire data set:

$$\kappa = 0.058r \exp\left(-\frac{r}{0.075}\right) \left[\frac{S}{cm}\right]. \quad (3.4)$$

At low salt concentrations, κ increases with increasing r due to the increase in charge carrier concentration. Equation 3.4 has an analytical maximum at $r = 0.075$, consistent with several reports on PEO electrolytes.^{66,97–100} The maximum is obtained because segmental motion, which plays an important role in ion transport, becomes slower with added salt.^{101,102}

Figure 3.2b shows the dependence of ρ_+ on r . The curve was obtained by fitting the entire data set to a 2nd order polynomial:

$$\rho_+ = 0.178 - 1.79r + 7.25r^2. \quad (3.5)$$

Equation 3.5 has an analytical minimum at $r = 0.123$, consistent with several reports in the literature.^{99,103} Computer simulations suggest that the non-monotonic dependence of ρ_+ on r is due to the formation of transient, negatively charged ion clusters.^{104,105} Equation 3.5 is remarkably similar to the fit reported by Galluzzo et al. for a series of mixtures of polystyrene-*b*-poly(ethylene oxide) copolymers and LiTFSI.¹⁰⁶

Figure 3.2c shows the dependence of D as a function of r . The curve was obtained by fitting the entire data set to a 2nd order polynomial:

$$D = (7.46 * 10^{-8}) + (2.75 * 10^{-7})r - (1.41 * 10^{-6})r^2 \quad [\frac{cm^2}{s}]. \quad (3.6)$$

D is a weak function of salt concentration in the range $0 < r < 0.20$. Equation 4.6 gives a weak analytical maximum at $r = 0.098$, which is consistently seen at all molecular weights (see Figure 3.2c).

Finally, we plot U as a function of $\ln(m)$ in Figure 3.2d. The abscissa was chosen because the quantity of interest is $\frac{dU}{d\ln(m)}$. The curve was obtained by fitting all data points to a power law equation:

$$U = 100 - 74.9m^{0.84} \quad [mV]. \quad (3.7)$$

Equation 3.7 has no analytical maximum or minimum within the salt concentrations measured, but there is an analytical zero found at $m = 1.41$ which corresponds to $r = 0.062$, closely matching the reference electrolyte concentration of $r = 0.06$, as expected.

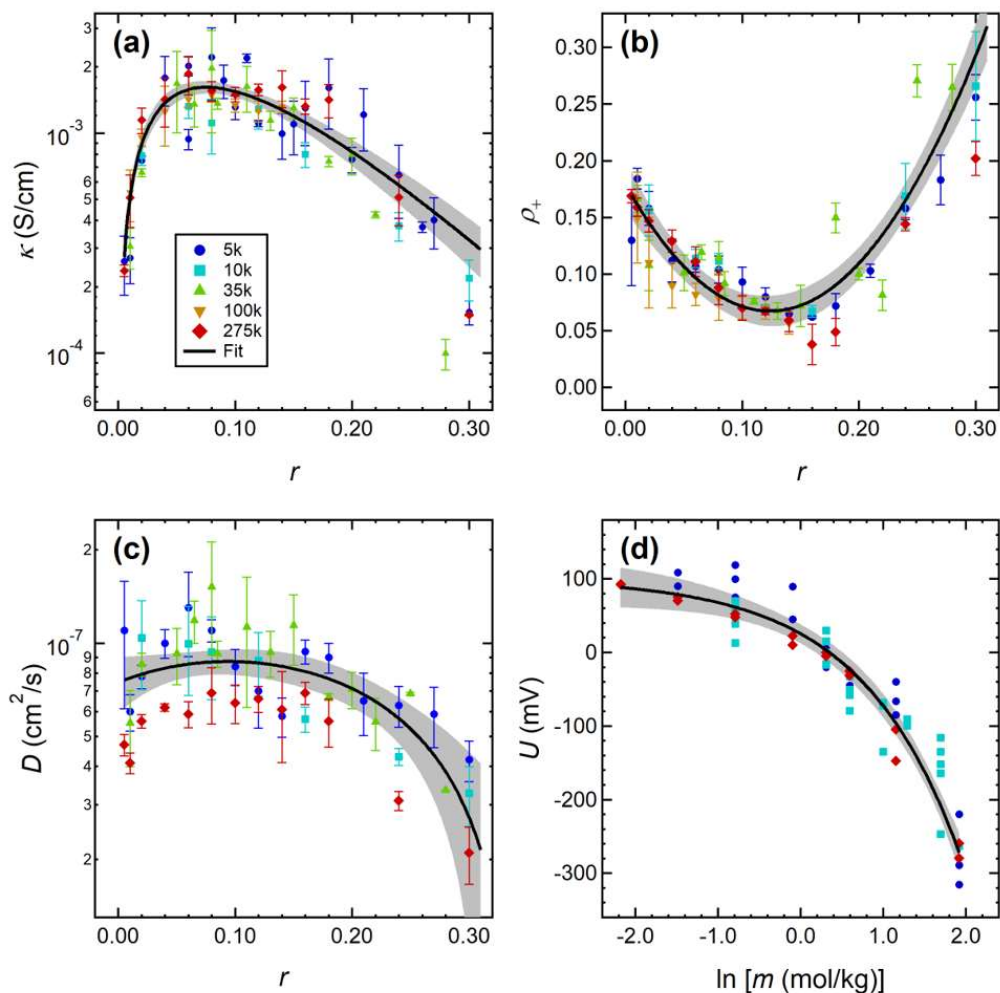


Figure 3.2. Electrochemical measurements of PEO/LiTFSI electrolytes at 90 °C for different salt concentrations and molecular weights (circles/5 kg mol⁻¹; squares/10 kg mol⁻¹; upward pointing triangles/35 kg mol⁻¹; downward pointing triangles/100 kg mol⁻¹; diamonds/275 kg mol⁻¹). The black line represents a fit through the entire data set. 95% confidence intervals for each fit are given by the gray shading. (a) Ionic conductivity, κ , from ac impedance spectroscopy of blocking electrode cells. (b) Current fraction, ρ_+ , from applying the Bruce-Vincent method to lithium symmetric cells. (c) Salt diffusion coefficient, D , from using restricted diffusion method with lithium symmetric cells. (d) Measured open circuit potential, U , from concentration cells. Each data point in (a) – (c) represents the average of at least independent 3 samples and the error bars correspond to the standard deviation. Each data point in (d) is an independent sample.

The uncertainty of the fits in Figure 3.2 are represented by a 95% confidence interval and shown as gray shading surrounding the fitted curves. They represent the uncertainty of the fitted Equations 3.4-3.7 based on the entire set of 64 samples. Details of our approach are given in the SI.

The curves shown in Figure 3.2 are parsimonious fits of the experimental data. In the case of conductivity, which has been studied extensively, the fit parameters in Equation 3.4 reflect

understanding of ion transport at the molecular level. The molecular underpinnings of the fit parameters in Equations 3.5-3.7 remain to be established. There is no molecular basis for the assumed functional forms of these equations.

We can use the data and fits in Figure 3.2 to calculate the cation transference number with respect to solvent velocity, t_+^0 from Equation 3.2 and the thermodynamic factor, T_f , from Equation 3.1. Figure 3.3a shows t_+^0 as a function of r . The curve was obtained by substituting Equations 3.4-3.7 into Equation 3.2. The data were obtained by inserting the measured values κ , D , ρ_+ , and $\frac{dU}{d\ln(m)}$ directly into Equation 3.2. The large uncertainty in the data is due to the propagation of error in individual experiments, quantified by Equation 3.3. The uncertainty of the curve, however, is much less as it is based on data from 64 electrolytes created from polymers with widely differing molecular weights. Our analysis shows that t_+^0 is a non-monotonic function of salt concentration. At values $0.093 \leq r \leq 0.189$, t_+^0 is negative. A negative t_+^0 means that when an electric field is applied to a PEO/LiTFSI mixture in this salt concentration range, the initial velocity of the cation and anion, measured using the solvent velocity as a reference, points toward the positive electrode. The implication is that in this range of salt concentrations, ion transport is dominated by negatively charged clusters.^{104,105,107-111} The phenomenon of triple ions or higher associates that may carry a net charge that is opposite to the "central" ion is well-known in electrochemistry.¹¹²⁻¹¹⁵ For $r > 0.189$, we see an increase in t_+^0 to positive values, which could be attributed to the breakup of negatively charged clusters.

Figure 3.3b shows T_f as a function of r . The curve was obtained by substituting Equations 3.4-3.7 into Equation 3.1. The data were obtained by inserting the measured values κ , D , ρ_+ , and $\frac{dU}{dl(m)}$ directly into Equation 3.1. The dependence of T_f on r falls into two regimes. In the regime $r < 0.17$, T_f is small and is a weak function of r . This implies that the dependence of the salt activity coefficient on salt concentration, $\frac{d\ln\gamma_{\pm}}{dl(m)}$, is small in this regime. Molecular dynamics simulations show that the most probable motif is one where each lithium ion is solvated by 6 ether oxygens in PEO.^{116,117} At $r = 1/6 = 0.17$, all the available oxygens are coordinated with lithium ions. When the salt concentration exceeds this value, the average coordination environment of the lithium ions must necessarily be different from the most favorable configuration, including anion coordination. One expects this to result in a rapid change in the chemical potential of the salt. We attribute the rapid increase of T_f in the $r > 0.17$ regime to this effect. In the limit of r tending to 0, the electrolytes should be thermodynamically ideal and T_f should approach unity. The Debye-Huckel theory indicates that T_f should be less than 1 in sufficiently dilute electrolytes.¹¹⁸ While our data are consistent with these expectations, the Debye-Huckel regime is outside the scope of our analysis.

The uncertainty in the fits in Figure 3.3 are represented by an approximate 95% confidence interval and shown as gray shading surrounding the fitted curves. They represent the uncertainty of the indirectly derived parameters T_f and t_+^0 using Equation 3.1 and 3.2 based on the entire set of 64 samples. The uncertainty was obtained utilizing a Monte Carlo method.^{119,120} We ran 10^5 trials sampling values for κ , D , ρ_+ , and $\frac{dU}{d\ln(m)}$ centered around their mean with standard deviations of the fits of Equations 3.4-3.7 and calculated the resulting values for T_f and t_+^0 using Equation 3.1 and 3.2 for each trial. The lower bound and upper bound of the 95% confidence interval is then given by the 2.5 and 97.5 percentile values in these trials. Details of our approach are given in the SI.

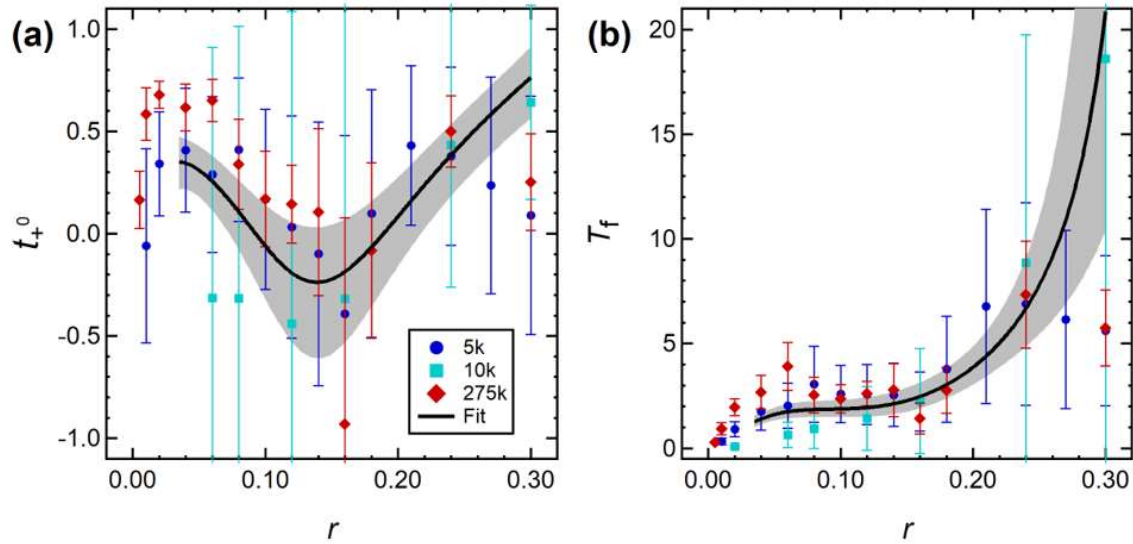


Figure 3.3. PEO/LiTFSI electrolyte properties at 90 °C of (a) cation transference number, t_+^0 , as calculated by Equation 4.2 and (b) thermodynamic factor, T_f , as calculated by Equation 3.1. Data points are the properties determined at each individual molecular weight (circles/5 kg mol⁻¹; squares/10 kg mol⁻¹; diamonds/275 kg mol⁻¹) and the error bars correspond to one standard deviation. The black line is calculated from Equations 3.1-3.2 using the fitted Equations 3.4-3.7 and is shown for $r \geq 0.035$. 95% confidence intervals are given by the gray shading.

The curves in both Figures 3.3a and 3.3b only extend to $r = 0.035$ in the dilute limit. At concentrations below this value, the curves are extremely sensitive to small changes in the fit parameters. In the dilute limit, ρ_+ approaches 0.18 and κ is proportional to c , implying that the magnitude of t_+^0 depends crucially on the magnitude of $\frac{dU}{d\ln(m)}$ that appears in the denominator.

However, $\frac{dU}{d\ln(m)}$ approaches a very small value in the dilute limit (see Figure 3.2d) and small changes in this value lead to very large changes in t_+^0 . Similar problems arise when one examines Equation 3.1 for T_f in the dilute limit. A parsimonious extrapolation of the curve representing the dependence of t_+^0 on r suggests that the transference number in the limit of $r = 0$ is 0.35. The fitted expression for t_+^0 does not give this result as it is affected by the scattered data at $r < 0.035$. Despite these limitations, the complete electrochemical characterization of three different sets of polymer electrolytes enable accurate quantification of ion transport over a large range of salt concentrations $0.035 \leq r \leq 0.30$. This is also the concentration range of practical relevance.

3.4 Conclusions

We have demonstrated that mixtures of lithium salt and entangled polymer chains are robust model systems for studying the fundamentals of ion transport. We present measurements of κ , D , ρ_+ , and $\frac{dU}{d\ln(m)}$ of PEO/LiTFSI using 64 independent electrolyte samples with PEO molecular weights ranging from 5 to 275 kg mol⁻¹ and salt concentrations $0.005 \leq r \leq 0.3$. Current methods for determining these transport and thermodynamic parameters involve four separate experiments.

The coupled nature of the equations used to determine the parameters results in large experimental uncertainty. A salient feature of this work is the rigorous quantification of experimental uncertainty. We minimize this uncertainty by taking advantage of the fact that transport and thermodynamics properties of polymer electrolytes above the entanglement threshold are independent of molecular weight. The dependence of transport parameters κ , D , t_+^0 , and the thermodynamic factor, T_f , on salt concentration are presented with a confidence interval of 95%. κ , D , and T_f are positive as required by the second law of thermodynamics. There are, however, no constraints on the sign of t_+^0 . We find that t_+^0 is negative in the salt concentration window of $0.093 \leq r \leq 0.189$.

3.5 Acknowledgements

This work was intellectually led by the Joint Center for Energy Storage Research (JCESR), an Energy Innovation Hub funded by the U.S. Department of Energy, Office of Science, Office of Basic Energy Science, under Contract No. DE-AC02-06CH11357. K.W.G. acknowledges funding from a National Defense and Science Engineering Graduate Fellowship. The authors thank Michael D. Galluzzo, Zach J. Hoffman, Calvin Luo, Deep B. Shah, and Lorenzo N. Venneri for helpful discussions related to this work.

3.6 Supporting Information

Data used in the uncertainty analysis for each electrochemical parameter is given in the Supplementary Material 2 file found at: <https://doi.org/10.1016/j.ssi.2021.115609>.

The uncertainty analysis was performed using Igor Pro 6.37 and MATLAB R2020b. Fitting κ , D , ρ_+ , and U to Equations 3.4-3.7 was done using either Igor's CurveFitting or MATLAB's nlinfit() function. 95% confidence intervals for these fits can be generated using Igor's built-in CurveFitting error analysis or MATLAB's nlpredci() function. The difference between the lower bound (LB) and upper bound (UB) of the 95% confidence interval is $2\Delta_i$; the half-width of these 95% confidence intervals is denoted by Δ_i where i is the electrochemical property of interest and the standard deviation is then $\frac{\Delta_i}{2}$. Note that $\Delta \frac{dU}{d \ln(m)}$ is given by $|\frac{d(\Delta U)}{dm} m|$ as $\frac{dU}{d \ln(m)} = \frac{dU}{dm} \frac{dm}{d \ln(m)} = \frac{dU}{dm} m$.

T_f and t_+^0 are indirectly derived parameters determined by using Equation 3.1 and 3.2. The 95% confidence intervals for these parameters was obtained utilizing a Monte Carlo method. The detailed code for this is given in the Appendices of this thesis. For each salt concentration, 10^5 trials are run, sampling values for κ , D , ρ_+ , and $\frac{dU}{d \ln(m)}$ centered around a normal distribution around the mean of the fit where the standard deviation is $\frac{\Delta_i}{2}$. MATLAB's normrnd() function is used to generate these values. The resulting values are then applied to Equations 3.1 and 3.2 to calculate the values of T_f and t_+^0 for each trial. The lower bound and upper bound of the 95% confidence interval is then given by the 2.5 and 97.5 percentile values. Because κ , D , ρ_+ , and $\frac{dU}{d \ln(m)}$ are dependent on salt concentration, these trials are then repeated for different salt concentrations until the 95% confidence interval is completed for the entire salt concentration range of interest.

3.7 Nomenclature

Table 3.2. List of symbols and abbreviations.

Symbol	Meaning
κ	Ionic conductivity
D	Salt diffusion coefficient
t_+^0	Cation transference number with respect to solvent velocity
T_f	Thermodynamic factor
PEO	Poly(ethylene) oxide
LiTFSI	Lithium bis(trifluoromethanesulfonyl)imide
r	Salt concentration given by the ratio of lithium ions in the salt to oxygen atoms in the polymer
γ_{+-}	Mean molal activity coefficient of the electrolyte
m	Salt concentration in molality
LiPF ₆	Lithium hexafluorophosphate
PC	Propylene carbonate
U	Open circuit potential
ρ_+	Current fraction
R	Gas constant
T	Temperature
c	Concentration in molarity
t_-^0	Anion transference number with respect to solvent velocity
F	Faraday constant
δ	Standard deviation

4 Dependence of the Salt Diffusion Coefficient on Molecular Weight

Abstract

Properties of polymer electrolytes often depend on molecular weight, though these properties become constant when the molecular weight increases beyond the entanglement threshold. We determined the salt diffusion coefficient in different molecular weights (5 kg mol^{-1} , 35 kg mol^{-1} , 275 kg mol^{-1}) of poly(ethylene oxide) electrolytes above its entanglement weight. The restricted diffusion method in lithium-lithium symmetric cells was used: various current densities were applied until a steady-state potential was reached, then the concentration gradient formed was allowed to relax. The salt diffusion coefficient was extracted by fitting the potential profile to an exponential equation. We find that the salt diffusion coefficient has no dependence on applied current density. A very weak correlation between salt diffusion coefficient and molecular weight was found. The implications of a salt diffusion coefficient dependency on molecular weight are discussed. Further investigation on different molecular weights of poly(ethylene oxide) electrolytes is needed to provide more evidence for the relationship between salt diffusion coefficient and molecular weight.

4.1 Introduction

Mixing polymers and lithium salt forms an electrolyte. These polymer electrolytes are nonflammable and thus of great interest as a safer alternative to the traditionally combustible liquid electrolytes found in typical lithium ion batteries. However, while typical electrolyte solvents such as ethylene carbonate or dimethyl carbonate have a fixed size and low molecular weight, polymers can have different sizes and increasing their chain length leads to high molecular weights. Many physical properties of a polymer are known to be dependent on its molecular weight, or chain length. For example, viscosity increases as molecular weight increases, and this relationship is given by the power law expression described in the Mark-Houwink equation.¹²¹ It is not too surprising that ion transport in polymer electrolytes is also related to polymer size. Ion transport in polymer electrolytes above the glass transition temperature is believed to take place through two primary mechanisms.^{122,123} One mechanism occurs through the diffusion of the entire polymer chain with the coordinated ions; such motion has a polymer chain length dependence. The other mechanism occurs via segmental motion of the polymer chains around the ions whereby ions hop between sites, and above a certain molecular weight, this is thought to be independent of the polymer chain length.¹²⁴

In high molecular weight polymer electrolytes, ion transport is assumed to be governed by segmental motion, as increasing molecular weight results in rapidly decreasing polymer diffusion coefficients as the solvation shell becomes entangled with the polymer.¹²⁵ Indeed, high molecular weight polymer electrolytes are typically above the entanglement threshold, where the polymer chains are entangled and many properties no longer change with increasing size.^{85,87,125} In the most studied polymer electrolyte system made up of poly(ethylene oxide) (PEO) and lithium bis(trifluoromethanesulfonyl)imide (LiTFSI) salt, this entanglement threshold is around 2 kg mol^{-1} . Above this molecular weight, it has been shown that transport properties such as conductivity and current fraction remain constant with increasing molecular weight.^{20,88}

The property of interest for this study is the salt diffusion coefficient. While no molecular weight dependence above the entanglement threshold was reported in prior studies, herein we present an in-depth investigation. We wish to probe the relationship between salt diffusion coefficient and molecular weight, and determine whether signatures of the polymer chain diffusion mechanism can be detected through electrochemical measurements.

We measured the salt diffusion coefficient using the restricted diffusion method in lithium-lithium symmetric cells for a range of PEO molecular weights (5 kg mol⁻¹, 35 kg mol⁻¹, 275 kg mol⁻¹). No signatures of changes in polymer chain diffusion were observed in the potential relaxation profiles measured in the restricted diffusion method. A very weak correlation between salt diffusion coefficient and molecular weight was found, but further studies at higher molecular weights of PEO are needed. This study highlights the challenges in determining salt diffusion coefficients and illustrates the need for both precise measurements and new measurement strategies. We note that in PEO/LiTFSI electrolytes, a major source of uncertainty in the calculated cation transference number with respect to the solvent velocity is a result of the uncertainty in the measured salt diffusion coefficients.²⁰

4.2 Experimental Methods

PEO (Polymer Source) of molecular weights of 35 kg mol⁻¹ and 275 kg mol⁻¹ was used in this study. All polymers were dried in a glovebox antechamber under vacuum at 90 °C for at least 24 h prior to use. LiTFSI (Sigma Aldrich) was dried under vacuum at 120 °C for at least 72 h.

PEO/LiTFSI electrolytes were prepared by mixing LiTFSI with PEO in tetrahydrofuran. The salt concentration of the electrolytes was $r = 0.08$ were prepared, where we define r as the molar ratio of oxygen atoms in PEO to lithium ions in the salt. All electrolyte solutions were transparent, indicating complete dispersion of all mixture components. The electrolytes were stirred on a hot plate at 70 °C until all of the tetrahydrofuran had evaporated and then further dried in a glovebox antechamber under vacuum at 90 °C for 24 h to remove any residual solvent.

All sample preparation was performed inside of an argon glovebox with water and oxygen levels below 1 and 2 ppm, respectively. Lithium symmetric cells were prepared by pressing the polymer electrolyte into a 508 μm thick silicone spacer with a 1/8 in. inner diameter and sandwiching between lithium foil backed with stainless steel shims. Nickel tabs were secured to the stainless steel shims to serve as electrical contacts, and the entire assembly was vacuum sealed in laminated aluminum pouch material. Each cell was taken out of the glovebox, placed in a custom-built heating stage and electrochemical characterization was performed via a Bio-Logic VMP3 potentiostat. At the conclusion of the experiments, samples were taken back into the glovebox to check for defects, and the assembly was measured to determine electrolyte thickness.

Electrochemical characterization was done at 90 °C. The cells were first conditioned for at least four charge/discharge cycles at a low current density of 0.02 mA cm⁻² to ensure a stable interfacial layer was introduced. Each conditioning cycle consisted of a 3 h charge followed by a 1.5 h rest, then a 3 h discharge and 1.5 h rest. After pre-conditioning the cells, we ran restricted diffusion experiments.⁹⁰ The experimental procedure can be summarized as follows (see Figure 4.1):

1. Galvano electrochemical impedance spectroscopy (GEIS) over a 0.1-10⁶ Hz frequency range at an amplitude of 80 mV to determine the initial bulk and interfacial resistances of the cell.
2. Chronopotentiometry (CP) step where the desired current density i_0 is applied to the cell. In these experiments, $i_0 = 0.02, 0.06, 0.1, 0.2, 0.4$ [mA cm⁻²]. We measure the potential response over 3 h, which is typically when steady-state potential is reached.
3. GEIS step with a controlled applied current equal to that of the applied current density in step 2, to determine the steady-state bulk and interfacial resistances.
4. Open circuit voltage (OCV) step where we allow the cell to relax. We measure the potential response over 1.5 h, which is typically how long it takes the potential to relax to a near-zero steady state value.
5. Repeat steps 1-4 but in the opposite direction, *i.e.* with negative applied current densities.

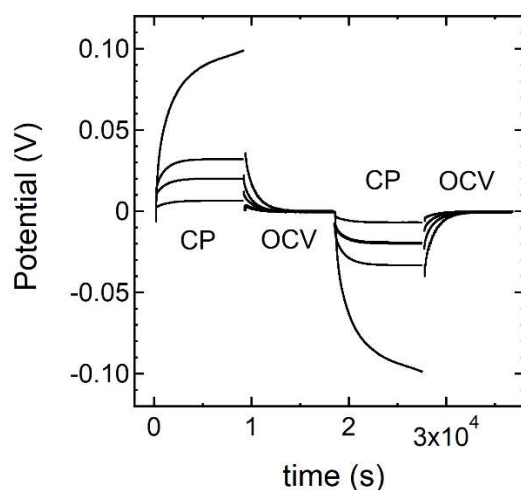


Figure 4.1. Example PEO (35 kg mol⁻¹) electrolyte data showing potential response to applied current density and open circuit relaxation. The chronopotentiometry (CP) step is when different current densities are applied to the symmetric cell, and the potential typically increases before reaching a steady state value. The value of this steady-state potential depends on the applied current density and the bulk and interfacial resistance of the symmetric cell. The cell is then allowed to relax under open circuit voltage (OCV). This procedure is then repeated with the applied current in the negative direction.

To determine the salt diffusion coefficient, D , we use the potential vs. time data obtained in the OCV steps. The relaxation curve can be fit to an exponential expression derived from Fick's Law. This restricted diffusion analysis is given in detail in ref⁹⁰ and the Appendix.

The ionic conductivity, κ , can be calculated from the bulk resistances measured in the GEIS steps, given a known thickness of the electrolyte and contact area between the electrolyte and lithium. This analysis is well known, and further discussion is included in the Appendix.

The current fraction, ρ_+ , can be calculated from the bulk and interfacial resistances measured in the GEIS steps as well as the potential values measured over time in the CP steps. We used the Bruce-Vincent method to determine the current fraction, but the traditional method uses chronoamperometry where a potential difference is applied to the system and the current response

is measured. Herein, we apply a current density and measure the potential response. An analogous, though perhaps simplified version of this expression is given by the following:

$$\rho_+ = \frac{V_0 - i_0 R_{i,i}}{V_f - i_0 R_{i,f}}, \quad (4.1)$$

where V_f is the steady-state potential, V_0 is the initial potential as determined by the expression $V_0 = i_0(R_{b,i} + R_{i,i})$, i_0 is the applied current density, and $R_{b,i}$, $R_{i,i}$, $R_{i,f}$ are the initial bulk resistance, initial interfacial resistance, and steady-state interfacial resistance respectively.

4.3 Results and Discussion

Figure 4.2a shows the salt diffusion coefficient of PEO of three molecular weights as determined at different current densities. We find that the relaxation of the steady-state potential follows similar behavior regardless of the applied current density to reach steady-state (see Figure 4.1). The calculated salt diffusion coefficients are more or less the same for all current densities. The 275 kg mol⁻¹ PEO has the lowest salt diffusion coefficient, with a value of around 9×10^{-8} cm² s⁻¹. The measured 35 kg mol⁻¹ PEO salt diffusion coefficient has a larger uncertainty and greater variance, but the salt diffusion coefficient is around 2.5×10^{-7} cm² s⁻¹. The larger uncertainty can be attributed to the more liquid-like behavior of the lower molecular weight polymer, leading to greater uncertainty of electrolyte thickness and contact area. Data for PEO of molecular weight 5 kg mol⁻¹ is shown by the dashed line, as reported by Pesko et al with a salt diffusion coefficient of around 1.1×10^{-7} cm² s⁻¹.⁶³ There is clearly a difference in the values of the salt diffusion coefficient for the three different molecular weights.

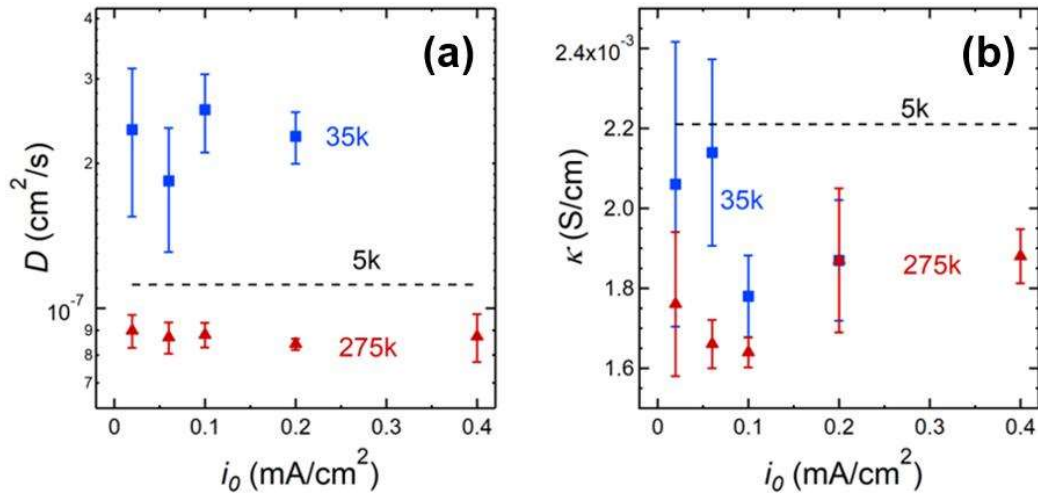


Figure 4.2. Salt diffusion coefficient and ionic conductivity calculated under different applied current densities, for a range of PEO molecular weights. (a) Salt diffusion coefficient for reported PEO (5 kg mol⁻¹) data shown by the dashed line from ref. ⁶³, PEO (35 kg mol⁻¹, blue squares), and PEO (275 kg mol⁻¹, red triangles). (b) Ionic conductivity for reported PEO (5 kg mol⁻¹) data shown by the dashed line from ref. ⁶³, PEO (35 kg mol⁻¹, blue squares), and PEO (275 kg mol⁻¹, red triangles). There appears to be no dependence of salt diffusion coefficient or ionic conductivity on the applied current density. Salt diffusion coefficient shows some correlation between molecular weights, while ionic conductivity does not.

Figure 4.2b shows the ionic conductivity of PEO of three molecular weights as determined at different current densities. We find no significant differences in the impedance data across applied current densities. The calculated ionic conductivity is more or less the same for all current densities. While we saw differences in the calculated salt diffusion coefficient, we find that the ionic conductivity is fairly similar across molecular weights of PEO. The ionic conductivity of 275 kg mol⁻¹ PEO ranges between 1.6 to 1.9 mS cm⁻¹, while for 35 kg mol⁻¹, it ranges between 1.8 to 2.1 mS cm⁻¹. The 5 kg mol⁻¹ PEO data, reported by Pesko et al., is 2.2 mS cm⁻¹.⁶³ While the average data values are not the same across molecular weights, accounting for the uncertainty of the measurements yields reasonable agreement between molecular weights. All in all, we find minor correlation between the salt diffusion coefficient and molecular weight of PEO, while ionic conductivity shows little to no correlation.

In Figure 4.3 we plot the average salt diffusion coefficient across all current densities and its dependence on molecular weight. We find that the salt diffusion coefficient has a very weak dependence on molecular weight. We can fit the data to a power law relationship where we have:

$$D = 1.61 * 10^{-7} (M^{-0.036}). \quad (4.2)$$

More measurements of different PEO molecular weights is needed to determine whether there is truly a correlation between salt diffusion coefficient and polymer chain length in PEO.

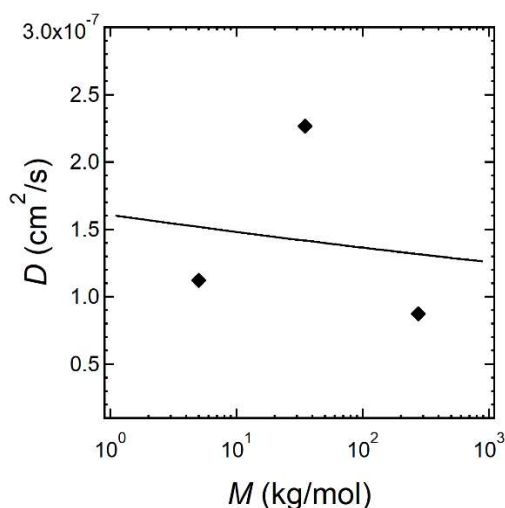


Figure 4.3. Dependence of salt diffusion coefficient on molecular weight of PEO. Data points shown are average salt diffusion coefficients determined across various current densities for molecular weights of 35 kg mol⁻¹ and 275 kg mol⁻¹ while the 5 kg mol⁻¹ data is taken from ref.⁶³. The black line represents a fit to a power law relationship between the salt diffusion coefficient and molecular weight: $D = 1.61 * 10^{-7} (M^{-0.036})$. D has a very weak dependence on M from the data available in this study.

There are several implications of a salt diffusion coefficient dependency on molecular weight in polymer electrolytes. Newman's concentrated solution theory provides a rigorous method for fully characterizing an electrolyte system and enables modeling of concentration gradients in electrolytes during battery operation.³⁸ An important transport parameter, the cation transference

numbers with respect to the solvent velocity, t_+^0 , can be derived from the measurement of several independent transport parameters, the salt diffusion coefficient among them.^{38,40} Figure 4.4a shows the dependence of t_+^0 on D for a PEO/LiTFSI electrolyte with $r = 0.08$ at 90 °C, where the transport properties are taken from ref. ⁶³. We see that t_+^0 only approaches unity at low values of $D < 10^{-8}$ cm² s⁻¹. Interestingly, as D increases, t_+^0 decreases, and becomes negative for $D > 10^{-7}$ cm² s⁻¹.

Figure 4.4b plots the dependence of t_+^0 on M using equation 4.2 as a simplified relationship between D and M in PEO/LiTFSI. For a range of molecular weights of interest from around 1 kg mol⁻¹ to 10⁴ kg mol⁻¹ (ultra high weight PEO^{126,127}) we find that t_+^0 can vary from -0.7 to -0.2. While the relationship in equation 4.2 may not be valid across larger molecular weights due to the lack of experimental data at these high molecular weights, and further measurements are needed to validate whether a relationship between D and M does exist, Figure 4.4 provides an illustration of its implications on an important transport parameter. A D dependence on M also has fundamental polymer physics implications. Insights may be gleaned when electrochemical experiments such as those described herein are coupled with other characterization techniques, such as NMR or neutron spin echo.^{128,129}

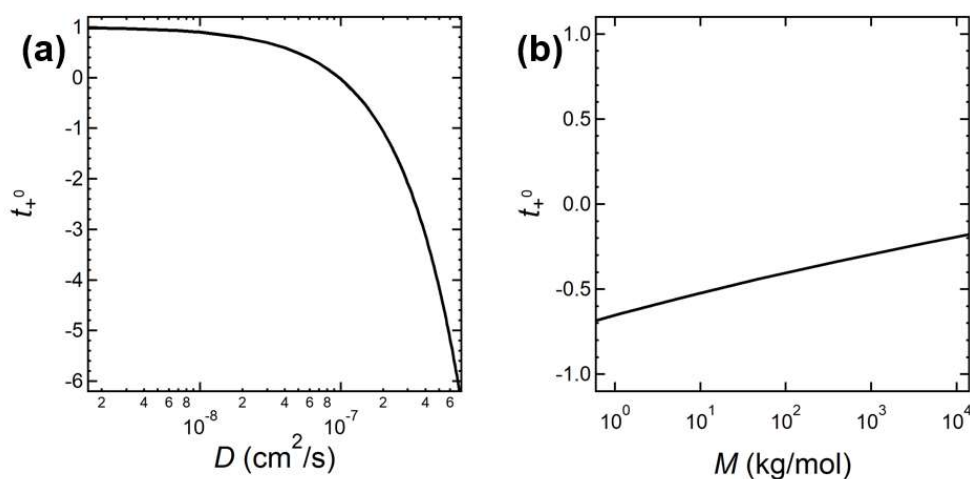


Figure 4.4. Effect of salt diffusion coefficient and molecular weight on the cation transference number in PEO. (a) The dependence of the cation transference number on salt diffusion coefficient for PEO/LiTFSI at $r = 0.08$, with all other parameters held constant. t_+^0 approaches 1 for lower values of D , while increasing D causes t_+^0 to decrease dramatically. (b) Applying the dependence of D on M to show the dependence of t_+^0 on M . When M increases, t_+^0 increases.

4.4 Conclusions

We have determined the salt diffusion coefficient using the restricted diffusion method in lithium-lithium symmetric cells for a range of PEO molecular weights (5 kg mol⁻¹, 35 kg mol⁻¹, 275 kg mol⁻¹). We applied various current densities until a steady-state potential was reached, then allowed the concentration gradient formed to relax. The potential relaxation profiles measured showed similar form for all applied current densities and the salt diffusion coefficient was extracted by fitting the potential profile to an exponential equation. A very weak correlation

between salt diffusion coefficient and molecular weight was found. Further studies on different molecular weights of PEO are needed to provide more evidence for the relationship between salt diffusion coefficient and molecular weight. This study highlights the challenges in determining salt diffusion coefficients. Future work optimizing the restricted diffusion measurement or development of new measurement techniques is warranted. Finally, a diffusion coefficient dependency on molecular weight has numerous important implications for electrolyte applications in lithium batteries.

4.5 Acknowledgements

This work was intellectually led by the Joint Center for Energy Storage Research (JCESR), an Energy Innovation Hub funded by the U.S. Department of Energy, Office of Science, Office of Basic Energy Science, under Contract No. DE-AC02-06CH11357, which supported characterization work conducted by K.W.G. under the supervision of N.P.B. K.W.G. acknowledges funding from a National Defense and Science Engineering Graduate Fellowship. We thank Jaeyong Lee and Zach Hoffman for helpful contributions and discussions.

4.6 Nomenclature

Table 4.1. List of symbols and abbreviations.

Symbol	Meaning
PEO	Poly(ethylene) oxide
LiTFSI	Lithium bis(trifluoromethanesulfonyl)imide
r	Salt concentration given by the ratio of lithium ions in the salt to oxygen atoms in the polymer
GEIS	Galvano electrochemical impedance spectroscopy
CP	Chronopotentiometry
OCV	Open circuit voltage
κ	Ionic conductivity
D	Salt diffusion coefficient
t_+^0	Cation transference number with respect to solvent velocity
ρ_+	Current fraction
V_0	Voltage
i_0	Current density
R	Resistance
M	Molar mass

5 Optimizing the Monomer Structure of Polyhedral Oligomeric Silsesquioxane for Ion Transport in Hybrid Organic-Inorganic Block Copolymers[†]

Abstract

Poly(ethylene oxide)-*b*-polyhedral oligomeric silsesquioxane (PEO-POSS) mixed with lithium bis(trifluoromethanesulfonyl)imide salt is a nanostructured hybrid organic-inorganic block copolymer electrolyte that may enable lithium metal batteries. The synthesis and characteristics of three PEO-POSS block copolymer electrolytes which only differ by their POSS silica cage substituents (ethyl, isobutyl, isooctyl) is reported. Changing the POSS monomer structure results in differences in both thermodynamics and ion transport. All three neat polymers exhibit lamellar morphologies. Adding salt results in the formation of a disordered window which closes and gives way to lamellae at higher salt concentrations. The width of disordered window decreases with increasing length of the POSS alkyl chain substituent from ethyl to isobutyl and is absent in the isooctyl sample. Rheological measurements demonstrate good mechanical rigidity when compared with similar all-organic block copolymers. While salt diffusion coefficient and current ratio are unaffected by substituent length, ionic conductivity increases as the length of the alkyl chain substituent decreases: the ethyl substituent is optimal for ion transport. This is surprising because conventional wisdom suggests that ion transport occurs primarily in the PEO-rich domains, *i.e.* ion transport should be unaffected by substituent length after accounting for the minor change in conducting phase volume fraction.

5.1 Introduction

Solid polymer electrolytes are of interest for developing safer lithium batteries as they are less flammable than more traditional organic liquid electrolytes.^{2,3,13} They may also enable the development of higher energy density batteries with lithium metal anodes.^{6,17} In order to be used in lithium metal batteries, polymer electrolytes must have good ion transport properties as well as high mechanical rigidity to prevent lithium dendrite growth.¹⁰ These two properties are decoupled in block copolymers such as polystyrene-*b*-poly(ethylene oxide) (SEO) wherein the polystyrene-rich microphase provides mechanical strength and the poly(ethylene oxide)-rich microphase enables ion transport when a salt such as lithium bis(trifluoromethanesulfonyl)imide (LiTFSI) is mixed with the copolymer.¹³⁰ The phase behavior of these materials is also important, as ion transport parameters such as ionic conductivity and salt diffusion coefficient are affected by morphology.²³ Most of the work in this area is restricted to all-organic block copolymer systems.^{23,28,31,131–140}

Recent work has shown that hybrid organic-inorganic poly(ethylene oxide)-*b*-polyhedral oligomeric silsesquioxane (PEO-POSS) block copolymers with LiTFSI self-assemble into a variety of morphologies with high mechanical rigidity and ionic conductivity when compared with SEO electrolytes of comparable molecular weight.¹⁴¹ Like in SEO, the PEO-rich microphase

[†] This chapter was reported in *Journal of Polymer Science*, **2020**, 58 (2), 363-371.

facilitates ion transport via segmental motion,¹⁰² while the POSS-rich microphase furnishes mechanical rigidity.¹⁴² While it is clear that the thermodynamic interactions between PEO and POSS chains depend on the chemical structure of the silica cage substituents on the POSS monomer, effect of the cage structure on ion transport is an open question. While the impact of cage substituents on the thermal and morphological characteristics of nanocomposite polymer – POSS blends has often been studied,^{24,143–151} sparse work on its effect upon phase behavior and ion transport in block copolymers exists.

In this paper, we report on the synthesis of PEO-POSS block copolymers from three different POSS containing monomers (methacrylethyl, methacrylisobutyl, methacrylisooctyl POSS) whose cage substituents systematically increase in alkyl chain length. We use small angle X-ray scattering (SAXS) and transmission electron microscopy (TEM) to determine the morphology of these systems with and without added salt. The mechanical properties of the neat polymers are determined through rheological measurements. Finally, electrochemical characterization is used to study ion transport.^{152–154}

Conventional wisdom suggests that the chemical composition of the non-conducting microphase does not affect ion transport of block copolymer electrolytes, after effects related to changes in the morphology and volume fraction of the conducting phase are accounted for.^{23,135,138,155,156} The purpose of this paper is to challenge this conventional wisdom.

5.2 Experimental Methods

5.2.1 Synthesis

The PEO-POSS copolymers were synthesized, purified, and characterized using methods described in ref¹⁴¹ and reported in the Supporting Information (Figures 5.9–5.15). The polymers used in this study are called PEO-POSS(5-1) where the 5 denotes the molecular weight of PEO in kg mol^{-1} and there is 1 POSS unit of varying molecular weight from 0.7 to 1.3 kg mol^{-1} due to the different alkyl chain substituent (ethyl, isobutyl, isooctyl) on the POSS silica cage. The chemical structure is shown in Figure 5.1.

We add LiTFSI salt to make electrolytes of varying salt concentration r , where we define r to be the molar ratio of lithium to ethylene oxide moieties. Electrolytes were prepared with methods described in ref¹⁴¹. A list of the polymer characteristics can be found in Table 5.1. The neat copolymers are colorless.

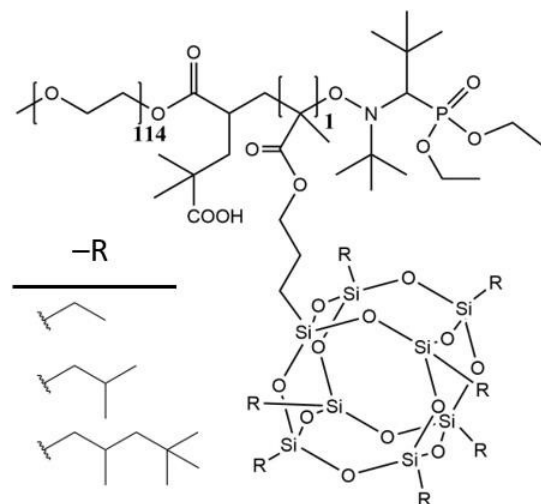


Figure 5.1. Chemical structure of PEO-POSS polymers synthesized. The alkyl substituent on the POSS silica cage increases in length from ethyl to isobutyl to isooctyl.

Table 5.1. Summary of PEO-POSS(5-1) characteristics

-R	M_{POSS} (kg/mol)	M_{PEO} (kg/mol)	$f_{\text{EO/LITFSI}}$	N
Ethyl	0.7	5	0.87 – 0.93	85
Isobutyl	0.9	5	0.85 – 0.92	87
Isooctyl	1.3	5	0.79 – 0.88	95

5.2.2 Small Angle X-ray Scattering (SAXS)

SAXS samples were prepared by melt pressing the polymer into a 0.766 cm thick rubber spacers with a 0.3175 cm inner diameter, and annealing them at 90 °C for 3 hours, then 70 °C for 48 hours before allowing them to cool slowly under vacuum to room temperature. The samples were sealed with Kapton windows in custom-designed airtight aluminum holders.

SAXS measurements were performed at beamline 1–5 at the Stanford Synchrotron Radiation Lightsource and SLAC National Accelerator Laboratory and beamline 7.3.3 at the Advanced Light Source at Lawrence Berkeley National Laboratory.¹⁵⁷ Silver behenate was used to determine the beam center and sample-to-detector distance. The scattered intensity was corrected for beam transmission and empty cell scattering. Two dimensional scattering patterns were integrated azimuthally using the Nika program for IGOR Pro to produce one-dimensional scattering profiles and are reported as scattering intensity, I , as a function of the magnitude of the scattering vector, q .¹⁵⁸ Absolute scattering intensity, I_{abs} , was obtained by calibrating to a glassy carbon absolute intensity standard and is reported in the Supporting Information (Figure 5.20). Measurements were taken in a custom-built 8-sample heating stage at 70 °C, 90 °C, and 110 °C. Samples were

equilibrated for about 20 min at each temperature before taking measurements. To a good approximation, the SAXS profiles of all our samples were independent of temperature in the temperature range of 70 – 110 °C and were similar upon heating and cooling. We only discuss data obtained at 70 °C in the main text in consistency with our electrochemical measurements. The temperature range of our SAXS experiments is above the melting temperature of the semi-crystalline PEO block.

5.2.3 Electrochemical Measurements

All sample preparation was performed inside of an argon glovebox with water and oxygen levels below 1 ppm and 2 ppm respectively. Conductivity cells were prepared by pressing the polymer electrolyte into a 254 μm thick silicone spacer with a 1/8 in. inner diameter and sandwiching between two 200 μm thick stainless-steel shim blocking electrodes. Lithium symmetric cells were prepared by pressing the polymer electrolyte into a 254 μm thick silicone spacer with a 1/8 in. inner diameter and sandwiching between two 180 μm thick lithium foils backed with stainless-steel shims. For both conductivity and lithium symmetric cells, nickel tabs were secured to the stainless-steel shims to serve as electrical contacts, and the assembly was vacuum sealed in laminated aluminum pouch material. Each cell was then taken out of the glovebox, placed in a custom-built heating stage, and annealed at 90 °C for 3 hours prior to electrochemical characterization. At the conclusion of the experiments, samples were taken back into the glovebox to check for defects and the assembly was measured to find the final sample thickness.

Complex impedance measurements were performed on the conductivity cells via a Bio-Logic VMP3 potentiostat over a 0.1 – 10⁶ Hz frequency range at an amplitude of 80 mV to find the ionic conductivity, κ . Representative Nyquist plots are shown in the Supporting Information (Figure 5.21). Lithium symmetric cells were first conditioned for at least 4 charge/discharge cycles at a low current density of 0.02 mA cm⁻² to ensure a stable interfacial layer was introduced. Each conditioning cycle consisted of a 4 h charge followed by a 2 h rest and a 4 h discharge. The Bruce and Vincent method was then used to find the current fraction, ρ_+ , defined as

$$\rho_+ = \frac{i_{ss}(\Delta V - i_{\Omega}R_{i,0})}{i_{\Omega}(\Delta V - i_{ss}R_{i,ss})}$$

where $R_{i,0}$ is the initial interfacial resistance, $R_{i,ss}$ is the interfacial resistance at steady-state, i_{ss} is the current measured at steady state, ΔV is the applied potential, i_{Ω} is a measure of the initial current, as defined by the ratio of the applied potential to the sum of the initial bulk and interfacial resistances.⁹¹ The restricted diffusion method was used to find the salt diffusion coefficient, D .⁹⁰ Cells were polarized at +/- 10 mV and +/- 20 mV until a steady-state current was reached, then allowed to relax under open circuit potentials. Impedance was taken before and after polarization. Measurements were done at 70 °C.

In the literature, the parameter we call ρ_+ is often referred to as the transference number.⁸² In our group, we have referred to it as the steady state cationic transference number, $t_{+,ss}$. It has been shown that ρ_+ (or $t_{+,ss}$) is equal to the transference number in dilute and ideal electrolytes.⁶² However, in concentrated electrolytes, and especially in concentrated polymer electrolytes, there is a significant difference in both magnitude and sign between ρ_+ and the transference

number.^{62,82,159} Since we are mainly interested in concentrated electrolytes in this work and it has been shown that PEO-containing electrolytes are highly non-ideal,¹⁵⁹ we use the term ρ_+ to indicate the results of these experiments using the Bruce and Vincent method.

5.2.4 Rheology

The viscoelastic properties of the neat polymers were studied using the procedure outlined in ref ¹⁶⁰, though samples were prepared by annealing at 70 °C instead of 120 °C. Measurements were repeated multiple times.

5.2.5 Transmission Electron Microscopy Imaging

Quenched PEO-POSS bulk samples were sectioned at -120 °C using a cryo-microtome (Leica Ultracut 6) to obtain ultrathin films (~100 nm). The ultrathin films were transferred to copper grids with lacey carbon supporting film and stored in an argon glovebox immediately after cryo-microtoming to minimize the effect of humidity. PEO-rich domains were stained to increase contrast and stability under the electron beam by exposing the ultrathin film to ruthenium tetroxide vapor for 10 minutes at room temperature. TEM micrographs were collected using Philips CM200 equipped with Gatan US1000 CCD camera.

5.3 Results and Discussion

We performed SAXS experiments to elucidate the morphology of our electrolytes. Typical data obtained are shown in Figure 5.2 where scattering intensity measured at 70 °C is plotted as a function of the magnitude of the scattering vector. In Figure 5.2a, we show data obtained from ethyl samples with varying salt concentration. In the neat state, the ethyl polymer exhibits a lamellar morphology, as evidenced by the scattering peaks at $q = q^*$, $2q^*$, and $3q^*$ where q^* indicates the location of the primary scattering peak. Upon salt addition, at $r = 0.02$, the peaks diminish in intensity, and at $r = 0.06$ the peaks vanish, indicating the formation of a disordered phase. Upon further increase in salt concentration to $r = 0.12$, weak scattering peaks corresponding to a lamellar phase appear and their intensity increases with increasing salt concentration. In Figure 5.2b, we show data obtained from isobutyl samples with varying salt concentration. This polymer also forms a lamellar phase in the neat state. Increasing r to 0.02 results in a loss of the peak at $q = 2q^*$ and a significant reduction in scattering intensity at $q = q^*$. We attribute this weak scattering peak to the presence of disordered concentration fluctuations.¹⁶¹ The isooctyl sample is lamellar in the neat state with relatively sharp peaks at q^* and $2q^*$, as can be seen in Figure 5.2c. The addition of salt results in an increase in the scattering intensity at q values below q^* (in the range $0.20 \text{ nm}^{-1} \leq q \leq 0.35 \text{ nm}^{-1}$). At $r = 0.08$, a distinct shoulder is apparent in this q range. This shoulder becomes more pronounced with increasing salt concentration. At $r = 0.3$, we obtain broad scattering peaks that are reminiscent of the scattering peaks seen in the ordered ethyl and isobutyl samples.

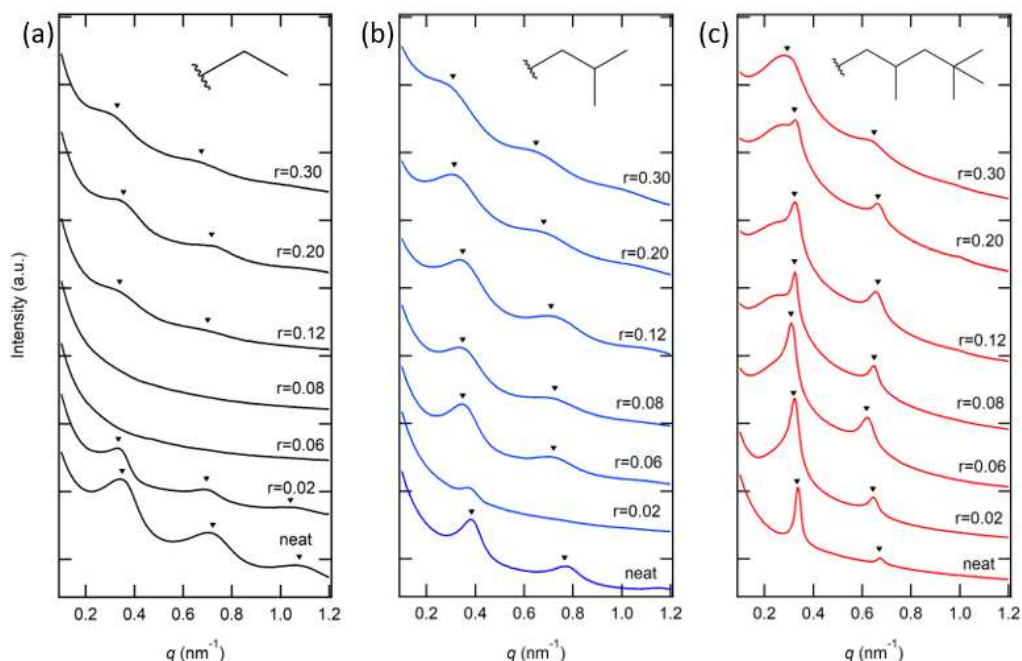


Figure 5.2. Scattering intensity at 70 °C of the three PEO-POSS polymers with various salt concentrations, plotted as a function of the magnitude of the scattering vector, q . (a) ethyl (b) isobutyl and (c) isooctyl. Profiles are shifted vertically. Triangles indicate peaks at q^* , $2q^*$, and $3q^*$ (when identified). These peaks signify lamellar order.

To better quantify the ordering in our systems, we analyze the absolute scattering intensities of each sample. These profiles, qualitatively similar to the raw scattering profiles of Figure 5.2, are given in Figure 5.20 in the Supporting Information. In Figure 5.3a, we show scattering in the vicinity of the primary peak for the ethyl sample at $r = 0.02$. A Lorentzian fit (with a linear background) through the data is shown by the curve. The primary peak after background subtraction is shown as a dashed curve in Figure 5.3a. This enables determination of the full-width-half-max (FWHM), which for the sample in Figure 5.3a is 0.082 nm^{-1} . In Figure 5.3b, we shown scattering in the vicinity of the primary peak for the isooctyl sample at $r = 0.12$. Clearly, a single Lorentzian is not consistent with this data set, and we thus use a two Lorentzian fit to characterize this sample. This enables determination of two FWHM values corresponding to the two peaks shown in Figure 5.3b (0.14 and 0.036 nm^{-1}). All of the scattering curves from the ethyl and isobutyl samples were analyzed using the approach shown in Figure 5.3a. The scattering curve from the neat isooctyl sample was analyzed using one Lorentzian while the salty samples were analyzed using two Lorentzians as in Figure 5.3b.

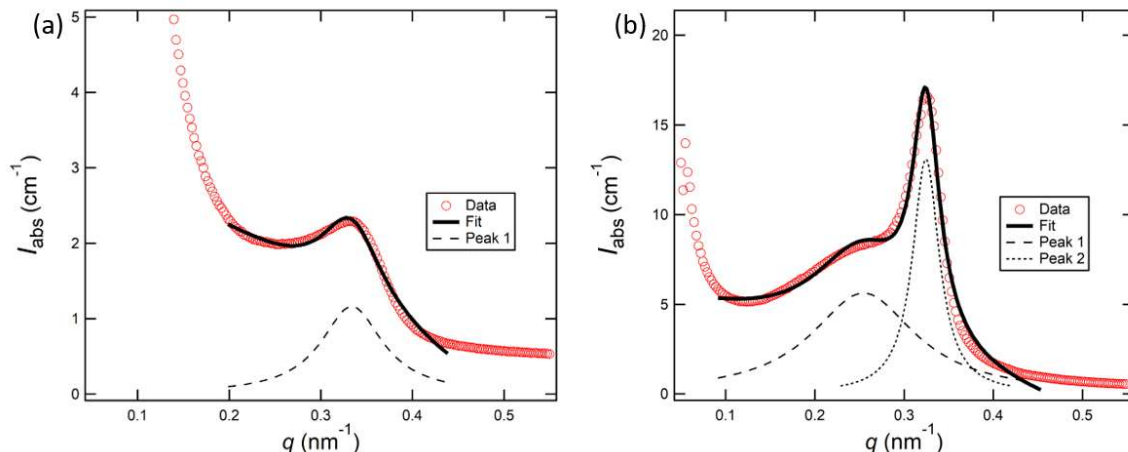


Figure 5.3. Lorentzian fits of the scattering around the primary peak. (a) $r = 0.02$ ethyl sample, with a FWHM of 0.082 nm^{-1} , and the (b) $r = 0.12$ isooctyl sample, which has FWHMs of 0.14 and 0.036 nm^{-1} .

In Figure 5.4a we compare the locations of the scattering peaks in the salty isooctyl samples. There is a clear distinction between the broad and sharp peaks. In Figure 5.4b, we plot the FWHMs obtained from our fitting procedure outlined above. The widths of the primary scattering peaks of the ethyl and isobutyl samples are similar, and we obtain FWHMs between 0.07 and 0.13 nm^{-1} . We obtain two sets of FWHM values for the isooctyl samples, one set that is qualitatively similar to that of the ethyl and isobutyl samples, and another with significantly lower FWHM values ranging from 0.02 to 0.04 nm^{-1} . It is perhaps interesting to note that the FWHM of the ordered phase formed in the neat isooctyl sample is qualitatively different than those obtained in the other samples, both with and without salt. The addition of salt to the isooctyl sample results in the emergence of a broad scattering profile that is qualitatively similar to that obtained from the other samples. The FWHM is generally assumed to be an indication of the extent of long range order. We conclude that the salt-containing isooctyl samples comprise two kinds of ordered phases with distinct extents of long range order. In Figure 5.4c we compare the volume fractions of the two coexisting phases in our salty isooctyl samples by integrating $I_{\text{abs}}q^2$ of the broad and sharp peaks (see Figure 5.3b) using a procedure outlined in ref ¹⁶². The volume fraction of the phase with greater long range order decreases with increasing salt concentration.

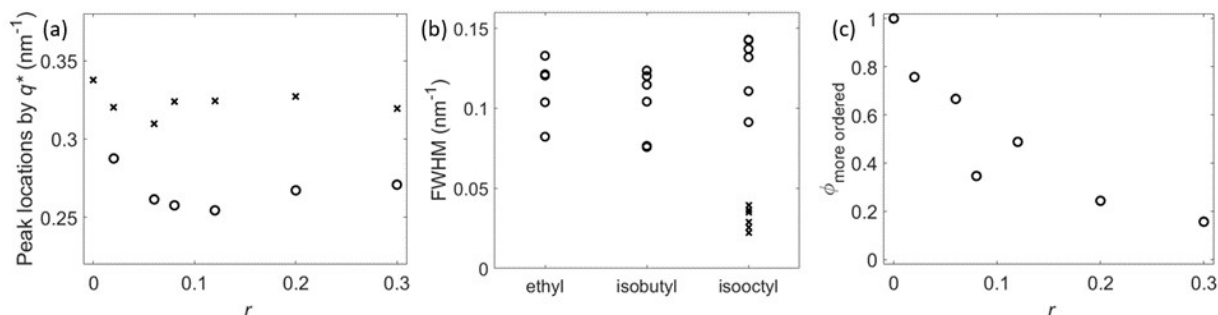


Figure 5.4. PEO-POSS scattering peak location, full-width-half-max, and volume fraction of more ordered phase. (a) Plot of the peak locations around q^* in the isooctyl samples versus salt concentration, where the circles denote the broad peaks and the x's denote the sharp peaks. (b) Plot of the full-width-half-max of the primary scattering peak versus POSS silica cage alkyl substituent, where circles denote the broad peaks found in the ethyl, isobutyl and salty isooctyl samples, and x's denote the sharp peaks in the isooctyl samples. (c) Plot of the volume fraction of the phase in the isooctyl electrolytes with more long range order versus salt concentration, r .

Samples were annealed at 70 °C and quenched in liquid nitrogen to “freeze” the morphology at these temperatures before performing electron microscopy. The resulting TEM micrographs are shown in Figure 5.5, where the dark phase represents the RuO₄ stained PEO-rich microphases. The micrographs obtained from those samples show similar alternating dark and bright stripes, PEO-rich and POSS-rich domains, representing the lamellar phase separation. Figure 5.5a shows the typical lamellar morphology in the neat ethyl sample. As shown in Figure 5.5b, the lamellar structure in the isooctyl sample exhibits a more long-range ordered structure with larger spacing (d). In addition, the Fourier transforms of the micrographs suggest that the isooctyl sample has the largest d as compared to the d in neat ethyl sample and the salty isooctyl sample ($r = 0.12$). The distinction between the two kinds of lamellar phases in salty isooctyl samples is not evident by the micrograph in Figure 5.5c. We note that similar data (i.e. the presence of an additional peak in the vicinity of the primary peak) have been obtained from other salty block copolymers. The presence of coexisting phases is clearly seen by TEM in some cases,^{28,141} but not in others.¹⁶³ In ref¹⁶³, the presence of an additional peak was attributed to the formation of a superlattice. Further work is needed to establish the origin of the SAXS pattern shown in Figure 5.4b.

The effect of added salt and monomer structure on morphology is summarized in Figure 5.6. In ethyl and isobutyl samples, we only see lamellae and disorder. In the isooctyl samples, we see lamellae in the neat state and coexisting phases in the presence of added salt. The thermodynamic interactions between the PEO and POSS blocks in the presence of salt is complex. Disordered phases are formed upon salt addition but this applies to a limited window of salt concentrations. When this window is exceeded, ordered phases reappear at high salt concentrations. The salt concentration window for which disordering occurs decreases as we increase the POSS alkyl substituent chain length and is absent in the isooctyl sample. There are many possible reasons for the complex phase behavior seen in Figure 5.6. This includes

differences in polarity of the POSS block, shielding of repulsive interactions between the POSS particle and PEO due to the presence of alkyl substituents, and the distribution of ions in PEO-rich and POSS-rich domains. Partial solubility of LiTFSI in the POSS-rich domains may account for

differences in phase behavior. It is evident that segregation and phase separation in PEO POSS(5-1) block copolymers is greatly affected by the functional groups on the POSS monomer.

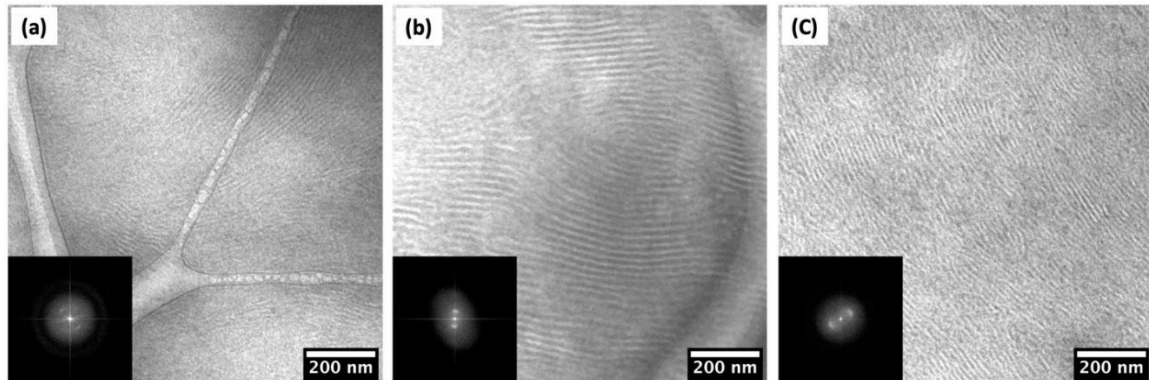


Figure 5.5. TEM micrographs of PEO-POSS. (a) neat ethyl sample, (b) neat isooctyl sample, and (c) isooctyl $r = 0.12$. The dark phase represents the RuO_4 stained PEO domain. Insets show the Fourier transforms of the micrographs. Lamellar order is seen in all cases.

The effect of added salt and monomer structure on morphology is summarized in Figure 5.6. In ethyl and isobutyl samples, we only see lamellae and disorder. In the isooctyl samples, we see lamellae in the neat state and coexisting phases in the presence of added salt. The thermodynamic interactions between the PEO and POSS blocks in the presence of salt is complex. Disordered phases are formed upon salt addition but this applies to a limited window of salt concentrations. When this window is exceeded, ordered phases reappear at high salt concentrations. The salt concentration window for which disordering occurs decreases as we increase the POSS alkyl substituent chain length and is absent in the isooctyl sample. There are many possible reasons for the complex phase behavior seen in Figure 5.6. This includes differences in polarity of the POSS block, shielding of repulsive interactions between the POSS particle and PEO due to the presence of alkyl substituents, and the distribution of ions in PEO-rich and POSS-rich domains. Partial solubility of LiTFSI in the POSS-rich domains may account for differences in phase behavior. It is evident that segregation and phase separation in PEO POSS(5-1) block copolymers is greatly affected by the functional groups on the POSS monomer.

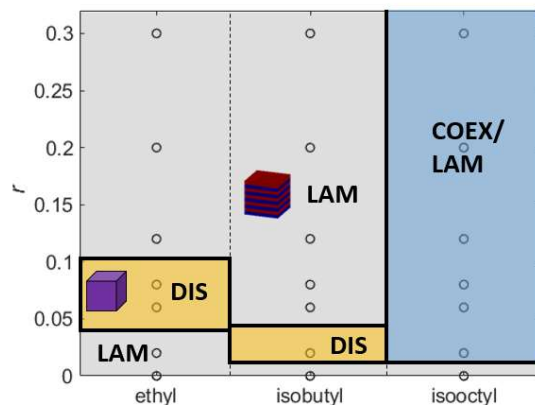


Figure 5.6. Morphology of phases on a salt concentration, r , versus POSS silica cage alkyl substituent plot. Lamellar (LAM) and disordered (DIS), as well as a coexistence of ordered phases (COEX/LAM) are seen.

We measured the ionic conductivity, salt diffusion coefficient, and the current ratio of the three PEO-POSS(5-1) systems in order to determine the effect of POSS alkyl substituent length on ion transport. In Figure 6a we see that upon salt addition, the conductivity for all three PEO-POSS(5-1) polymers increase until they reach a maximum at around $r = 0.12$ before decreasing at higher salt concentrations. Ionic conductivity in polymer electrolytes depends on both charge concentration and segmental motion.¹⁰² The glass transition temperature is a simple measure of this segmental relaxation. In our system, the glass transition temperature increases as salt is added (see Figures 5.16-5.18) due to ion and polymer associations, from $-45\text{ }^{\circ}\text{C}$ at $r = 0.08$ to $-15\text{ }^{\circ}\text{C}$ at $r = 0.30$ (all of the PEO-POSS(5-1) samples exhibit similar behavior; see Figure 5.19). The peak in the conductivity curves in Figure 5.7a arises due to the interplay between the increase in charge carrier concentration and the slowing down of segmental relaxation. We can account for the volume fraction of the conducting phase, φ_c , to get a better idea of the differences in intrinsic conductivities across the three systems by utilizing the following equation: $\kappa_n = \kappa_{\text{PEO/POSS}}\varphi_c^{-1}\kappa_{\text{PEO}}^{-1}$, where κ_{PEO} is the ionic conductivity of PEO (10 kg mol^{-1}) at $70\text{ }^{\circ}\text{C}$. Previous studies suggest that the ionic conductivity of PEO/LiTFSI mixtures is independent of molecular weight when it exceeds 2 kg mol^{-1} .⁸⁸ Increasing the length of the alkyl substituents reduces φ_c at fixed chain length. The plot of normalized conductivity, κ_n , versus POSS silica cage alkyl substituent is shown in Figure 5.7b. Even after accounting for differences in φ_c (see Figure 5.22), the ethyl samples show the highest conductivity, especially in the vicinity of the conductivity maximum. It is perhaps surprising that the greatest normalized conductivity is at the highest salt concentration, $r = 0.30$. We posit that at high salt concentration, some of the LiTFSI molecules are located in the POSS-rich microphase due to entropic reasons. This will result in a lower salt concentration in the conducting PEO-rich domains, which, in turn, will increase the intrinsic conductivity of these domains as the conductivity of PEO decreases with increasing salt concentration for $r > 0.10$.¹⁵⁹ The concentration dependence of the salt diffusion coefficient is shown in Figure 5.7c. Neither salt concentration nor alkyl chain length has a strong influence on this parameter, which falls around $10^{-8}\text{ cm}^2\text{ s}^{-1}$ for all three PEO-POSS(5-1) systems. The concentration dependence of the current fraction shown in Figure 5.7d is similar to that reported for SEO/LiTFSI mixtures and is independent of alkyl chain length.¹⁵⁹

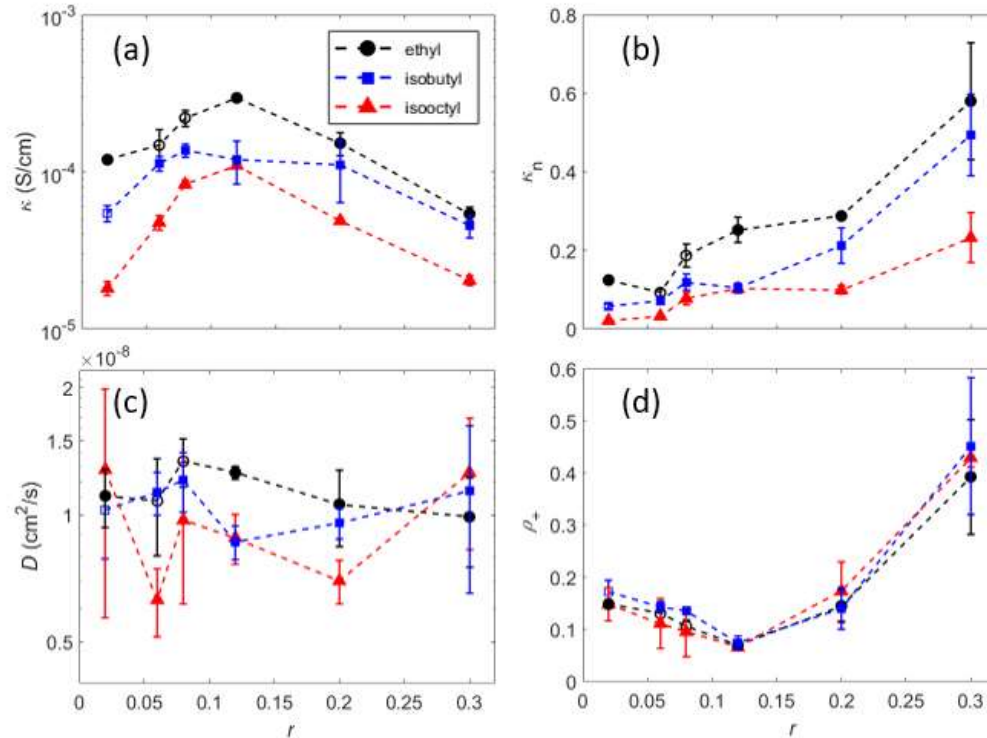


Figure 5.7. Electrochemical data for PEO-POSS. (a) Ionic conductivity from ac impedance spectroscopy of symmetric cells with blocking electrodes. (b) Normalized conductivity, κ_n , using PEO (10 kg mol^{-1}) data. For all salt concentrations, the normalized conductivity decreases as we increase the alkyl substituent length. (c) Salt diffusion coefficient from restricted diffusion measurements in a lithium symmetric cell. (d) Current fractions calculated from the Bruce-Vincent method using a lithium symmetric cell. Data was taken at $70 \text{ }^\circ\text{C}$. The solid markers denote ordered morphologies while open face markers correspond to a disordered phase.

We compare the mechanical properties of neat PEO-POSS(5-1) to neat PEO(20) with a molecular weight of 20 kg mol^{-1} and neat SEO(5-5) which has two blocks of molecular weight 5 kg mol^{-1} . (We choose SEO(5-5) because it exhibits lamellar order.) The storage modulus, G' , of the PEO-POSS(5-1) polymers, shown in Figure 5.8a, is a weak function of frequency, typical of solid-like polymers. The magnitude of G' of all three of our PEO-POSS(5-1) polymers is similar. In the low frequency limit, $G' \sim \omega^{0.2}$ for all three PEO-POSS(5-1) polymers. Amongst the polymers covered in this study, the isobutyl sample exhibits the highest storage modulus. G' of PEO-POSS(5-1) polymers is higher than that of PEO(20) and SEO(5-5) by factors between 10^2 and 10^3 . The frequency dependence of the loss modulus, G'' , is shown in Figure 5.8b. G'' is a weak function of frequency for PEO-POSS(5-1) polymers. In the low frequency limit, $G'' \sim \omega^{0.2}$ for the ethyl and isobutyl samples. For the isooctyl sample $G'' \sim \omega^{0.5}$. At high frequencies, G'' of these polymers is comparable to that of PEO(20) and SEO(5-5). At low frequencies, G'' of PEO-POSS(5-1) polymers is about a factor of 10 higher than SEO(5-5). Both G' and G'' of PEO(20) and SEO(5-5) decrease rapidly with decreasing frequency.

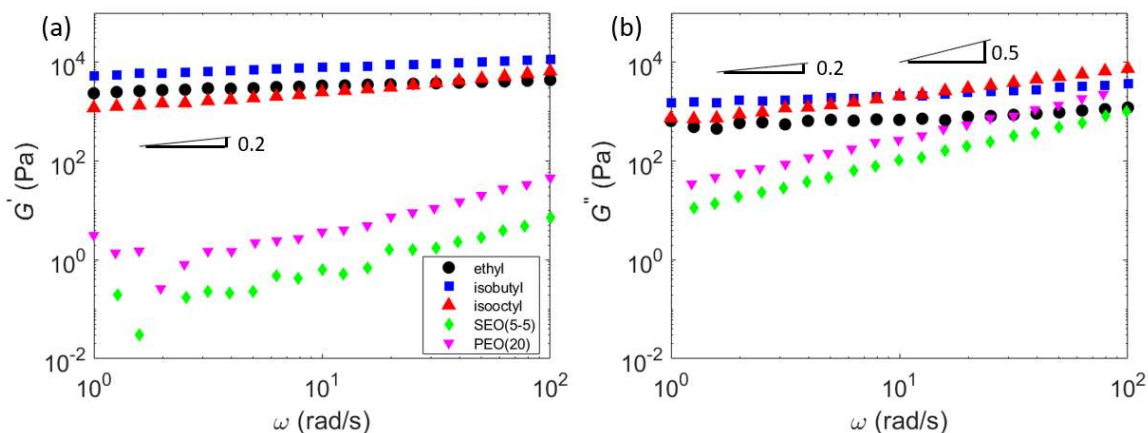


Figure 5.8. Storage and loss moduli as a function of frequency for PEO-POSS.(a) Storage and (b) loss moduli as a function of frequency for PEO-POSS(5-1), SEO(5-5), and PEO(20). All three PEO-POSS(5-1) polymers exhibit greater mechanical rigidity than SEO(5-5) and PEO(20).

5.4 Conclusions

We have synthesized and characterized a set of three PEO-POSS(5-1) block copolymer electrolytes with ethyl, isobutyl, and isooctyl substituents on the POSS silica cage. These electrolytes primarily exhibit lamellar morphologies. If only interactions between the salt and PEO were important, then changing the monomer structure of the non-conducting block would have a minimal effect on both thermodynamics and transport. We show, however, that this is not the case. Increasing the length of the POSS alkyl chain substituent leads to a smaller salt concentration window for disorder. In the isooctyl case, no disordered window is observed. Instead, we find coexisting ordered phases that are absent in the ethyl and isobutyl samples. The ethyl samples exhibit the highest ionic conductivity even after normalizing for the volume fraction of conducting phase. The salt diffusion coefficient and current ratio are not affected by the alkyl substituent length. These results indicate that the ethyl systems are optimal for ion transport applications. Further investigation is needed to better understand the relationship between the thermodynamic behavior and ion transport in these hybrid organic-inorganic systems.

5.5 Acknowledgements

This work was intellectually led by the Joint Center for Energy Storage Research (JCESR), an Energy Innovation Hub funded by the U.S. Department of Energy, Office of Science, Office of Basic Energy Science, under Contract No. DE-AC02-06CH11357, which supported both synthesis and characterization work conducted by K.W.G. under the supervision of N.P.B. Work at the Donner Lab, the Molecular Foundry, and the Advanced Light Source, which is a DOE Office of Science User Facility, was supported by Contract No. DE-AC02-05CH11231. Work at the Stanford Synchrotron Radiation Light Source, a user facility at SLAC National Accelerator Laboratory, was supported by the U.S. Department of Energy, Office of Science, Office of Basic Energy Science under Contract No. DE-AC02-76SF00515. K.W.G. acknowledges funding from a National Defense and Science Engineering Graduate Fellowship.

5.6 Supporting Information

5.6.1 Synthesis of PEO-POSS Block Copolymer.

Poly(ethylene oxide)-methyl-ether acrylate (PEO-acrylate) ($M_w = 5 \text{ kg mol}^{-1}$), anhydrous ethanol, anhydrous xylene, diethyl ether and tetrahydrofuran (THF) were purchased from Sigma-Aldrich; methacrylethyl, methacryloisobutyl, and methacryloisooctyl polyhedral oligomeric silsesquioxane (POSS) were purchased from Hybrid Plastic; BlocBuilder MA was kindly provided by Arkema. All chemicals were used as received. Lithium bis(trifluoromethanesulfone)imide, $\text{Li}[\text{N}(\text{SO}_2\text{CF}_3)_2]$ (LiTFSI), was purchased from Novolyte and dried at $120 \text{ }^\circ\text{C}$ for at least 48 hours before use.

The three PEO-POSS block copolymers were synthesized by nitroxide-mediated radical polymerization. PEO-acrylate was first reacted with BlocBuilder MA (10 eq) in anhydrous ethanol at $100 \text{ }^\circ\text{C}$ under argon for 4 h. PEO-based macroalkoxyamine was collected by precipitation in cold diethylether. Each POSS monomer (10 eq) was then polymerized using the PEO-based macroalkoxyamine as initiator in anhydrous xylene at $115 \text{ }^\circ\text{C}$ for 24 h. The product was isolated by precipitation in cold diethyl ether and centrifuged at 6500 rpm for 15 min. This step was repeated three times to obtain a solid white powder. Molecular weight of the POSS block was determined using $^1\text{H-NMR}$ to be 0.7, 0.9, and 1.3 kg mol^{-1} respectively for the ethyl, isobutyl, and isooctyl PEO-POSS block copolymers.

PEO-POSS-ethyl $^1\text{H-NMR}$ (CDCl_3 , 400 MHz, δ): 3.64 (s, 2H, $-\text{CH}_2-$), 0.98 (t, 3H, $-\text{CH}_3$), 0.61 (m, 4H, $-\text{CH}_2-$).

PEO-POSS-isobutyl $^1\text{H-NMR}$ (CDCl_3 , 400 MHz, δ): 3.64 (s, 2H, $-\text{CH}_2-$), 1.80 (m, H, $-\text{CH}-$), 0.96 (d, 6H, $-\text{CH}_3$), 0.59 (m, 4H, $-\text{CH}_2-$).

PEO-POSS-isooctyl $^1\text{H-NMR}$ (CDCl_3 , 400 MHz, δ): 3.64 (s, 2H, $-\text{CH}_2-$), 1.14–1.29 (m, 3H, $-\text{CH}-\text{CH}_2-$), 1.00 (d, 3H, $-\text{CH}_3$), 0.89 (s, 9H, $-\text{CH}_3$), 0.56–0.73 (m, 4H, $-\text{CH}_2-$).

The composition of the inorganic-organic copolymers was determined using $^1\text{H NMR}$ (CDCl_3 , Bruker AV400) measurements by integrating the characteristic peaks of the ethylene protons of PEO block at 3.64 ppm versus protons at 0.98 ppm of the ethyl POSS block, 0.96 ppm of the isobutyl POSS block, and 0.89 ppm of the isooctyl POSS block in Figure 5.9 -5.11, respectively.

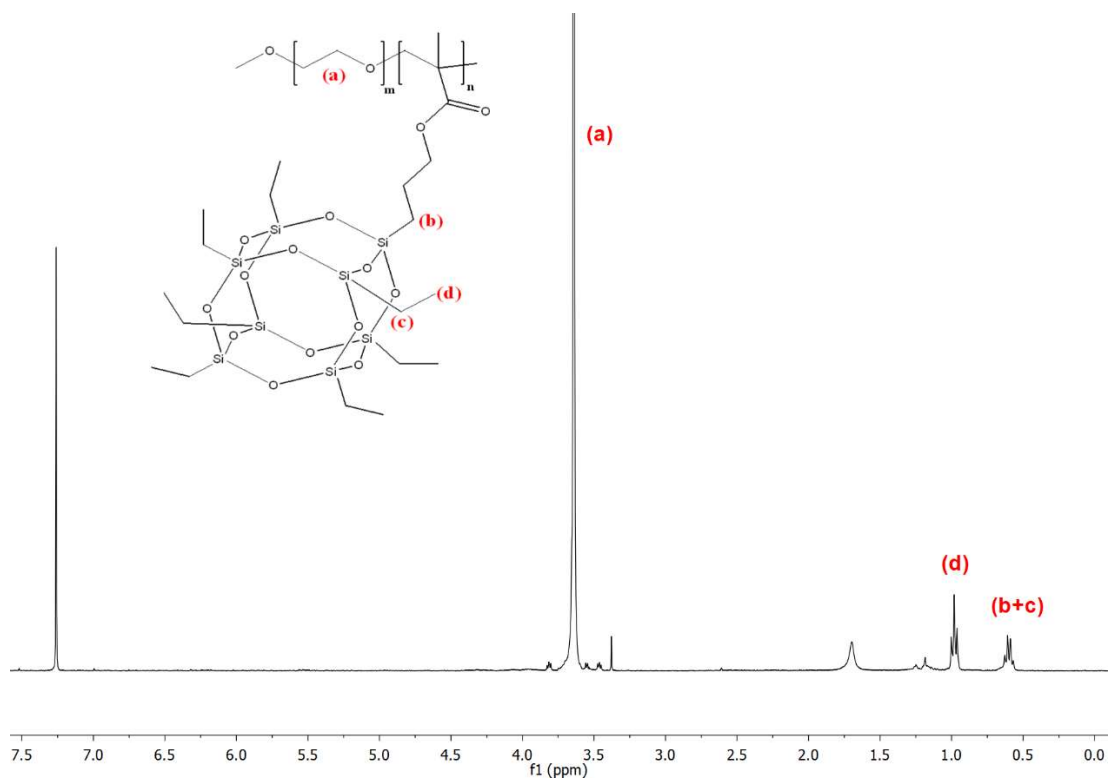


Figure 5.9. ¹H-NMR spectra of PEO-POSS-ethyl. A sharp peak due to PEO is visible at a chemical shift, δ , of 3.64 and POSS at 0.61 and 0.98 ppm. The corresponding hydrogens are indicated on the PEO-POSS-ethyl chemical structure labeled (a) from the PEO chain, (b+c) from the acrylate chain and two hydrogens on the ethyl groups, and (d) from the end hydrogens on the ethyl groups.

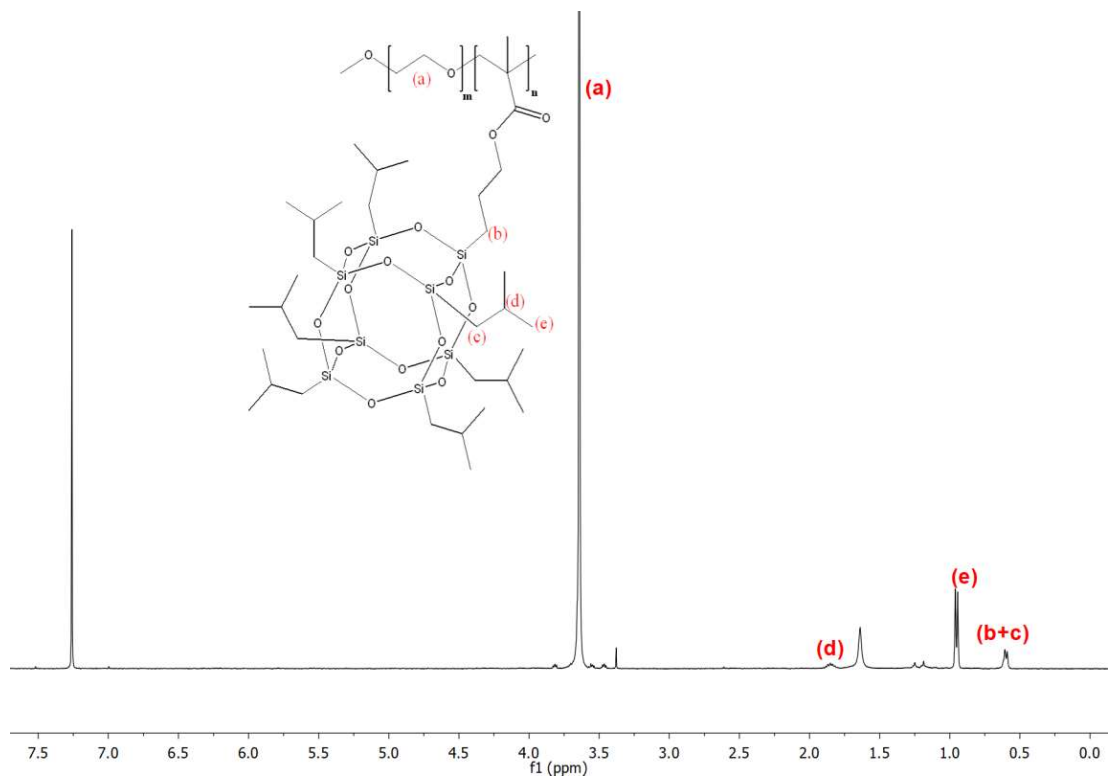


Figure 5.10. ¹H-NMR spectra of PEO-POSS-isobutyl. A sharp peak due to PEO is visible at a chemical shift, δ , of 3.64 and POSS at 0.59, 0.96, and 1.80 ppm. The corresponding hydrogens are indicated on the PEO-POSS-isobutyl chemical structure labeled (a) from the PEO chain, (b+c) from the acrylate chain and two hydrogens on the isobutyl groups, (e) from the end hydrogens on the isobutyl groups, and (d) from the single hydrogen on the isobutyl groups.

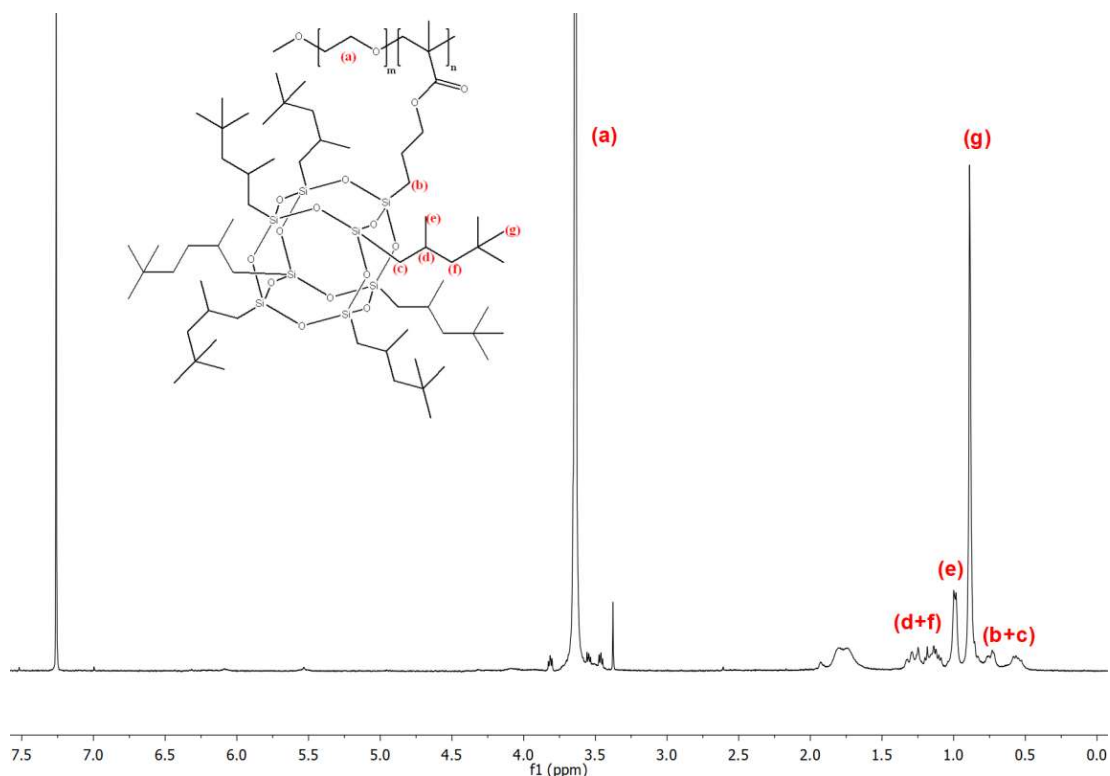


Figure 5.11. $^1\text{H-NMR}$ spectra of PEO-POSS-isoctyl. A sharp peak due to PEO is visible at a chemical shift, δ , of 3.64 and POSS at 0.56–0.73, 0.89, 1.00, and 1.14–1.29 ppm. The corresponding hydrogens are indicated on the PEO-POSS-isoctyl chemical structure labeled (a) from the PEO chain, (b+c) from the acrylate chain and two hydrogens closest to the POSS cage on the isoctyl groups, (g) from the hydrogens on the three methyl carbons on the end of the isoctyl groups, (e) from the hydrogens on the lone methyl carbon on the isoctyl groups, and (d+f) from the hydrogens in the middle of the isoctyl groups.

PEO-POSS was characterized by a Malvern Viscotek TDAmx system gel permeation chromatography (GPC) system with a mobile phase of THF using an injection volume of 100 μL and polymer concentration of around 5.0 g L^{-1} . GPC traces of the PEO-POSS copolymers in relation to PEO-based macroalkoxyamine starting material confirm the polymerization of the POSS block, shown in Figure 5.12. Due to the complex molecular structure of the PEO-POSS copolymer and potential interactions between the polymer segments and the columns, we only use the GPC data to confirm addition of POSS segments onto the PEO chain.

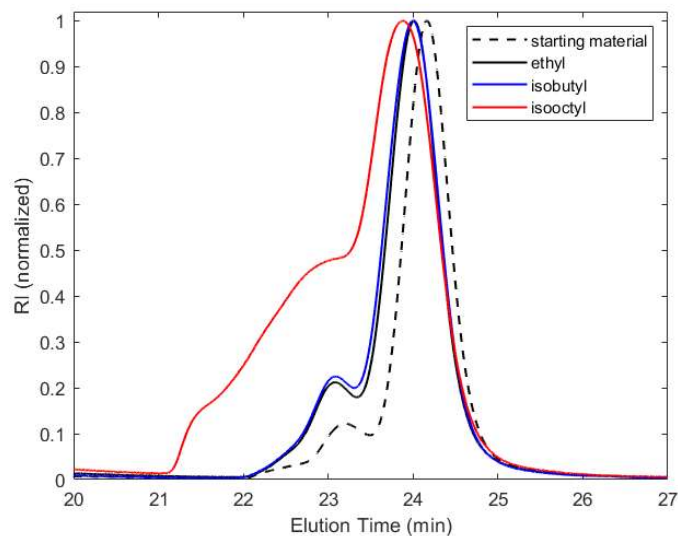


Figure 5.12. GPC data for PEO-POSS block copolymers and PEO-based macroalkoxyamine starting material. The shoulders at lower elution times before the primary GPC peak is likely due to polymer aggregation in THF.

The polymer thermal degradation temperature was determined via thermogravimetric analysis (TGA) using TA Instruments Q5500 TGA-MS at the Molecular Foundry, LBNL. Data are shown in Figures 5.13–5.15.

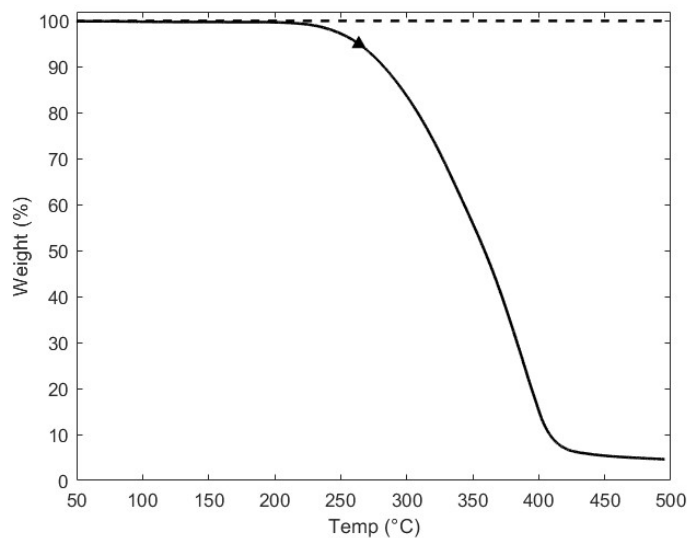


Figure 5.13. TGA data for PEO-POSS-ethyl plotting weight percent versus temperature. 100% is marked in the y-axis with a dashed line. The temperature at 5% decrease in weight, T₉₅, noted with a triangle, is 270 °C.

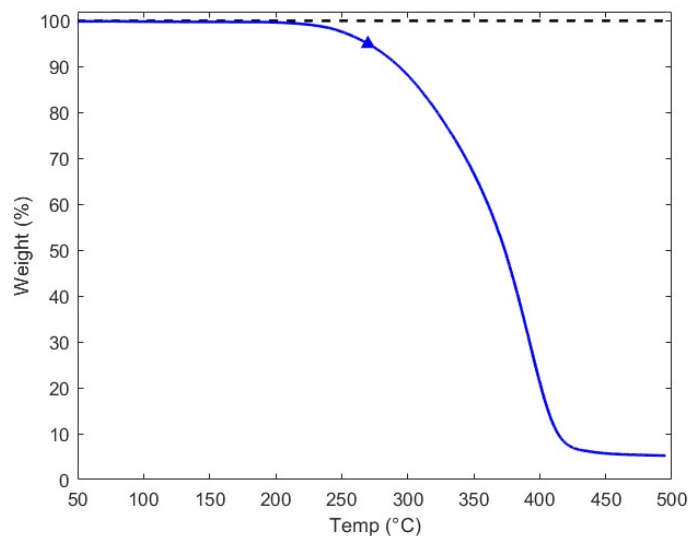


Figure 5.14. TGA data for PEO-POSS-isobutyl plotting weight percent versus temperature. 100% is marked in the y-axis with a dashed line. The temperature at 5% decrease in weight, T_{95} , noted with a triangle, is 270 °C.

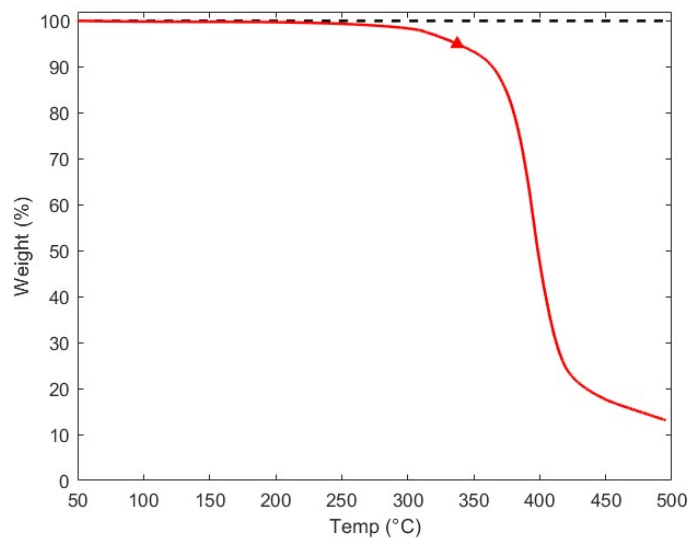


Figure 5.15. TGA data for PEO-POSS-isooctyl plotting weight percent versus temperature. 100% is marked in the y-axis with a dashed line. The temperature at 5% decrease in weight, T_{95} , noted with a triangle, is 338 °C.

5.6.2 Differential Scanning Calorimetry (DSC)

Samples were hermetically sealed in aluminum pans in an argon glovebox. Differential scanning calorimetry (DSC) experiments were run with two heating and cooling cycles with 10 °C min⁻¹

heating rates and $2\text{ }^{\circ}\text{C min}^{-1}$ cooling rates using a Thermal Advantage Q200 calorimeter at the Molecular Foundry, LBNL. The temperature ranged from -80 to $140\text{ }^{\circ}\text{C}$. Melting and glass transition temperatures were obtained from analysis of the second heating stage. Data are shown in Figure 5.16-5.18.

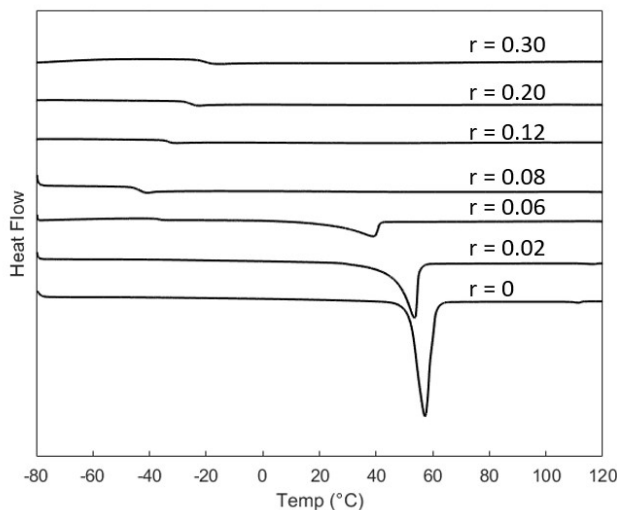


Figure 5.16. DSC curves of PEO-POSS-ethyl from $r = 0$ to $r = 0.30$ upon second heating cycle. The glass transition temperature is visible for salt concentrations $r = 0.06$ to $r = 0.30$. A melting transition occurs in salt concentrations $r = 0$ to $r = 0.06$.

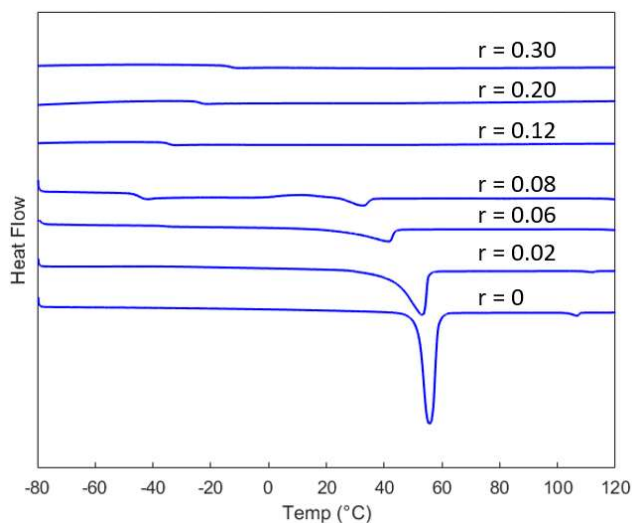


Figure 5.17. DSC curves of PEO-POSS-isobutyl from $r = 0$ to $r = 0.30$ upon second heating cycle.

The glass transition temperature is visible for salt concentrations $r = 0.06$ to $r = 0.30$. A melting transition occurs in salt concentrations $r = 0$ to $r = 0.08$.

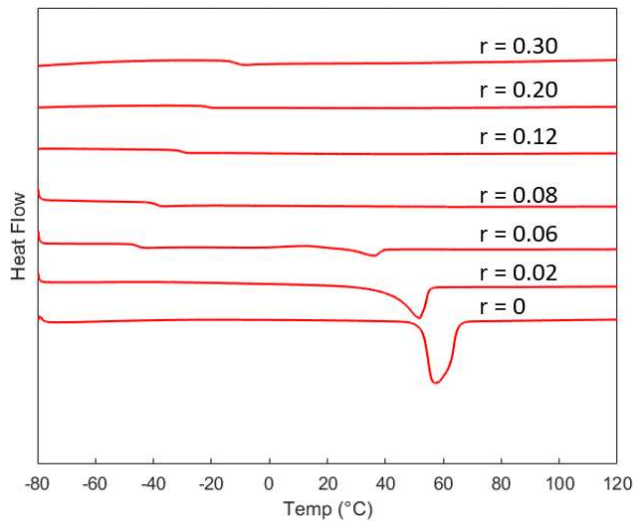


Figure 5.18. DSC curves of PEO-POSS-isoctyl from $r = 0$ to $r = 0.30$ upon second heating cycle. The glass transition temperature is visible for salt concentrations $r = 0.06$ to $r = 0.30$. A melting transition occurs in salt concentrations $r = 0$ to $r = 0.06$.

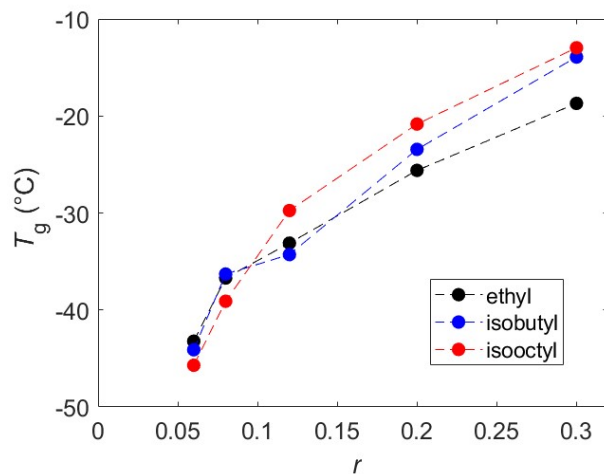


Figure 5.19. Glass transition temperature, T_g , as a function of salt concentration, r , for the three PEO-POSS(5-1) polymers. We see similar behavior across the three polymers with increasing salt concentration.

5.6.3 Absolute SAXS Data

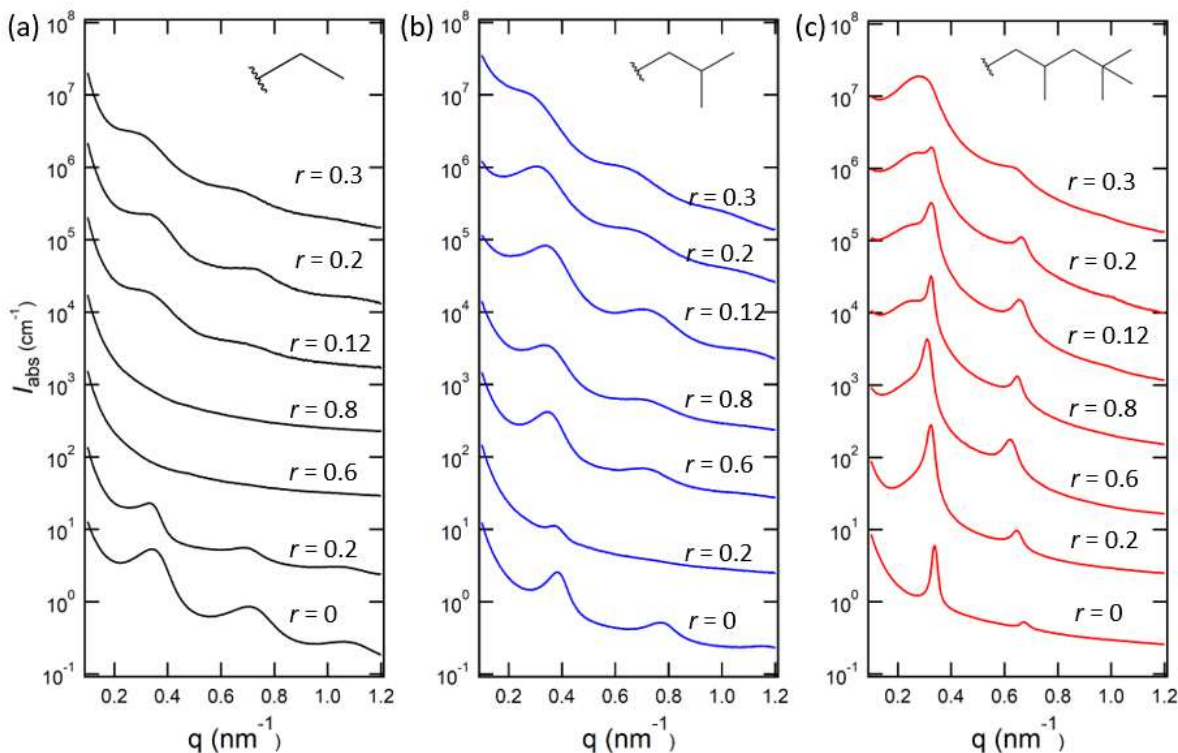


Figure 5.20. Absolute scattering intensities for PEO-POSS(5-1) (a) ethyl (b) isobutyl (c) isoctyl. The neat profiles are unscaled while every successive salt concentration is scaled by a factor of 10. The absolute scattering profiles are qualitatively similar to the raw scattering profiles.

5.6.4 Impedance Spectroscopy.

Complex impedance measurements were performed on conductivity cells using a Bio-Logic VMP3 potentiostat over a $0.1 - 10^6$ Hz frequency range at an amplitude of 80 mV to find the ionic conductivity, κ . The ionic conductivity is given by the following equation:

$$\kappa = \frac{l}{R_b A}$$

where l is the thickness of the electrolyte, R_b is the bulk electrolyte resistance and A is the electrolyte to electrode area.

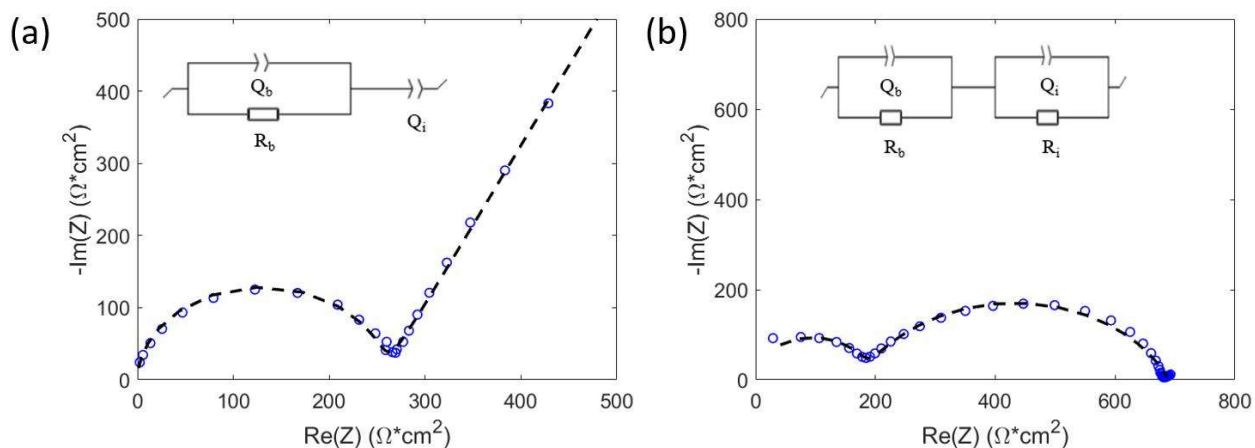


Figure 5.21. Nyquist plots at 90 °C for (a) blocking electrode conductivity cell for an isobutyl $r = 0.12$ sample and (b) lithium symmetric cell for an isobutyl $r = 0.12$ sample. The equivalent circuit is shown in the inset, where Q_b is the bulk capacitance, R_b is the bulk resistance of the electrolyte, Q_i is the interfacial capacitance, and R_i is the interfacial resistance. The conductivity calculated from (a) and (b) is 0.000166 S/cm and 0.000168 S/cm respectively

5.6.5 Density Measurements and Volume Fraction Calculations

Samples were heated to 90 °C, weighed, and filled into pre-weighed aluminum pans with a known volume of 0.04 cm³. Pans were hermetically sealed in an argon glovebox and excess polymer was carefully cleaned from the pan. The final weight was recorded. Density of the PEO-POSS diblock copolymers was determined by dividing the mass by the known volume of sample pan. Measurements were repeated three times. The neat ethyl density was 1.11 ± 0.04 g cm⁻³. The neat isobutyl density was 1.13 ± 0.03 g cm⁻³. The neat isooctyl density was 1.10 ± 0.04 g cm⁻³.

The volume fraction of the EO/LiTFSI-rich phase in the polymers was calculated using the following equation:

$$\varphi_{\text{EO/LiTFSI}} = \frac{v_{\text{EO}} + rv_{\text{LiTFSI}}}{v_{\text{EO}} + rv_{\text{LiTFSI}} + \frac{M_{\text{PPOSS}}M_{\text{EO}}}{M_{\text{POSS}}M_{\text{PEO}}}v_{\text{POSS}}}$$

where

v_{EO} = molar volume of ethylene oxide monomer units

v_{POSS} = molar volume of POSS monomer units

v_{LiTFSI} = molar volume of LiTFSI

$r = [\text{Li}]/[\text{EO}]$

M_{PPOSS} = molar mass of polymerized POSS = [0.7 kg mol⁻¹, 0.9 kg mol⁻¹, 1.3 kg mol⁻¹] respectively for ethyl, isobutyl, and isooctyl

M_{POSS} = molar mass of POSS monomer = M_{PPOSS}

M_{EO} = molar mass of EO monomer = 44 g mol⁻¹

M_{PEO} = molar mass of PEO = 5.0 kg mol⁻¹

Molar volumes are calculated using the following equation:

$$v_i = M_i/\rho_i$$

where M_i and ρ_i are the molar masses of unit i and density of unit i respectively.

$\rho_{\text{PEO}} = 1.13 \text{ g cm}^{-3}$

The densities of block copolymers were given in the previous section:

$\rho_{\text{PEOPOSS,ethyl}} = 1.11 \text{ g cm}^{-3}$

$\rho_{\text{PEOPOSS,isobutyl}} = 1.13 \text{ g cm}^{-3}$

$\rho_{\text{PEOPOSS,isoctyl}} = 1.10 \text{ g cm}^{-3}$

The density of the POSS-rich phase was determined under the assumption that the volumes of the EO-rich and POSS-rich phases are additive. The densities of the POSS-rich phase were calculated using the following equation:

$$\rho_{\text{POSS}} = \frac{M_{\text{POSS}}}{\left(\frac{M_{\text{PEO}} + M_{\text{POSS}}}{\rho_{\text{PEOPOSS}}} - \frac{M_{\text{PEO}}}{\rho_{\text{PEO}}}\right)}$$

$\rho_{\text{POSS,ethyl}} = 1.09 \text{ g cm}^{-3}$

$\rho_{\text{POSS,isobutyl}} = 1.13 \text{ g cm}^{-3}$

$\rho_{\text{POSS,isoctyl}} = 1.03 \text{ g cm}^{-3}$

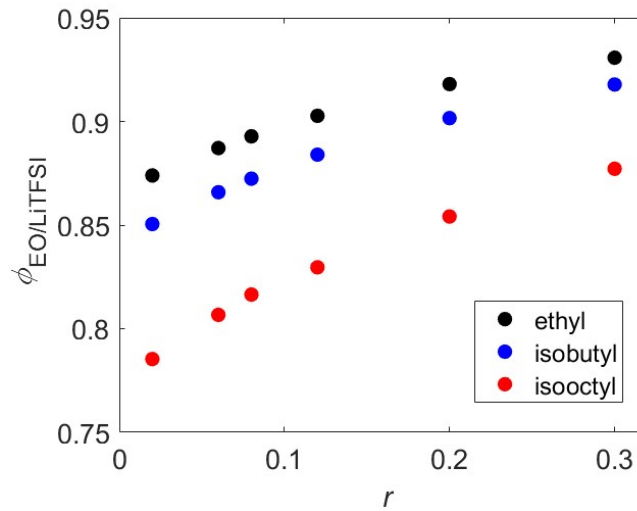


Figure 5.22. Volume fraction of the EO/LiTFSI-rich phase, $\phi_{\text{EO/LiTFSI}}$, as a function of r .

5.7 Nomenclature

Table 5.2. List of symbols and abbreviations.

Symbol	Meaning
PEO	Poly(ethylene oxide)
POSS	Polyhedral oligomeric silsesquioxane
LiTFSI	Lithium bis(trifluoromethanesulfonyl)imide
SEO	Polystyrene- <i>b</i> -poly(ethylene oxide)
SAXS	Small angle X-ray scattering
TEM	Transmission electron microscopy
r	Salt concentration given by the ratio of lithium ions in the salt to oxygen atoms in the polymer
M	Molar mass
f	Volume fraction
I	Intensity
q	Scattering vector
I_{abs}	Absolute intensity
κ	Ionic conductivity
ρ_+	Current fraction
$R_{i,0}$	Initial interfacial resistance
$R_{i,ss}$	Steady-state interfacial resistance
ΔV	Applied voltage difference
i_{Ω}	Initial current as defined as the ratio of applied voltage difference divided by the sum of the initial bulk and interfacial resistances
D	Salt diffusion coefficient
$t_{+,ss}$	Steady-state cation transference number
FWHM	Full-width-half-max
d	Domain spacing
RuO ₄	Ruthenium tetroxide
LAM	Lamellar morphology
DIS	Disordered morphology
COEX	Coexisting morphologies
ϕ	Volume fraction
κ_n	Normalized ionic conductivity (with respect to the conducting phase volume fraction)
G'	Storage modulus
G''	Loss modulus
ω	Frequency
THF	Tetrahydrofuran
NMR	Nuclear magnetic resonance
CDCl ₃	Deuterated chloroform
GPC	Gel permeation chromatography
TGA	Thermogravimetric analysis

DSC	Differential scanning calorimetry
T_g	Glass transition temperature
l	Thickness
R_b	Bulk resistance
A	Area of electrolyte
Q_b	Bulk capacitance
R_i	Interfacial resistance
Q_i	Interfacial capacitance
v	Molar volume
ρ	Density

6 Miscible Polyether/Poly(ether-acetal) Electrolyte Blends[†]

Abstract

This study shows that it is possible to obtain homogeneous mixtures of two chemically distinct polymers with a lithium salt for electrolytic applications. This approach is motivated by the success of using mixtures of organic solvents in modern lithium-ion batteries. The properties of mixtures of a polyether, poly(ethylene oxide) (PEO), a poly(ether-acetal), poly(1,3,6-trioxocane) (P(2EO-MO)), and lithium bis(trifluoromethanesulfonyl)imide (LiTFSI) salt were studied using small angle neutron scattering (SANS) and electrochemical characterization in symmetric cells. The SANS data are used to determine the miscibility window and quantify the effect of added salt on the thermodynamic interactions between the polymers. In the absence of salt, PEO/P(2EO-MO) blends are homogeneous and characterized by attractive interactions, i.e., a negative Flory-Huggins interaction parameter, χ . The addition of small amounts of salt results in a positive effective Flory-Huggins interaction parameter, χ_{eff} , and macrophase separation. Surprisingly, miscible blends and negative χ_{eff} parameters are obtained when salt concentration is increased beyond a critical value. The electrochemical properties of PEO/P(2EO-MO)/LiTFSI blends at a given salt concentration were close to those obtained in PEO/LiTFSI electrolytes at the same salt concentration. This suggests that in the presence of PEO, the electrochemical properties exhibited by P(2EO-MO) chains are similar to those of PEO chains. This work opens the door to a new direction for creating new and improved polymer electrolytes either by combining existing polymers and salt, or by synthesizing new polymers with the specific aim of including them in miscible polymer blend electrolytes.

6.1 Introduction

There is considerable interest in replacing flammable organic solvents with non-volatile polymers in rechargeable lithium batteries. It has long been recognized that high dielectric constant and low viscosity are necessary for rapid ion transport. In the case of lithium-ion batteries designed to operate at room temperature, this is achieved by blending materials. Ethylene carbonate has a dielectric constant of 89.8 but is solid at room temperature (m.p. = 36.4 °C) while dimethyl carbonate is a low viscosity liquid (m.p. = 4.6 °C) but has a dielectric constant of 3.1.⁵ Neither is a suitable solvent for electrolytic applications. However, a blend of ethylene carbonate and dimethyl carbonate is an excellent solvent for these applications and are major components of lithium-ion battery electrolytes.

Translating the notion of liquid electrolyte mixtures to polymer electrolyte blends is non-trivial. While most low molar mass liquids are miscible with each other (e.g. polar molecules like ethanol are miscible in non-polar liquids such as hexanes), finding pairs of miscible polymers is extremely rare.^{164,165} Polymers with seemingly minor differences in monomer structure are entirely immiscible. For example, the solubility of polyethylene in polypropylene (both polymers have

[†] This chapter was reported in *Macromolecules*, **2020**, 53 (14), 5728-5739.

empirical formulae CH_2) is negligible.^{166,167} The reason for this is well established: mixing is usually promoted by entropic considerations. The entropic gain of mixing polymers with long chains, however, is orders of magnitude smaller due to the connectivity of the monomers.

The purpose of this paper is to demonstrate that it is possible to create homogeneous mixtures of polymers with different polarities to create a new type of material for use in lithium batteries: miscible polymer blend electrolytes.

Our system of interest is a blend of a polyether, poly(ethylene oxide) (PEO), a poly(ether-acetal), poly(1,3,6-trioxocane) (P(2EO-MO)), and lithium bis(trifluoromethanesulfonyl)imide (LiTFSI) salt (see Figure 6.1). PEO has been thoroughly studied as a potential electrolyte for lithium batteries due to its non-volatility, electrochemical stability, and compatibility with lithium salts.^{12,13,17} The ability of PEO to dissolve lithium salts is due to the presence of ether oxygen groups. The properties of P(2EO-MO)/LiTFSI electrolytes were reported in ref⁹⁴. We expect P(2EO-MO) to be more polar than PEO due to the increased concentration of ether and acetal oxygens. Ternary blends with polymer components of different polarities have been discussed as a means for improving ion transport in a recent theoretical paper using a coarse-grained bead-spring model.¹⁶⁸

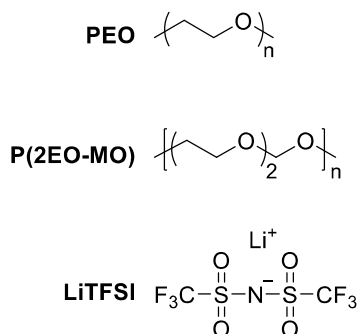


Figure 6.1. Chemical structure of poly(ethylene oxide) (PEO), poly(1,3,6-trioxocane) (P(2EO-MO)), and lithium bis(trifluoromethanesulfonyl)imide (LiTFSI).

In this work, we demonstrate that PEO is miscible with P(2EO-MO) in the neat, salt-free, state. We have also identified a range of salt concentrations over which PEO/P(2EO-MO)/LiTFSI blends remain miscible. We use the term conventional polymer electrolytes to refer to binary mixtures of a polymer and a salt such as PEO/LiTFSI or P(2EO-MO)/LiTFSI. We use the term polymer blend electrolyte to refer to ternary mixtures of two distinct polymers and a salt. The thermodynamic properties of PEO/P(2EO-MO)/LiTFSI were determined by small angle neutron scattering (SANS) experiments. The SANS results are consistent with phase behavior inferences based on differential scanning calorimetry (DSC) experiments. Ion transport in the polymer blend electrolytes is compared with that obtained from conventional polymer electrolytes (PEO/LiTFSI and P(2EO-MO)/LiTFSI) using both blocking and non-blocking electrodes.

6.2 Experimental Methods

6.2.1 Synthesis of 1,3,6-trioxocane, (2EO-MO)

Diethylene glycol (100 g, 0.942 mol), paraformaldehyde (37 g, 1.3 equiv), polyphosphoric acid (4.0 g, 0.03 equiv), and heptane (160 mL) were combined in a 250 mL flask fitted with a Dean-Stark adapter and condenser. The reaction was stirred at 115 °C for 12 h and water (~15 mL) was collected as the bottom layer in the trap. After cooling the reaction mixture to room temperature, heptane was removed *via* rotary evaporation to give a cloudy, viscous solution. This oligomerized product was distilled at 150–180 °C under high vacuum into a receiving flask cooled in a dry ice/acetone bath. The crude mixture of diethylene glycol and 1,3,6-trioxocane was then fractionally distilled under high vacuum at 80 °C to give clear, colorless, 1,3,6-trioxocane in 70% yield. The monomer was dried over CaH₂ for 3 days, distilled, and degassed *via* three freeze-pump-thaw cycles. Spectral data matched that previously reported in ref ⁹⁴. **¹H NMR** (500 MHz, CDCl₃) δ 4.57 (s, 2H), 3.50 (s, 8H) ppm. **¹³C NMR** (125 MHz, CDCl₃) δ 97.91, 72.58, 70.61 ppm. **HRMS** (DART-MS): *m/z* calculated for C₅H₁₀O₃ [H]⁺ 119.0703, found 119.0703.

6.2.2 Synthesis of Poly(1,3,6-trioxocane), P(2EO-MO)

In a glovebox under N₂ atmosphere, 1,3,6-trioxocane (6.0 g, 51 mmol) and CH₂Cl₂ (25.4 mL) were combined in a 100 mL flask equipped with a stir bar. Then, BF₃·OEt₂ (0.130 mL, 0.02 equiv) was added instantaneously and the flask was sealed with a rubber septum. The reaction gelled after 30 minutes such that stirring ceased, and the solution gradually turned pink. After 1 h, the reaction was removed from the glove box and quenched with a 1:1 mixture of acetonitrile:water (40 mL) to give a clear, colorless solution. The crude mixture was extracted with CH₂Cl₂ (30 mL × 3), dried with Na₂SO₄, filtered, and rotovapped until reaching a total volume of ~30 mL. The polymer was then precipitated into hexanes (400 mL), redissolved in CH₂Cl₂ (30 mL), and precipitated again into cold isopropanol (400 mL) to give a white solid. The polymer was dried under high vacuum overnight. Typical yields ranged from 50–60% and ¹H and ¹³C NMR analyses suggest that the polymerization proceeds with excellent regioregularity. Notably, polymerization is initiated by adventitious water in the reaction mixture. Furthermore, monomer conversion is highly dependent on monomer concentration and reaction temperature. Therefore, molar mass is difficult to control in this system, and variance was expected across multiple batches. **Sample 1:** *M_n* = 26.1, *Đ* = 1.83. **Sample 2:** *M_n* = 16.1, *Đ* = 1.76. **Sample 3:** *M_n* = 26.7, *Đ* = 1.66. **Sample 4:** *M_n* = 55.2, *Đ* = 1.97. *T_g* = -66 °C, *T_m* = 39 °C. Spectral data matched that previously reported in ref ⁹⁴. **¹H NMR** (500 MHz, CDCl₃) δ 4.74 (s, 2H), 3.69 (m, 8H) ppm. **¹³C NMR** (125 MHz, CDCl₃) δ 95.73, 70.60, 67.02 ppm.

6.2.3 Polymer Blend Electrolyte Preparation and Composition

The molar masses, *M_n*, and dispersities, *Đ*, of PEO (Polymer Source), deuterated PEO (dPEO) (Polymer Source), and P(2EO-MO) (synthesized as described above) used in this study are summarized in Table 1.

Table 6.1. Molar masses and dispersities of PEO and P(2EO-MO) homopolymers used.

polymer	M_n (kg·mol ⁻¹)	\mathcal{D}
PEO	35.0	1.08
dPEO	35.0	1.09
P(2EO-MO) Sample 1	26.1	1.83
P(2EO-MO) Sample 2	26.7	1.66
P(2EO-MO) Sample 3	16.0	1.76
P(2EO-MO) Sample 4	55.2	1.97

Electrolytes used for SANS experiments were made up of blends of dPEO, P(2EO-MO) ($M_n = 26.7$ kg·mol⁻¹ or 16.0 kg·mol⁻¹), and LiTFSI, while electrolytes for DSC and electrochemical experiments were made up of blends of PEO, P(2EO-MO) ($M_n = 26.1$ kg·mol⁻¹), and LiTFSI (see Table 6.2). Electrochemical measurements were also performed on conventional polymer electrolytes of P(2EO-MO) ($M_n = 55.2$ kg·mol⁻¹) with LiTFSI. All polymers were dried in a glovebox antechamber under vacuum at 90 °C for at least 24 h prior to use. LiTFSI was dried under vacuum at 120 °C for at least 72 h.

Table 6.2. Polymer components of blends used in each experiment.

experiment	polymer component 1	polymer component 2
DSC and electrochemical measurements	PEO	P(2EO-MO) Sample 1
SANS	dPEO	P(2EO-MO) Sample 2
SANS	dPEO	P(2EO-MO) Sample 3

The polymer composition of the blends was 50/50 by weight. We denote component 1 as PEO and component 2 as P(2EO-MO). The volume fraction of each component, on a salt-free basis, is given by:

$$\phi_1 = \frac{\frac{w_1}{\rho_1}}{\frac{w_1}{\rho_1} + \frac{w_2}{\rho_2}} \quad (6.1)$$

and

$$\phi_2 = 1 - \phi_1 \quad (6.2)$$

where w_i and ρ_i are the mass and density, respectively, of component i in the blend. The volume fractions are approximately equal (see Table 6.3). The volume fraction occupied by the polymer components in the blends containing LiTFSI is given by:

$$\phi_{\text{polymer}} = \frac{\frac{w_1}{\rho_1} + \frac{w_2}{\rho_2}}{\frac{w_1}{\rho_1} + \frac{w_2}{\rho_2} + \frac{w_{\text{salt}}}{\rho_{\text{salt}}}} \quad (6.3)$$

where w_{salt} is the mass of LiTFSI in the blend, and $\rho_{\text{salt}} = 2.023 \text{ g}\cdot\text{cm}^{-3}$.⁶³ Volume changes of mixing are ignored in our analysis.

We assume that the salt is uniformly distributed in the blend. The salt concentration of the blends was quantified by the molar ratio of Li atoms in the salt to O atoms in the polymers ($r = [\text{Li}]/[\text{O}]$), calculated as follows:

$$r = \frac{\frac{w_{\text{salt}}}{M_{\text{salt}}}}{\frac{w_1}{M_{\text{EO}}} + \frac{3w_2}{M_{2(\text{EO-MO})}}} \quad (6.4)$$

where M_{EO} is the monomer molar mass of PEO ($M_{\text{EO}} = 44.05 \text{ g}\cdot\text{mol}^{-1}$), $M_{2(\text{EO-MO})}$ is the monomer molar mass of P(2EO-MO) ($M_{2(\text{EO-MO})} = 118.1 \text{ g}\cdot\text{mol}^{-1}$), and M_{salt} is the molar mass of LiTFSI ($M_{\text{salt}} = 287.1 \text{ g}\cdot\text{mol}^{-1}$). A factor of three was included as 2EO-MO contains three oxygen atoms, while EO contains one oxygen atom per monomer, as shown in Figure 6.1.

The volume fraction of PEO and the LiTFSI associated with PEO in the polymer blend electrolytes, f , is estimated using the following equation:

$$f = \frac{\frac{w_1 + \frac{rw_1M_{\text{salt}}}{M_1}}{\rho_1}}{\frac{w_1 + \frac{rw_1M_{\text{salt}}}{M_1}}{\rho_1} + \frac{w_2 + \frac{3rw_2M_{\text{salt}}}{M_2}}{\rho_2}} \quad (6.5)$$

Equation 6.5 is based on the assumption that the value of r in the PEO-rich fluctuations is the same as that in the P(2EO-MO)-rich fluctuations.

Electrolyte r values ranged from 0 to 0.14. All electrolyte solutions in acetonitrile were transparent, indicating complete dispersion of all mixture components. The electrolytes were stirred on a hot plate at 80 °C until all of the acetonitrile had evaporated, and then further dried in a glovebox antechamber under vacuum at 90 °C for 24 h to remove any residual solvent.

Density measurements for neat P(2EO-MO) at 90 °C were taken by measuring the mass of electrolyte within a known volume, following procedures described previously.⁶³ The average of three density measurements ($\rho_2 = 1.32 \pm 0.04 \text{ g}\cdot\text{cm}^{-3}$) was used for subsequent calculations.

6.2.4 DSC Sample Preparation and Experiments

Samples (~10 mg) were hermetically sealed in aluminum pans in an argon glovebox. DSC experiments were run with two heating and cooling cycles a heating rate of 20 °C·min⁻¹ and cooling rate of 5 °C·min⁻¹ using a Thermal Advantage Q200 calorimeter at the Molecular Foundry, Lawrence Berkeley National Lab. The temperature ranged from -80 to 120 °C. The glass transition temperature (T_g) values are obtained from analysis of the second heating run.

6.2.5 Small Angle Neutron Scattering (SANS) Sample Preparation and Experiments

Sample preparation for SANS experiments was conducted following procedures outlined previously.¹⁶⁹ The blends were made such that the volume fractions of each component were approximately 0.5 (see Table 6.3).

SANS experiments were conducted on the NG7SANS beamline at the National Institute of Standards and Technology Center for Neutron Research.¹⁷⁰ Measurements were performed with a neutron wavelength of 6 Å, and up to three sample-to-detector distances (SDDs) of 13 m, 4 m, and 1 m. The shortest, 1 m distance, was used with a detector offset of 25 cm to extend the scattering angle (2θ) attainable. Overall, the three configurations allowed for access to a scattering wave-vector magnitude, $q = \frac{4\pi}{\lambda} \sin(\theta)$, ranging from 0.03 nm⁻¹ to 5.5 nm⁻¹. The neutron beam size was defined by a 9.5×10^{-3} m aperture. Data were collected at 10 °C increments between 60 °C and 110 °C. All measurements were reversible and repeatable upon either heating or cooling. Samples were equilibrated for at least 30 minutes at each temperature. A 9-position Peltier cooling/heating sample changer block was used to drive and maintain constant sample temperature. Samples of thickness of 1 mm were used. Data were reduced using the software package for IGOR provided by the NIST Center for Neutron Research.¹⁷¹ The total scattering intensity was corrected for detector sensitivity, background, and empty cell contributions as well as sample transmission and thickness.^{171,172}

6.2.6 Electrochemical Sample Preparation and Experiments

Electrochemical sample preparation and experiments were conducted following the procedures previously described,¹⁰³ using 508 μm thick silicone spacers and conducting the measurements at 90 °C.

6.3 Results and Discussion

A commonly used method to determine polymer miscibility is the measurement of the glass transition temperature, T_g , via DSC. The existence of a single T_g is indicative of a miscible blend.¹⁷³ Figure 6.2a shows DSC curves for PEO/P(2EO-MO)/LiTFSI blends at $r = 0.04$ and 0.10. The $r = 0.04$ blend exhibits two glass transitions ($T_{g1} = -46$ °C, $T_{g2} = -38$ °C) which indicates the blend is phase separated. In contrast, the $r = 0.10$ blend exhibits a single glass transition ($T_g = -24$ °C), which indicates that the blend is comprised of a single phase. The absence of a melting transition

in the DSC data from the higher salt blend is consistent with numerous reports in the literature indicating that the addition of salt suppresses crystallization of PEO.^{66,94,103,174} All of the thermodynamic and electrochemical data presented in this paper were obtained above the melting temperatures of the blends.

Figure 6.2b shows the complete set of glass transition temperatures for each polymer blend electrolyte and the corresponding conventional polymer electrolyte taken from ref⁹⁴. In the neat blend, the T_g values of PEO and P(2EO-MO) are too close to be distinguished by DSC. For r values between 0.02 and 0.06, the polymer blend electrolytes exhibit two T_g values, denoted by open squares, indicating immiscibility. However, from $r = 0.08$ to 0.14, the blend has a single T_g , indicating miscibility at these higher salt concentrations. The T_g for all systems generally increases with increasing salt concentration. The correlation between T_g and salt loading is attributed to the solvated ions inducing physical cross-linking of the polymer chains.¹⁷⁵

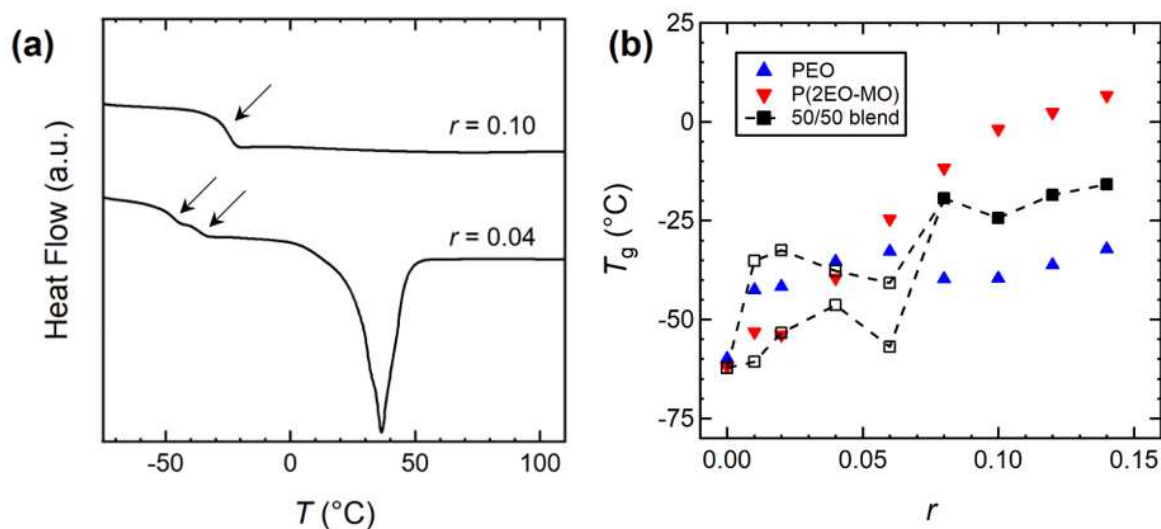


Figure 6.2. Sample DSC data and glass transition data for blends. (a) Representative DSC curves showing one T_g for a 50/50 blend of PEO ($M_n = 35.0 \text{ kg}\cdot\text{mol}^{-1}$) and P(2EO-MO) ($M_n = 26.1 \text{ kg}\cdot\text{mol}^{-1}$) at $r = 0.10$ and two T_g values at $r = 0.04$. Arrows denote regions associated with the glass transition. (b) T_g as a function of salt concentration, r , for each conventional polymer electrolyte system (solid blue triangles for PEO ($M_n = 100 \text{ kg}\cdot\text{mol}^{-1}$) and solid red triangles for P(2EO-MO) ($M_n = 55.2 \text{ kg}\cdot\text{mol}^{-1}$)) and the polymer blend electrolytes. Polymer blends possessing a single T_g at high r values ($0.08 \leq r \leq 0.14$) and blends exhibiting two T_g values at low r values ($0.02 \leq r \leq 0.06$) are denoted by closed black squares and open black squares, respectively. The uncertainty of the T_g measurements is assumed to be that of the instrument's given calorimetric reproducibility and precision ($\pm 0.05\%$). Data for PEO and P(2EO-MO) were taken from ref⁹⁴.

The measured absolute SANS intensity, $I(q)$, as a function of the magnitude of the scattering vector, q , for the dPEO/P(2EO-MO)/LiTFSI blends at 90 °C is shown in Figure 6.3. Also shown as a reference is a dPEO/PEO/LiTFSI blend with $r = 0.10$ at 90 °C. Distinct differences are apparent between the scattering profiles of dPEO/P(2EO-MO)/LiTFSI blends with low salt concentrations ($0.02 \leq r \leq 0.06$) and that of the neat blend ($r = 0$) and blends with high salt concentrations ($r \geq$

0.08). The blends with low salt concentration show a rapid rise in $I(q)$ at low q ($q < 0.1 \text{ nm}^{-1}$), indicative of phase separation. The neat blend and high r blends have similar scattering profiles as that of the dPEO/PEO/LiTFSI sample. In the range $0.4 < q \text{ (nm}^{-1}\text{)} < 2$, $I(q)$ from these blends is approximately proportional to q^{-2} while $I(q)$ is a much weaker function of q for $q < 0.4 \text{ nm}^{-1}$. These features are characteristic of scattering from a homogeneous binary polymer blend wherein the polymer chains obey random walk statistics.⁸⁵ The SANS results regarding polymer blend miscibility are consistent with the results obtained from DSC.

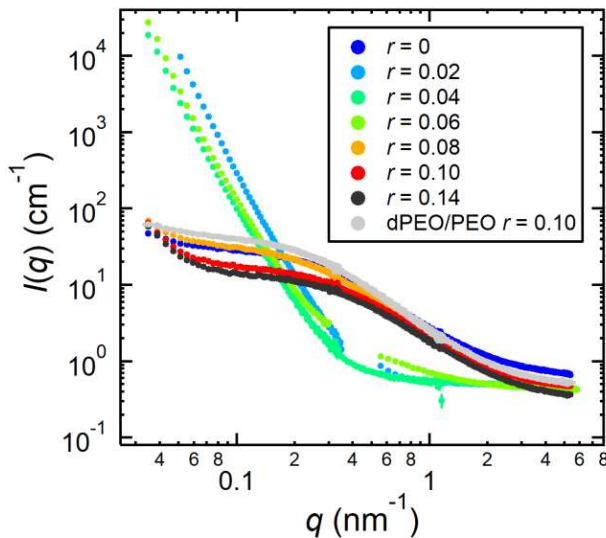


Figure 6.3. Measured absolute SANS intensity, $I(q)$, vs scattering vector, q , at $90 \text{ }^\circ\text{C}$ for blends. Shown are dPEO ($M_n = 35.0 \text{ kg}\cdot\text{mol}^{-1}$) and P(2EO-MO) ($M_n = 26.7 \text{ kg}\cdot\text{mol}^{-1}$) at varying LiTFSI salt concentrations, r , and a dPEO/PEO sample with $r = 0.10$. Note that for $r = 0.02$ and $r = 0.06$ there is an intermediate range of q (corresponding to an SDD of 4 m) that was not recorded due to insufficient beamtime. Error bars represent one standard deviation of the scattering data, and in most cases are smaller than the data points.

Analysis of SANS data begins with a thermodynamic model for the polymer blend electrolytes. We start with the thermodynamics of mixing in a two component polymer blend in the absence of salt. The Gibbs free energy of mixing of a homogeneous mixture of two polymers can be described by the

$$\text{the Flory-Huggins theory:} \quad v \frac{\Delta G_m}{k_B T} = \frac{\phi_1 \ln \phi_1}{N_1} + \frac{\phi_2 \ln \phi_2}{N_2} + \chi \phi_1 \phi_2 \quad (6.6)$$

where ΔG_m is the free energy of mixing per unit volume, k_B is the Boltzmann constant, T is the absolute temperature, ϕ_i is the volume fraction of component i , N_i is the number of repeat units in chain i , and χ is the Flory-Huggins interaction parameter which describes the thermodynamic incompatibility between component 1 and 2.^{176,177} N_1 , N_2 , and χ are based on a reference volume, $v = 0.1 \text{ nm}^3$. A miscible blend, one that is homogeneous down to the molecular level, requires both

a negative Gibbs free energy of mixing ($\Delta G_m < 0$) and a positive second derivative ($\frac{\partial^2 \Delta G_m}{\partial \phi_1^2} > 0$).¹⁷³ The critical Flory-Huggins interaction parameter value, χ_{crit} , is given by the following:

$$\chi_{\text{crit}} = \frac{1}{2} \left(\frac{1}{\sqrt{N_1}} + \frac{1}{\sqrt{N_2}} \right)^2. \quad (6.7)$$

Blends with $\chi < \chi_{\text{crit}}$ are predicted to be miscible, regardless of composition.

For salt-containing mixtures, we use a simple extension of Equation 6.6:

$$v \frac{\Delta G_m}{k_B T} = \phi_{\text{polymer}} \left(\frac{\phi_1 \ln \phi_1}{N_1} + \frac{\phi_2 \ln \phi_2}{N_2} + \chi_{\text{eff}} \phi_1 \phi_2 \right) \quad (6.8)$$

where ϕ_{polymer} is the total polymer volume fraction and ϕ_i ($i = 1$ or 2) are the salt-free polymer volume fractions. The effect of added salt is captured mainly by an effective Flory-Huggins parameter, χ_{eff} , which depends on salt concentration. In the limit of $r \rightarrow 0$, $\phi_{\text{polymer}} \rightarrow 1$, Equation 6.8 reduces to Equation 6.6, and χ_{eff} reduces to the conventional χ parameter for polymer blends.

Following the analysis in ref¹⁷⁸, the absolute SANS intensity was corrected for the contributions from scattering of the deuterated chains as well as the contributions from the incoherent scattering to obtain the absolute coherent SANS intensity:

$$I_{\text{coh}}(q) = I(q) - f I_{\text{dPEO/LiTFSI}}(q) - I_{\text{inc}}(q) \quad (6.9)$$

where f is the estimated volume fraction of dPEO and LiTFSI in our polymer blend electrolytes ($f \approx 0.5$) and $I_{\text{dPEO/LiTFSI}}(q)$ is the scattering from dPEO/LiTFSI mixtures taken from ref¹⁶⁹. $I_{\text{inc}}(q)$ is the incoherent scattering background contribution to the intensities, determined by fitting $I(q)$ to the following expression:

$$I(q) = aP(q) + b \quad (6.10)$$

where $P(q)$ is a form factor given by the Debye function (see Equation 6.14), a is a constant scaling factor, and b is a constant assumed to be equal to $I_{\text{inc}}(q)$.^{171,172,179} Figure 6.4 shows the coherent SANS profiles, $I_{\text{coh}}(q)$, of the miscible blends at 90 °C.

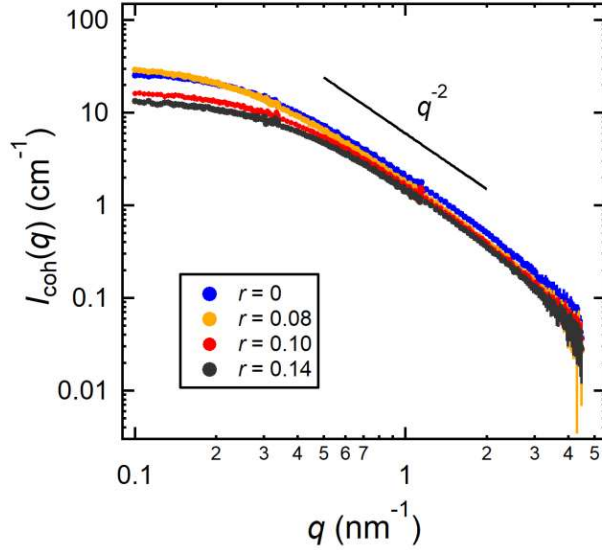


Figure 6.4. SANS intensities, $I_{\text{coh}}(q)$, plotted as a function of the magnitude of the scattering vector, q , at 90 °C for the dPEO/P(2EO-MO)/LiTFSI (P(2EO-MO) $M_n = 26.7 \text{ kg}\cdot\text{mol}^{-1}$) blends at the miscible salt concentrations. Error bars represent one standard deviation of the scattering data and in most cases are smaller than the data points.

The coherent scattering intensity for homogeneous PEO/P(2EO-MO)/LiTFSI blends is calculated using the Random Phase Approximation (RPA):

$$I_{\text{coh}}(q) = \phi_{\text{polymer}}(B_1 - B_2)^2 v \left(\frac{1}{S_{11}} + \frac{1}{S_{22}} - 2\chi_{\text{eff}} \right)^{-1}. \quad (6.11)$$

In our analysis, component 1 is dPEO, component 2 is P(2EO-MO), ϕ_{polymer} is the volume fraction of both polymer components, dPEO and P(2EO-MO), B_i is the coherent neutron scattering length density of component i given by $B_i = \frac{b_i}{v_i}$, v_i and b_i are the molar monomer volumes and neutron scattering lengths of component i , respectively, and χ_{eff} is the effective Flory-Huggins interaction parameter between dPEO and P(2EO-MO) both with and without salt.^{85,178,180–182} In the limit $q \rightarrow 0$, Equation 6.11 is consistent with Equation 6.8. The neutron scattering lengths of dPEO and P(2EO-MO) are $4.58 \times 10^{-12} \text{ cm}$ and $1.32 \times 10^{-12} \text{ cm}$, respectively. The molar monomer volumes of dPEO and P(2EO-MO) were calculated in the absence of salt ($v_1 = 38.98 \text{ cm}^3\cdot\text{mol}^{-1}$ and $v_2 = 89.47 \text{ cm}^3\cdot\text{mol}^{-1}$ at 90 °C). We assume dPEO occupies the same molar volume as hydrogenous PEO. We thus obtain $\rho_1 = 1.23 \text{ g}\cdot\text{cm}^{-3}$ and $\rho_2 = 1.32 \text{ g}\cdot\text{cm}^{-3}$ at 90 °C. The temperature dependence of monomer volumes was applied to the contrast terms, and was determined using the following equations: $\rho_1 = 1.23 - 7.31 \cdot 10^{-4} \cdot (T - 363) \text{ g}\cdot\text{cm}^{-3}$ and $\rho_2 = 1.32 - 7.31 \cdot 10^{-4} \cdot (T - 363) \text{ g}\cdot\text{cm}^{-3}$ where T is the temperature in K.¹⁸³ The thermal expansion coefficient of P(2EO-MO) has not been measured; it was assumed to be the same as that of PEO.

The structure factor, S_{ii} , is given by

$$S_{ii} = \phi_i N_i P_i(q) \quad (6.12)$$

where ϕ_i is the volume fraction of polymer i on a salt-free basis.

$I_{\text{coh}}(q)$ depends on three volume fractions: ϕ_1 , ϕ_2 , and ϕ_{polymer} (see Equations 6.11 and 6.12). For the blends covered in this study, these volume fractions are listed in Table 6.3.

N_i is the number of repeat units in each polymer calculated by

$$N_i = \frac{M_i}{\rho_i N_{\text{av}} \nu} \quad (6.13)$$

where N_{av} is Avogadro's number and M_i and ρ_i are the molar masses (g mol^{-1}) and densities (g cm^{-3}) of component i , and

$$P_i(q) = 2 \left[\frac{\exp(-x_i) - 1 + x_i}{x_i^2} \right] \quad (6.14)$$

with $x_i = q^2 R_{\text{g},i}^2$. Both components are modeled as flexible Gaussian chains according to

$$R_{\text{g},i}^2 = \frac{N_i l_i^2}{6} \quad (6.15)$$

where l_i is the statistical segment length of each component. The statistical segment length of PEO is $l_1 = 0.58 \text{ nm}$ (based on a 0.1 nm^3 reference volume).¹⁶⁹ The statistical segment length of P(2EO-MO) has not been measured. In our calculations, we assume $l_1 = l_2 = l = 0.58\alpha \text{ nm}$ where α is a fitting parameter that accounts for differences in the statistical segment length of PEO and P(2EO-MO) and distortions of chains (e.g. chain stretching) in the blends.

Table 6.3. Volume fractions, ϕ_i and α values used in RPA fits of dPEO/P(2EO-MO)/LiTFSI blends. The errors shown correspond to one standard deviation from the temperature averaging.

	dPEO/P(2EO-MO)/LiTFSI (dPEO $M_n = 35.0 \text{ kg}\cdot\text{mol}^{-1}$; P(2EO-MO) $M_n = 26.7 \text{ kg}\cdot\text{mol}^{-1}$)				dPEO/P(2EO-MO)/LiTFSI (dPEO $M_n = 35.0 \text{ kg}\cdot\text{mol}^{-1}$; P(2EO-MO) $M_n = 16.0 \text{ kg}\cdot\text{mol}^{-1}$)			
	ϕ_1	ϕ_2	ϕ_{polymer}	α	ϕ_1	ϕ_2	ϕ_{polymer}	α
$r = 0$	0.516	0.484	1	1.274 ± 0.007	0.517	0.483	1	1.331 ± 0.044
$r = 0.08$	0.517	0.483	0.742	1.205 ± 0.014				
$r = 0.10$	0.518	0.482	0.696	1.173 ± 0.001	0.517	0.483	0.705	1.212 ± 0.011
$r = 0.14$	0.515	0.485	0.621	1.122 ± 0.002				

$I_{\text{coh}}(q)$ for the miscible blends were first fit to Equation 6.11 with two adjustable parameters: α and χ_{eff} . For each blend, α was found to be essentially invariant with temperature so α was averaged across all temperatures and fixed. The parameter α is greater than 1 for all blends, likely due to the increased stiffness of P(2EO-MO) chains relative to that of the PEO chains. These values are given in Table 6.3. $I_{\text{coh}}(q)$ was then fit to Equation 6.11 with only χ_{eff} as a fitting parameter.

Representative RPA fits of $I_{\text{coh}}(q)$ for a dPEO/P(2EO-MO) blend with $r = 0.08$ are shown in Figure 6.5. χ_{eff} values of -4.67×10^{-3} and 7.64×10^{-4} are obtained from the profiles at 70 and 90 °C, respectively. At 110 °C, the blend is phase separated and cannot be analyzed by RPA. Note that χ_{eff} increases with increasing temperature.

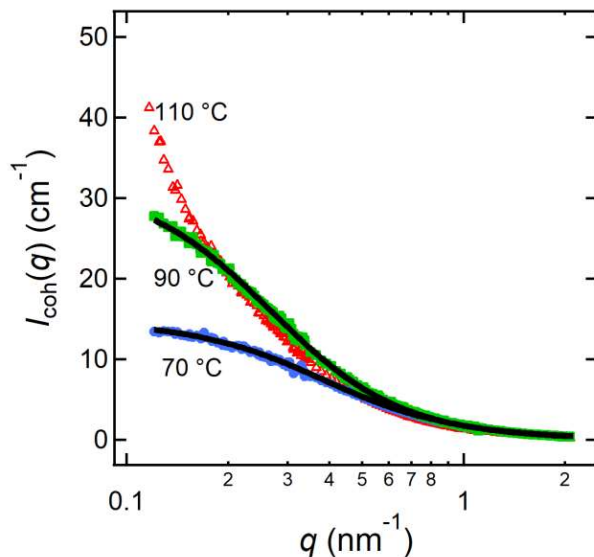


Figure 6.5. RPA fits (solid black lines) for a dPEO/P(2EO-MO)/LiTFSI (P(2EO-MO) $M_n = 26.7 \text{ kg}\cdot\text{mol}^{-1}$) blend with $r = 0.08$ at different temperatures. The 70 °C (filled blue circles) and 90 °C (filled green squares) data can be fit to RPA. The 110 °C measurements (open red triangles) indicate phase separation. Error bars represent one standard deviation of the scattering data and in most cases are smaller than the data points.

Effective Flory-Huggins interaction parameters were extracted by fitting $I_{\text{coh}}(q)$ to RPA for all miscible blends across a range of temperatures ($60 \leq T \text{ (}^\circ\text{C)} \leq 110$) for the high molar mass P(2EO-MO)-containing ($M_n = 26.7 \text{ kg}\cdot\text{mol}^{-1}$) blends at $r = 0, 0.08, 0.10, 0.14$ and the low molar mass P(2EO-MO)-containing ($M_n = 16.0 \text{ kg}\cdot\text{mol}^{-1}$) blends at $r = 0$ and 0.10. The temperature dependence of χ_{eff} is given by:

$$\chi_{\text{eff}} = \frac{A}{T} + B \quad (6.16)$$

where A and B are empirically determined constants.^{165,184} For each blend sample, χ_{eff} was linearly fit to inverse temperature using Equation 6.16 to extract values for A and B . These values are summarized in Table 6.4.

Table 6.4. A and B constants for dPEO/P(2EO-MO)/LiTFSI blends at various salt concentrations, r , and their linear fit R^2 values. The errors shown represent one standard deviation of uncertainty for the fit for A and B according to Equation 6.16.

	dPEO/P(2EO-MO)/LiTFSI (P(2EO-MO) $M_n = 26.7 \text{ kg}\cdot\text{mol}^{-1}$)			dPEO/P(2EO-MO)/LiTFSI (P(2EO-M) $M_n = 16.0 \text{ kg}\cdot\text{mol}^{-1}$)		
	A	B	R^2	A	B	R^2
$r = 0$	-5.401 ± 0.241	0.0133 ± 0.0007	0.986	-5.773 ± 0.172	0.0149 ± 0.0005	0.994
$r = 0.08$	-32.127 ± 1.146	0.0891 ± 0.0032	0.997			
$r = 0.10$	-17.682 ± 0.305	0.0460 ± 0.0008	0.998	-21.537 ± 0.480	0.0576 ± 0.0013	0.997
$r = 0.14$	1.383 ± 1.350	-0.0072 ± 0.0037	0.344			

All χ_{eff} parameters calculated in this study and their temperature and molar mass dependence are shown in Figure 6.6. Solid markers represent experimental measurements, and the solid lines are a fit to the data according to Equation 6.16. The dashed line denotes χ_{crit} , which was calculated from Equations 6.7 and 6.13 for blends comprising P(2EO-MO) of lower ($16.0 \text{ kg}\cdot\text{mol}^{-1}$) and higher ($26.7 \text{ kg}\cdot\text{mol}^{-1}$) molar masses. Figure 6.6a shows the temperature dependence of χ_{eff} in the higher molar mass P(2EO-MO)-containing blends. In the neat state, χ_{eff} is negative with a value of -3.07×10^{-3} at $60 \text{ }^\circ\text{C}$ and increases with increasing temperature ($A = -5.401$), increasing to a value of -9.67×10^{-4} at $110 \text{ }^\circ\text{C}$. χ_{eff} is a more sensitive function of temperature in the salt-containing blends where $0.08 \leq r \leq 0.10$. For the $r = 0.08$ blend, χ_{eff} increases from -4.67×10^{-3} at $70 \text{ }^\circ\text{C}$ to 2.77×10^{-3} at $100 \text{ }^\circ\text{C}$, and phase separation is observed experimentally at $110 \text{ }^\circ\text{C}$ (see Figure 6.5). At $110 \text{ }^\circ\text{C}$, χ_{eff} predicted by extrapolating the data below $100 \text{ }^\circ\text{C}$ is larger than $\chi_{\text{crit}} = 5.06 \times 10^{-3}$, as expected. For $r = 0.10$, we see a similarly strong dependence with temperature and χ_{eff} varies from -7.29×10^{-3} at $60 \text{ }^\circ\text{C}$ to -3.41×10^{-4} at $110 \text{ }^\circ\text{C}$. The value of A is negative and B is positive for all miscible blends except at $r = 0.14$. At this concentration, A is positive and B is negative, and there is a very weak dependence on temperature.

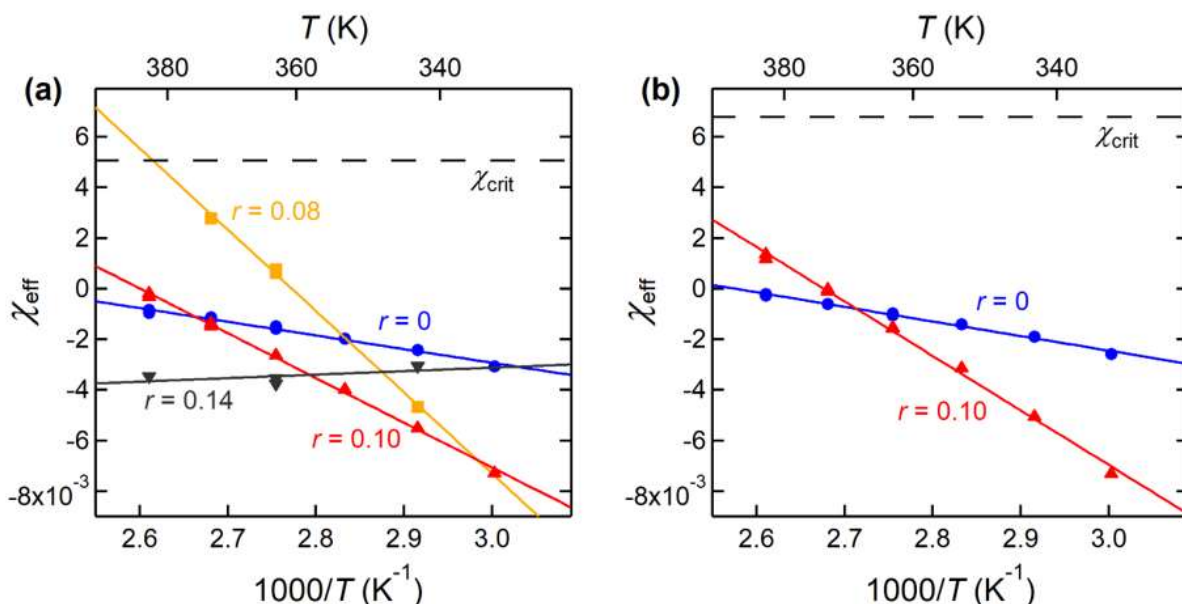


Figure 6.6. Effective Flory-Huggins interaction parameter, χ_{eff} , as a function of inverse temperature, $1/T$, for the dPEO/P(2EO-MO)/LiTFSI blends. (a) With higher P(2EO-MO) molar mass ($M_n = 26.7 \text{ kg}\cdot\text{mol}^{-1}$) and (b) with lower P(2EO-MO) molar mass ($M_n = 16.0 \text{ kg}\cdot\text{mol}^{-1}$). The solid lines are linear fits to the data according to Equation 6.16; values for A and B are reported in Table 6.4. Error bars represent one standard deviation of the χ_{eff} fits and are smaller than the symbols. Typical error bars on χ range between 5 and 20%, as previously shown in ref¹⁷⁸.

Similarly, Figure 6.6b shows the temperature dependence of χ_{eff} in the lower molar mass P(2EO-MO)-containing blends. At the same salt concentration, the temperature dependence of χ_{eff} obtained from lower and higher molar mass P(2EO-MO) blends are similar. At $r = 0$, the difference in A and B values is less than 10%, while at $r = 0.10$, A is within 10% while the value of B differs by about 20% (see Table 6.4). The absolute value of χ_{eff} is greater in the lower molar mass P(2EO-MO)-containing blends than in the higher molar mass blends. χ_{eff} is always below $\chi_{\text{crit}} = 6.78 \times 10^{-3}$ for these lower molar mass blends.

In all cases where χ_{eff} is a sensitive function of temperature, R^2 values for the linear fits are greater than 0.98 (see Table 6.4). The R^2 value for the $r = 0.14$ blend is 0.344 which is expected as χ_{eff} is insensitive to temperature in this case.

Salt concentration is known to affect χ_{eff} in multicomponent polymer systems.^{185,186} This effect has primarily been studied in phase-separated or microphase-separated systems, e.g. polystyrene and PEO.^{27,28,30,139,140,187–191} In the dPEO/P(2EO-MO) ($M_n = 26.7 \text{ kg}\cdot\text{mol}^{-1}$) blend, the addition of salt up to $r = 0.02$ induces phase separation, while sufficient salt concentrations ($r \geq 0.08$) render the mixture miscible again. The dependence of χ_{eff} on r is shown in Figure 6.7 for three temperatures (70, 90, and 110 °C). χ_{eff} is slightly negative in the neat blend, with similar values across the three temperatures. Addition of salt to $r = 0.02$ increases χ_{eff} above $\chi_{\text{crit}} = 5.06 \times 10^{-3}$. χ remains above this critical value at $r = 0.04$ and $r = 0.06$. Because the samples at $0.02 \leq r \leq 0.06$ were immiscible at all temperatures studied, no information on χ_{eff} is available besides a lower bound, as indicated in Figure 6.7. At 90 and 110 °C, χ_{eff} decreases with increasing r for $r \geq 0.08$. The data in Figure

6.7 suggests that χ_{eff} goes through a maximum at a value of r between 0.02 and 0.08 at 90 and 110 °C. At 70 °C, χ_{eff} is a non-monotonic function of r for $r \geq 0.08$. At this temperature, χ_{eff} exhibits both a maximum and a minimum with respect to r .

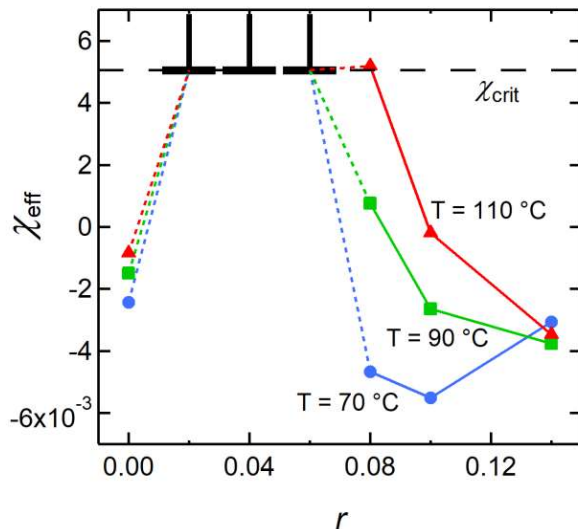


Figure 6.7. Effective Flory-Huggins interaction parameter, χ_{eff} , for the dPEO/P(2EO-MO)/LiTFSI (P(2EO-MO) $M_n = 26.7 \text{ kg}\cdot\text{mol}^{-1}$) blends as a function of salt concentration, r , at three different temperatures. 70 °C (blue circles), 90 °C (green squares), and 110 °C (red triangles). The lower limit of the error bars at $0.02 \leq r \leq 0.06$ is the critical value for the Flory-Huggins interaction parameter, χ_{crit} , at which this system phase separates. Error bars for the solid markers represent one standard deviation of the χ_{eff} fits and are smaller than the symbols.

We now discuss the ion transport properties of the higher molar mass polymer blend electrolytes. For reference, we also include ion transport properties of conventional PEO/LiTFSI ($M_n = 35.0 \text{ kg}\cdot\text{mol}^{-1}$) and P(2EO-MO)/LiTFSI ($M_n = 55.2 \text{ kg}\cdot\text{mol}^{-1}$) electrolytes.³⁵ The ionic conductivity of the PEO/P(2EO-MO)/LiTFSI blend as a function of r is shown in Figure 6.8a. The conductivity increases with increasing r due to the higher concentration of charge carrying species. To a good approximation, the conductivity of the blend matches that of PEO/LiTFSI at all values of r .

The salt diffusion coefficient, D , of the blend, shown in Figure 6.8b is similar to that of the conventional P(2EO-MO)/LiTFSI polymer electrolyte system for $r \leq 0.02$ but is nearly equal to that of PEO/LiTFSI for higher r . The dependence of the current fraction, ρ_+ , of the polymer blend on r , plotted in Figure 6.8c, matches that of PEO/LiTFSI at all salt concentrations.⁸²

One measure of the efficacy of an electrolyte is the product of the ionic conductivity and current fraction. This measure gives a metric for sustaining steady currents in battery applications at low current densities. The efficacies of all three electrolyte systems are similar, as shown in Figure 6.8d.

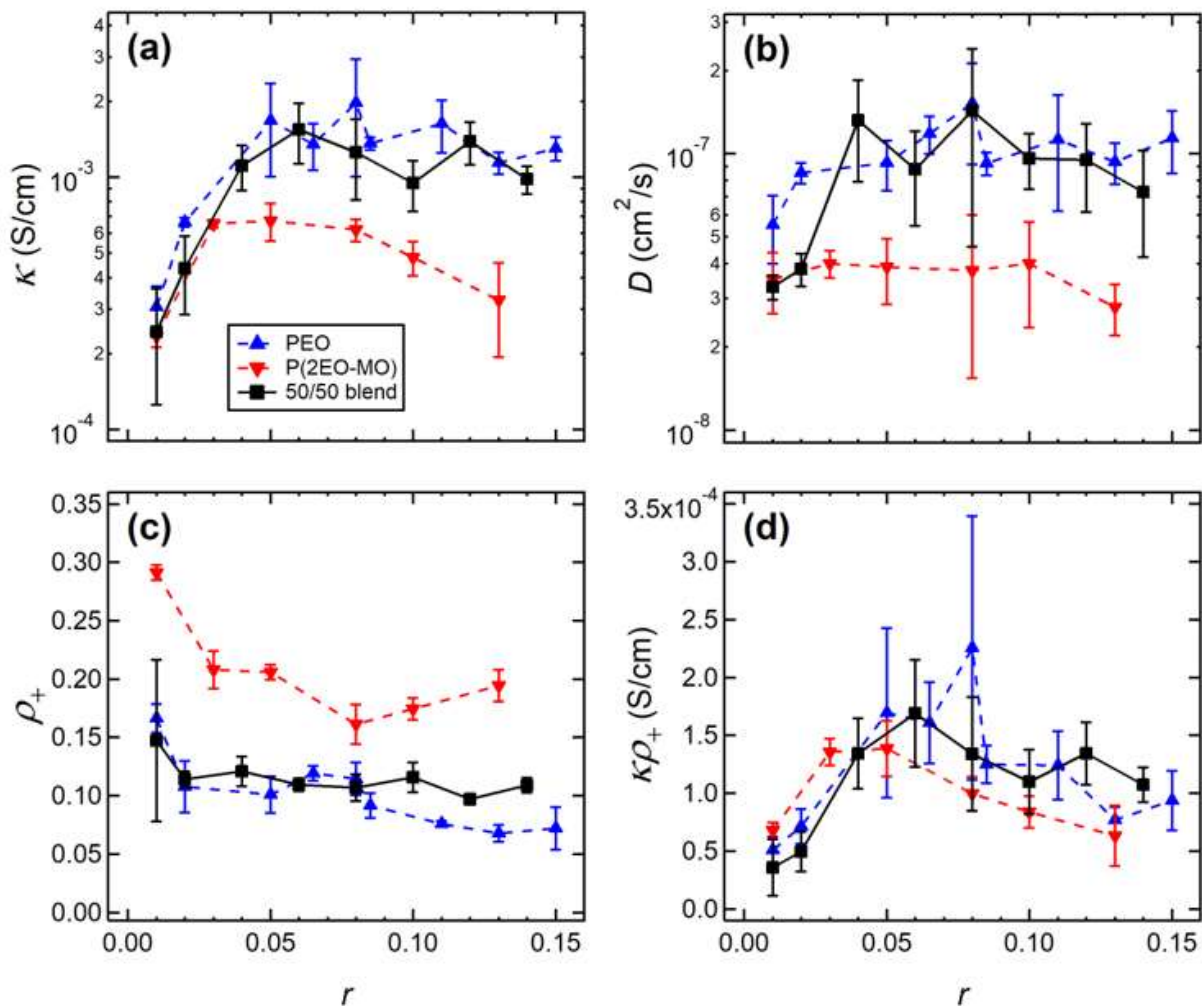


Figure 6.8. Electrochemical characterization of the PEO/P(2EO-MO)/LiTFSI blend as a function of salt concentration, r , compared with conventional PEO/LiTFSI ($M_n = 35.0 \text{ kg}\cdot\text{mol}^{-1}$) and P(2EO-MO)/LiTFSI ($M_n = 55.2 \text{ kg}\cdot\text{mol}^{-1}$) polymer electrolyte systems. (a) Ionic conductivity, κ , from ac impedance spectroscopy of symmetric cells with blocking electrodes. (b) Salt diffusion coefficient, D , from restricted diffusion measurements in a lithium symmetric cell. (c) Current fractions, ρ_+ , calculated from the Bruce-Vincent method using a lithium symmetric cell. (d) Efficacy, $\kappa\rho_+$. Data was taken at 90°C . PEO/LiTFSI data was taken from ref³⁵. Error bars represent the standard deviation of three measurements.

The immiscible blends obtained in the regime $0.01 \leq r \leq 0.06$ undoubtedly contain macroscopic PEO-rich and P(2EO-MO)-rich domains. However, we expect a considerable concentration of P(2EO-MO) in the PEO-rich domains and vice-versa. The fact that the ion transport data (see Figure 6.8) obtained from immiscible blends do not differ significantly from that of miscible blends may be attributed to this effect. A more thorough investigation into the impact of miscibility on ion transport is warranted, but beyond the scope of this study.

We were curious if ion transport behavior in miscible polymer blend electrolytes can be predicted based on the known properties of conventional polymer electrolytes. It is well established that

ionic conductivity in polymers depends on the relative segmental motion of the polymer backbone, which can be gauged by the T_g value.^{66,94,102,117} The T_g values of the miscible polymer blend electrolytes (PEO/P(2EO-MO)/LiTFSI) were consistently between the T_g values of the PEO/LiTFSI and P(2EO-MO)/LiTFSI electrolytes (see Figure 6.2b). However, conductivity measurements indicate that PEO, the component with the lower T_g , dominates conductivity. At most salt concentrations, this general behavior also applies to the measured current fractions and salt diffusion coefficients (see Figures 6.8b and 6.8c). These observations do not indicate that only PEO chains contribute to conductivity; if this were the case, then the conductivity of the 50/50 polymer blend electrolytes would be half that of PEO/LiTFSI. The data in Figures 6.2b, 6.8b, and 6.8c suggests that the P(2EO-MO) chains in the miscible polymer blend electrolytes behave as if they were PEO. It is evident that ion transport in miscible polymer blend electrolytes differs qualitatively from that in conventional polymer electrolytes.

We conclude this section by reviewing previous studies of ion transport in polymer blends. It is important to distinguish between oligomers and polymers: PEO analogues such as tetraethylene glycol dimethyl ether (tetraglyme), a short chain molecule comprising four ethylene oxide units, are commonly used as solvents for electrolytic applications.^{192–194} The ionic conductivity of PEO/LiTFSI mixtures is independent of chain length when the molar mass of the PEO chains exceeds $2 \text{ kg}\cdot\text{mol}^{-1}$.⁸⁸ The entanglement molar mass of PEO is also reported to be $2 \text{ kg}\cdot\text{mol}^{-1}$.¹⁹⁵ This value ($2 \text{ kg}\cdot\text{mol}^{-1}$) serves as an approximate marker to distinguish between oligomers and polymers in the context of electrolytes. There have been a few reports of mixtures of polymers, salts, and a third component.^{196–205} Tsuchida *et al.* studied mixtures of PEO, poly(methyl methacrylate) (PMMA) and lithium perchlorate (LiClO_4); however, the molar masses of examined PEO ranged from 0.7 to $2 \text{ kg}\cdot\text{mol}^{-1}$.¹⁹⁶ While in the absence of salt, the miscibility of PEO and PMMA is well-established,²⁰⁶ the effect of added salt on miscibility is not yet known. Abraham *et al.* blended PEO and poly[bis-(methoxyethoxyethoxide)phosphazene] (MEEP) with different lithium salts.¹⁹⁷ The molar mass of MEEP was not reported. Interestingly, the blends exhibited two exothermic melting transitions, one similar to that of pure PEO in the vicinity of $55 \text{ }^\circ\text{C}$, and an additional peak at $140 \text{ }^\circ\text{C}$, in spite of the fact that MEEP is amorphous. This suggests the presence of two phases in the PEO/MEEP electrolytes. Li *et al.* prepared blends of PEO, poly(2-vinylpyridine) (P2VP), and LiClO_4 . While PEO and P2VP are miscible in the absence of salt,²⁰⁷ the possibility of salt-induced phase separation was not addressed. Kim *et al.* report both conductivity and current fraction in mixtures of PEO, poly(oligo[oxyethylene]oxysebacoyl), and LiClO_4 .²⁰¹ This is one of the few studies on electrochemical properties in polymer blends that go beyond conductivity; however, miscibility of the polymers in the presence of salt was not established. Rocco *et al.* studied mixtures of PEO, poly(methyl vinyl ether-maleic acid), and LiClO_4 as well as PEO, poly(bisphenol A-*co*-epichlorohydrin), poly(vinyl ethyl ether), and LiClO_4 blends for use as electrolytes.^{203,204} Inferences regarding miscibility were mainly made on the basis of DSC. In contrast to all previous studies,^{196–205} this paper definitively demonstrates the miscibility of a polymer blend electrolyte system using a rigorous approach based on SANS, wherein concentration fluctuations on the nanometer length scale are quantified. Unlike previous studies,^{196–205} this work compares the characteristics of the PEO/P(2EO-MO)/LiTFSI polymer blend electrolyte system to that of its constituent polymer electrolytes (PEO/LiTFSI and P(2EO-MO)/LiTFSI).

6.4 Conclusions

This study demonstrates that it is possible to create homogeneous mixtures of chemically distinct polymers and a lithium salt for use in lithium batteries. This demonstration is non-trivial because polymers rarely mix with each other. Blending polymers for electrolytic applications is advantageous because of the ease of preparation and control of physical properties by simple changes in composition or chain lengths of the components. This initial study, based on PEO/P(2EO-MO)/LiTFSI, can serve as a template for future work aimed at optimizing ion transport in polymer electrolytes in a manner that mirrors the development of mixtures of organic solvents used in current day lithium ion batteries. The thermodynamic properties of PEO/P(2EO-MO)/LiTFSI blends, determined by SANS, are surprisingly complex. This initial study is restricted to blends with roughly equal volume fractions of PEO and P(2EO-MO). Neat PEO/P(2EO-MO) blends exhibit a negative Flory-Huggins interaction parameter across the accessible temperature window. If we assume that the phase behavior of PEO/P(2EO-MO)/LiTFSI blends can be approximated by Flory-Huggins theory for binary blends of homopolymers with an effective interaction parameter that accounts for the presence of salt, it would imply that these blends would be miscible irrespective of blend composition and chain lengths of the components. Adding a small amount of LiTFSI ($0.02 \leq r \leq 0.06$) renders the PEO/P(2EO-MO) blends immiscible; blends containing either $26.7 \text{ kg}\cdot\text{mol}^{-1}$ or $16.0 \text{ kg}\cdot\text{mol}^{-1}$ P(2EO-MO) were immiscible. Increasing the salt concentration to $r > 0.08$ results in negative effective Flory-Huggins interaction parameters across the accessible temperature window, implying miscibility irrespective of blend composition and chain lengths of the components.

Ion transport in the blends was characterized by measuring the ionic conductivity, salt diffusion coefficient, and current fraction. Surprisingly, the values of these parameters in blends with a given value of salt concentration, r , were close to those obtained in conventional PEO/LiTFSI electrolytes at the same value of r . In other words, the blends that we have characterized thus far do not exhibit superior ion transport properties. However, a wide variety of ether- and carbonate-containing polymers have been synthesized for electrolytic applications.^{14,18,208,209} This work opens the door to a new direction for creating new and improved polymer electrolytes by either combining existing polymers with salt or by synthesizing new polymers with the specific aim of including them in miscible polymer blend electrolytes.

6.5 Acknowledgements

This work was intellectually led by the Joint Center for Energy Storage Research (JCESR), an Energy Innovation Hub funded by the U.S. Department of Energy, Office of Science, Office of Basic Energy Science, under Contract No. DE-AC02-06CH11357, which supported synthesis work conducted by R.L.S. and B.A.A. under the supervision of G.W.C and characterization work conducted by K.W.G., W.S.L., and Y.C. under the supervision of N.P.B. Characterization work conducted by A.L. under the supervision of B.A.G. was supported by the National Science Foundation through Award DMR-1904537. Work at the Molecular Foundry, which is a DOE Office of Science User Facility, was supported by Contract No. DE-AC02-05CH11231. S.C.M.T. acknowledges the Center for Neutron Studies at the University of Delaware and funding under cooperative agreements #370NANB17H302 and #70NANB15H260 from NIST, U.S. Department of Commerce. We acknowledge the support of the National Institute of Standards and Technology, U.S. Department of Commerce, in providing the neutron facilities used in this work. K.W.G.

acknowledges funding from a National Defense and Science Engineering Graduate Fellowship. W.S.L. acknowledges funding from the National Science Foundation Graduate Student Research Fellowship DGE-1106400.

6.6 Supporting Information

6.6.1 General Synthetic Considerations

All manipulations of air and water sensitive compounds were carried out under nitrogen in an MBraun Labmaster glovebox or by using standard Schlenk line techniques.

Dichloromethane for air sensitive reactions was purchased from Fisher, sparged with ultrahigh purity (UHP) grade nitrogen, and passed through two columns of alumina and dispensed into an oven-dried Straus flask, followed by three freeze-pump-thaw cycles. Otherwise, solvents (heptane, hexanes, acetonitrile, and isopropanol) were used as received. All other chemicals and reagents, except for 1,3,6-trioxocane (*vide infra*), were purchased from commercial sources (Millipore Sigma, Oakwood Chemical, TCI, and Fisher) and used without further purification.

6.6.2 Instrumentation

^1H and ^{13}C NMR spectra were recorded on a Bruker AV III HD (^1H , 500 MHz) spectrometer with a broad band Prodigy cryoprobe or Varian INOVA 400 (^1H , 400 MHz) spectrometer. Chemical shifts (δ) for ^1H and ^{13}C NMR spectra were referenced to protons on the residual solvent (for ^1H) and deuterated solvent itself (for ^{13}C).

High-resolution mass spectrometry (HRMS) analyses were performed on a Thermo Scientific Exactive Orbitrap MS system equipped with an Ion Sense DART ion source.

Thermogravimetric Analysis (TGA) was performed on a TA Instruments Q500 Thermogravimetric Analyzer. The measurement was performed on 8–10 mg samples, which were heated in a nitrogen atmosphere from 25 °C to 600 °C at a rate of 10 °C/min.

Gel permeation chromatography (GPC) analyses were carried out using an Agilent 1260 Infinity GPC System equipped with an Agilent 1260 Infinity autosampler and a refractive index detector. The Agilent GPC system was equipped with two Agilent PolyPore columns (5 micron, 4.6 mm ID) which were eluted with THF at 30 °C at 0.3 mL/min and calibrated using monodisperse polystyrene standards.

AC impedance measurements were performed on lithium symmetric cells using a Bio-Logic VMP3 potentiostat over a 0.1– 10^6 Hz frequency range at an amplitude of 80 mV.

6.6.3 Polymer Characterization

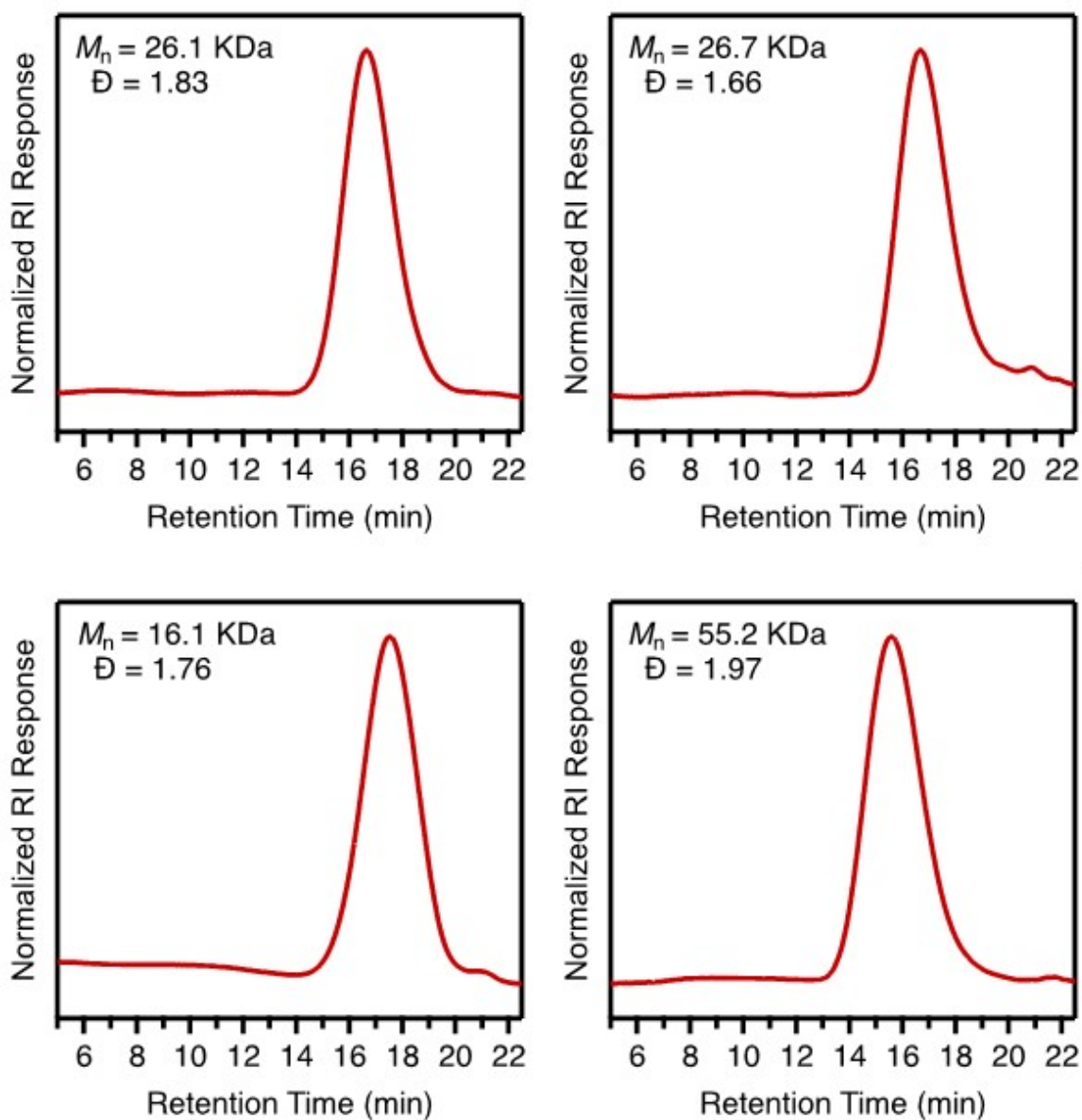


Figure 6.9. GPC traces of P(2EO-MO). Sample 1 (upper left), sample 2 (upper right), sample 3 (lower left) and sample 4 (lower right) show monomodal distributions.

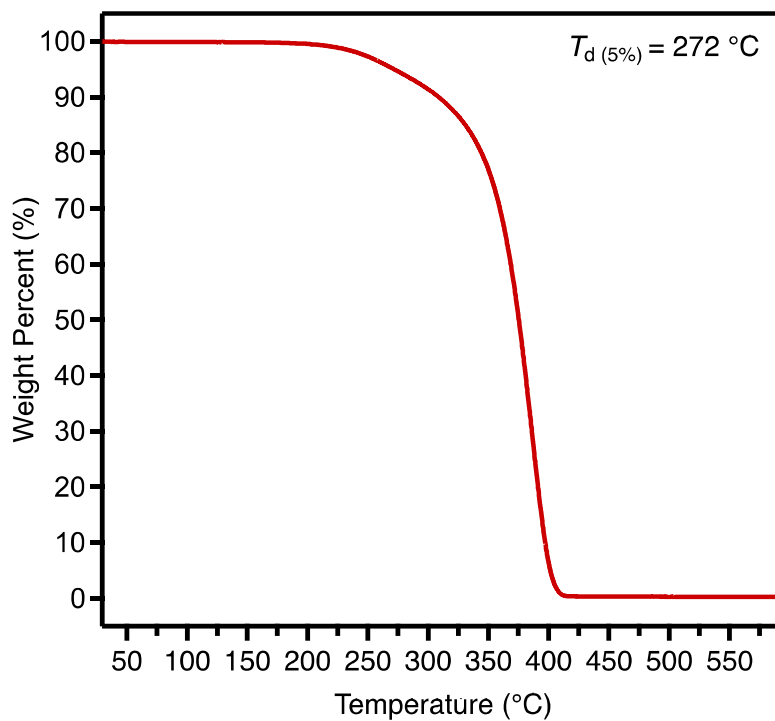


Figure 6.10. Representative thermogravimetric analysis of poly(1,3,6-trioxocane). Weight loss due to thermal degradation begins near 230 °C and reaches 5% loss at 272 °C.

6.6.4 NMR Spectra

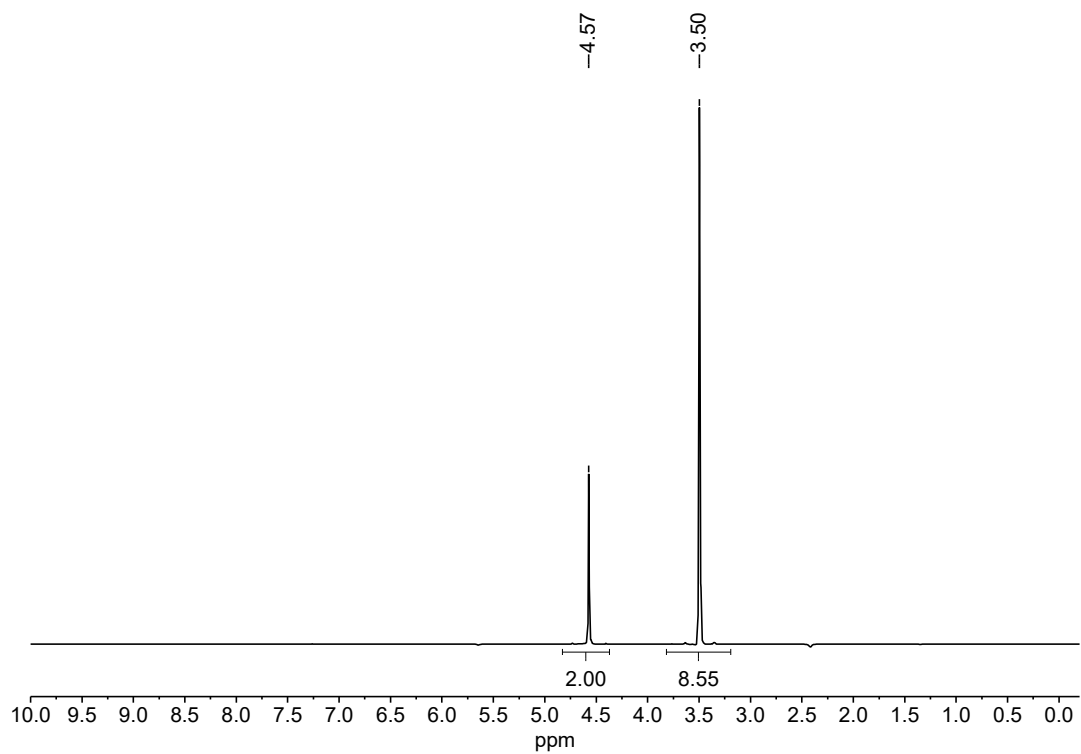


Figure 6.11. 1,3,6-trioxocane (2EO-MO) ^1H NMR Spectrum (500 MHz, CDCl_3).

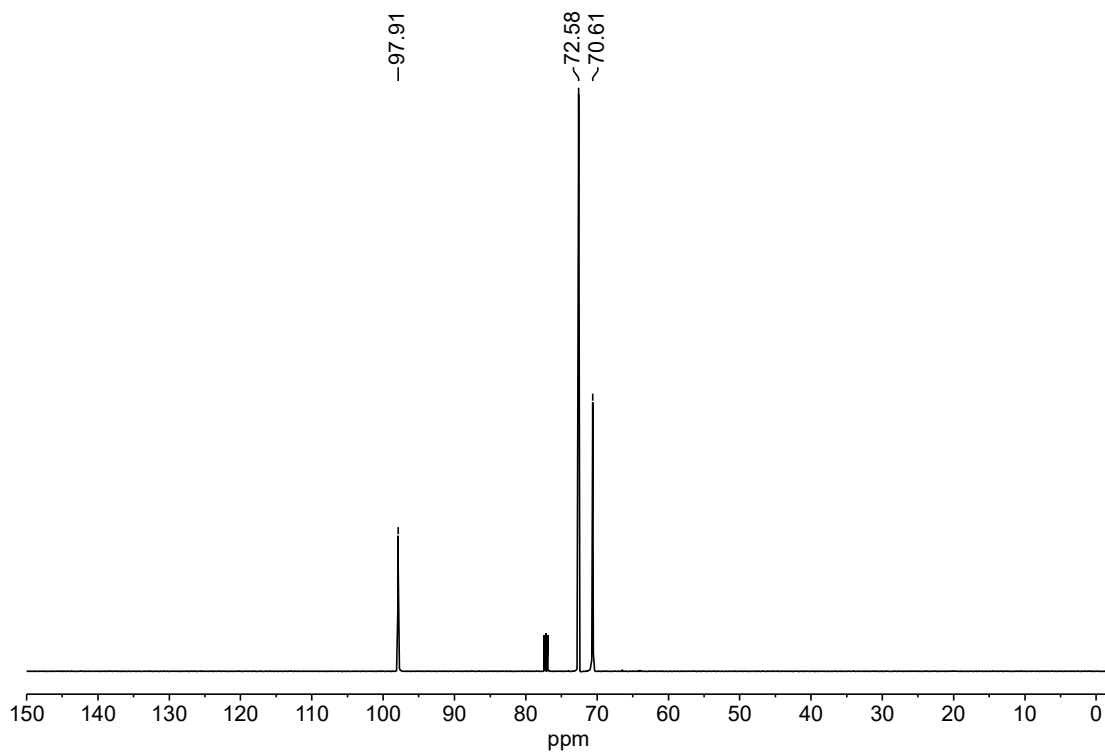


Figure 6.12. 1,3,6-trioxocane (2EO-MO) ^{13}C NMR Spectrum (125 MHz, CDCl_3).

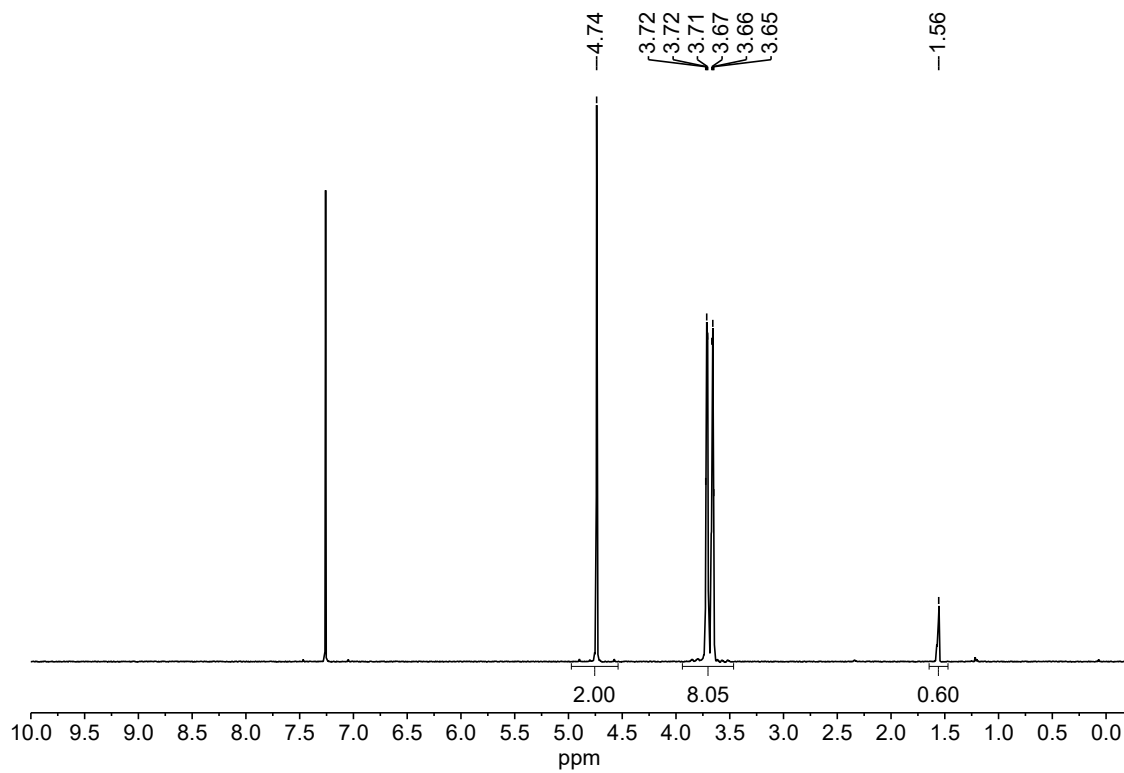


Figure 6.13. Poly(1,3,6-trioxocane) (P(2EO-MO)) ^1H NMR Spectrum (500 MHz, CDCl_3).

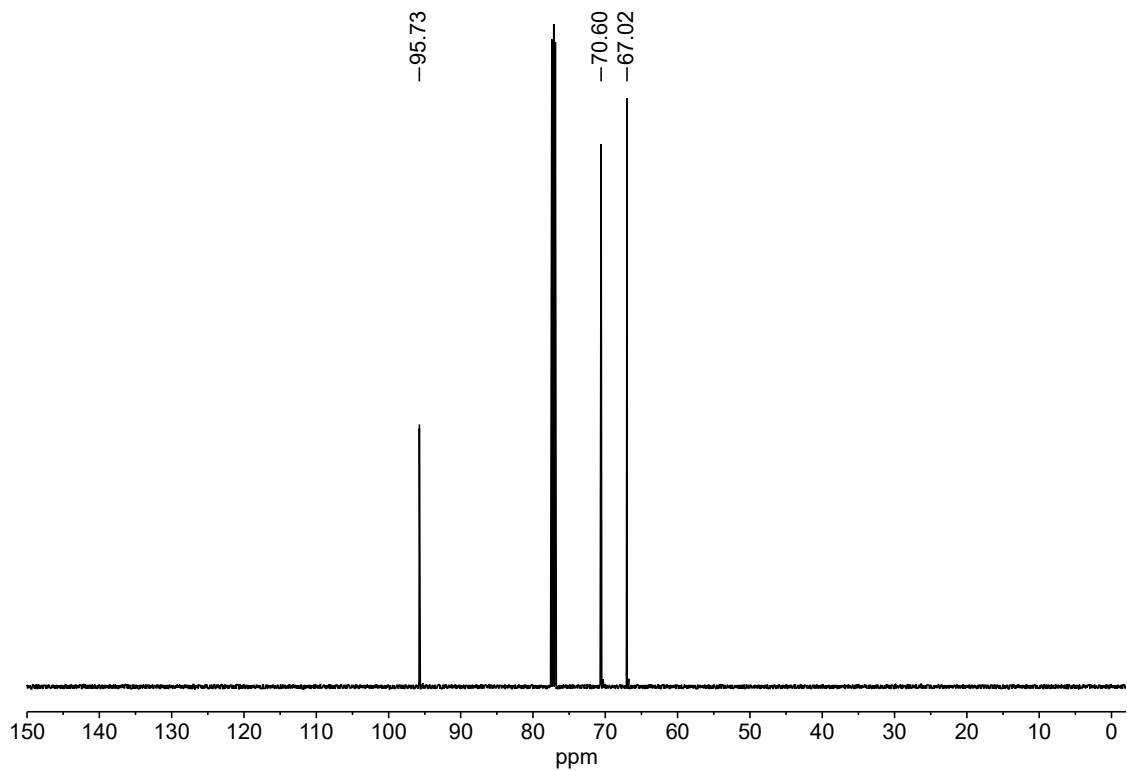


Figure 6.14. Poly(1,3,6-trioxocane) (P(2EO-MO)) ¹³C NMR Spectrum (125 MHz, CDCl₃).

6.6.5 AC Impedance Spectroscopy

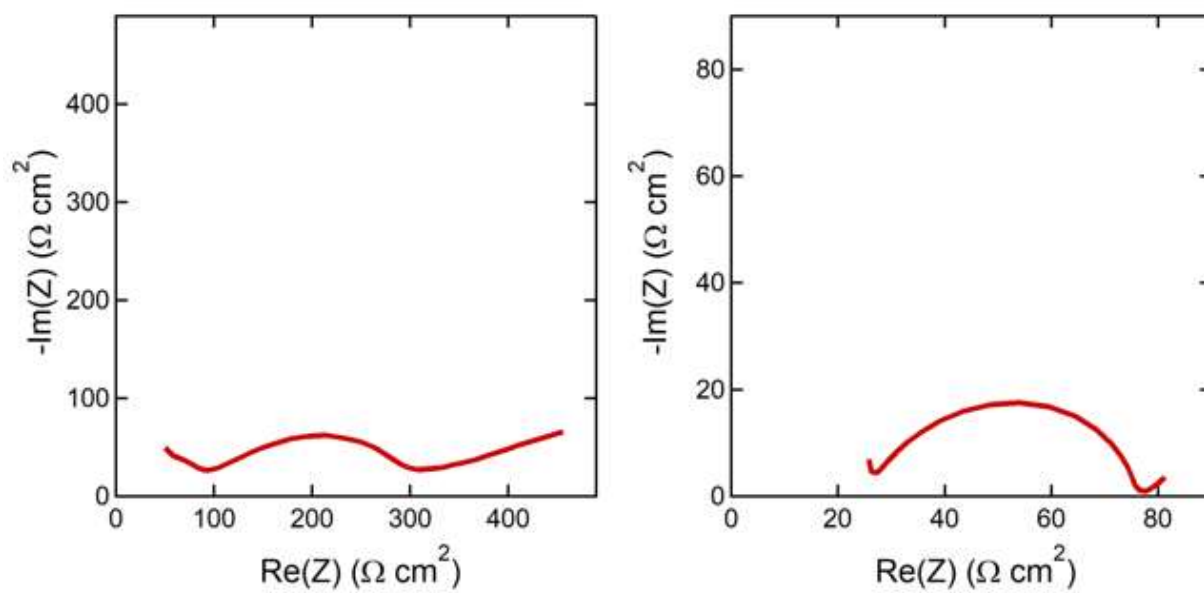


Figure 6.15. Nyquist plots at 90 °C for lithium symmetric cells of PEO/P(2EO-MO)/LiTFSI blends. With salt concentration $r = 0.04$ (left) and $r = 0.10$ (right). The $r = 0.04$ blend is immiscible while the $r = 0.10$

blend is miscible. The difference in magnitude between the two plots is directly proportional to differences in ionic conductivity and interfacial resistance.

6.6.6 Disclaimer

The statements, findings, conclusions and recommendations are those of the authors and do not necessarily reflect the view of NIST or the U.S. Department of Commerce. Certain commercial equipment, instruments, suppliers and software are identified in this paper to foster understanding. Such identification does not imply recommendation or endorsement by the National Institute of Standards and Technology, nor does it imply that the materials or equipment identified are necessarily the best available for the purpose.

6.7 Nomenclature

Table 6.5. List of symbols and abbreviations.

Symbol	Meaning
PEO	Poly(ethylene oxide)
P(2EO-MO)	Poly(1,3,6-trioxocane)
LiTFSI	Lithium bis(trifluoromethanesulfonyl)imide
SANS	Small angle neutron scattering
DSC	Differential scanning calorimetry
2EO-MO	1,3,6-trioxocane
M_n	Number average molar mass
\bar{D}	Dispersity
dPEO	Deuterated PEO
ϕ_i	Volume fraction of component i
ϕ_{polymer}	Volume fraction of polymer components
w_i	Weight of component i
w_{salt}	Weight of LiTFSI salt
ρ_i	Density of component i
ρ_{salt}	Density of LiTFSI salt
r	Molar ratio of lithium ions in the salt to oxygen atoms in the polymers
M_{EO}	Monomer molar mass of PEO
$M_{2(\text{EO-MO})}$	Monomer molar mass of P(2EO-MO)
M_{salt}	Molar mass of LiTFSI salt
f	Volume fraction of PEO and LiTFSI associated with PEO
T_g	Glass transition temperature
SDD	Sample-to-detector distance
θ	Scattering angle
q	Magnitude of the scattering vector
λ	Wavelength
$I(q)$	Measured absolute SANS intensity
ΔG_m	Free energy of mixing per unit volume

k_B	Boltzmann constant
v	Reference volume (0.1 nm ³)
T	Absolute temperature
N_i	Number of repeat units per chain
χ	Flory-Huggins interaction parameter
χ_{crit}	Critical Flory-Huggins interaction parameter
χ_{eff}	Effective Flory-Huggins interaction parameter
$I_{coh}(q)$	Coherent scattering intensity
$I_{dPEO/LiTFSI}(q)$	SANS intensity from dPEO/LiTFSI mixtures (cm ⁻¹)
$I_{inc}(q)$	Incoherent scattering intensity
$P_i(q)$	Form factor
B_i	Neutron scattering length density of component i
b_i	Neutron scattering length of component i
v_i	Monomer molar volume of component i
S_{ii}	Structure factor
M_i	Molar mass of component i
$R_{g,i}$	Radius of gyration
l_i	Statistical segment length of component i
RPA	Random phase approximation
α	RPA fitting parameter accounting for chain distortion
A, B	Empirical constants for fitting Flory-Huggins interaction parameters
R^2	Coefficient of determination
κ	Ionic conductivity
D	Salt diffusion coefficient
ρ_+	Current fraction
$\kappa\rho_+$	Efficacy
PMMA	poly(methyl methacrylate)
LiClO ₄	Lithium perchlorate
MEEP	Poly[bis-(methoxyethoxyethoxide)phosphazene]
P2VP	Poly(2-vinylpyridine)

7 Relationship between Ion Transport and Phase Behavior in Polymer Blend Electrolytes Studied by Electrochemical Characterization and Neutron Scattering[†]

We have studied ion transport in electrolytes created by blending two different polymers and lithium bis(trifluoromethanesulfonyl)imide (LiTFSI). The polymers covered in this study are polyethylene oxide (PEO), poly(1,3,6-trioxocane) (P(2EO-MO)), and poly(1,3-dioxolane) (P(EO-MO)). Ion transport is quantified by the product $\kappa\rho_+$ which is defined as the efficacy of the electrolytes, where κ is conductivity and ρ_+ is the current fraction determined by the Bruce-Vincent method. Polymer blends can be either one-phase or macrophase-separated. We used small angle neutron scattering (SANS) to distinguish between these two possibilities. The random phase approximation (RPA) was used to interpret SANS data from one-phase blends. The effect of added salt on polymer blend thermodynamics is quantified by an effective Flory-Huggins interaction parameter. All polymer blends were one-phase in the absence of salt. Adding salt in small concentrations results in macrophase separation in all cases. One-phase systems were obtained in the PEO/P(EO-MO)/LiTFSI blends at high salt concentrations. In most of the polymer blend electrolytes, the measured $\kappa\rho_+$ was either lower than or comparable to that of the homopolymer electrolytes. An exception to this was one-phase PEO/P(EO-MO)/LiTFSI blends electrolytes at high salt concentrations.

7.1 Introduction

Polymer electrolytes are our current interest as they can replace the flammable organic solvents used in current rechargeable lithium batteries.^{2,7,210,211} While large varieties of mixtures of diverse polymers and different lithium salts have been studied,²¹² poly(ethylene oxide) (PEO) mixed with lithium bis(trifluoromethanesulfonyl)imide (LiTFSI) continues to serve as a standard in the field.^{117,124,209} Ionic conductivity, κ , is an important parameter but it reflects the motion of both cations and anions. While the conductivity of PEO/LiTFSI mixtures is reasonably high at elevated temperatures such as 90 °C, it is dominated by the motion of anions. The performance of electrolytes in lithium batteries depends on the mobility of cations, and an approach for evaluating this was developed by Bruce, Vincent, and Watanabe et al.^{60,61} In this method, one measures the current fraction, ρ_+ , which relates the amount of current carried by the cation. In the limit of small applied currents, the efficacy of electrolytes is related to the product $\kappa\rho_+$. Unfortunately, the value of ρ_+ of PEO/LiTFSI mixtures is relatively low; at salt concentration where κ is maximized, ρ_+ is only about 0.08. While there are few recent reports of promising electrolytes with high values of κ and ρ_+ ,²¹³ the challenge of designing electrolytes with $\kappa\rho_+$ values higher than that of PEO/LiTFSI is significant.⁸² In most polymers, efforts to increase ρ_+ led to a disproportionate decrease in κ .^{94,214,215}

[†] This chapter will be reported in Lee, J.*; Gao, K. W.*; Shah, N. J.; Kang, C.; Snyder, R. L.; Abel, B. A.; Teixeira, S. C. M.; Coates, G. W.; Balsara, N. P. Relationship between Ion Transport and Phase Behavior in Polymer Blend Electrolytes Studied by Electrochemical Characterization and Neutron Scattering. 2022, *In preparation*. *denotes equal contribution

7.2 Materials and Methods

7.2.1 Polymer Blend Electrolyte Preparation and Composition

The molar masses, M_n , and dispersities, \mathcal{D} , of PEO (Polymer Source), deuterated PEO (dPEO) (Polymer Source), P(EO-MO) (synthesized as described in ref ²¹⁷), P(2EO-MO), and deuterated P(EO-MO) (dP(EO-MO)) (synthesized as described in the Supporting Information) used in this study are summarized in Table 7.1.

Table 7.1. Molar masses and dispersities of homopolymers, and type of experiments used in this study.

Polymer	M_n (kg·mol ⁻¹)	\mathcal{D}	Experiments
dPEO	35.0	1.09	SANS
P(EO-MO)	25.3	1.69	Electrochemical Measurements / SANS
PEO	35.0	1.08	Electrochemical Measurements
dP(EO-MO)	21.8	1.79	SANS
P(2EO-MO)	21.0	1.58	Electrochemical Measurements / SANS
P(EO-MO)	18.4	1.86	Electrochemical Measurements

Electrolytes used for SANS experiments were dPEO/P(EO-MO)/LiTFSI and dP(EO-MO)/P(2EO-MO)/LiTFSI blends. Electrochemical measurements were also performed on PEO/P(EO-MO)/LiTFSI and P(EO-MO)/P(2EO-MO)/LiTFSI blends (no deuterated polymers). All polymers were dried in a glovebox antechamber under vacuum at 90 °C for at least 24 h prior to use. LiTFSI was dried under vacuum at 120 °C for at least 72 h. The polymer composition of the blends was 50/50 by weight. We assume that the salt is uniformly distributed in the blend. The salt concentration of the blends was quantified by the molar ratio of Li atoms in the salt to O atoms in the polymers ($r = [Li]/[O]$), calculated as in ref ²⁶. Electrolyte r values ranged from 0 to 0.14. Blends were created by mixing the required amounts of polymers and salt in acetonitrile. These solutions were transparent and homogeneous. The electrolytes were prepared by evaporating the acetonitrile on a hot plate in a glove box at 80 °C overnight. This was followed by a final drying step in the glovebox antechamber under vacuum at 90 °C for 24 h.

7.2.2 SANS Sample Preparation and Experiment

Sample preparation for SANS experiments was conducted following procedures outlined previously.¹⁶⁹

SANS experiments on dPEO/P(EO-MO)/LiTFSI blends were conducted on the NG7SANS beamline at the National Institute of Standards and Technology Center for Neutron Research.¹⁷⁰ Measurements were performed with a neutron wavelength of 6 Å, and up to three sample-to-detector distances (SDDs) of 13 m, 4 m, and 1 m. The shortest, 1 m distance, was used with a detector offset of 25 cm to extend the scattering angle (2θ) attainable. Overall, the three

configurations allowed for access to a scattering wave-vector magnitude, $q = \frac{4\pi}{\lambda} \sin(\theta)$, ranging from 0.03 nm^{-1} to 5.5 nm^{-1} . The neutron beam size was defined by a $9.5 \times 10^{-3} \text{ m}$ aperture. Data were collected at $20 \text{ }^\circ\text{C}$ increments between $70 \text{ }^\circ\text{C}$ and $110 \text{ }^\circ\text{C}$. All measurements were reversible and repeatable upon either heating or cooling. Samples were equilibrated for at least 30 minutes at each temperature. A 9-position Peltier cooling/heating sample changer block was used to drive and maintain constant sample temperature. Samples of thickness of 1 mm were used. Data were reduced using the software package for IGOR provided by the NIST Center for Neutron Research.¹⁷¹ The total scattering intensity was corrected for detector sensitivity, background, and empty cell contributions as well as sample transmission and thickness.^{171,172}

SANS experiments on dP(EO-MO)/P(2EO-MO)/LiTFSI blends were conducted on the HFIR GP-SANS CG-2 beamline at Oak Ridge National Laboratory.²²⁰ Measurements were performed with a neutron wavelength of 6 \AA , and up to three SDDs of 19m, 6 m, and 1 m. Overall, the three configurations allowed for access to q ranging from 0.03 nm^{-1} to 5.5 nm^{-1} . The neutron beam size was defined by a 12 mm diameter sample aperture. Data were collected at $20 \text{ }^\circ\text{C}$ increments between $70 \text{ }^\circ\text{C}$ and $110 \text{ }^\circ\text{C}$. All measurements were reversible and repeatable upon either heating or cooling. Samples were equilibrated for at least 30 minutes at each temperature. A 12-position Peltier cooling/heating sample changer block was used to drive and maintain constant sample temperature. Samples of thickness was 1 mm. Data were reduced using a software package in Jupyter provided by the Oak Ridge National Laboratory.²²¹ The total scattering intensity was corrected for detector sensitivity, background, and empty cell contributions as well as sample transmission and thickness. The intensity was placed on an absolute scale using a secondary standard.

7.2.3 Electrochemical Sample Preparation and Experiments

Electrochemical sample preparation and experiments were conducted following the procedures previously described,^{26,103} using $380 \text{ }\mu\text{m}$ and $500 \text{ }\mu\text{m}$ thick silicone spacers. All experiments were conducted at $90 \text{ }^\circ\text{C}$. The polymer composition of the blends was 50/50 by weight. Because these experiments were conducted with hydrogenated polymers, the volume fractions of polymers in these samples were slightly different from those used in SANS experiments.

7.3 Results and Discussion

Electrochemical characterization of all our polymer blend electrolytes as a function of salt concentration (r) is shown in Figure 7.2. The ionic conductivity (κ) of PEO/LiTFSI is about a factor of 3 or 4 higher than that of P(EO-MO)/LiTFSI at the same value of r . The ionic conductivity of the polymer blend electrolyte PEO/P(EO-MO)/LiTFSI, is, however, similar to that of PEO at all values of r (Figure 7.2(a)). The current fraction (ρ_+) of PEO/LiTFSI is about a factor of 5 lower than that of P(EO-MO)/LiTFSI at the same value of r . The current fraction of the polymer blend electrolyte PEO/P(EO-MO)/LiTFSI, is, however, similar to that of PEO when $r < 0.08$. At higher r values, ρ_+ of the blend electrolyte is higher than that of PEO/LiTFSI; at $r = 0.14$, ρ_+ of the blend electrolyte is a factor of 2 higher. One might have expected the transport properties of the polymer blend electrolytes to be averages of values obtained from the homopolymer electrolytes. The data in Figures 7.2(a) and 7.2(b) clearly show this is not the case.

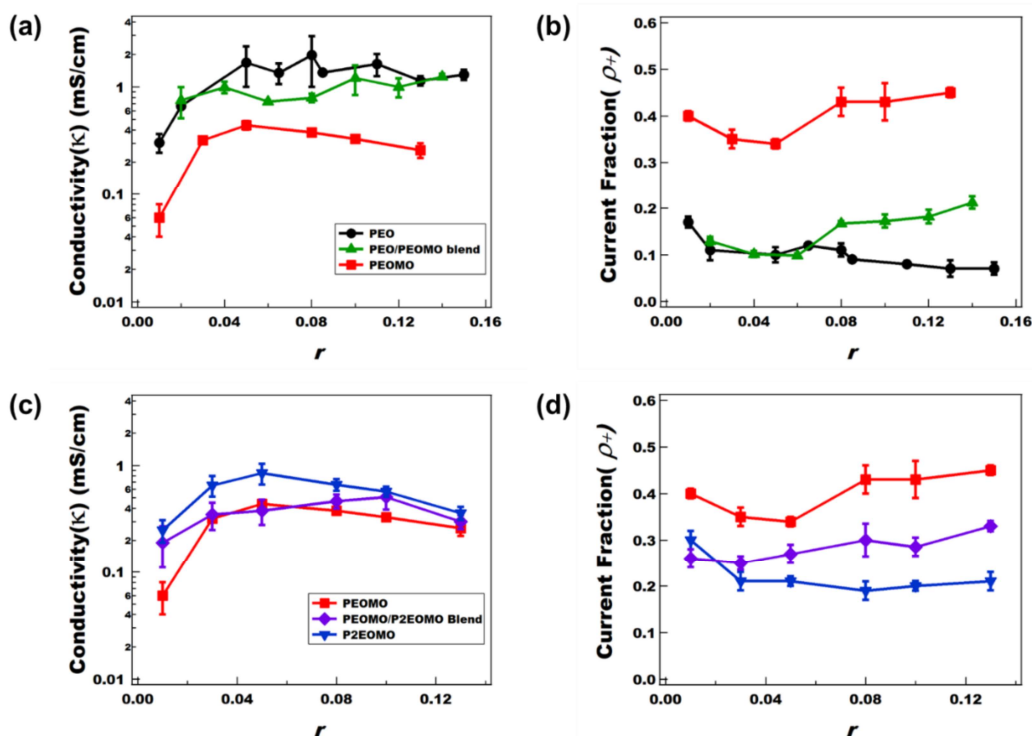


Figure 7.2. Electrochemical characterization of the PEO/P(EO-MO)/LiTFSI and P(EO-MO)/P(2EO-MO)/LiTFSI blend electrolytes as a function of LiTFSI concentration. Compared with each homopolymer/LiTFSI (PEO; 35.0 kg mol^{-1} , P(EO-MO); 23.4 kg mol^{-1} , P(2EO-MO); 55.2 kg mol^{-1}) polymer electrolyte system from ref. ²¹⁷ and ²⁶. (a), (c) Ionic conductivity (κ) measured by ac impedance using symmetric cells with blocking stainless steel electrodes. (b), (d) Current fraction (ρ_+) measured by the Bruce-Vincent method using symmetric cell with nonblocking lithium electrodes. Data was taken at 90°C . Error bars represent the standard deviation of at least three measurements.

The ionic conductivity of P(2EO-MO)/LiTFSI is about a factor of 2 higher than that of P(EO-MO)/LiTFSI at $r = 0.02$ (Figure 7.2(c)). This factor decreases with increasing r ; at $r = 0.13$, κ of P(2EO-MO)/LiTFSI is only 30 % higher than that of P(EO-MO)/LiTFSI. At most r values, κ of

the P(EO-MO)/P(2EO-MO)/LiTFSI polymer blend electrolytes lie between those of the homopolymer electrolytes, P(2EO-MO)/LiTFSI and P(EO-MO)/LiTFSI. The current fraction (ρ_+) of P(2EO-MO)/LiTFSI is about a factor of 2 lower than that of P(EO-MO)/LiTFSI at most the r values (Figure 7.2(d)). At most r values, ρ_+ of the P(EO-MO)/P(2EO-MO)/LiTFSI polymer blend electrolytes lie between those of the homopolymer electrolytes, P(2EO-MO)/LiTFSI and P(EO-MO)/LiTFSI.

The ion transport properties of polymer blend electrolytes will depend on whether the blends are one-phase or macrophase-separated. We note in passing that most pairs of polymers are immiscible with each other.^{165,183} We conducted SANS experiments to determine the miscibility windows in our polymer blend electrolytes.^{85,178,182}

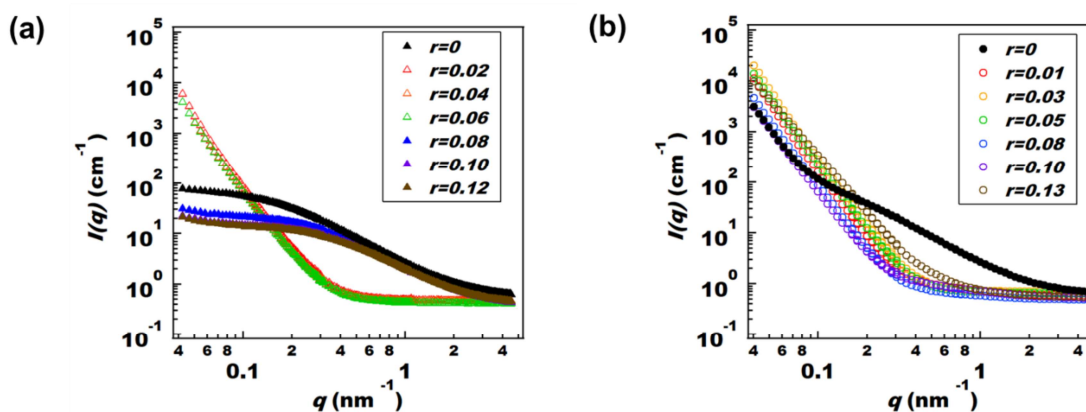


Figure 7.3. Measured absolute SANS intensity ($I(q)$) versus the magnitude of scattering vector (q) at 90 °C for (a) dPEO/P(EO-MO)/LiTFSI and (b) dP(EO-MO)/P(2EO-MO)/LiTFSI polymer blend electrolytes at different salt concentration (r). Filled symbols correspond to one-phase electrolytes. Open symbols correspond to macrophase-separated electrolytes. Error bars represent one standard deviation of the scattering data and in most cases are smaller than the data points

The measured absolute SANS intensity ($I(q)$) as a function of the magnitude of scattering vector (q) for the dPEO/P(EO-MO)/LiTFSI and dP(EO-MO)/P(2EO-MO)/LiTFSI polymer blends electrolytes is shown in Figure 7.3. We used the measured $I(q)$ in the q range $0.4 \text{ nm}^{-1} < q < 1.0 \text{ nm}^{-1}$ to determine if the electrolytes are one-phase or macrophase-separated. In principle, this could be determined by examining $I(q)$ in the limit $q \rightarrow 0$. However, the pure deuterated polymers exhibit strong scattering in this limit which may be due to impurities or voids, as noted in previous publication. The macrophase-separated dPEO/P(EO-MO)/LiTFSI blends show a sharp upturn of $I(q)$ below $q = 0.4 \text{ nm}^{-1}$, as shown in Figure 7.3(a). The macrophase-separated dP(EO-MO)/P(2EO-MO)/LiTFSI blends show a similar signature but the sharp upturn of $I(q)$ is seen at q values ranging from 0.4 to 1.0 nm^{-1} , as shown in Figure 7.3(b). The lack of a sharp upturn of $I(q)$ in the q range noted above it is taken as a signature of a one-phase blend. In the absence of salt, both dPEO/P(EO-MO) and dP(EO-MO)/P(2EO-MO) blends are one-phase. Adding LiTFSI in dilute concentrations results in macrophase separation in both cases. At higher salt concentrations above $r = 0.08$, the dPEO/P(EO-MO)/LiTFSI blends become one-phase again. In contrast, the dP(EO-MO)/P(2EO-MO)/LiTFSI blends remain macrophase-separated in all salt concentrations studied.

We analyze the SANS data from homogenous blends using the Flory-Huggins theory. In this theory, which applies to blends of two homopolymers,

$$v \frac{\Delta G_m}{k_B T} = \frac{\phi_1 \ln \phi_1}{N_1} + \frac{\phi_2 \ln \phi_2}{N_2} + \chi \phi_1 \phi_2, \quad (7.1)$$

where ΔG_m is the free energy of mixing per unit volume, k_B is the Boltzmann constant, T is the absolute temperature, labels 1 and 2 refer to the two polymers, ϕ_i is the volume fraction of component i , N_i is the number of repeat units in chain i , and χ is the Flory-Huggins interaction parameter between monomers of type 1 and 2.^{176,177} N_1 , N_2 , and χ are based on a reference volume, $v = 0.1 \text{ nm}^3$. The critical Flory-Huggins interaction parameter value, $\chi_{critical}$, is given by the following:

$$\chi_{critical} = \frac{1}{2} \left(\frac{1}{\sqrt{N_1}} + \frac{1}{\sqrt{N_2}} \right)^2, \quad (7.2)$$

Blends with $\chi < \chi_{critical}$ implies miscible phase, regardless of composition.

To account for added salt, we use a simple extension of eq 7.1.

$$v \frac{\Delta G_m}{k_B T} = \phi_{polymer} \left(\frac{\phi_1 \ln \phi_1}{N_1} + \frac{\phi_2 \ln \phi_2}{N_2} + \chi_{eff} \phi_1 \phi_2 \right), \quad (7.3)$$

where $\phi_{polymer}$ is the total polymer volume fraction and ϕ_i ($i = 1$ or 2) are the salt-free polymer volume fractions. The effect of added salt on thermodynamics is captured mainly by an effective Flory-Huggins parameter, χ_{eff} , which depends on salt concentration.^{27,222} When $r \rightarrow 0$, $\phi_{polymer} \rightarrow 1$, eq 7.3 reduces to eq 7.1, and χ_{eff} reduces to the conventional χ parameter for polymer blends. After checking the qualitative phase behavior of the two blend systems as a function of r , we analyzed the $I(q)$ data to determine χ_{eff} as a function of blend composition. Before calculating χ_{eff} , the absolute SANS intensity was corrected for the contributions from coherent scattering of the deuterated chains and additional background scattering that includes the incoherent scattering from hydrogen atoms to obtain the absolute coherent SANS intensity from each blend, $I_{coh}(q)$,¹⁷⁸

$$I_{coh}(q) = I(q) - f I_{deuterated}^{polymer}(q) - I_{inc}, \quad (7.4)$$

where f is the volume fraction of deuterated polymer which is calculated using eq 7.5.

$$f = \frac{w_1 + \frac{r n_1 w_1 M'_{salt}}{M'_1}}{\frac{\rho_1}{w_1 + \frac{r n_1 w_1 M'_{salt}}{M'_1}} + \frac{\rho_2}{w_2 + \frac{r n_2 w_2 M'_{salt}}{M'_2}}}, \quad (7.5)$$

Label 1 refers to the deuterated component and label 2 refers to the nondeuterated polymer, w_i is mass of component i , ρ_i is the density ($\rho_{PEO}=1.23 \text{ g cm}^{-3}$; $\rho_{dPEO}=1.34 \text{ g cm}^{-3}$; $\rho_{P(EO-MO)}=1.32 \text{ g cm}^{-3}$; $\rho_{dP(EO-MO)}=1.44 \text{ g cm}^{-3}$; $\rho_{P(2EO-MO)}=1.32 \text{ g cm}^{-3}$; $\rho_{LiTFSI} = 2.023 \text{ g cm}^{-3}$), M'_i is monomer molar mass ($M'_{EO} = 44.05 \text{ g mol}^{-1}$; $M'_{EO-MO} = 68.05 \text{ g mol}^{-1}$; $M'_{2EO-MO} = 118.05 \text{ g mol}^{-1}$; $M'_{dPEO} = 48.05 \text{ g mol}^{-1}$; $M'_{dP(EO-MO)} = 74.03$; M'_{salt} is 287.1 g mol^{-1}), and n_i is the number of

oxygen atoms in each monomer (see Figure 7.1). We assumed that the densities of P(2EO-MO) and P(EO-MO) are equal, and the volumes occupied by monomers of deuterated and nondeuterated polymers are identical. SANS profiles reflect concentration fluctuations which we assume are dominated by fluctuations in polymer concentration; we neglect the partitioning of salt across these fluctuations. $I_{deuterated\ polymer/LiTFSI}$ is the scattering from deuterated polymer/LiTFSI mixtures: $I_{dPEO/LiTFSI}$ was taken from ref. ¹⁶⁹ and $I_{dP(EO-MO)/LiTFSI}$ was measured (Supporting Information). I_{inc} is the incoherent scattering from hydrogen atoms which we estimate by fitting the measured SANS profile in the high q range $0.2\text{ nm}^{-1} < q < 5.0\text{ nm}^{-1}$,

$$I(q) = aP(q) + I_{inc} \quad (7.6)$$

where

$$P(q) = 2 \left[\frac{\exp(-q^2 R_g^2) - 1 + q^2 R_g^2}{q^4 R_g^4} \right], \quad (7.7)$$

a , I_{inc} , and R_g are fitting constants.¹⁷⁹ After subtracting $I_{deuterated\ polymer/LiTFSI}(q)$ and I_{inc} from $I(q)$, we obtain $I_{coh}(q)$ for miscible blends using eq 7.4. The results we obtained are shown in Figure 7.4.

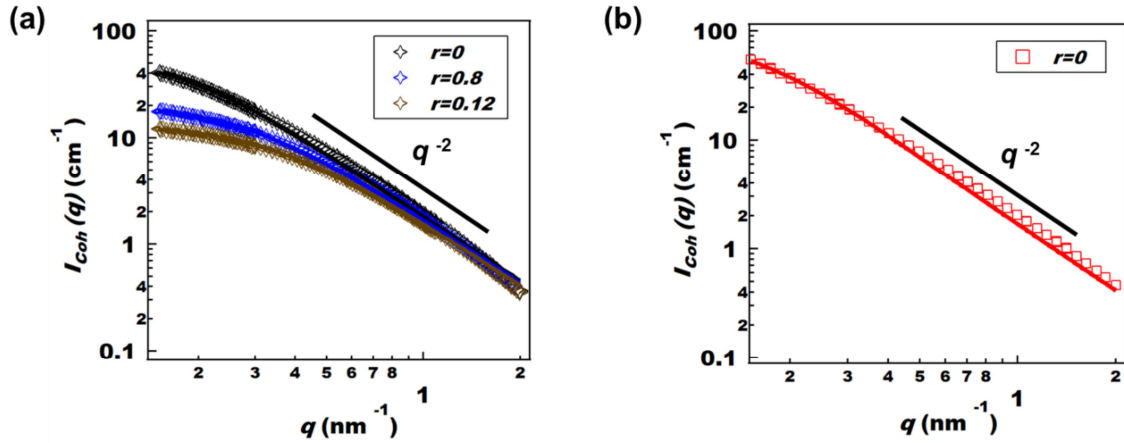


Figure 7.4. Coherent SANS intensity profiles $I_{coh}(q)$ (open symbols) and corresponding RPA fits (solid curves) for miscible blends at 90 °C. (a) dPEO/P(EO-MO)/LiTFSI blends, and (b) dP(EO-MO)/P(2EO-MO). Error bars represent one standard deviation of the scattering data and in most cases are smaller than the data points.

Following ref. ²⁶, we use the following expression for analyzing $I_{coh}(q)$ based on the random phase approximation (RPA) method,^{85,178,181,223,224}

$$I_{coh}(q) = \phi_{polymer} (B_1 - B_2)^2 v \left(\frac{1}{S_{11}(q)} + \frac{1}{S_{22}(q)} - 2\chi_{eff} \right)^{-1}. \quad (7.8)$$

where B_i is the coherent neutron scattering length density of component i , calculated as in ref. ²⁶ ($B_{dPEO} = 128.0 \times 10^{-15} \text{ mol cm}^{-2}$; $B_{P(EO-MO)} = 17.7 \times 10^{-15} \text{ mol cm}^{-2}$; $B_{dP(EO-MO)} = 139.0 \times 10^{-15} \text{ mol cm}^{-2}$; $B_{P(2EO-M)} = 14.8 \times 10^{-15} \text{ mol cm}^{-2}$), v is reference volume (0.1 nm^3), and $S_{ii}(q)$ is the ideal structure factor of polymer i given by,

$$S_{ii}(q) = \phi_i N_i P_i(q). \quad (7.9)$$

and N_i is the number of repeat units in each polymer, given by

$$N_i = \frac{M_i}{\rho_i N_{av} v}, \quad (7.10)$$

where N_{av} is Avogadro's number and M_i and ρ_i are the polymer molar mass (g mol^{-1}) and density (g cm^{-3}), and $P_i(q)$ is the Debye function of the polymer i ,

$$P_i(q) = 2 \left[\frac{\exp(-q^2 R_{gi}^2) - 1 + q^2 R_{gi}^2}{q^4 R_{gi}^4} \right], \quad R_{gi}^2 = \frac{N_i l_i^2}{6}, \quad (7.11)$$

where R_{gi} is the radius of gyration of polymer i , and l_i is the statistical segment length of polymer i . We assumed that the l_i value of PEO is 0.58 nm .¹⁶⁹ The nominal values for l_i of P(EO-MO) and P(2EO-MO) were taken to be 0.58 nm . The scattering data in Figure 7.4 were fit to eq 7.8 with two adjustable constants, χ_{eff} and α where the values of l_i of P(EO-MO) and P(2EO-MO) were also assumed to be $0.58\alpha \text{ nm}$ (α is constant). α was found to be a weak function of temperature. To minimize errors in fitting, we used a temperature-average value of α for each miscible blend ($70 \text{ }^\circ\text{C}$, $90 \text{ }^\circ\text{C}$, and $110 \text{ }^\circ\text{C}$; Supporting Information). The final fits were obtained with χ_{eff} as the only adjustable parameter. The blend compositions and α parameters obtained using RPA fitting are listed in Table 7.2. The curves in Figure 7.4 show those fits from which we estimate χ_{eff} for all one-phase polymer blends.

Table 7.2. Component volume fractions ϕ_i and α values of miscible blends.

Polymer Blend	ϕ_1	ϕ_2	$\phi_{polymer}$	α
dPEO/P(EO-MO) ($r = 0$)	0.50	0.50	1.00	1.37 ± 0.03
dPEO/P(EO-MO) ($r = 0.08$)	0.50	0.50	0.72	1.17 ± 0.03
dPEO/P(EO-MO) ($r = 0.10$)	0.50	0.50	0.67	1.15 ± 0.01
dPEO/P(EO-MO) ($r = 0.12$)	0.50	0.50	0.63	1.14 ± 0.01
dP(EO-MO)/P(2EO-MO) ($r = 0$)	0.52	0.48	1.00	1.46 ± 0.01

ϕ_1 : volume fraction of deuterated polymer, ϕ_2 : volume fraction of nondeuterated polymer.

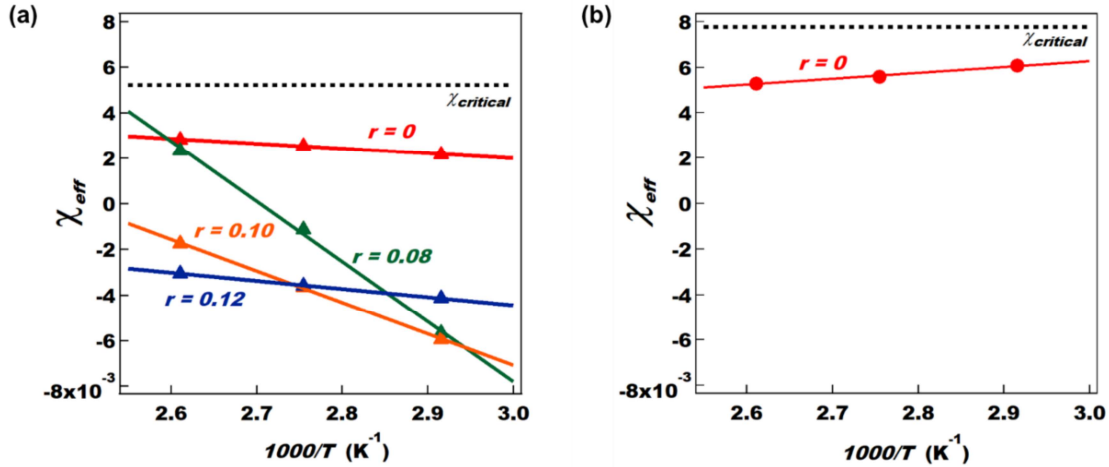


Figure 7.5. Effective Flory-Huggins interaction parameter χ_{eff} as a function of inverse temperature ($1/T$) for the one-phase (a) dPEO/P(EO-MO)/LiTFSI polymer blend electrolytes and (b) dP(EO-MO)/P(2EO-MO) polymer blends. All dP(EO-MO)/P(2EO-MO)/LiTFSI blends were macrophase-separated. $\chi_{critical}$ is calculated by eq 7.2. Error bars represent one standard deviation of the χ_{eff} fits and are smaller than the symbols.

The temperature dependence of χ_{eff} of the miscible polymer blends, obtained by the fitting procedure described in the previous paragraph, is shown in Figure 7.5. We fit this dependence to the function of form

$$\chi_{eff} = \frac{A}{T} + B, \quad (7.12)$$

where A and B are constants.^{165,184} These constants are given in Table 7.3. As shown in Figure 7.5(a) χ_{eff} of dPEO/P(EO-MO) ($r = 0$) decreases slightly with increasing T . The value of B for the system is small, $(8.50 \pm 0.36) \times 10^{-3} \text{K}^{-1}$. Also shown in Figure 7.5(a) $\chi_{critical}$ is calculated using eq 7.2. We assume the χ_{eff} for macrophase-separated systems exceeds $\chi_{critical}$. Adding salt to this blend results in macrophase separation up to $r = 0.06$. We conclude that χ_{eff} of dPEO/P(EO-MO)/LiTFSI blends with $0.02 < r < 0.06$ is greater than $\chi_{critical}$ (5.2×10^{-3}). Further increase in salt concentration $r = 0.08$ results in a one-phase blend with χ_{eff} that decreases significantly with increasing T . The value of B for the system is large, $(71.2 \pm 3.3) \times 10^{-3} \text{K}^{-1}$. χ_{eff} of dPEO/P(EO-MO)/LiTFSI blends with $r = 0.10$ and 0.12 also decrease with increasing T , but exhibit smaller values of B . (see Table 7.3) As shown in Figure 7.5(b), χ_{eff} of dP(EO-MO)/P(2EO-MO) ($r = 0$) increase slightly with increasing T . The value of B for the system is small but negative, $(-1.55 \pm 0.71) \times 10^{-3} \text{K}^{-1}$. Adding salt results in macrophase separation at all values of r between 0.01 to 0.13 . In this window, χ_{eff} is greater than $\chi_{critical}$ (7.7×10^{-3}).

Table 7.3. A and B values for dPEO/P(EO-MO)/LiTFSI and dP(EO-MO)/P(2EO-MO) blends at various r .

Polymer Blend	A	$B \times 10^{-3} (\text{K}^{-1})$
dPEO/P(EO-MO) ($r = 0$)	-2.19 ± 0.13	8.50 ± 0.36
dPEO/P(EO-MO) ($r = 0.08$)	-26.4 ± 1.2	71.2 ± 3.3
dPEO/P(EO-MO) ($r = 0.10$)	-13.8 ± 0.3	34.4 ± 0.7
dPEO/P(EO-MO) ($r = 0.12$)	-3.57 ± 0.06	6.27 ± 0.17
dP(EO-MO)/P(2EO-MO) ($r = 0$)	2.61 ± 0.26	-1.55 ± 0.71

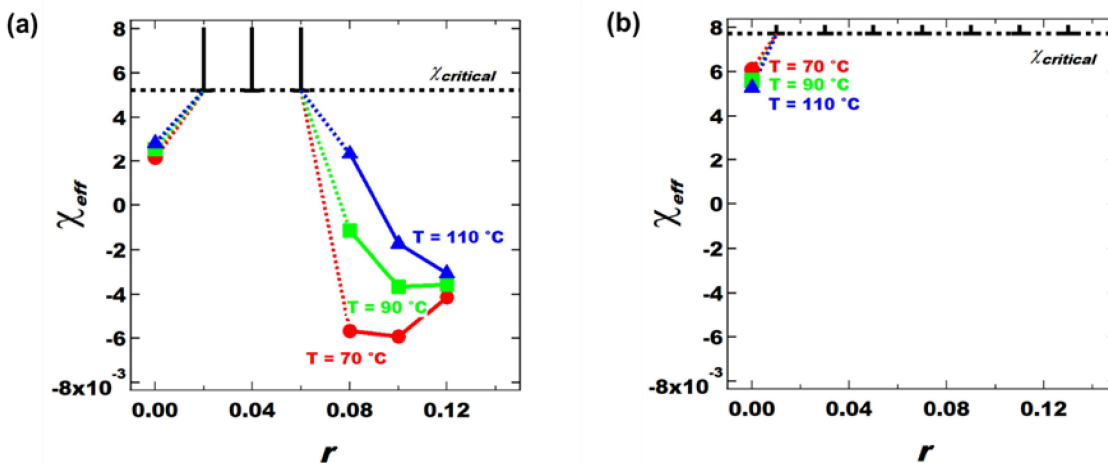


Figure 7.6. Effective Flory-Huggins interaction parameter χ_{eff} as a function of salt concentration, r , for the (a) dPEO/P(EO-MO)/LiTFSI, and (b) dP(EO-MO)/P(2EO-MO)/LiTFSI polymer blends at different temperatures.

(a) In the salt concentration range, $0.02 \leq r < 0.08$, we can only determine the lower bound of the error bar for χ_{eff} of dPEO/P(EO-MO)/LiTFSI due to macrophase separation. (b) dP(EO-MO)/P(2EO-MO)/LiTFSI polymer blends are macrophase-separated at all salt concentrations and temperatures. $\chi_{critical}$ is calculated by eq 7.2. Error bars represent one standard deviation of the χ_{eff} fits and are smaller than the symbols.

Figure 7.6(a) shows the dependence of χ_{eff} on r for the dPEO/P(EO-MO)/LiTFSI blends at different temperatures. At low salt concentrations ($0.02 \leq r \leq 0.06$), we only get a lower bound for χ_{eff} which is $\chi_{critical}$. We thus only present the lower bounds of the error bars for χ_{eff} in this salt concentration window. At higher salt concentrations, χ_{eff} generally decreases with increasing salt concentration. We have very limited information on the dependence of χ_{eff} on r for the dP(EO-

MO)/P(2EO-MO)/LiTFSI blends, as shown in Figure 7.6(b). In these blends, we only conclude χ_{eff} increases above $\chi_{critical}$ when r increases from 0 to 0.01.

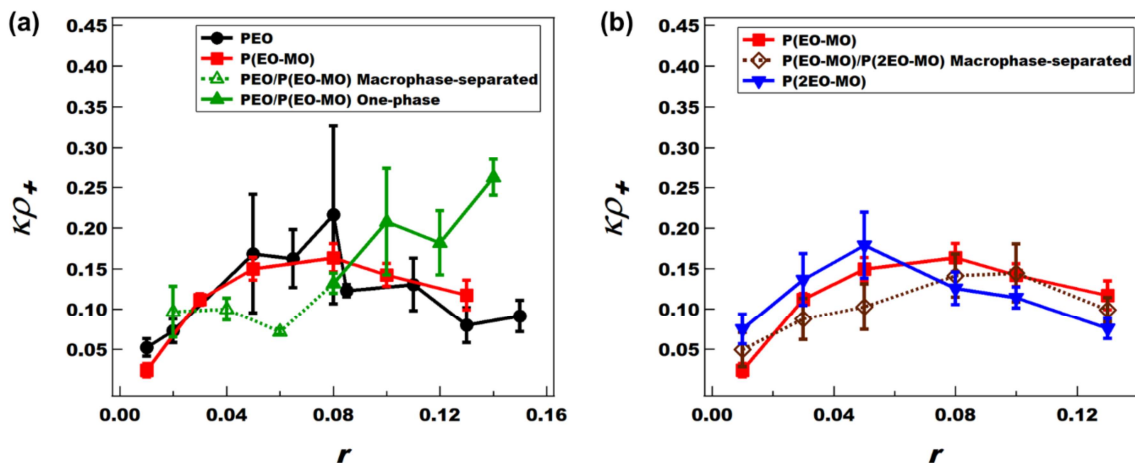


Figure 7.7. Efficacy, $\kappa\rho_+$, of PEO/P(EO-MO)/LiTFSI and P(EO-MO)/P(2EO-MO)/LiTFSI polymer blend electrolytes as a function of r compared with each homopolymer/LiTFSI at 90 °C. (PEO; 35.0 kg mol⁻¹, P(EO-MO); 23.4 kg mol⁻¹, P(2EO-MO); 55.2 kg mol⁻¹). Homopolymer/LiTFSI data were collected from ref. ²¹⁷. Solid lines imply one-phase systems and dashed lines imply macrophase-separated systems. Error bars represent the standard deviation of at least three measurements.

We now discuss the relationship between the electrochemical properties of the polymer blend electrolyte and the blend phase behavior. Under a small applied potential gradient, the dc current is proportional to the product $\kappa\rho_+$. We thus refer to $\kappa\rho_+$ as the efficacy of electrolyte. In Figure 7.7(a), we plot $\kappa\rho_+$ as a function of r for three systems: PEO/LiTFSI, P(EO-MO)/LiTFSI, and PEO/P(EO-MO)/LiTFSI blends. The dependence of $\kappa\rho_+$ of PEO/LiTFSI and P(EO-MO)/LiTFSI on r is similar, within experimental error. Given this fact, one might expect the dependence of $\kappa\rho_+$ of PEO/P(EO-MO)/LiTFSI blends on r to be similar to that of the homopolymer electrolytes. Figure 7.7(a) shows that this is not the case. At $r = 0.05$, $\kappa\rho_+$ of polymer blend electrolytes is 0.08 mS/cm while that of the homopolymer electrolytes is 0.16 mS/cm. In contrast, at $r = 0.14$, $\kappa\rho_+$ of polymer blend electrolytes is 0.26 mS/cm while that of the homopolymer electrolytes is 0.10 mS/cm. The main difference between the two chosen r values is their phase behavior: the polymer blend electrolyte at $r = 0.14$ is one-phase, while the polymer blend electrolyte at $r = 0.05$ is macrophase-separated. It is evident that one-phase polymer blend electrolytes can exhibit efficacies that are higher than homopolymer electrolytes. For completeness, in Figure 7.7(b), we plot $\kappa\rho_+$ as a function of r for three systems: P(EO-MO)/LiTFSI, P(2EO-MO)/LiTFSI, and P(EO-MO)/P(2EO-MO)/LiTFSI blends. The dependence of $\kappa\rho_+$ on r is similar for all three systems. All of the polymer blend electrolytes in Figure 7.7(b) are macrophase-separated.

Finally, we compare our findings with literature on polymer blend electrolytes. Theoretical work of Wheatle et al. (ref. ¹⁶⁸) shows that conductivity of polymer blend electrolytes can be higher than that of homopolymer electrolytes, especially if the polarity of the blended polymers are different and the blend is one-phase. In the simulations, the conductivity of macrophase-separated blends was systematically lower than the average conductivity of the two homopolymer electrolytes. Our

experimental data on macrophase-separated blends are consistent with this result. (see Figure 7.2(a), (c)). In experimental work, Caradant et al. (ref.²¹⁹) studied the conductivity of PEO blended with polymers with different polarity, polycaprolactone (PCL), polypropylene carbonate (PPC) and polyvinylpyrrolidone (PVP). All of the blends in this study were macrophase-separated and exhibited lower conductivity when compared with PEO electrolytes. To our knowledge, Figure 7.7(a) is the only data set in the literature thus far that shows higher efficacy of a polymer blend electrolyte relative to PEO.

7.4 Conclusions

In this study, we have examined the possibility of optimizing ion transport in polymer electrolytes by blending two different polymers. The polymers covered in this study are PEO, P(2EO-MO), and P(EO-MO). LiTFSI is added to the polymers to create electrolytes. The properties of PEO/P(2EO-MO)/LiTFSI blends were reported in ref. ²⁶. The properties of PEO/P(EO-MO)/LiTFSI and P(EO-MO)/P(2EO-MO)/LiTFSI are reported in this paper. Ion transport is quantified by the product $\kappa\rho_+$ which is defined as the efficacy of the electrolytes. Polymer blends can be either one-phase or macrophase-separated. We used SANS to distinguish between two possibilities and the results thus obtained are summarized in Figure 7.8. All polymer blends were one-phase the absence of salt. Adding salt in small concentration results in macrophase separation in all cases. One-phase systems were obtained in the two blends containing PEO at high salt concentrations ($r \geq 0.08$). The boundaries between one-phase and macrophase-separated systems is assumed to be at the average value of r where the two types of system were observed. In most of the polymer blend electrolytes, the measured $\kappa\rho_+$ was either lower than or comparable to that of the homopolymer electrolytes. An exception to this was one-phase PEO/P(EO-MO)/LiTFSI blends electrolytes with $r \geq 0.10$, as shown in Figure 7.8. The molecular underpinnings of both thermodynamic and ion transport properties remain to be established.

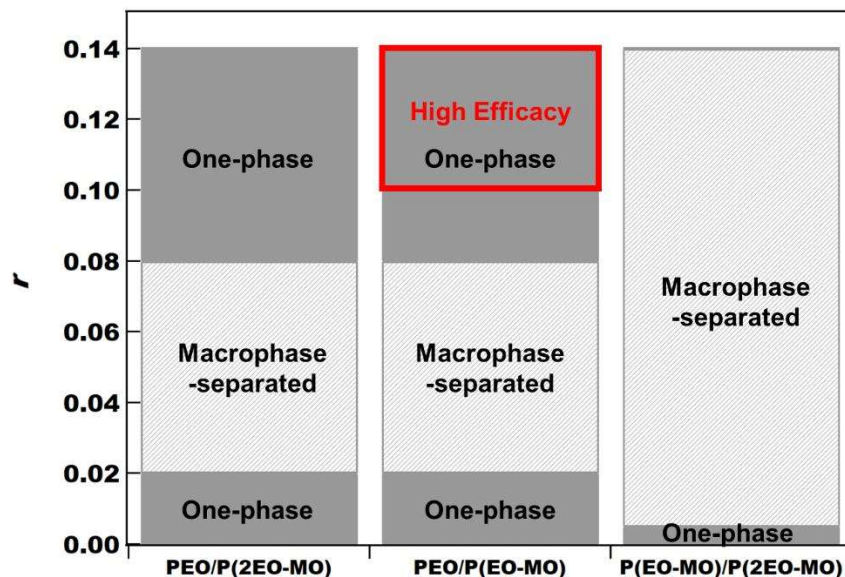


Figure 7.8. Summary of phase behavior and ion transport efficacy, $\kappa\rho_+$, of polymer blend electrolytes with added LiTFSI salt at 90 °C. We distinguish between one-phase and macrophase-separated blends. The red box identifies one-phase systems with efficacies higher than that of homopolymer electrolytes.

7.5 Acknowledgements

This work was intellectually led by the Joint Center for Energy Storage Research (JCESR), an Energy Innovation Hub funded by the U.S. Department of Energy, Office of Science, Office of Basic Energy Science, under Contract No. DE-AC02-06CH11357, which supported synthesis work conducted by C.K., R.L.S., and B.A.A. under the supervision of G.W.C and characterization work conducted by J.L. and K.W.G. under the supervision of N.P.B. Work at the Molecular Foundry, which is a DOE Office of Science User Facility, was supported by Contract No. DE-AC02-05CH11231. S.C.M.T. acknowledges the Center for Neutron Studies at the University of Delaware and funding under cooperative agreements #370NANB17H302 and #70NANB15H260 from NIST, U.S. Department of Commerce. We acknowledge the support of the National Institute of Standards and Technology, U.S. Department of Commerce, in providing the neutron facilities used in this work. K.W.G. acknowledges funding from a National Defense and Science Engineering Graduate Fellowship.

7.6 Supporting Information

7.6.1 General Synthetic Considerations

All manipulations of air and water sensitive compounds were carried out under nitrogen in a MBraun Labmaster glovebox or by using standard Schlenk line techniques. Solvents for air sensitive reactions were purchased from Fisher, sparged with ultrahigh purity (UHP) grade nitrogen, and either passed through two columns containing reduced copper (Q-5) and alumina (THF) or passed through two columns of alumina (CH_2Cl_2) and dispensed into an oven-dried Straus flask, degassed via three freeze-pump-thaw cycles, and stored under nitrogen over activated

3 Å molecular sieves in a glovebox. Otherwise, solvents (Et₂O, heptane, isopropanol) were used as received. All other chemicals and reagents, except for polymerization materials (*vide infra*), were purchased from commercial sources (Cambridge Isotope Laboratories, Aldrich, Oakwood Chemical, Strem, Chemicals, Alfa Aesar, Acros, and Fisher) and used without further purification.

InBr₃ (Strem, 99.999%) was used without further purification. Bromomethyl methyl ether (MOM Br, TCI Chemicals, 97%) was distilled under nitrogen under partial static vacuum, degassed via three freeze-pump-thaw cycles, and stored under nitrogen in a glovebox freezer at -30 °C. 2,6-Di-*tert*-butylpyridine (DTBP) was dried over CaH₂ for three days and vacuum distilled, degassed via three freeze-pump-thaw cycles and stored at room temperature under nitrogen over activated 3 Å molecular sieves. All cyclic acetal monomers were dried over CaH₂ for three days, vacuum distilled, and degassed via three freeze-pump-thaw cycles followed by storage at room temperature under nitrogen over 3 Å molecular sieves.

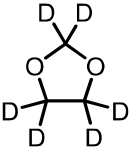
7.6.2 Instrumentation

¹H, ²H, and ¹³C NMR spectra were recorded on a Bruker AV III HD (¹H, 500 MHz) spectrometer with a broad band Prodigy cryoprobe or Varian INOVA 400 (¹H, 400 MHz) spectrometer. Chemical shifts (δ) for ¹H and ¹³C NMR spectra were referenced to protons of the residual solvent (for ¹H) and deuterated solvent itself (for ²H and ¹³C).

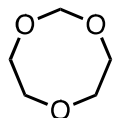
GPC analyses were carried out using an Agilent 1260 Infinity GPC System equipped with an Agilent 1260 Infinity autosampler and a refractive index detector. The Agilent GPC system was equipped with two Agilent Polypore columns (5 μm, 4.6 mm ID), which were eluted with THF at 30 °C at a rate of 0.3 mL/min and calibrated using monodisperse polystyrene standards.

7.6.3 Synthetic Procedures

1,3-Dioxolane-*d*₆ (*d*EEO-MO)

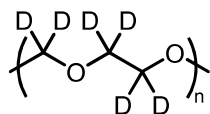
 Paraformaldehyde-*d*₂ (4.03 g, 126 mmol, 1.00 equiv), ethylene glycol-*d*₄ (9.98 g, 151 mmol, 1.20 equiv) and *p*-toluenesulfonic acid (718 mg, 3.77 mmol, 0.03 equiv) were combined in a 25 mL flask with a magnetic stir bar and fitted with a reflux condenser. The reaction mixture was refluxed at 90 °C for 3 h, then distilled at 130 – 190 °C under ambient atmosphere to obtain a mixture of 1,3-dioxolane-*d*₆, water, and other minor impurities such as trioxane and trioxepane. An excess amount of K₂CO₃ was added to salt out the organic phase. The organic phase was fractionally distilled at 95 °C to obtain pure 1,3-dioxolane-*d*₆ as a clear, colorless liquid. The product was dried over CaH₂ for 3 days, vacuum transferred, and degassed via three freeze-pump-thaw cycles (7.48 g, 74% yield). ²H NMR (77 MHz, CDCl₃): δ 4.87 (s, 2H), 3.84 (s, 4H) ppm. ¹³C NMR (126 MHz, CDCl₃) δ 94.53 (p, *J* = 25.4 Hz), 63.85 (p, *J* = 22.7 Hz).

1,3,6-Trioxocane (2EO-MO)



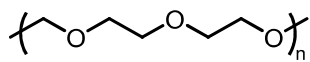
Diethylene glycol (100 g, 0.94 mol, 1.0 equiv), paraformaldehyde (37 g, 1.2 mol, 1.3 equiv), polyphosphoric acid (4.0 g, 28 mmol, 0.030 equiv), and heptane (160 mL) were combined in a 250 mL flask with a magnetic stir bar and fitted with a Dean-Stark adapter and condenser. The reaction was stirred at 115 °C for 12 h and water was collected as the bottom layer in the trap. After cooling the reaction mixture to room temperature, heptane was removed via rotary evaporation to give a cloudy, viscous solution. This oligomerized product was distilled at 150 – 180 °C under high vacuum into a receiving flask cooled with a dry ice/acetone bath. The crude mixture of diethylene glycol and 2EO-MO was then fractionally distilled under high vacuum at 80 °C to give clear, colorless, 2EO-MO in 70% yield. The monomer was dried over CaH₂ for 3 days, distilled, and degassed via three freeze-pump-thaw cycles. Spectral data match previous reports.²¹⁷ ¹H NMR (500 MHz, CDCl₃) δ 4.57 (s, 2H), 3.50 (s, 8H) ppm. ¹³C NMR (125 MHz, CDCl₃) δ 97.91, 72.58, 70.61 ppm. HRMS (DART-MS): *m/z* calculated for C₅H₁₀O₃ [H]⁺ 119.0703, found 119.0703.

*d*P(EO-MO)



In a glovebox under nitrogen atmosphere, 1,3-dioxolane-*d*₆ (7.17 g, 89.5 mmol, 200 equiv), di-*tert*-butyl pyridine (0.222 mL, 0.99 mmol) and CH₂Cl₂ (1.5 mL) were combined in a 100 mL round bottom flask with a stir bar. MOMBr (0.0365 mL, 0.448 mmol) was added to the reaction mixture using a gas-tight microliter syringe. In a separate vial, InBr₃ (70.2 mg, 0.198 mmol) was dissolved in anhydrous diethyl ether (1.0 mL), and sealed with a pierceable cap. The InBr₃ stock solution and polymerization flask were removed from the glovebox, and the reaction mixture was cooled to 0 °C in an ice bath for at least 10 min. The polymerization was initiated by addition of an InBr₃ stock solution (1.0 mL) directly to the reaction mixture under nitrogen using a 1 mL plastic syringe ([*d*EO-MO]₀ = 9.0 M). After the reaction became too viscous to stir, the reaction mixture was quenched by adding 5.0 mL of a 0.5 M solution of sodium methoxide in THF and mixing vigorously at 0 °C. Once quenched, the solution was stirred with K₂CO₃ (20 g) for 1 h to quench any residual acidic species. The K₂CO₃ was removed via vacuum filtration through a basic alumina and Celite pad, and the polymer was isolated by precipitating into cold diethyl ether. The white fibrous solid was isolated via vacuum filtration, dried at 70 °C under vacuum for 24 h to remove residual solvent and give a semi-crystalline white solid product (4.89 g, 68 %). *M*_n = 21.8 kDa; *D* = 1.79. ²H NMR (77 MHz, CDCl₃): δ 4.71 (s, 2H), 3.67 (s, 4H) ppm. ¹³C NMR (126 MHz, CDCl₃): δ 94.9 (p, *J* = 24.7 Hz), 66.0 (p, *J* = 21.5 Hz) ppm.

P(2EO-MO)



In a glovebox under nitrogen atmosphere, 2EO-MO (10.0 g, 84.7 mmol, 100 equiv), di-*tert*-butyl pyridine (0.539 mL, 2.82 mmol) and CH₂Cl₂ (16.8 mL) were combined in a 100 mL round bottom flask with a stir bar. MOMBr (69 μL, 0.847 mmol) was added to the reaction mixture using a gas-tight microliter syringe. In a separate vial, InBr₃ (100 mg, 0.282 mmol) was dissolved in anhydrous diethyl ether (1.0 mL), and sealed with a pierceable cap. The InBr₃ stock solution and polymerization flask were removed from the glovebox, and the reaction mixture was cooled to 0 °C in an ice bath for at least 10 min. The polymerization was initiated by addition of an InBr₃ stock solution (1.0 mL) directly to the reaction

mixture under nitrogen using a 1 mL plastic syringe ($[2\text{EO-MO}]_0 = 3.0 \text{ M}$). After the reaction became too viscous to stir, the reaction mixture was quenched by adding 5.0 mL of a 0.5 M solution of sodium methoxide in THF and mixing vigorously at room temperature. Once quenched, the solution was stirred with K_2CO_3 (20 g) for 1 h to quench any residual acidic species. The K_2CO_3 was removed via vacuum filtration through a basic alumina and Celite pad, and the polymer was isolated by precipitating into cold isopropanol. The white fibrous solid was isolated via vacuum filtration, dried at $90 \text{ }^\circ\text{C}$ under vacuum for 24 h to remove residual solvent and give a semi-crystalline white solid product (4.57 g, 46 %). $M_n = 21.0 \text{ kDa}$; $D = 1.58$. Spectral data match previous reports.²¹⁷

7.6.4 NMR Spectra

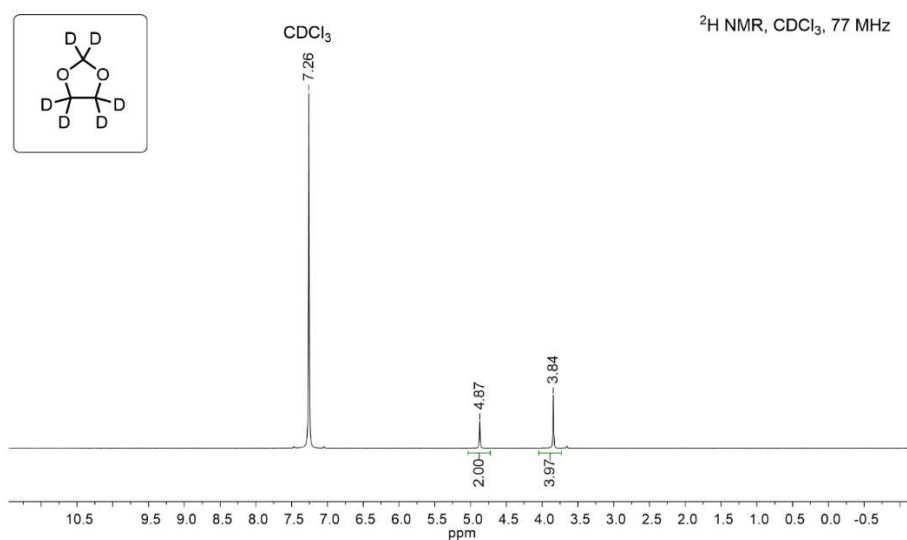


Figure 7.9. ^1H NMR spectrum of *d*EO-MO.

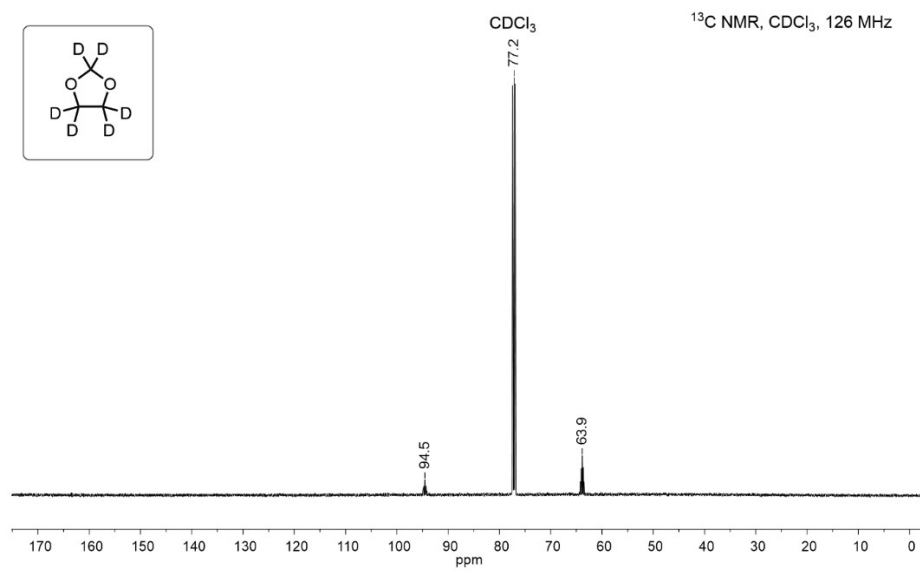


Figure 7.10. ¹³C NMR spectrum of *d*EO-MO.

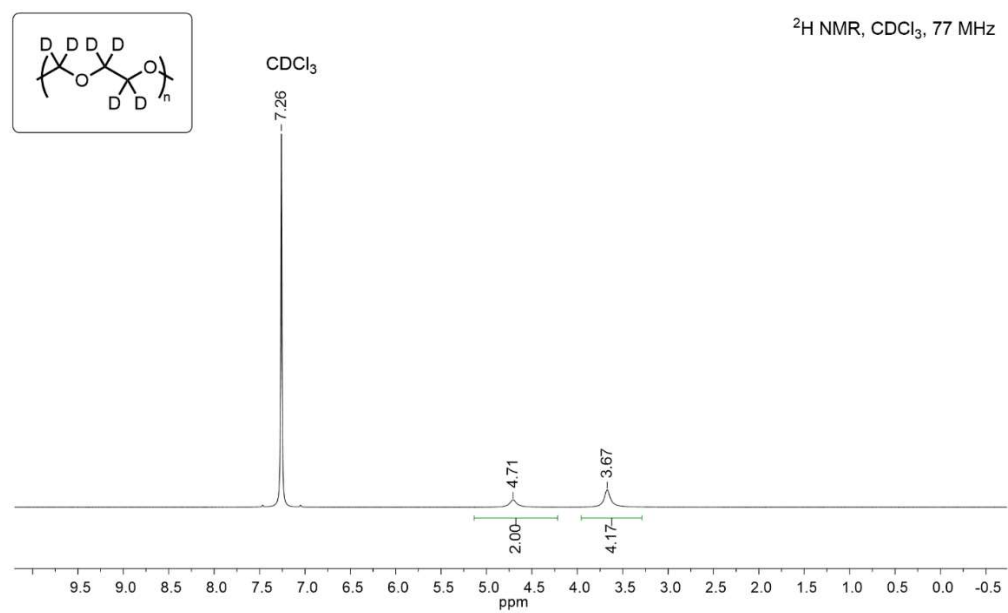


Figure 7.11. ¹H NMR spectrum of *d*P(EO-MO).

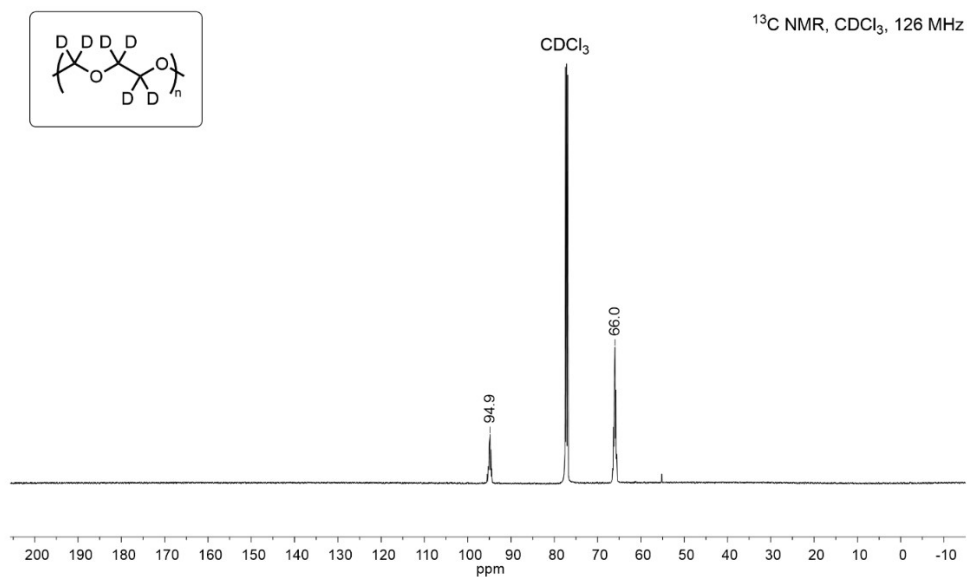


Figure 7.12. ¹³C NMR spectrum of $\underline{d}P(\text{EO-MO})$.

7.6.5 Additional SANS Data

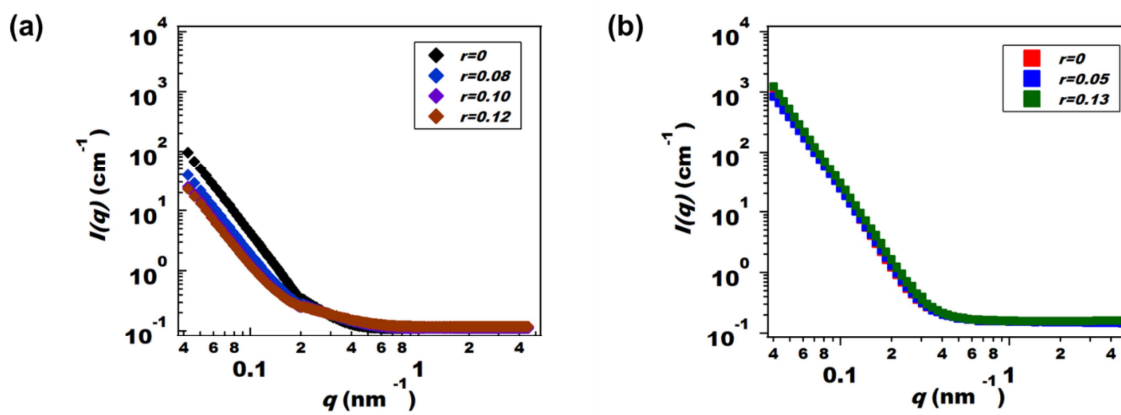


Figure 7.13. Absolute SANS scattering intensity of deuterated homopolymers ($I(q)$) of (a) dPEO/LiTFSI and (b) dP(EO-MO)/LiTFSI as a function of scattering vector (q) at different salt concentration (r) and at 90 °C.

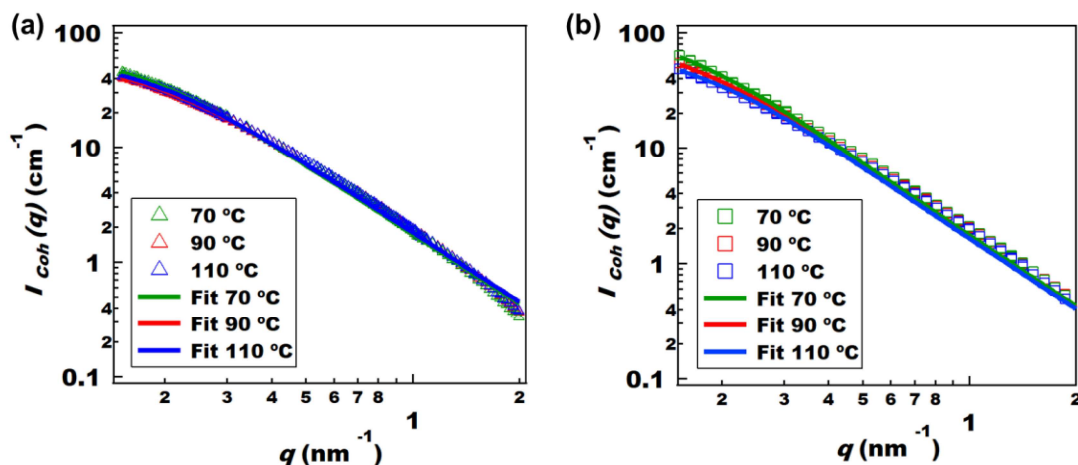


Figure 7.14. Coherent SANS scattering intensity of salt free polymer blends ($I_{coh}(q)$) of (a) dPEO/P(EO-MO) and (b) dP(EO-MO)/P(2EO-MO) as a function of scattering vector (q) at different temperature (open symbols), and corresponding RPA fits (solid curves). In both cases, $I_{coh}(q)$ is a weak function of temperature.

7.7 Nomenclature

Table 7.4. List of symbols and abbreviations.

Symbol	Meaning
PEO	Poly(ethylene oxide)
P(2EO-MO)	Poly(1,3,6-trioxocane)
P(EO-MO)	Poly(1,3-dioxolane)
LiTFSI	Lithium bis(trifluoromethanesulfonyl)imide
SANS	Small angle neutron scattering
DSC	Differential scanning calorimetry
2EO-MO	1,3,6-trioxocane
EO-MO	1,3-dioxolane
M_n	Number average molar mass
\bar{D}	Dispersity
dPEO	Deuterated PEO
dP(EO-MO)	Deuterated P(EO-MO)
ϕ_i	Volume fraction of component i
ϕ_{polymer}	Volume fraction of polymer components
w_i	Weight of component i
w_{salt}	Weight of LiTFSI salt
ρ_i	Density of component i
ρ_{salt}	Density of LiTFSI salt
r	Molar ratio of lithium ions in the salt to oxygen atoms in the polymers
M'_i	Monomer molar mass of i
M'_{salt}	Molar mass of LiTFSI salt
f	Volume fraction of PEO and LiTFSI associated with PEO
T_g	Glass transition temperature
SDD	Sample-to-detector distance

θ	Scattering angle
q	Magnitude of the scattering vector
λ	Wavelength
$I(q)$	Measured absolute SANS intensity
ΔG_m	Free energy of mixing per unit volume
k_B	Boltzmann constant
v	Reference volume (0.1 nm ³)
T	Absolute temperature
N_i	Number of repeat units per chain
χ	Flory-Huggins interaction parameter
χ_{crit}	Critical Flory-Huggins interaction parameter
χ_{eff}	Effective Flory-Huggins interaction parameter
$I_{coh}(q)$	Coherent scattering intensity
$I_{duterated\ polymer/LiTFSI}(q)$	SANS intensity from dPEO/LiTFSI mixtures (cm ⁻¹)
$I_{inc}(q)$	Incoherent scattering intensity
$P_i(q)$	Form factor
B_i	Neutron scattering length density of component i
b_i	Neutron scattering length of component i
v_i	Monomer molar volume of component i
S_{ii}	Structure factor
M_i	Molar mass of component i
$R_{g,i}$	Radius of gyration
l_i	Statistical segment length of component i
RPA	Random phase approximation
α	RPA fitting parameter accounting for chain distortion
A, B	Empirical constants for fitting Flory-Huggins interaction parameters
R^2	Coefficient of determination
κ	Ionic conductivity
D	Salt diffusion coefficient
ρ_+	Current fraction
$\kappa\rho_+$	Efficacy
PCL	Polycaprolactone
PPC	Polypropylene carbonate
PVP	Polyvinylpyrrolidone

8 Increased Donnan Exclusion in Charged Polymer Networks at High Salt Concentrations[†]

Abstract

The swelling of univalent and multivalent charged polymeric networks in electrolytic solutions is studied using a classical thermodynamic model. Such systems were first modeled by Donnan, who derived an expression for the chemical potential of the ions by introducing an electric potential that is commonly referred to as the Donnan potential. This well-established theory leads to a simple quadratic relationship for the partitioning of ions between the network and the external solution. When the concentration of fixed charges in the swollen gel is large enough, the electrolyte in the external solution is “excluded” from the gel (commonly referred to as Donnan exclusion). In the standard Donnan theory, and in virtually all subsequent theories, the magnitude of Donnan exclusion decreases with increasing electrolyte concentration in the external solution. Our model predicts this is not necessarily true; we show that the magnitude of Donnan exclusion increases with increasing electrolyte concentration over a broad range of parameter space (average chain length between crosslinks, fraction of charged monomers in the network, the nature of the interactions between the ions, solvent molecules and polymer chains, and ion concentration in the external solution). We also present explicit bounds for the validity of Donnan’s original theory. Model predictions are compared to simulations and experimental data obtained for a cationic gel immersed in electrolytic solutions of salts containing univalent and bivalent cations.

8.1 Introduction

The partitioning of ionic species between a solution and a charged polymeric network is usually described by the term Donnan equilibrium.^{225–227} This phenomenon, originally introduced in the context of physiology,^{228–232} is important in several technological contexts^{233,234} such as desalination and ion exchange resins. In the biological context, partitioning of ionic species into charged polymeric phases is important for the functioning of the lining of organs like the stomach and the colon^{228–230} and assemblies of charged biomolecules such as proteins and RNA.^{231,232}

The system of interest is illustrated in Figure 8.1. A charged gel with polymer strands comprising N repeat units between crosslinks is swollen in an ionic solution. The solution could contain an acid, a base, or a salt – we refer to this species as the electrolyte. For concreteness, we assume that the polymer has a fraction f of polymer repeat units that are negatively charged. We use volume fractions to describe the concentration of species (ions, polymer, and solvent). The standard result for partitioning of the electrolyte between the gel and solvent phases is:

$$\frac{\phi_-}{\phi^e} = -\frac{1}{2} \frac{\phi_{-,b}}{\phi^e} + \frac{1}{2} \sqrt{\left(\frac{\phi_{-,b}}{\phi^e}\right)^2 + 4} \quad (8.1)$$

[†] This chapter was reported in *Solid State Ionics*, **2022**, 18 (2), 282-292.

where ϕ_- and ϕ_-^e are the volume fractions of the free negative ions in the gel and external solution, respectively.²²⁵ The volume fraction of the negative ions covalently bound to the polymer strands in the gel phase is $\phi_{-,b}$. Donnan exclusion refers to the regime wherein the ratio ϕ_-/ϕ_-^e is small, *i.e.*, the free ions are excluded from the gel. The use of concentration ratios in equation 1 minimizes the effect of the variable used to quantify ion concentrations. Molar concentrations are often used to describe Donnan equilibrium. In contrast, volume fractions are usually used in polymer physics; the molar concentration of polymer in the gel phase in Figure 8.1 is neither meaningful nor useful. We have thus chosen to use volume fractions in our analysis.

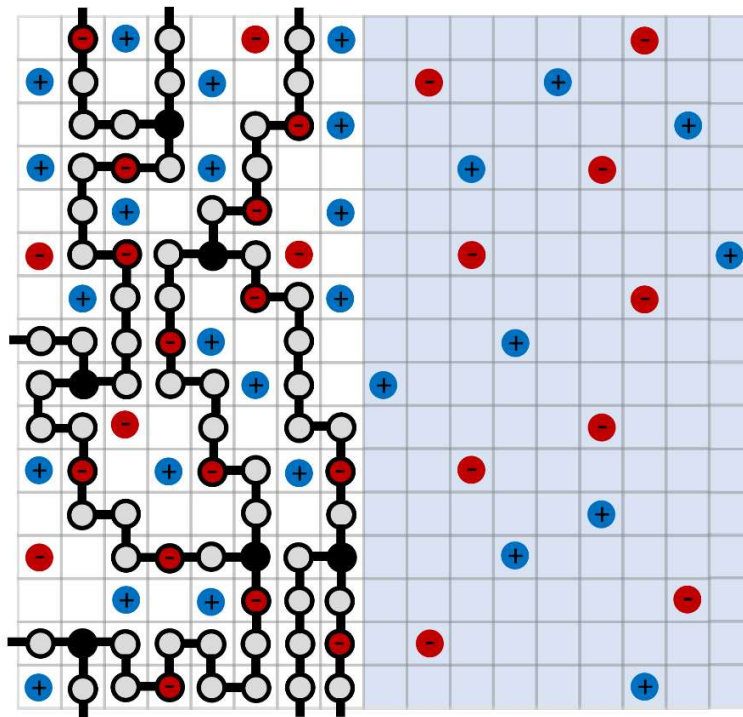


Figure 8.1. Schematic of a crosslinked polymer phase with negative charges covalently bound to the polymer chains in contact with a reservoir containing an electrolytic solution. Black circles represent crosslinks. The empty lattice sites are filled with solvent; solvent molecules are not shown explicitly for clarity. Some of the solvent molecules and ions in the electrolytic solution (shaded for clarity) enter the polymeric phase. The gel shown has $N = 9$ and $f = 2/9 = 0.22$.

Equation 8.1 predicts that ϕ_-/ϕ_-^e increases monotonically and smoothly approaches unity as the ion concentration in the external solution increases, *i.e.*, there is less Donnan exclusion with increasing external ion concentration. In previous theories on this subject,^{235–238} separate thermodynamic models such as the Flory-Rehner theory²³⁹ are used to determine $\phi_{-,b}$; equation 8.1 is assumed to apply regardless of the nature of ion-polymer interactions, solvent-polymer interactions, and the extent of crosslinking. Equation 8.1 is frequently used to describe swelling and ion partitioning in heterogeneous ionic polymers comprising solvophilic and solvophobic domains, wherein swelling due to uptake of solvent anions occurs exclusively in the solvophilic domains; the solvent is frequently water.

In Figure 8.2, we show swelling data obtained from a block copolymer containing charged polystyrenesulfonyllithium(trifluoromethylsulfonyl)imide (PSLiTFSI) chains equilibrated in an electrolytic mixture of ethylene carbonate (EC), dimethyl carbonate (DMC), and lithium bis(trifluoromethanesulfonyl)imide (LiTFSI) salt. The PSLiTFSI-*block*-polyethylene-*block*-PSLiTFSI (or PSLiTFSI-*b*-PE-*b*-PSLiTFSI) block copolymer was synthesized and characterized a recently submitted paper.²⁴⁰ In Figure 8.2a, we show that total swelling, as quantified by the dependence of $\phi_{p,total}$, is a monotonic function of ϕ_-^e . In Figure 8.2b, we show the partitioning of the TFSI⁻ anions in the solvophilic domains in the block copolymer as a function of the TFSI⁻ anion volume fraction in the external solution. The noteworthy observation is that ϕ_-/ϕ_-^e does not increase monotonically and smoothly approach unity as the concentration of the external electrolyte solution is increased. In fact, ϕ_-/ϕ_-^e decreases slightly when ϕ_-^e is increased from 0.07 to 0.18.

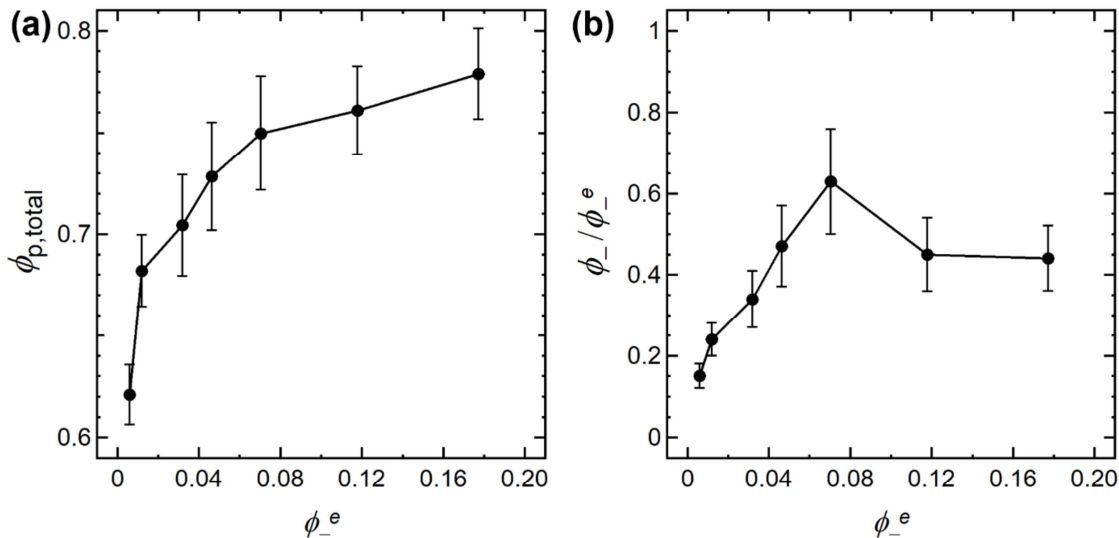


Figure 8.2. Experimental data for the swelling and salt partitioning between a PSLiTFSI-*b*-PE-*b*-PSLiTFSI triblock copolymer membrane and external solutions of LiTFSI in an EC/DMC mixture. (a) Swelling of the block copolymer, quantified by the total polymer volume fraction, $\phi_{p,total}$, as a function of the TFSI⁻ anion volume fraction in the external solution, ϕ_-^e . (b) Dependence of the ratio of volume fraction of anions in the membrane to that in the external EC/DMC solution, ϕ_-/ϕ_-^e , on ϕ_-^e . Swelling is a monotonic function of ϕ_-^e but salt partitioning is not. Donnan exclusion increases with increasing salt concentration in the external solution in the $\phi_-^e > 0.07$ regime.

The question of what thermodynamic forces underly this behavior is difficult to address due to the complex interplay between morphology, chain deformation, and osmotic effects. As a first step toward answering this question, we sought to answer a much simpler question: what are the necessary ingredients for obtaining results that are qualitatively similar to the results shown in Figure 8.2. To answer this question, we present a simple model for the gel shown in Figure 8.1 based on Flory-Huggins theory^{176,177,241} where the stretching of an ideal polymer network as quantified by the Flory-Rehner theory,²³⁹ is incorporated directly into the framework originally

developed by Donnan. Our approach is similar in spirit to those developed in ref ²⁴² and ²⁴³ but differ significantly from approaches in many other recent theories^{244,245} that use equation 8.1 as the primary governing equation. Consequently, regimes where the equilibrium properties of the gel deviate substantially from equation 8.1 are identified. We develop expressions that are applicable to symmetric (*e.g.*, MgSO₄) and asymmetric electrolytes (*e.g.*, MgCl₂).

8.2 Theory

We propose the following expression for the total Gibbs free energy change of mixing of the gel phase comprising the crosslinked polymer, electrolyte, and solvent molecules as shown in Figure 8.1 using the Flory-Huggins and Flory-Rehner theories:

$$\frac{\Delta G_m}{kT} = n \left[\frac{n_s}{n} \ln(\phi_s) + \frac{n_+}{n} \ln(\phi_+) + \frac{n_-}{n} \ln(\phi_-) + \chi \frac{n_p}{n} (1 - \phi_p) \right] + \frac{3n_p}{2N} \left(\phi_p^{-\frac{2}{3}} - 1 \right) \quad (8.2)$$

where n_i is the number of lattice sites occupied by each component, n is the total number of lattice sites, ϕ_i is the volume fraction of component i ($\phi_i = n_i/n$), and N is the number of polymer repeat units in each crosslinked strand.^{176,177,239,241} The subscripts s , $+$ and $-$ stand for solvent, free cations, and free (unbound) anions in the gel, respectively. A fraction of the polymer repeat units f is negatively charged. Our model does not account for effects such as counterion condensation.^{246,247} The first three terms on the right side of equation 8.2 represent entropic contributions and the fourth term represents the enthalpic contribution. χ is a lumped Flory-Huggins interaction parameter that quantifies the internal energy change of mixing between the polymer and all other species in the systems. This interaction parameter can be related to the individual interaction parameters between the constituents (see Equation 8.32 in the SI). The internal energy change of mixing solvent and electrolyte is ignored for simplicity. One can readily extend this approach to include separate parameters for the interaction between the solvent and polymer, the ions and polymer, and the ions and solvent. However, methods to evaluate multiple interaction parameters from typical experimental data have not yet been developed, and we thus present results as a function of a single χ parameter. The standard states are the pure components in the amorphous state; because pure ionic solids are often crystalline, the standard state may be hypothetical. The last term on the right side of equation 8.2 represents the deformation free energy of an ideal polymer network.^{238,239} Following the Donnan approach, the expression for the free energy does not account for the charged nature of the phases of interest; both phases are, of course, electrically neutral.

The chemical potential of the species is given by:

$$\Delta\mu_i = \left(\frac{\partial \Delta G_m}{\partial m_i} \right)_{m_j, j \neq i} \quad (8.3)$$

where m_i are the moles of species i ; $m_i = n_i/N_{AV}$, and N_{AV} is Avogadro's number. Using equations 8.2 and 8.3, we get expressions for the chemical potential of the solvent and the ions in the gel:

$$\frac{\Delta\mu_s}{RT} = \ln(\phi_s) + \phi_p + \chi\phi_p^2 + \frac{\phi_p^{\frac{1}{3}}}{N}, \quad (8.4)$$

$$\frac{\Delta\mu_+}{RT} = \ln(\phi_+) + \phi_p + \chi\phi_p^2 + \frac{\phi_p^{\frac{1}{3}}}{N}, \quad (8.5)$$

$$\frac{\Delta\mu_-}{RT} = \ln(\phi_-) + \phi_p + \chi\phi_p^2 + \frac{\phi_p^{\frac{1}{3}}}{N}. \quad (8.6)$$

Assuming that the solution in equilibrium with the gel is ideal, we obtain:

$$\frac{\Delta\mu_s^e}{RT} = \ln(\phi_s^e), \quad (8.7)$$

$$\frac{\Delta\mu_+^e}{RT} = \ln(\phi_+^e), \quad (8.8)$$

$$\frac{\Delta\mu_-^e}{RT} = \ln(\phi_-^e), \quad (8.9)$$

where the superscript e stands for the external solution. Relaxing this assumption requires knowledge of activity coefficients, which are tabulated for many electrolytic solutions³⁸ but not for charged gels.

Equating the chemical potentials of the solvent in the two phases, we obtain:

$$\ln(\phi_s^e) = \ln(\phi_s) + \phi_p + \chi\phi_p^2 + \frac{\phi_p^{\frac{1}{3}}}{N}. \quad (8.10)$$

The same approach cannot be used for the ions as the chemical potential of charged species depends on the electric field. This effect is accounted for by defining a potential U , and postulating an additive contribution to the chemical potentials of the ions as proposed by Donnan:

$$\ln(\phi_+^e) = \ln(\phi_+) + \phi_p + \chi\phi_p^2 + \frac{\phi_p^{\frac{1}{3}}}{N} + \frac{z_+FU}{RT} \quad (8.11)$$

and

$$\ln(\phi_-^e) = \ln(\phi_-) + \phi_p + \chi\phi_p^2 + \frac{\phi_p^{\frac{1}{3}}}{N} + \frac{z_-FU}{RT}, \quad (8.12)$$

where the charges numbers on the positive and negative ions are z_+ and z_- .²²⁵ The charge numbers of the free and bound negative ions are assumed to be the same. The Donnan potential, which now contains elastic contributions, and can be thought of as a quasi-electrostatic potential as defined by Newman,³⁸ is introduced for computational purposes only. It cannot be measured; because the gel and solution phases in Figure 8.1 are at equilibrium, the electric potential difference between them measured with a suitable reference electrode is zero.^{38,248}

Charge neutrality of the external solution implies:

$$\phi_+^e = \frac{-z_- \phi_-^e}{z_+} \quad (8.13)$$

Charge neutrality of the gel phase implies:

$$\phi_+ = \frac{-z_-}{z_+} (f\phi_p + \phi_-) \quad (8.14)$$

and

$$\phi_s = 1 - \left(1 - \frac{z_-}{z_+} f\right) \phi_p - \left(1 - \frac{z_-}{z_+}\right) \phi_- . \quad (8.15)$$

Eliminating U from equations 8.11 and 8.12 gives:

$$\ln \left((\phi_-^e)^{\left(\frac{1}{z_+} - \frac{1}{z_-}\right)} \left(\frac{-z_-}{z_+}\right)^{\frac{1}{z_+}} \right) = \ln \left((\phi_-^e)^{\frac{1}{z_+}} (\phi_+^e)^{\frac{1}{-z_-}} \right) + \left(\frac{1}{z_+} - \frac{1}{z_-}\right) \left(\phi_p + \chi\phi_p^2 + \frac{\phi_p^3}{N} \right) \quad (8.16)$$

which can be rewritten using equation 8.14 as:

$$\ln \left((\phi_-^e)^{\left(\frac{1}{z_+} - \frac{1}{z_-}\right)} \left(\frac{-z_-}{z_+}\right)^{\frac{1}{z_+}} \right) = \ln \left(\left(\frac{-z_-}{z_+} (f\phi_p + \phi_-)\right)^{\frac{1}{z_+}} (\phi_-)^{\frac{1}{-z_-}} \right) + \left(\frac{1}{z_+} - \frac{1}{z_-}\right) \left(\phi_p + \chi\phi_p^2 + \frac{\phi_p^3}{N} \right) . \quad (8.17)$$

Equations 8.10 and 8.15 can be combined to give:

$$\ln \left(1 - \phi_-^e \left(1 - \frac{z_-}{z_+}\right) \right) = \ln \left(1 - \left(1 - \frac{z_-}{z_+} f\right) \phi_p - \left(1 - \frac{z_-}{z_+}\right) \phi_- \right) + \phi_p + \chi\phi_p^2 + \frac{\phi_p^3}{N} . \quad (8.18)$$

Equations 8.17 and 8.18 are the main results of our theory. Equation 8.17 arises due to equilibration of the free ions in the gel and the external solution while equation 8.18 arises from equilibration of the solvent between the two phases. For an electrolytic solution with a given value of ϕ_-^e , equations 8.17 and 8.18 can be solved simultaneously to determine the ion concentration in the gel, ϕ_- , and the extent of swelling quantified by ϕ_p , provided χ, f , and N are known. The Donnan potential may then be calculated using the following expression, which is based on equation 8.12:

$$U = \frac{RT}{z_- F} \left(\ln(\phi_-^e) - \ln(\phi_-) - \phi_p - \chi\phi_p^2 - \frac{\phi_p^3}{N} \right) . \quad (8.19)$$

For the case when both ϕ_p and ϕ_- are small, the logarithmic terms in the ionic equilibrium condition dominate, and equation 8.17 reduces to an algebraic equation,

$$\left(\frac{\phi_-}{\phi_-^e}\right)^{\left(\frac{1}{z_+} - \frac{1}{z_-}\right)} \left(\frac{f\phi_p}{\phi_-} + 1\right)^{\frac{1}{z_+}} - 1 = 0 \quad (8.20)$$

that can be solved for ϕ_- if f , ϕ_p and ϕ_-^e are known. Equation 8.20 is consistent with the treatment of multivalent Donnan equilibrium in ref. ²³⁵.

If $z_+ = -z_-$, equations 8.17, 8.18, and 8.20 reduce to:

$$\ln(\phi_-^e) = \frac{1}{2} \ln\left((f\phi_p + \phi_-)\phi_-\right) + \phi_p + \chi\phi_p^2 + \frac{\phi_p^3}{N} \quad (8.21)$$

and

$$\ln(1 - 2\phi_-^e) = \ln\left(1 - (1 + f)\phi_p - 2\phi_-\right) + \phi_p + \chi\phi_p^2 + \frac{\phi_p^3}{N}, \quad (8.22)$$

and if both ϕ_p and ϕ_- are small, the logarithmic terms in the ionic equilibrium condition dominate, and equation 8.20 reduces to:

$$\frac{\phi_-}{\phi_-^e} = -\frac{1}{2} \frac{f\phi_p}{\phi_-^e} + \frac{1}{2} \sqrt{\left(\frac{f\phi_p}{\phi_-^e}\right)^2 + 4} = \frac{2}{\frac{f\phi_p}{\phi_-^e} + \sqrt{\left(\frac{f\phi_p}{\phi_-^e}\right)^2 + 4}} \quad (8.23)$$

Equation 8.23 is identical to equation 8.1 because the bound ion concentration $\phi_{-,b}$ is equal to $f\phi_p$. The second form of equation 8.23 avoids problems associated with subtracting two large numbers to obtain a small positive number, as is the case when the external solution becomes increasingly dilute.

8.3 Results and Discussion

The solution to equations 8.21 and 8.22 for $\chi = 1$ (the solvent and ions are poor solvents for the polymer) and $N = 10$ (a tightly crosslinked network) is shown in Figure 8.3, where ϕ_p and ϕ_- are plotted as a function of ϕ_-^e for a range of f values between 0.1 and 0.9. In Figure 8.3a, we see that gel swelling decreases (*i.e.*, ϕ_p increases) as ϕ_-^e increases. This is expected as interactions between the ions and polymer are unfavorable. Increasing the charge on the polymer, f , increases swelling at fixed ϕ_-^e due to the expected increase of free ions inside the gel. In Figure 8.4b, we see that the ratio ϕ_-/ϕ_-^e , which provides a measure of Donnan exclusion (low values of ϕ_-/ϕ_-^e indicate a greater extent of Donnan exclusion), increases monotonically with increasing ϕ_-^e , reaching a plateau that is a function of f . Increasing f results in decreased exclusion at fixed ϕ_-^e . One might have expected that increasing the charge on the polymer would lead to increased exclusion but the interplay between swelling and ionic interactions leads to the opposite conclusion.

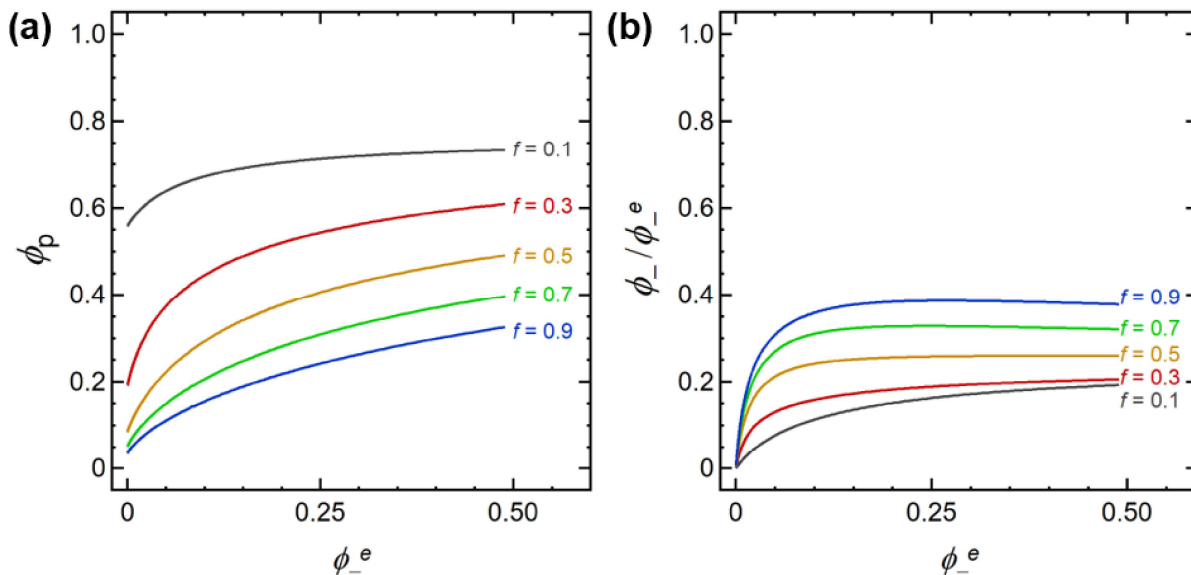


Figure 8.3. Polymer volume fraction in the gel phase and ion exclusion dependence on volume fraction of anions in the external solution for $z_+ = -z_-$, $N = 10$, and $\chi = 1$, various f . (a) Dependence of the polymer volume fraction in the gel phase, ϕ_p , on the volume fraction of anions in the external solution, ϕ_-^e . (b) Exclusion of ions in the gel: dependence of the ratio of volume fraction of anions in the gel to that in the external solution, ϕ_-/ϕ_-^e , on ϕ_-^e . Curves are shown for selected values of the fraction of charged monomers on the polymer strands, f . Parameters held fixed: $z_+ = -z_-$, $N = 10$, and $\chi = 1$.

Figure 8.4 shows results for $\chi = 1$ and $N = 50$ using the same format as Figure 8.3. The dependence of ϕ_p on ϕ_-^e is similar to that shown in Figure 8.3a: swelling reduces as ϕ_-^e increases. The dependence of ϕ_-/ϕ_-^e on ϕ_-^e is, however, non-monotonic for most of the values of f examined. Monotonic behavior is seen only at $f = 0.1$. For $f = 0.3$, for example, ϕ_-/ϕ_-^e increases with increasing ϕ_-^e in the dilute limit, reaches a maximum value of 0.373 at $\phi_-^e = 0.023$, before leveling off at 0.288 in the concentrated limit. The value of ϕ_-^e at the peak increases and the ϕ_-/ϕ_-^e peak broadens as f increases. Figure 8.5 shows results for $\chi = 1$ and $N = 200$. These results are qualitatively similar to Figure 8.4, except for the more pronounced maxima in the ϕ_-/ϕ_-^e versus ϕ_-^e curves. At $f = 0.1$, the maximum in ϕ_-/ϕ_-^e is followed by a shallow minimum before leveling off.

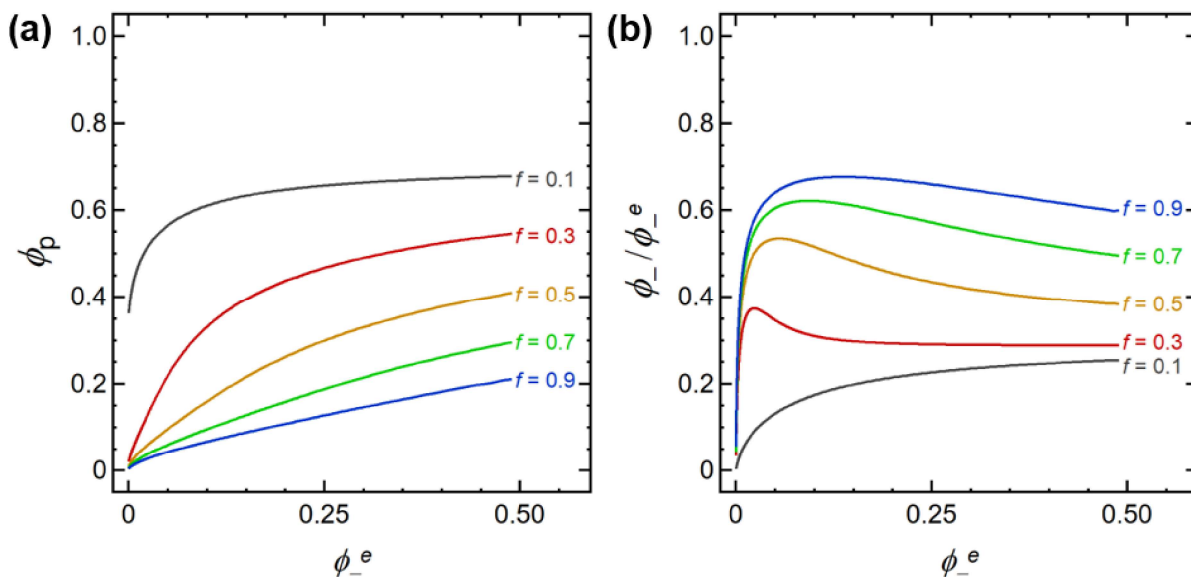


Figure 8.4. Polymer volume fraction in the gel phase and ion exclusion dependence on volume fraction of anions in the external solution for $z_+ = -z_-$, $N = 50$, and $\chi = 1$, various f . (a) Dependence of the polymer volume fraction in the gel phase, ϕ_p , on the volume fraction of anions in the external solution, ϕ_e^- . (b) Exclusion of ions in the gel: dependence of the ratio of volume fraction of anions in the gel to that in the external solution, ϕ_-/ϕ_e^- , on ϕ_e^- . Curves are shown for selected values of the fraction of charged monomers on the polymer strands, f . Parameters held fixed: $z_+ = -z_-$, $N = 50$, and $\chi = 1$.

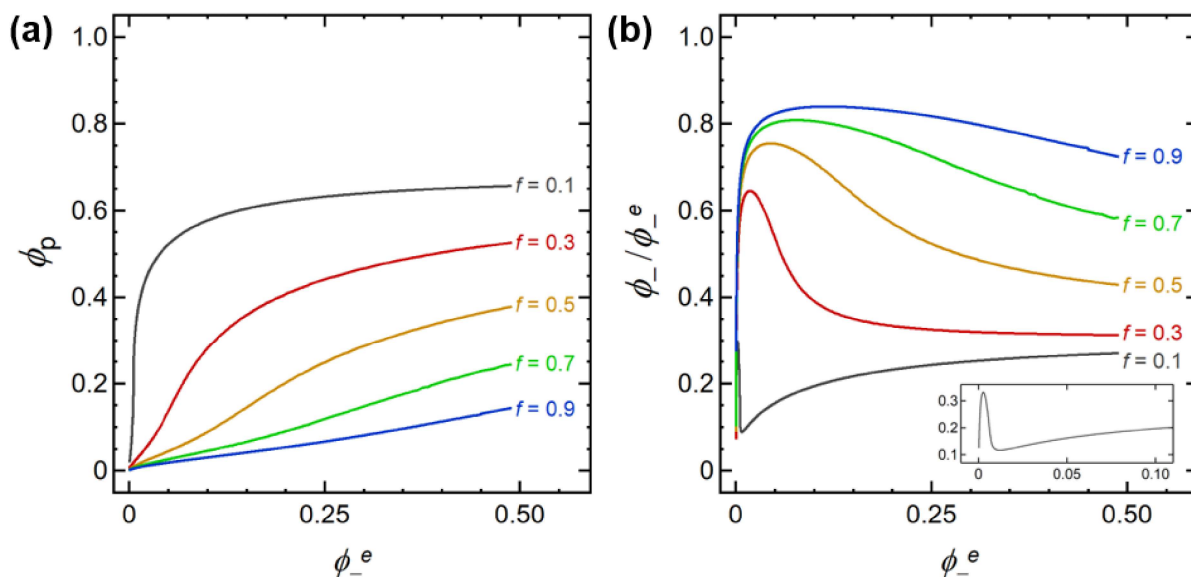


Figure 8.5. Polymer volume fraction in the gel phase and ion exclusion dependence on volume fraction of anions in the external solution for $z_+ = -z_-$, $N = 200$, and $\chi = 1$, various f . (a) Dependence of the polymer volume fraction in the gel phase, ϕ_p , on the volume fraction of anions in the external solution, ϕ_e^- . (b) Exclusion of ions in the gel: dependence of the ratio of volume fraction of anions in the gel to that in the

external solution, ϕ_-/ϕ_-^e , on ϕ_-^e . Curves are shown for selected values of the fraction of charged monomers on the polymer strands, f . Parameters held fixed: $z_+ = -z_-$, $N = 200$, and $\chi = 1$. Inset shows $f = 0.1$ curve on an expanded scale for clarity.

Figure 8.6 shows the effect of changing χ on Donnan equilibrium at fixed values of $f = 0.3$ and $N = 50$. As seen in Figure 8.6a, the gels swell to greater extents as χ decreases from 1.5 to -1. At $\chi = -1$, the plateau value of ϕ_p is only 0.0728. The dependence of ϕ_-/ϕ_-^e on ϕ_-^e is monotonic only when $\chi \leq 0.5$. $\chi = 0.5$ represents the “theta condition” in polymer/solvent mixtures; this value of χ represents the border between favorable and unfavorable interactions between polymer segments and diluents. Significant Donnan exclusion at high concentrations is only seen when χ is greater than 0.5, as shown in Figure 8.6b. The non-monotonic dependence of ion exclusion in the gel arises from the competition between electrical effects which dominate at low values of ϕ_-^e , and thermodynamic interactions that are lumped into the χ parameter which dominate at high values of ϕ_-^e .

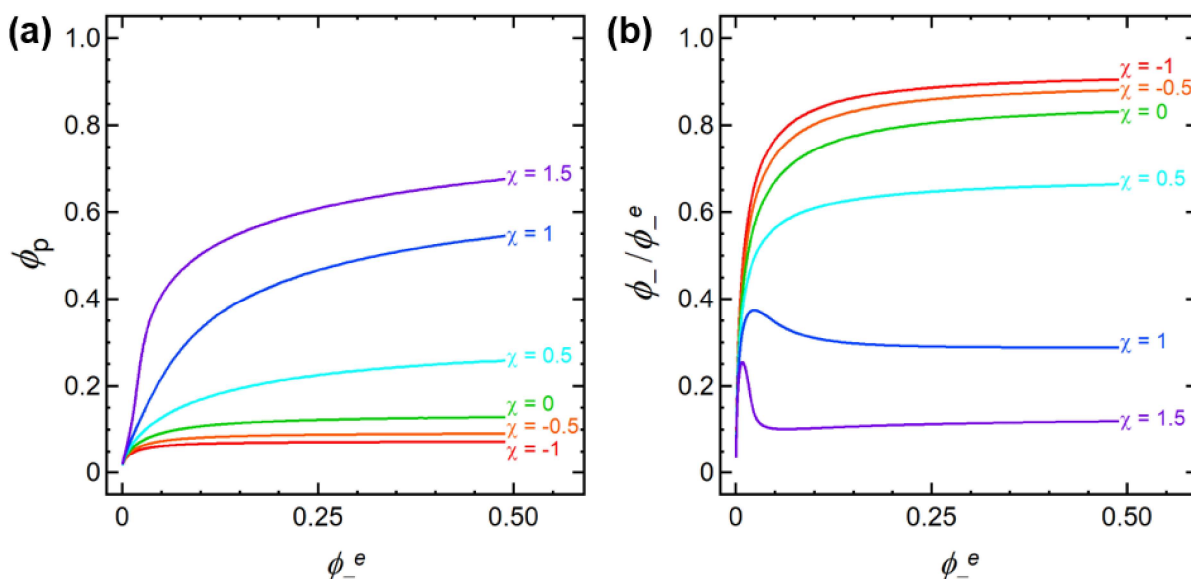


Figure 8.6. Polymer volume fraction in the gel phase and ion exclusion dependence on volume fraction of anions in the external solution for $z_+ = -z_-$, $N = 200$, and $f = 0.3$, various χ .

(a) Dependence of the polymer volume fraction in the gel phase, ϕ_p , on the volume fraction of anions in the external solution, ϕ_-^e . (b) Exclusion of ions in the gel: dependence of the ratio of volume fraction of anions in the gel to that in the external solution, ϕ_-/ϕ_-^e , on ϕ_-^e . Curves are shown for selected values of χ . Parameters held fixed: $z_+ = -z_-$, $N = 50$ and $f = 0.3$.

Figure 8.7a shows the effect of changing the charge on the ionic species at fixed f , N , and χ . In all cases, gel swelling decreases as ϕ_-^e increases. Increasing the charge on the bound and free negative ions (setting $z_- = -2$ but keeping $z_+ = +1$) results in increased swelling. This is expected because

more positive ions are necessary in the gel to enforce charge neutrality. On the other hand, increasing the charge on the free positively charged ions (setting $z_+ = +2$ but keeping $z_- = -1$) results in decreased swelling, as expected. The extent of Donnan exclusion is non-monotonic in all cases, as shown in Figure 9.8b. The peak is less pronounced in the $z_+ = +2$ case compared to the $z_- = -2$ case. In the $z_+ = +2$ case, the maximum is followed by a shallow minimum, before ϕ_-/ϕ_-^e approaches a plateau. Regardless of the nature of the charged species, the plateau value of ϕ_-/ϕ_-^e is in the vicinity of 0.3.

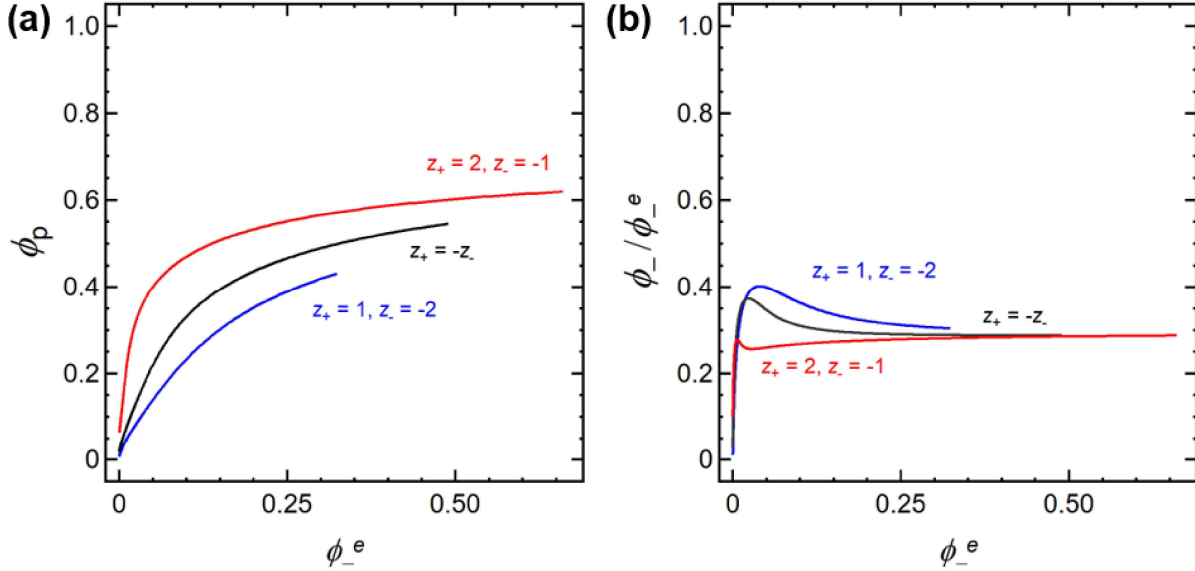


Figure 8.7. Polymer volume fraction in the gel phase and ion exclusion dependence on volume fraction of anions in the external solution for $\chi = 1$, $N = 200$, and $f = 0.3$, various $z_+ = -z_-$. (a) Dependence of the polymer volume fraction in the gel phase, ϕ_p , on the volume fraction of anions in the external solution, ϕ_-^e . (b) Exclusion of ions in the gel: dependence of the ratio of volume fraction of anions in the gel to that in the external solution, ϕ_-/ϕ_-^e , on ϕ_-^e . Curves are shown for selected values of the charge numbers, z_+ and z_- . Parameters held fixed: $N = 50$, $\chi = 1$, and $f = 0.3$.

In Figure 8.8, we show the results of our calculations on a plot of ϕ_-/ϕ_-^e versus $\phi_{-,b}/\phi_-^e$ for three values of N , at fixed $f = 0.3$, $\chi = 1$, and $z_+ = z_-$. This format enables comparison of our results with that of Donnan; the dashed curve in Figure 8.8 represents equation 8.23. For $N = 10$, the results are qualitatively similar to the classical Donnan result but ϕ_-/ϕ_-^e is lower at all concentrations. Results for $N = 50$ and 200 obtained at sufficiently large values of $\phi_{-,b}/\phi_-^e$ are more-or-less coincident with the classical Donnan result. In this regime, using equation 8.23 as one of the governing equations is reasonable. The curves obtained for $N = 50$ and 200 at low values of $\phi_{-,b}/\phi_-^e \leq 2$, however, cannot be anticipated from the classical Donnan theory. The range of concentrations over which the classical Donnan result is a valid approximation depends on f , χ , N , and charge numbers. If we assume for concreteness that we are willing to accept an error of 10%, for $N = 200$, $\phi_{-,b}/\phi_-^e$ must be less than 0.74, and for $N = 50$, $\phi_{-,b}/\phi_-^e$ must be less than 3.3 ($f = 0.3$, $\chi = 1$, and $z_+ = z_-$). The range of validity decreases rapidly with increasing N , and at $N = 10$,

there Donnan approximation is not valid over the entire $\phi_{-,b}/\phi_-^e$ range. For concreteness, we also show the dependence of $\phi_{-,b}$ on ϕ_-^e in the SI (see Figures 8.11-8.15).

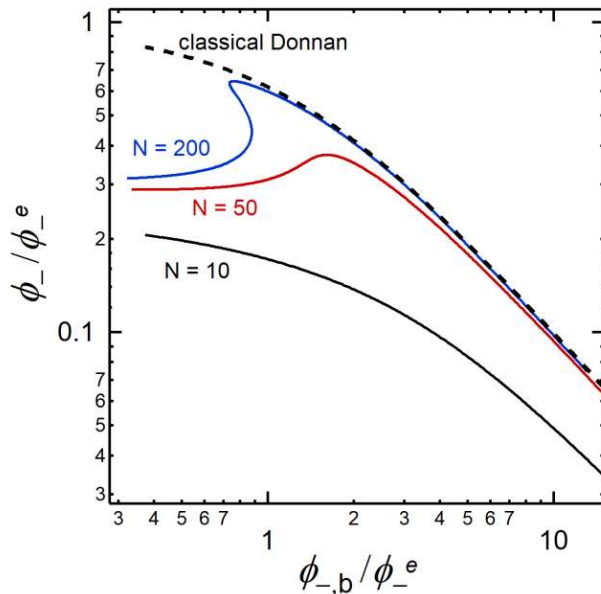


Figure 8.8. Comparing present theory with the classical Donnan prediction. Dependence of the ratio of volume fraction of anions in the gel to that in the external solution, ϕ_-/ϕ_-^e , on the ratio of covalently bound anion volume fraction in the gel to that in the external solution, $\phi_{-,b}/\phi_-^e$. Dashed curve is the classical Donnan prediction, equation 8.23. Curves are shown for selected values of N . Parameters held fixed in the solid curves: $z_+ = -z_-$, $\chi = 1$, and $f = 0.3$. Each curve is a parametric plot wherein ϕ_-^e is varied from 0.007 to 0.49. The dependence of $\phi_{-,b}$ on ϕ_-^e is given in the SI.

Figures 8.5-8.8 demonstrate that Donnan exclusion can increase as the electrolyte concentration in the external solution increases over a broad range of parameter space (average chain length between crosslinks, fraction of charged monomers in the network, the nature of the interactions between the ions, solvent molecules and polymer chains, and ion concentration in the external solution). This conclusion was not evident in previous theoretical and experimental studies,^{242,244,245,249-251} including theories that are similar in spirit to the theory presented here (*e.g.*, ref. ²⁴²). The only example of increasing Donnan exclusion with increasing electrolyte concentration in the external solution is reported in computer simulations of ionic gel swelling, reported in ref. ²⁵².

We use the framework described above to qualitatively understanding the salt partitioning results obtained in swollen the PSLiTFSI-*b*-PE-*b*-PSLiTFSI block copolymer discussed in Figure 8.2. Before we begin a quantitative analysis, it is important note that there are many parameter sets that give results that are qualitatively similar to Figure 8.2; in Figures 8.4 and 8.5 we see many examples where ϕ_p is a monotonically increasing function of ϕ_-^e as is the case in Figure 8.4a, but ϕ_-/ϕ_-^e first increases with increasing ϕ_-^e but ultimately decreases with increasing ϕ_-^e in the high

salt concentration regime. Yet such behavior is seldom reported in the theoretical and experimental literature on Donnan equilibrium.^{235–238,253–257}

The quantitative data set obtained from our experimental system is provided in the SI. The total polymer volume fraction of the gel phase, $\phi_{p,\text{total}}$, was calculated from the following equation:

$$\phi_{p,\text{total}} = \frac{\frac{1}{\rho_p}}{\left(\frac{1}{\rho_p} + \frac{W_e}{\rho_e}\right)}, \quad (8.24)$$

where ρ_p is the density of the PSLiTFSI-*b*-PE-*b*-PSLiTFSI triblock copolymer ($\rho_p = 1.06 \frac{\text{g}}{\text{cm}^3}$), W_e is the external EC/DMC/LiTFSI solution uptake in grams, and ρ_e is the density of the external solution in g cm^{-3} . The polymer volume fraction of the charged PSLiTFSI-rich microphase only, ϕ_p , was estimated using the following equation and neglecting volume changes of mixing:

$$\phi_p = \phi_{p,\text{total}} \left(\frac{\frac{2M_{\text{PSLiTFSI}}}{\rho_{\text{PSLiTFSI}}}}{\frac{M_{\text{PE}}}{\rho_{\text{PE}}} + \frac{2M_{\text{PSLiTFSI}}}{\rho_{\text{PSLiTFSI}}}} \right), \quad (8.25)$$

where M_i and ρ_i are the molecular weight and density of block i in the triblock copolymer respectively ($M_{\text{PSLiTFSI}} = 10 \frac{\text{kg}}{\text{mol}}$, $M_{\text{PE}} = 50 \frac{\text{kg}}{\text{mol}}$; $\rho_{\text{PSLiTFSI}} = 1.57 \frac{\text{g}}{\text{cm}^3}$, $\rho_{\text{PE}} = 0.94 \frac{\text{g}}{\text{cm}^3}$). The external anion volume fraction, ϕ_-^e , was calculated from the following equation:

$$\phi_-^e = \frac{1}{2} \left(\frac{\frac{m\rho_s V_{\text{LiTFSI}}}{1000}}{\frac{m\rho_s V_{\text{LiTFSI}}}{1000} + 1} \right), \quad (8.26)$$

where m is the molality of the external salt solution, ρ_s is the density of the EC/DMC solvent, and V_{LiTFSI} is the molar volume of LiTFSI ($V_{\text{LiTFSI}} = 99 \frac{\text{cm}^3}{\text{mol}}$).²⁵⁸

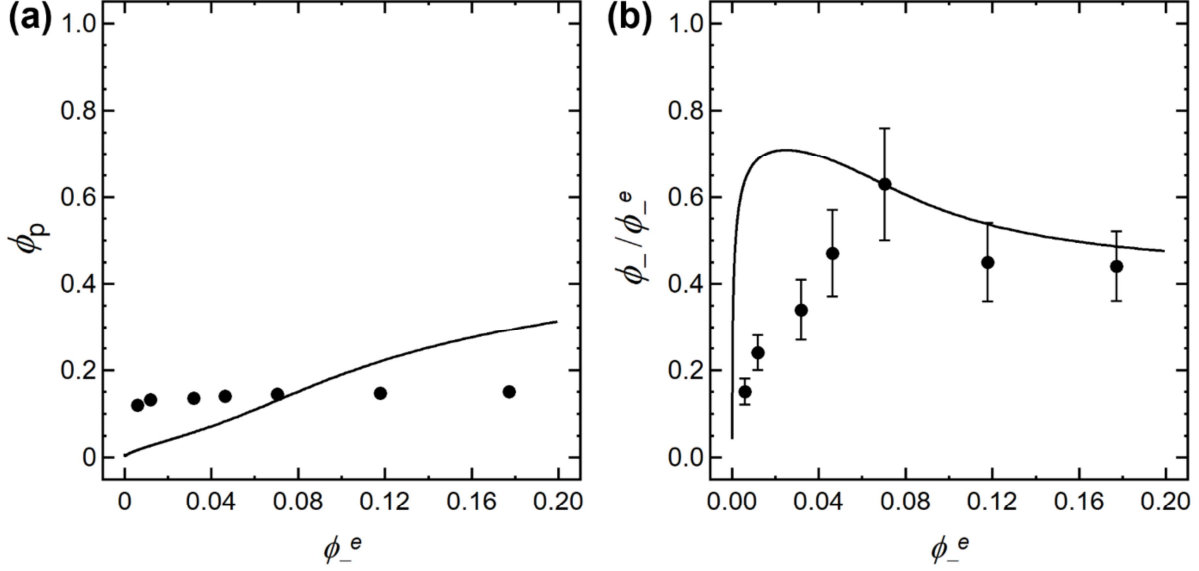


Figure 8.9. Experimental data for the swelling and salt partitioning between a PSLiTFSI-*b*-PE-*b*-PSLiTFSI triblock copolymer membrane and external solutions of LiTFSI in an EC/DMC mixture. (a) Dependence of the polymer volume fraction of the electrolyte-rich microphase, ϕ_p , on the volume fraction of anions in the external solution, ϕ_-^e . (b) Exclusion of ions in the gel: dependence of the ratio of volume fraction of anions in the gel to that in the external solution, ϕ_- / ϕ_-^e , on ϕ_-^e . Curves were calculated using $\chi = 0.85$, $z_+ = -z_-$, $N = 250$ and $f = 0.3$.

In Figure 8.9 we compare the experimental data with theoretical predictions for a particular set of parameters ($\chi = 0.85$, $z_+ = -z_-$, $N = 250$ and $f = 0.3$). It is evident that our simple model is in qualitative agreement with the experimental observations. We do not expect quantitative agreement because our theory does not address microphase separation, among other complexities beyond the scope of this work. These complexities include counterion condensation, non-ideality of mixing that is beyond Flory-Huggins theory, and the fact that the model used to quantify swelling does not account for the presence of charges.

We also compare the predictions of our theory with experimental data on the partitioning of NaCl and MgCl₂ in a negatively charged polymer network taken from the literature.²⁵⁷ In Figure 8.10, we show the dependence of ϕ_p and ϕ_- / ϕ_-^e on ϕ_-^e for the two systems. These parameters were obtained from the data reported in ref.²⁵⁷ using the following relationships:

$$\phi_p = \frac{\frac{1}{\rho_p}}{\left(\frac{1}{\rho_p} + \frac{W_u}{\rho_w} + v_- \frac{C_- W_u V_-}{1000} + v_+ \frac{C_+ W_u V_+}{1000}\right)}, \quad (8.27)$$

$$\phi_- = \frac{v_- \frac{C_- W_u V_-}{1000}}{\left(\frac{1}{\rho_p} + \frac{W_u}{\rho_w} + v_- \frac{C_- W_u V_-}{1000} + v_+ \frac{C_+ W_u V_+}{1000}\right)}, \quad (8.28)$$

$$\phi_-^e = v_- \frac{C_e V_-}{1000}, \quad (8.29)$$

where ρ_p is the density of the dry polymer network ($\rho_p = 1.40 \frac{\text{g}}{\text{cm}^3}$), ρ_w is the density of water ($\rho_w = 1.00 \frac{\text{g}}{\text{cm}^3}$), W_u is the water uptake in grams (Figure 4a in ref. ²⁵⁷), v_- and v_+ are the stoichiometric coefficients of the free anion (Cl^-) and cation (Na^+ or Mg^{2+}) respectively, C_- and C_+ are the concentrations of the free anions and cations in moles per liter in the gel phase (Figures 6-8 in ref. ²⁵⁷), V_- and V_+ are the molar volumes of the anion ($V_- = V_{\text{Cl}^-} = 27.21 \frac{\text{cm}^3}{\text{mol}}$, ref. ²⁵⁹) and cation ($V_+ = V_{\text{Na}^+} = 1.94 \frac{\text{cm}^3}{\text{mol}}$; $V_+ = V_{\text{Mg}^{2+}} = 20.97 \frac{\text{cm}^3}{\text{mol}}$, ref. ²⁵⁹), and C_e is the electrolyte concentration in the external solution in moles per liter (Figures 6-7 in ref. ²⁵⁷). Each term in equations 8.27 and 8.28 represents the volume occupied by one of the constituents in the system: the denominator is the total volume composed of the volumes of polymer, water uptake, anions, and cations, respectively. We assume additive volumes and note that equations 8.27 and 8.28 are derived using 1 gram weight of dry polymer as the basis. There are no widely accepted values for the molar volumes of individual ions; the values reported in ref. ²⁵⁹ that we have used are based on simulations while a different approach based on ion transport parameters is presented in ref. ⁹⁰ (transport parameters for multivalent salts have not yet been determined).

The data in Figure 8.10 are in qualitative agreement with the theory. Both the extent of swelling and Donnan exclusion are lower for MgCl_2 ($z_+ = +2$ and $z_- = -1$) compared to NaCl ($z_+ = -z_-$). The curves through the data in Figure 8.10 represent theoretical predictions with $N = 9$, $f = 0.1$, $\chi = 0.65$ for NaCl and $\chi = 0.52$ for MgCl_2 . Our objective here is not to suggest that the present theory is more accurate than those previously described^{235–238,253–257} in the field; the main point of Figure 8.10 is that the present theory appears to be a reasonable starting point for studying the partitioning of electrolytes into charged gels. More work is needed to study the variety of regimes predicted by our theory.

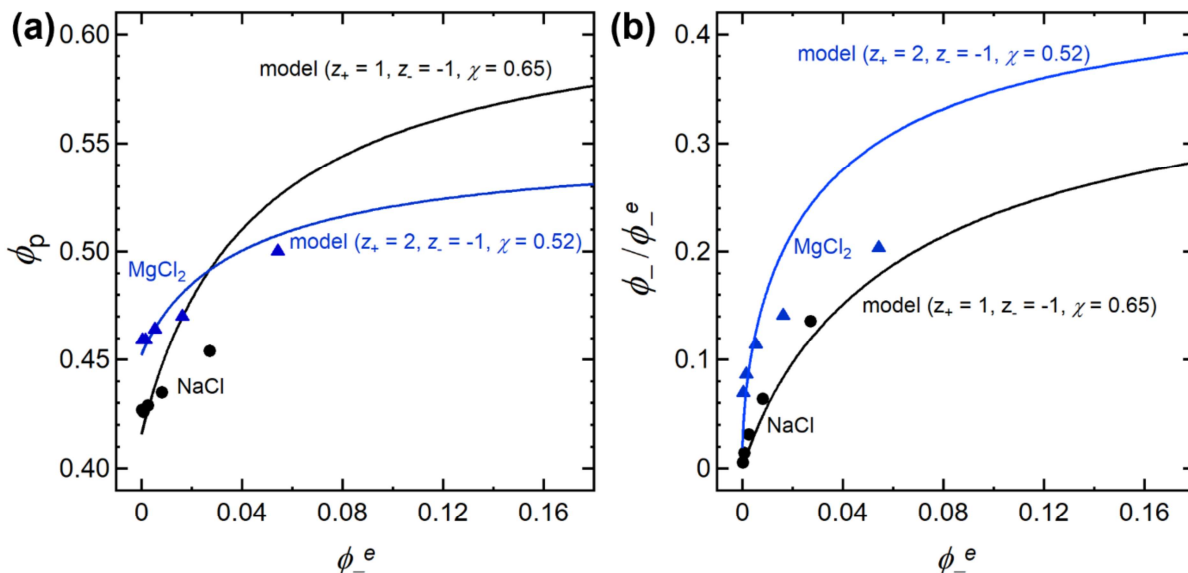


Figure 8.10. Comparing experimental data with theoretical predictions. Data points represent partitioning of NaCl and MgCl₂ from an aqueous solution into an acrylamide-based polymeric gel with sulfonic acid groups. (a) Dependence of the polymer volume fraction in the gel phase, ϕ_p , on the volume fraction of anions in the external solution, ϕ_-^e . (b) Exclusion of ions in the gel: dependence of the ratio of volume fraction of anions in the gel to that in the external solution, ϕ_-/ϕ_-^e , on ϕ_-^e . Curves were calculated using $\chi = 0.65$ and $z_+ = -z_-$ for comparisons with the NaCl data, and $\chi = 0.52$, $z_+ = 2$ and $z_- = -1$ for comparisons with the MgCl₂ data. Parameters held fixed: $N = 9$ and $f = 0.1$.

8.4 Conclusions

We present a new set of equations for describing Donnan equilibrium – the partitioning of ions between a charged gel and an electrolytic solution that accounts for the elasticity of the gel. The original Donnan theory accounts for ion interactions and correctly predicts that when the ion concentration in the external liquid ϕ_-^e is sufficiently low, they are excluded from the gel. Our main accomplishment is to combine Donnan’s original approach with a rudimentary model that accounts for the free energy changes associated with gel swelling. The original quadratic equation is replaced by two coupled algebraic equations that must be solved to self-consistently predict both gel swelling, as quantified by ϕ_p , and Donnan exclusion, as quantified by ϕ_-/ϕ_-^e . Our analysis applies to both univalent and multivalent ions. We present limited comparisons of our predictions with experimental data, noting that substantial work is required to compare experimental data with predictions based on independently determined model parameters (χ , f , and N).

8.5 Acknowledgements

This work was intellectually led by the Joint Center for Energy Storage Research (JCESR), an Energy Innovation Hub funded by the U.S. Department of Energy, Office of Science, Office of Basic Energy Science, under Contract No. DE-AC02-06CH11357, which supported work done by K.W.G. and X.P. under the supervision of N.P.B and R.M.D. K.W.G. acknowledges funding

from a National Defense and Science Engineering Graduate Fellowship. We thank Benny Freeman for stimulating discussions.

8.6 Supporting Information

8.6.1 Materials

(PSLiTFSI)_{10k}-*b*-(PE)_{50k}-*b*-(PSLiTFSI)_{10k} triblock copolymer was used in this study. Cyclooctadiene was first polymerized by ring-opening metathesis polymerization to give a prepolymer with nitroxide end groups. Styrenesulfonyllithium(trifluoromethylsulfonyl)imide monomer was then polymerized at the chain ends using nitroxide-mediated polymerization. In the final step, the unsaturated polymer was hydrogenated using Wilkinson catalyst. End group analysis on ¹H NMR spectrum of the prepolymer and elemental analysis of the final polymer were used to determine the average chain lengths of the blocks. A polydispersity index of 2 was determined via gel permeation chromatography on the prepolymer. More detailed synthetic procedure and characterization details of (PSLiTFSI)_{10k}-*b*-(PE)_{50k}-*b*-(PSLiTFSI)_{10k} were described in ref. ²⁴⁰.

8.6.2 Measurement of Electrolyte Uptake and Salt Partitioning.

The ionic separator was placed in solutions of EC/DMC (50/50 wt%) with varying amounts of LiTFSI. After 24 hours, the separator was removed from solution and all residual solution on the surface was wiped away. The swollen membrane was weighed to determine the uptake mass. The swollen membrane was then placed into 1 gram of EC/DMC (50/50 wt%) solvent. After 24 hours, 500 μL of the extracted solution was mixed with 50 μL of trifluoromethanesulfonamide (CF₃SO₂NH₂) solution in EC/DMC (10 mg/g) as the internal standard and subjected to ¹⁹F NMR experiments. These experiments were conducted at room temperature (22 °C). The moles of salt uptake, n_{LiTFSI} , and the electrolyte partitioning as quantified by $\frac{\phi_-}{\phi_-^e}$, can then be calculated from the following equations:

$$n_{LiTFSI} = \frac{10 \frac{mg}{g}}{M_{CH_3SO_2NH_2}} \times \frac{\frac{P_{LiTFSI}}{6}}{\frac{P_{CF_3SO_2NH_2}}{3}} \times \frac{50}{500} \times 1 g \quad (8.30)$$

$$\frac{\phi_-}{\phi_-^e} = \frac{n_{LiTFSI}}{W_u - n_{LiTFSI}M_{LiTFSI}} \times \frac{1}{m_{ext}} \quad (8.31)$$

where M_i is the molecular weight, P_i is the peak integration in the NMR spectra, W_u is the weight of total uptake, and m_{ext} is the molality of the external solution.

8.6.3 Flory-Huggins Interaction Parameter

We use a lumped Flory-Huggins parameter, χ , to capture the individual interaction parameters between the solvent and ions, polymer and solvent, and polymer and ions. This lumped Flory-Huggins parameter can be expressed as the following:

$$\chi = \frac{\chi_{ions,p}(\phi_+ + \phi_-)\phi_p + \chi_{s,p}\phi_s\phi_p + \chi_{ions,s}(\phi_+ + \phi_-)\phi_s}{\phi_p(1 - \phi_p)}, \quad (8.32)$$

where $\chi_{ions,p}$ is the interaction parameter between ions and polymer, $\chi_{s,p}$ is the interaction parameter between solvent and polymer, and $\chi_{ions,s}$ is the interaction parameter between ions and solvent.

8.6.4 Volume Fraction of Bound Negative Ions in the Gel Phase

We show the dependence of the volume fraction of bound negative ions in the gel phase, $\phi_{-,b}$, on the volume fraction of anions in the external solution, ϕ_-^e . Recall that $\phi_{-,b} = f\phi_p$. Figures 8.11-8.15 show the predicted behavior from using the original quadratic Donnan exclusion expression (see Equation 8.1 and Figure 8.8).

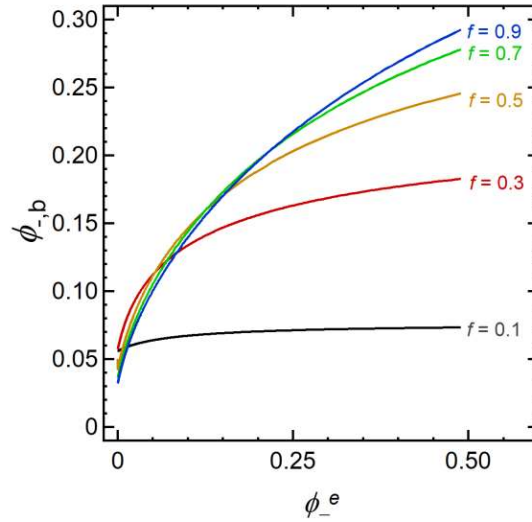


Figure 8.11. Dependence of the volume fraction of bound negative ions in the gel phase, $\phi_{-,b}$, on the volume fraction of anions in the external solution, ϕ_-^e for $z_+ = -z_-$, $N = 10$, $\chi = 1$, various f . Curves are shown for selected values of the fraction of charged monomers on the polymer strands, f . Parameters held fixed: $z_+ = -z_-$, $N = 10$, and $\chi = 1$.

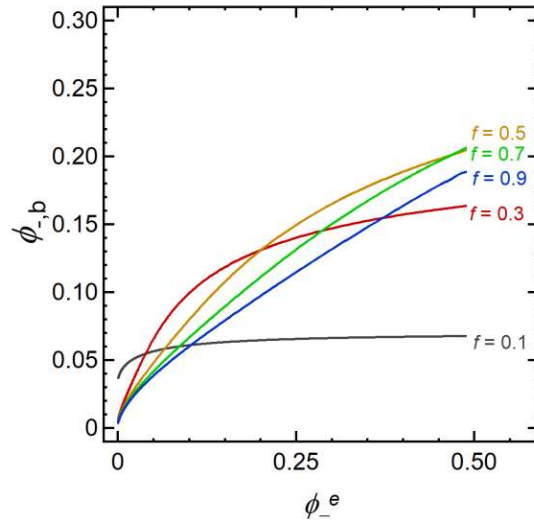


Figure 8.12. Dependence of the volume fraction of bound negative ions in the gel phase, $\phi_{-,b}$, on the volume fraction of anions in the external solution, $\phi_{-,e}$ for $z_+ = -z_-$, $N = 50$, $\chi = 1$, various f . Curves are shown for selected values of the fraction of charged monomers on the polymer strands, f . Parameters held fixed: $z_+ = -z_-$, $N = 50$, and $\chi = 1$.

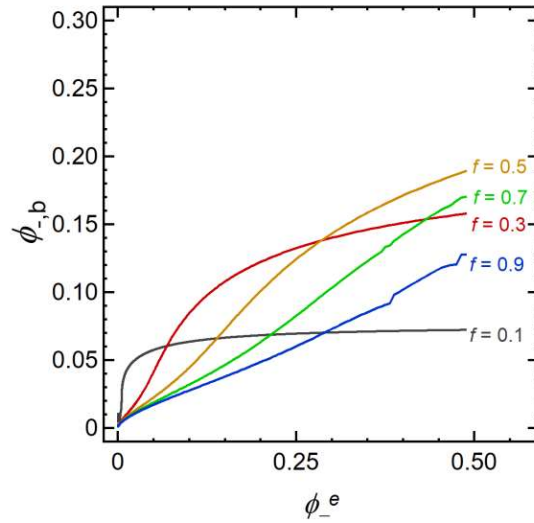


Figure 8.13. Dependence of the volume fraction of bound negative ions in the gel phase, $\phi_{-,b}$, on the volume fraction of anions in the external solution, $\phi_{-,e}$ for $z_+ = -z_-$, $N = 200$, $\chi = 1$, various f . Curves are shown for selected values of the fraction of charged monomers on the polymer strands, f . Parameters held fixed: $z_+ = -z_-$, $N = 200$, and $\chi = 1$.

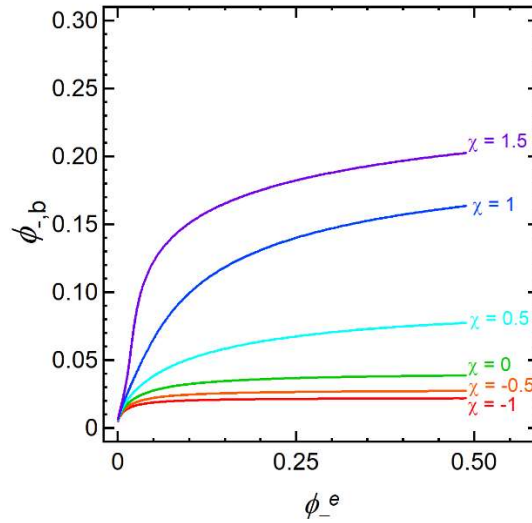


Figure 8.14. Dependence of the volume fraction of bound negative ions in the gel phase, $\phi_{-,b}$, on the volume fraction of anions in the external solution, $\phi_{-,e}$ for $z_+ = -z_-$, $N = 50$, $f = 0.3$, various χ . Curves are shown for selected values of χ . Parameters held fixed: $z_+ = -z_-$, $N = 50$ and $f = 0.3$.

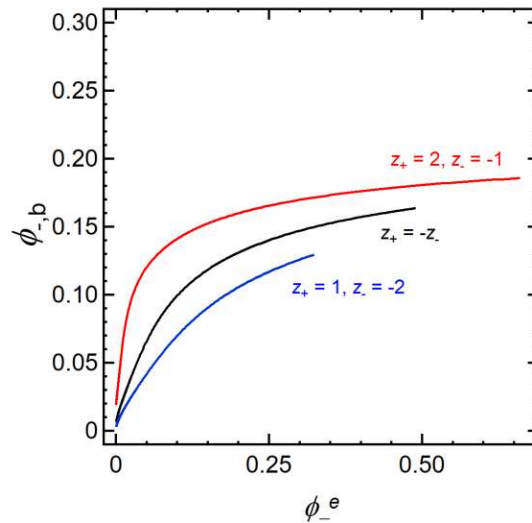


Figure 8.15. Dependence of the volume fraction of bound negative ions in the gel phase, $\phi_{-,b}$, on the volume fraction of anions in the external solution, $\phi_{-,e}$ for $N = 50$, $\chi = 1$, $f = 0.3$, various z_+ and z_- . Curves are shown for selected values of the charge numbers, z_+ and z_- . Parameters held fixed: $N = 50$, $\chi = 1$, and $f = 0.3$.

8.6.5 Comparing Experimental Donnan Exclusion Data and Theoretical Predictions.

We show the exclusion of ions in the gel; the dependence of the ratio of concentration of anions in the gel to that in the external solution, C_{in}/C_e , on C_e , the concentration of ions in the external

solution, which has units of moles of ions per liter of solvent. We also show the dependence of the concentration of ions in the gel, C_{in} , to that in the external solution, C_e . Figure 8.16 and Figure 8.17 recast Figure 8.9b and Figure 8.10b from the main text from volume fractions into units of concentration. For Figure 8.16, to calculate the theoretical values of C_e from volume fraction, we use Equation 8.26 to solve for m , the molality of the external solution, given ϕ_-^e , the volume fraction of anions in the external solution. C_e is then obtained from m by multiplying by the density of the solvent. C_{in} is obtained by assuming that the ratio C_{in}/C_e is equal to ϕ_-/ϕ_-^e . For Figure 8.17, to calculate the theoretical values of C_e from volume fraction, we use Equation 8.29. C_{in} is obtained by using Equation 8.28 to solve for C . ($C = C_{in}$). We use interpolated values of the water uptake, W_u , and C_+ , the moles of the counterion per liter of solvent, from the experimental data from ref. ²⁵⁷, for a given value of ϕ_-^e .

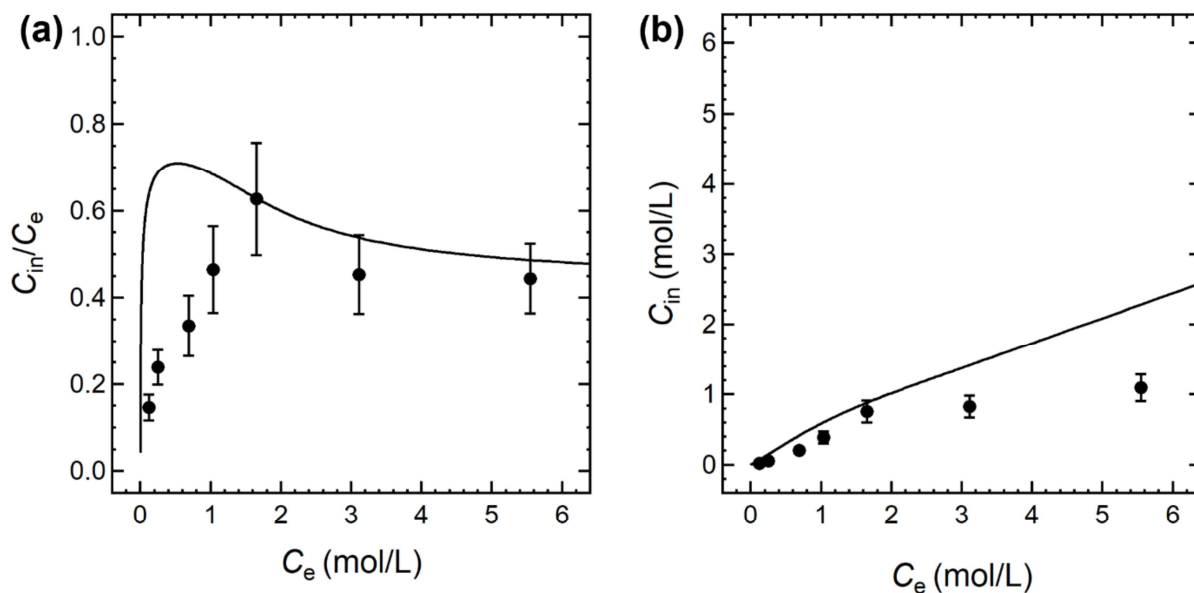


Figure 8.16. Experimental data for the swelling and salt partitioning between a PSLiTFSI-*b*-PE-*b*-PSLiTFSI triblock copolymer membrane and external solutions of LiTFSI in an EC/DMC mixture. (a) Exclusion of ions in the gel: dependence of the ratio of ion concentration in the gel to the concentration of ions in the external solution, C_{in}/C_e , on C_e . (b) Dependence of ion concentration in the gel, C_{in} , on the concentration of ions in the external solution, C_e . We give the concentration as the moles of ions per liter of solvent. Curves are the comparison to theory and were calculated using $\chi = 0.85$, $z_+ = -z_-$, $N = 250$ and $f = 0.3$. See Figure 8.9 in the main text for more details.

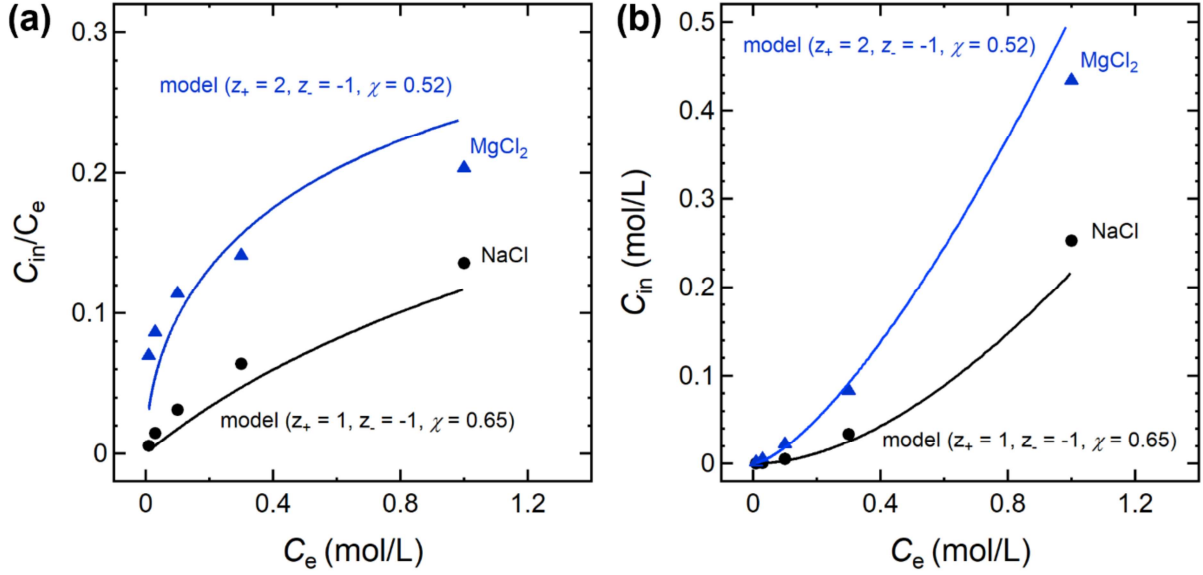


Figure 8.17. Comparing experimental data with theoretical predictions. Data points represent partitioning of NaCl and MgCl₂ from an aqueous solution into an acrylamide-based polymeric gel with sulfonic acid groups. (a) Exclusion of ions in the gel: dependence of the ratio of ion concentration in the gel to the concentration of ions in the external solution, C_{in}/C_e , on C_e . (b) Dependence of ion concentration in the gel, C_{in} , on the concentration of ions in the external solution, C_e . We give the concentration as the moles of ions per liter of solvent. Curves are the comparison to theory and were calculated using $\chi = 0.65$ and $z_+ = -z_-$ for comparisons with the NaCl data, and $\chi = 0.52$, $z_+ = 2$ and $z_- = -1$ for comparisons with the MgCl₂ data. Parameters held fixed: $N = 9$ and $f = 0.1$. See Figure 8.10 in the main text for more details.

8.7 Nomenclature

Table 8.1. List of symbols and abbreviations.

Symbol	Meaning
PSLiTFSI	Polystyrenesulfonyllithium(trifluoromethanesulfonyl)imide
EC	Ethylene carbonate
DMC	Dimethyl carbonate
LiTFSI	Lithium bis(trifluoromethanesulfonyl)imide
PE	Polyethylene
MgSO ₄	Magnesium sulfate
MgCl ₂	Magnesium chloride
NaCl	Sodium chloride
N	Number of repeat units between crosslinks
f	Fraction of charged monomers in the gel phase
ϕ_i	Volume fraction of component i in the gel phase
ϕ_i^e	Volume fraction of component i in the external solution phase
$\phi_{-,b}$	Volume fraction of the bound negative ions in the gel phase
$\phi_{p,total}$	Total polymer volume fraction of gel phase after swelling
ΔG_m	Gibbs free energy of mixing

k	Boltzmann constant
T	Absolute temperature
n_i	Number of lattice sites occupied by component i
n	Total number of lattice sites
χ	Flory-Huggins interaction parameter
μ_i	Chemical potential of species i
m_i	Moles of species i
N_{AV}	Avogadro's number
R	Molar gas constant
z_+	Charge number of positive ion
z_-	Charge number of negative ion
F	Faraday constant
U	Donnan potential
ρ_i	Density of component i
W_e	External solution uptake
M_i	Molecular weight of component i
m	Molality
V_i	Intrinsic molar volume of species i
W_u	Water uptake
v_i	Stoichiometric coefficient of ion i
C_i	Concentration of species i in the gel phase
C_e	Anion concentration of external solution

9 Conclusions and Outlook

Developing safe polymer electrolytes with good ion transport properties will lead to widespread adoption for use in next generation lithium batteries. Understanding ion transport and thermodynamics in polymer electrolytes is important for both design and development of new polymer electrolytes and optimization of electrolyte performance during battery usage. Newman's concentrated solution theory enables a full description of the transport processes occurring in the electrolyte via the measurement of multiple transport parameters. In this dissertation, we present a thorough analysis of ion transport in PEO/LiTFSI electrolytes, with an emphasis on uncertainty analysis and error propagation. Going beyond homopolymer electrolytes, we examine the ion transport and thermodynamic properties of inorganic-organic block copolymers and polymer blends. Finally, we develop a set of equations to describe Donnan equilibrium in polymer membranes in electrolytic solutions by accounting for the elasticity and enthalpic interactions.

In Chapter 2 we discuss the nuances of the cation transference number, especially with regards to the reference frame. We differentiate between the commonly reported current fraction (sometimes referred to as the cation transference number at steady-state) measured from the Bruce-Vincent method, the cation transference number with respect to the solvent velocity, and the cation transference number with respect to mass-average velocity. It is important to understand the differences, as these parameters are only equal in the dilute limit of an electrolyte. In this dissertation, we primarily use the cation transference number with respect to the solvent velocity determined via Newman's concentrated solution theory framework. Chapter 3 details the measurement of the transport parameters in PEO/LiTFSI electrolytes needed to calculate the cation transference number with respect to the solvent velocity, and discusses the uncertainty analysis and error propagation that goes into these measurements. We also show that the transport properties in PEO/LiTFSI no longer change with increasing molecular weight above their entanglement threshold and demonstrate improved precision of property measurements enabled by sampling multiple molecular weights of PEO.

In Chapter 2-4, we study PEO/LiTFSI, which is a commonly studied homopolymer (*i.e.* single polymer) electrolyte. In Chapter 5 we present the synthesis and characterization of PEO-POSS electrolytes, a hybrid inorganic-organic block copolymer system. In this heterogeneous electrolyte system, thermodynamic interactions between the PEO chains and POSS chains lead to self-assembly into different morphologies. We show that ion transport is affected by the morphology. In Chapter 6 we show that it is possible to obtain homogeneous mixtures of two chemically distinct polymers with a lithium salt for electrolytic applications. We characterize the phase behavior and ion transport properties and find that the electrochemical properties of the PEO/P(2EO-MO)/LiTFSI blends are similar to those obtained in the homopolymer PEO/LiTFSI electrolytes. This work showcases a new methodology for creating new and improved polymer electrolytes by blending different polymers to create miscible polymer blend electrolytes. Chapter 7 examines the relationship between ion transport and phase behavior in two more polymer blend systems, including one that does not use PEO. In Chapter 8, we develop a new set of equations describing the thermodynamics of a polymer membrane in an electrolytic solution, in what is commonly referred to as Donnan equilibrium. Central to Chapters 6-8 is the Flory-Huggins interaction

parameter, χ , which describes the enthalpic interaction between two different polymers. Depending on the value (and sign) of the χ , the polymer blend system may be miscible or phase separated; similarly, the amount of solution uptake in the polymer membrane soaked in an electrolyte is also affected by χ .

Developing a safe polymer electrolyte with good ion transport properties remains a long standing goal in the field. This dissertation provides a direct strategy toward this goal by establishing the feasibility of miscible polymer blend electrolytes, and the ion transport in polymer electrolytes can be characterized by Newman's concentrated solution theory, as shown herein.

10 References

- (1) U. S. Energy Information Administration. *International Energy Outlook 2021*.
- (2) Goodenough, J. B.; Kim, Y. Challenges for Rechargeable Li Batteries. *Chemistry of Materials*. 2010, pp 587–603. <https://doi.org/10.1021/cm901452z>.
- (3) Tarascon, J. M.; Armand, M. Issues and Challenges Facing Rechargeable Lithium Batteries. *Nature* **2001**, *414* (6861), 359–367. <https://doi.org/10.1038/35104644>.
- (4) Xie, J.; Lu, Y. C. A Retrospective on Lithium-Ion Batteries. *Nature Communications*. 2020. <https://doi.org/10.1038/s41467-020-16259-9>.
- (5) Xu, K. Nonaqueous Liquid Electrolytes for Lithium-Based Rechargeable Batteries. *Chemical Reviews* **2004**, *104* (10), 4303–4417. <https://doi.org/10.1021/cr030203g>.
- (6) Balsara, N. P.; Newman, J. Comparing the Energy Content of Batteries, Fuels, and Materials. *Journal of Chemical Education* **2013**, *90* (4), 446–452. <https://doi.org/10.1021/ed3004066>.
- (7) Cheng, X. B.; Zhang, R.; Zhao, C. Z.; Zhang, Q. Toward Safe Lithium Metal Anode in Rechargeable Batteries: A Review. *Chemical Reviews*. 2017, pp 10403–10473. <https://doi.org/10.1021/acs.chemrev.7b00115>.
- (8) Zhai, P.; Liu, L.; Gu, X.; Wang, T.; Gong, Y. Interface Engineering for Lithium Metal Anodes in Liquid Electrolyte. *Advanced Energy Materials*. 2020. <https://doi.org/10.1002/aenm.202001257>.
- (9) Frenck, L.; Sethi, G. K.; Maslyn, J. A.; Balsara, N. P. Factors That Control the Formation of Dendrites and Other Morphologies on Lithium Metal Anodes. *Frontiers in Energy Research*. 2019. <https://doi.org/10.3389/fenrg.2019.00115>.
- (10) Monroe, C.; Newman, J. The Impact of Elastic Deformation on Deposition Kinetics at Lithium/Polymer Interfaces. *Journal of The Electrochemical Society* **2005**, *152* (2), A396. <https://doi.org/10.1149/1.1850854>.
- (11) Stone, G. M.; Mullin, S. A.; Teran, A. A.; Hallinan, D. T.; Minor, A. M.; Hexemer, A.; Balsara, N. P. Resolution of the Modulus versus Adhesion Dilemma in Solid Polymer Electrolytes for Rechargeable Lithium Metal Batteries. *Journal of The Electrochemical Society* **2012**, *159* (3), A222–A227. <https://doi.org/10.1149/2.030203jes>.
- (12) Xue, Z.; He, D.; Xie, X. Poly(Ethylene Oxide)-Based Electrolytes for Lithium-Ion Batteries. *Journal of Materials Chemistry A*. 2015, pp 19218–19253. <https://doi.org/10.1039/c5ta03471j>.
- (13) Fenton, D. E.; Parker, M.; Wright, P. v. Complexes of Alkali Metal Ions with Poly(Ethylene Oxide). *Polymer (Guildf)* **1973**, *14*, 589. [https://doi.org/10.1016/0032-3861\(73\)90146-8](https://doi.org/10.1016/0032-3861(73)90146-8).

- (14) Sun, B.; Mindemark, J.; Edström, K.; Brandell, D. Polycarbonate-Based Solid Polymer Electrolytes for Li-Ion Batteries. *Solid State Ionics* **2014**, *262*, 738–742. <https://doi.org/10.1016/j.ssi.2013.08.014>.
- (15) Mindemark, J.; Lacey, M. J.; Bowden, T.; Brandell, D. Beyond PEO—Alternative Host Materials for Li⁺-Conducting Solid Polymer Electrolytes. *Progress in Polymer Science*. 2018, pp 114–143. <https://doi.org/10.1016/j.progpolymsci.2017.12.004>.
- (16) Bocharova, V.; Sokolov, A. P. Perspectives for Polymer Electrolytes: A View from Fundamentals of Ionic Conductivity. *Macromolecules*. 2020, pp 4141–4157. <https://doi.org/10.1021/acs.macromol.9b02742>.
- (17) Armand, M. Polymer Solid Electrolytes - An Overview. *Solid State Ionics* **1983**, *9 & 10*, 745–754. [https://doi.org/10.1016/0167-2738\(83\)90083-8](https://doi.org/10.1016/0167-2738(83)90083-8).
- (18) Watanabe, M.; Hirakimoto, T.; Mutoh, S.; Nishimoto, A. Polymer Electrolytes Derived from Dendritic Polyether Macromonomers. *Solid State Ionics* **2002**, *148*, 399–404. [https://doi.org/10.1016/S0167-2738\(02\)00079-6](https://doi.org/10.1016/S0167-2738(02)00079-6).
- (19) Young, W. S.; Kuan, W. F.; Epps, T. H. Block Copolymer Electrolytes for Rechargeable Lithium Batteries. *Journal of Polymer Science, Part B: Polymer Physics* **2014**, *52* (1), 1–16. <https://doi.org/10.1002/polb.23404>.
- (20) Gao, K. W.; Balsara, N. P. Electrochemical Properties of Poly(Ethylene Oxide) Electrolytes above the Entanglement Threshold. *Solid State Ionics* **2021**, *364*. <https://doi.org/10.1016/j.ssi.2021.115609>.
- (21) Nakamura, I. Microphase Separation of Ionic Liquid-Containing Diblock Copolymers: Effects of Dielectric Inhomogeneity and Asymmetry in the Molecular Volumes and Interactions between the Cation and Anion. *Macromolecules* **2020**, *53* (10), 3891–3899. <https://doi.org/10.1021/acs.macromol.0c00318>.
- (22) Jayanthi, S. Studies on Ionic Liquid Incorporated Polymer Blend Electrolytes for Energy Storage Applications. *Advanced Composites and Hybrid Materials* **2019**, *2*, 351–360. <https://doi.org/10.1007/s42114-019-00102-x>.
- (23) Villaluenga, I.; Chen, X. C.; Devaux, D.; Hallinan, D. T.; Balsara, N. P. Nanoparticle-Driven Assembly of Highly Conducting Hybrid Block Copolymer Electrolytes. *Macromolecules* **2015**, *48* (2), 358–364. <https://doi.org/10.1021/ma502234y>.
- (24) Lu, Y. S.; Kuo, S. W. Functional Groups on POSS Nanoparticles Influence the Self-Assembled Structures of Diblock Copolymer Composites. *RSC Advances* **2014**, *4* (66), 34849–34859. <https://doi.org/10.1039/c4ra06193d>.
- (25) Hallinan, D. T.; Balsara, N. P. Polymer Electrolytes. *Annual Review of Materials Research* **2013**, *43* (1), 503–525. <https://doi.org/10.1146/annurev-matsci-071312-121705>.
- (26) Gao, K. W.; Loo, W. S.; Snyder, R. L.; Abel, B. A.; Choo, Y.; Lee, A.; Teixeira, S. C. M.; Garetz, B. A.; Coates, G. W.; Balsara, N. P. Miscible Polyether/Poly(Ether-Acetal)

- Electrolyte Blends. *Macromolecules* **2020**, *53*, 5728–5739. <https://doi.org/10.1021/acs.macromol.0c00747>.
- (27) Loo, W. S.; Balsara, N. P. Organizing Thermodynamic Data Obtained from Multicomponent Polymer Electrolytes: Salt-Containing Polymer Blends and Block Copolymers. *Journal of Polymer Science, Part B: Polymer Physics* **2019**, *57* (18), 1177–1187. <https://doi.org/10.1002/polb.24800>.
- (28) Loo, W. S.; Jiang, X.; Maslyn, J. A.; Oh, H. J.; Zhu, C.; Downing, K. H.; Balsara, N. P. Reentrant Phase Behavior and Coexistence in Asymmetric Block Copolymer Electrolytes. *Soft Matter* **2018**, *14* (15), 2789–2795. <https://doi.org/10.1039/c8sm00175h>.
- (29) Shah, N. J.; Dadashi-Silab, S.; Galluzzo, M. D.; Chakraborty, S.; Loo, W. S.; Matyjaszewski, K.; Balsara, N. P. Effect of Added Salt on Disordered Poly(Ethylene Oxide)-Block-Poly(Methyl Methacrylate) Copolymer Electrolytes. *Macromolecules* **2021**, *54* (3), 1414–1424. <https://doi.org/10.1021/acs.macromol.0c02493>.
- (30) Xie, S.; Lodge, T. P. Phase Behavior of Binary Polymer Blends Doped with Salt. *Macromolecules* **2018**, *51* (1), 266–274. <https://doi.org/10.1021/acs.macromol.7b02310>.
- (31) Epps, T. H.; Bailey, T. S.; Waletzko, R.; Bates, F. S. Phase Behavior and Block Sequence Effects in Lithium Perchlorate-Doped Poly(Isoprene-*b*-Styrene-*b*-Ethylene Oxide) and Poly(Styrene-*b*-Isoprene-*b*-Ethylene Oxide) Triblock Copolymers. *Macromolecules* **2003**, *36* (8), 2873–2881. <https://doi.org/10.1021/ma021231o>.
- (32) Gao, K. W.; Yu, X.; Darling, R. M.; Newman, J.; Balsara, N. P. Increased Donnan Exclusion in Charged Polymer Networks at High Salt Concentrations. *Soft Matter* **2022**, *18* (2), 282–292. <https://doi.org/10.1039/d1sm01511g>.
- (33) Hallinan, D. T.; Villaluenga, I.; Balsara, N. P. Polymer and Composite Electrolytes. *MRS Bulletin* **2018**, *43* (10), 759–767. <https://doi.org/10.1557/mrs.2018.212>.
- (34) Maslyn, J. A.; Frenck, L.; Veeraraghavan, V. D.; Müller, A.; Ho, A. S.; Marwaha, N.; Loo, W. S.; Parkinson, D. Y.; Minor, A. M.; Balsara, N. P. Limiting Current in Nanostructured Block Copolymer Electrolytes. *Macromolecules* **2021**, *54* (9), 4010–4022. <https://doi.org/10.1021/acs.macromol.1c00425>.
- (35) Gribble, D. A.; Frenck, L.; Shah, D. B.; Maslyn, J. A.; Loo, W. S.; Mongcopa, K. I. S.; Pesko, D. M.; Balsara, N. P. Comparing Experimental Measurements of Limiting Current in Polymer Electrolytes with Theoretical Predictions. *Journal of The Electrochemical Society* **2019**, *166* (14), A3228–A3234. <https://doi.org/10.1149/2.0391914jes>.
- (36) Shah, D. B.; Kim, H. K.; Nguyen, H. Q.; Srinivasan, V.; Balsara, N. P. Comparing Measurements of Limiting Current of Electrolytes with Theoretical Predictions up to the Solubility Limit. *Journal of Physical Chemistry C* **2019**, *123* (39), 23872–23881. <https://doi.org/10.1021/acs.jpcc.9b07121>.

- (37) Onsager, L. Theories and Problems of Liquid Diffusion. *Ann N Y Acad Sci* **1945**, *46* (5), 241–265. <https://doi.org/10.1111/j.1749-6632.1945.tb36170.x>.
- (38) Newman, J.; Balsara, N. P. *Electrochemical Systems*, 4th ed.; Wiley, 2021.
- (39) Gao, K. W.; Fang, C.; Halat, D. M.; Mistry, A.; Newman, J.; Balsara, N. P. The Transference Number. *Energy and Environmental Materials*. John Wiley and Sons Inc April 1, 2022, pp 366–369. <https://doi.org/10.1002/eem2.12359>.
- (40) Ma, Y.; Doyle, M.; Fuller, T. F.; Doeff, M. M.; Jonghe, L. C. de; Newman, J. The Measurement of a Complete Set of Transport Properties for a Concentrated Solid Polymer Electrolyte Solution. *Journal of The Electrochemical Society* **1995**, *142* (6), 1859–1868. <https://doi.org/10.1149/1.2044206>.
- (41) Yokota, I. On the Theory of Mixed Conduction with Special Reference to the Conduction in Silver Sulfide Group Semiconductors. *Journal of the Physical Society of Japan* **1961**, *16* (11), 2213–2223. <https://doi.org/https://doi.org/10.1143/JPSJ.16.2213>.
- (42) Prigogine, I. *Introduction to Thermodynamics of Irreversible Processes*, 3rd ed.; Interscience Publishers, Inc., 1967.
- (43) de Groot, S. R.; Mazur, P. *Non-Equilibrium Thermodynamics*; Interscience Publishers, Inc., 1969.
- (44) Maier, J.; Schwitzgebel, G. Theoretical Treatment of the Diffusion Coupled with Reaction, Applied to the Example of a Binary Solid Compound MX. *Physica Status Solidi (B)* **1982**, *113* (2), 535–547. <https://doi.org/10.1002/pssb.2221130218>.
- (45) Kraaijeveld, G.; Wesselingh, J. A. Negative Maxwell-Stefan Diffusion Coefficients. *Industrial and Engineering Chemistry Research* **1993**, *32* (4), 738–742. <https://doi.org/10.1021/ie00016a022>.
- (46) Barthel, J. M. G.; Krienke, H.; Kunz, W. *Physical Chemistry of Electrolyte Solutions*; Springer, 1998.
- (47) Bockris, J. O.; Reddy, A. K. N. *Modern Electrochemistry*, 2nd ed.; Kluwer Academic Publishers, 2002.
- (48) Maier, J. Salt Concentration Polarization of Liquid Electrolytes and Determination of Transport Properties of Cations, Anions, Ion Pairs and Ion Triples. *Electrochimica Acta* **2014**, *129*, 21–27. <https://doi.org/10.1016/j.electacta.2014.01.078>.
- (49) Fong, K. D.; Bergstrom, H. K.; McCloskey, B. D.; Mandadapu, K. K. Transport Phenomena in Electrolyte Solutions: Nonequilibrium Thermodynamics and Statistical Mechanics. *AIChE Journal* **2020**, *66* (12), 1–50. <https://doi.org/10.1002/aic.17091>.
- (50) Pfeifer, S.; Ackermann, F.; Sälzer, F.; Schönhoff, M.; Roling, B. Quantification of Cation-Cation, Anion-Anion and Cation-Anion Correlations in Li Salt/Glyme Mixtures by Combining Very-Low-Frequency Impedance Spectroscopy with Diffusion and

- Electrophoretic NMR. *Phys Chem Chem Phys* **2021**, *23* (1), 628–640.
<https://doi.org/10.1039/d0cp06147f>.
- (51) Onsager, L. Reciprocal Relations in Irreversible Processes. I. *Physical Review* **1931**, *37*, 405–426. https://doi.org/10.1142/9789814293273_0013.
- (52) Onsager, L. Reciprocal Relations in Irreversible Processes. II. *Physical Rev* **1931**, *38*, 2265–2279. <https://doi.org/10.3109/09546639309082148>.
- (53) Faraday, M.; Hittorf, J. W.; Kohlrausch, F. W. G. *The Fundamental Laws of Electrolytic Conduction: Memoirs by Faraday, Hittorf and F. Kohlrausch*; Harper & Brothers, 1899.
- (54) Hittorf, W. Das Verhalten Der Diaphragmen Bei Der Elektrolyse von Salzlösungen. *Zeitschrift für Physikalische Chemie* **1903**, *43U* (1), 239–249.
<https://doi.org/10.1515/zpch-1903-4319>.
- (55) Lewis, G. N. The Theory of the Determination of Transference Numbers by the Method of Moving Boundaries. *J Am Chem Soc* **1910**, *32*, 862–869.
<https://doi.org/10.1021/ja01925a002>.
- (56) Longworth, L. G.; MacInnes, D. A. Transference Numbers by the Method of Moving Boundaries. *Chemical Reviews* **1932**, *4* (2), 171–230.
<https://doi.org/10.1021/ja01249a027>.
- (57) Milios, P. Moving Boundary Measurement of Transference Numbers, University of California, Berkeley, 1967.
- (58) Hou, T.; Monroe, C. W. Composition-Dependent Thermodynamic and Mass-Transport Characterization of Lithium Hexafluorophosphate in Propylene Carbonate. *Electrochimica Acta* **2020**, *332*, 135085. <https://doi.org/10.1016/j.electacta.2019.135085>.
- (59) Bruce, P. G.; Vincent, C. A. Steady State Current Flow in Solid Binary Electrolyte Cells. *Journal of Electroanalytical Chemistry* **1987**, *225* (1–2), 1–17.
[https://doi.org/10.1016/0022-0728\(87\)80001-3](https://doi.org/10.1016/0022-0728(87)80001-3).
- (60) Evans, J.; Vincent, C. A.; Bruce, P. G. Electrochemical Measurement of Transference Numbers in Polymer Electrolytes. *Polymer (Guildf)* **1987**, *28* (13), 2324–2328.
[https://doi.org/10.1016/0032-3861\(87\)90394-6](https://doi.org/10.1016/0032-3861(87)90394-6).
- (61) Watanabe, M.; Nagano, S.; Sanui, K.; Ogata, N. Estimation of Li⁺ Transport Number in Polymer Electrolytes by the Combination of Complex Impedance and Potentiostatic Polarization Measurements. *Solid State Ionics* **1988**, *28–30*, 911–917.
[https://doi.org/10.1016/0167-2738\(88\)90303-7](https://doi.org/10.1016/0167-2738(88)90303-7).
- (62) Balsara, N. P.; Newman, J. Relationship between Steady-State Current in Symmetric Cells and Transference Number of Electrolytes Comprising Univalent and Multivalent Ions. *J Electrochem Soc* **2015**, *162* (14), A2720–A2722. <https://doi.org/10.1149/2.0651514jes>.

- (63) Pesko, D. M.; Timachova, K.; Bhattacharya, R.; Smith, M. C.; Villaluenga, I.; Newman, J.; Balsara, N. P. Negative Transference Numbers in Poly(Ethylene Oxide)-Based Electrolytes. *Journal of The Electrochemical Society* **2017**, *164* (11), E3569–E3575. <https://doi.org/10.1149/2.0581711jes>.
- (64) Wheeler, D.; Newman, J. Molecular Dynamics Simulations of Multicomponent Diffusion. 1. Equilibrium Method. *Journal of Physical Chemistry B* **2004**, *108* (47), 18353–18361. <https://doi.org/10.1021/jp047850b>.
- (65) Wheeler, D. R.; Newman, J. Molecular Dynamics Simulations of Multicomponent Diffusion. 2. Nonequilibrium Method. *Journal of Physical Chemistry B* **2004**, *108* (47), 18362–18367. <https://doi.org/10.1021/jp047849c>.
- (66) Lascaud, S.; Perrier, M.; Vallée, A.; Besner, S.; Prud'homme, J.; Armand, M. Phase Diagrams and Conductivity Behavior of Poly(Ethylene Oxide)-Molten Salt Rubbery Electrolytes. *Macromolecules* **1994**, *27* (25), 7469–7477. <https://doi.org/10.1021/ma00103a034>.
- (67) Fuller, T. F.; Doyle, M.; Newman, J. Simulation and Optimization of the Dual Lithium Ion Insertion Cell. *The Journal of the Electrochemical Society* **1993**, *141* (1). <https://doi.org/10.1149/1.2054684>.
- (68) Landesfeind, J.; Gasteiger, H. A. Temperature and Concentration Dependence of the Ionic Transport Properties of Lithium-Ion Battery Electrolytes. *Journal of The Electrochemical Society* **2019**, *166* (14), A3079–A3097. <https://doi.org/10.1149/2.0571912jes>.
- (69) Walls, H. J.; Zawodzinski, T. A. Anion and Cation Transference Numbers Determined by Electrophoretic NMR of Polymer Electrolytes Sum to Unity. *Electrochemical and Solid-State Letters* **2000**, *3* (7), 321–324. <https://doi.org/10.1149/1.1391136>.
- (70) Zhang, Z.; Madsen, L. A. Observation of Separate Cation and Anion Electrophoretic Mobilities in Pure Ionic Liquids. *Journal of Chemical Physics* **2014**, *140* (8). <https://doi.org/10.1063/1.4865834>.
- (71) Timachova, K.; Newman, J.; Balsara, N. P. Theoretical Interpretation of Ion Velocities in Concentrated Electrolytes Measured by Electrophoretic NMR. *Journal of The Electrochemical Society* **2019**, *166* (2), A264–A267. <https://doi.org/10.1149/2.0591902jes>.
- (72) Fong, R.; von Sacken, U.; Dahn, J. R. Studies of Lithium Intercalation into Carbons Using Nonaqueous Electrochemical Cells. *Journal of The Electrochemical Society* **1990**, *137* (7), 2009–2013. <https://doi.org/10.1149/1.2086855>.
- (73) Tarascon, J. M.; Guyomard, D. New Electrolyte Compositions Stable over the 0 to 5 V Voltage Range and Compatible with the $\text{Li}_1+x\text{Mn}_2\text{O}_4/\text{Carbon}$ Li-Ion Cells. *Solid State Ionics* **1994**, *69* (3–4), 293–305. [https://doi.org/10.1016/0167-2738\(94\)90418-9](https://doi.org/10.1016/0167-2738(94)90418-9).

- (74) Doyle, M.; Fuller, T. F.; Newman, J. The Importance of the Lithium Ion Transference Number in Lithium/Polymer Cells. *Electrochimica Acta* **1994**, *39* (13), 2073–2081. [https://doi.org/10.1016/0013-4686\(94\)85091-7](https://doi.org/10.1016/0013-4686(94)85091-7).
- (75) Pesko, D. M.; Feng, Z.; Sawhney, S.; Newman, J.; Srinivasan, V.; Balsara, N. P. Comparing Cycling Characteristics of Symmetric Lithium-Polymer-Lithium Cells with Theoretical Predictions. *Journal of The Electrochemical Society* **2018**, *165* (13), A3186–A3194. <https://doi.org/10.1149/2.0921813jes>.
- (76) Kondo, K.; Sano, M.; Hiwara, A.; Omi, T.; Fujita, M.; Kuwae, A.; Iida, M.; Mogi, K.; Yokoyama, H. Conductivity and Solvation of Li⁺ Ions of LiPF₆ in Propylene Carbonate Solutions. *J. Phys. Chem. B* **2000**, *104*, 5040–5044. <https://doi.org/10.1021/jp000142f>.
- (77) Stewart, S.; Newman, J. Measuring the Salt Activity Coefficient in Lithium-Battery Electrolytes. *Journal of The Electrochemical Society* **2008**, *155* (6), A458. <https://doi.org/10.1149/1.2904526>.
- (78) Hwang, S.; Kim, D.; Shin, J. H.; Jang, J. E.; Ahn, K. H.; Lee, C.; Lee, H. Ionic Conduction and Solution Structure in LiPF₆ and LiBF₄ Propylene Carbonate Electrolytes. *J. Phys. Chem. C* **2018**, *122*, 19438–19446. <https://doi.org/10.1021/acs.jpcc.8b06035>.
- (79) Nishida, T.; Nishikawa, K.; Fukunaka, Y. Diffusivity Measurement of LiPF₆, LiTFSI, LiBF₄ in PC. *ECS Transactions* **2008**, *6* (18), 1–14. <https://doi.org/10.1149/1.2831921>.
- (80) Shah, D. B. Ion Transport Properties in Novel and Traditional Liquid Electrolytes for Lithium-Based Batteries, University of California, Berkeley, 2020.
- (81) Liu, Q.; Du, C.; Shen, B.; Zuo, P.; Cheng, X.; Ma, Y.; Yin, G.; Gao, Y. Understanding Undesirable Anode Lithium Plating Issues in Lithium-Ion Batteries. *RSC Advances* **2016**, *6* (91), 88683–88700. <https://doi.org/10.1039/c6ra19482f>.
- (82) Galluzzo, M. D.; Maslyn, J. A.; Shah, D. B.; Balsara, N. P. Ohm's Law for Ion Conduction in Lithium and beyond-Lithium Battery Electrolytes. *Journal of Chemical Physics* **2019**, *151* (2). <https://doi.org/10.1063/1.5109684>.
- (83) Wang, A. A.; Hou, T.; Karanjavala, M.; Monroe, C. W. Shifting-Reference Concentration Cells to Refine Composition-Dependent Transport Characterization of Binary Lithium-Ion Electrolytes. *Electrochimica Acta* **2020**, *358*, 136688. <https://doi.org/10.1016/j.electacta.2020.136688>.
- (84) Zhao, J.; Wang, L.; He, X.; Wan, C.; Jiang, C. Determination of Lithium-Ion Transference Numbers in LiPF₆-PC Solutions Based on Electrochemical Polarization and NMR Measurements. *Journal of The Electrochemical Society* **2008**, *155* (4), A292. <https://doi.org/10.1149/1.2837832>.
- (85) de Gennes, P. G. *Scaling Concepts in Polymer Chemistry*; Cornell University Press, 1979.
- (86) Wool, R. P. Polymer Entanglements. *Macromolecules* **1993**, *26* (7), 1564–1569. <https://doi.org/10.1021/ma00059a012>.

- (87) Shi, J.; Vincent, C. A. The Effect of Molecular Weight on Cation Mobility in Polymer Electrolytes. *Solid State Ionics* **1993**, *60* (1–3), 11–17. [https://doi.org/10.1016/0167-2738\(93\)90268-8](https://doi.org/10.1016/0167-2738(93)90268-8).
- (88) Teran, A. A.; Tang, M. H.; Mullin, S. A.; Balsara, N. P. Effect of Molecular Weight on Conductivity of Polymer Electrolytes. *Solid State Ionics* **2011**, *203*, 18–21. <https://doi.org/10.1016/j.ssi.2011.09.021>.
- (89) Chatteraj, J.; Knappe, M.; Heuer, A. Dependence of Ion Dynamics on the Polymer Chain Length in Poly(Ethylene Oxide)-Based Polymer Electrolytes. *Journal of Physical Chemistry B* **2015**, *119* (22), 6786–6791. <https://doi.org/10.1021/jp512734g>.
- (90) Newman, J.; Chapman, T. W. Restricted Diffusion in Binary Solutions. *AIChE Journal* **1973**, *19* (2), 343–348. <https://doi.org/10.1002/aic.690190220>.
- (91) Bruce, P. G.; Vincent, C. A. Steady State Current Flow in Solid Binary Electrolyte Cells. *Journal of Electroanalytical Chemistry and Interfacial Electrochemistry* **2002**, *271* (1–2), 27–34. [https://doi.org/10.1016/0022-0728\(89\)80061-0](https://doi.org/10.1016/0022-0728(89)80061-0).
- (92) Chintapalli, M.; Le, T. N. P.; Venkatesan, N. R.; Mackay, N. G.; Rojas, A. A.; Thelen, J. L.; Chen, X. C.; Devaux, D.; Balsara, N. P. Structure and Ionic Conductivity of Polystyrene-Block-Poly(Ethylene Oxide) Electrolytes in the High Salt Concentration Limit. *Macromolecules* **2016**, *49* (5), 1770–1780. <https://doi.org/10.1021/acs.macromol.5b02620>.
- (93) Hoffman, Z. J.; Shah, D. B.; Balsara, N. P. Temperature and Concentration Dependence of the Ionic Transport Properties of Poly(Ethylene Oxide) Electrolytes. *Solid State Ionics* **2021**, *370*. <https://doi.org/10.1016/j.ssi.2021.115751>.
- (94) Zheng, Q.; Pesko, D. M.; Savoie, B. M.; Timachova, K.; Hasan, A. L.; Smith, M. C.; Miller, T. F.; Coates, G. W.; Balsara, N. P. Optimizing Ion Transport in Polyether-Based Electrolytes for Lithium Batteries. *Macromolecules* **2018**, *51* (8), 2847–2858. <https://doi.org/10.1021/acs.macromol.7b02706>.
- (95) Ku, H. H. Notes on the Use of Propagation of Error Formulas. *Journal of Research of the National Bureau of Standards - C. Engineering and Instrumentation* **1966**, *70* (4), 75–79. <https://doi.org/10.6028/jres.070c.025>.
- (96) Mongcopa, K. I. S.; Tyagi, M.; Mailoa, J. P.; Samsonidze, G.; Kozinsky, B.; Mullin, S. A.; Gribble, D. A.; Watanabe, H.; Balsara, N. P. Relationship between Segmental Dynamics Measured by Quasi-Elastic Neutron Scattering and Conductivity in Polymer Electrolytes. *ACS Macro Letters* **2018**, *7*, 504–508. <https://doi.org/10.1021/acsmacrolett.8b00159>.
- (97) Fullerton-Shirey, S. K.; Maranas, J. K. Effect of LiClO₄ on the Structure and Mobility of PEO-Based Solid Polymer Electrolytes. *Macromolecules* **2009**, *42* (6), 2142–2156. <https://doi.org/10.1021/ma802502u>.

- (98) Robitaille, C. D.; Fauteux, D. Phase Diagrams and Conductivity Characterization of Some PEO-LiX Electrolytes. *Journal of The Electrochemical Society* **1986**, *133* (2), 315–325. <https://doi.org/10.1149/1.2108569>.
- (99) Pożyczka, K.; Marzantowicz, M.; Dygas, J. R.; Krok, F. IONIC CONDUCTIVITY AND LITHIUM TRANSFERENCE NUMBER OF POLY(ETHYLENE OXIDE):LiTFSI SYSTEM. *Electrochimica Acta* **2017**, *227*, 127–135. <https://doi.org/10.1016/j.electacta.2016.12.172>.
- (100) Devaux, D.; Bouchet, R.; Glé, D.; Denoyel, R. Mechanism of Ion Transport in PEO/LiTFSI Complexes: Effect of Temperature, Molecular Weight and End Groups. *Solid State Ionics* **2012**, *227*, 119–127. <https://doi.org/10.1016/j.ssi.2012.09.020>.
- (101) Schantz, S.; Torell, L. M.; Stevens, J. R. Ion Pairing Effects in Poly(Propylene Glycol)-Salt Complexes as a Function of Molecular Weight and Temperature: A Raman Scattering Study Using NaCF₃SO₃ and LiClO₄. *The Journal of Chemical Physics* **1991**, *94* (10), 6862–6867. <https://doi.org/10.1063/1.460265>.
- (102) Ratner, M. A.; Johansson, P.; Shriver, D. F. Polymer Electrolytes: Ionic Transport Mechanisms and Relaxation Coupling. *MRS Bulletin* **2000**, *25*, 31–37. <https://doi.org/10.1557/mrs2000.16>.
- (103) Gao, K. W.; Jiang, X.; Hoffman, Z. J.; Sethi, G. K.; Chakraborty, S.; Villaluenga, I.; Balsara, N. P. Optimizing the Monomer Structure of Polyhedral Oligomeric Silsesquioxane for Ion Transport in Hybrid Organic–Inorganic Block Copolymers. *Journal of Polymer Science* **2020**, *58* (2), 363–371. <https://doi.org/10.1002/pol.20190073>.
- (104) Gouverneur, M.; Schmidt, F.; Schönhoff, M. Negative Effective Li Transference Numbers in Li Salt/Ionic Liquid Mixtures: Does Li Drift in the “Wrong” Direction? *Phys. Chem. Chem. Phys.* **2018**, *20*, 7470–7478. <https://doi.org/10.1039/c7cp08580j>.
- (105) Molinari, N.; Mailoa, J. P.; Kozinsky, B. Effect of Salt Concentration on Ion Clustering and Transport in Polymer Solid Electrolytes: A Molecular Dynamics Study of PEO-LiTFSI. *Chemistry of Materials* **2018**, *30* (18), 6298–6306. <https://doi.org/10.1021/acs.chemmater.8b01955>.
- (106) Galluzzo, M. D.; Loo, W. S.; Wang, A. A.; Walton, A.; Maslyn, J. A.; Balsara, N. P. Measurement of Three Transport Coefficients and the Thermodynamic Factor in Block Copolymer Electrolytes with Different Morphologies. *Journal of Physical Chemistry B* **2020**, *124* (5), 921–935. <https://doi.org/10.1021/acs.jpccb.9b11066>.
- (107) France-Lanord, A.; Wang, Y.; Xie, T.; Johnson, J. A.; Shao-Horn, Y.; Grossman, J. C. Effect of Chemical Variations in the Structure of Poly(Ethylene Oxide)-Based Polymers on Lithium Transport in Concentrated Electrolytes. *Chemistry of Materials* **2020**, *32* (1), 121–126. <https://doi.org/10.1021/acs.chemmater.9b02645>.
- (108) Kim, H.-K.; Balsara, N. P.; Srinivasan, V. Continuum Description of the Role of Negative Transference Numbers on Ion Motion in Polymer Electrolytes. *Journal of The*

- Electrochemical Society* **2020**, 167 (11), 110559. <https://doi.org/10.1149/1945-7111/aba790>.
- (109) MacCallum, J. R.; Tomlin, A. S.; Vincent, C. A. An Investigation of the Conducting Species in Polymer Electrolytes. *European Polymer Journal* **1986**, 22 (10), 787–791. [https://doi.org/10.1016/0014-3057\(86\)90017-0](https://doi.org/10.1016/0014-3057(86)90017-0).
- (110) Gray, F. Conductance and Conducting Species in Amorphous Polyether-Lithium Perchlorate Systems at Very Low Salt Concentration. *Solid State Ionics* **1990**, 40–41, 637–640. [https://doi.org/10.1016/0167-2738\(90\)90086-7](https://doi.org/10.1016/0167-2738(90)90086-7).
- (111) Bruce, P. G. Ion Association in Polymer Electrolytes: Transport and Materials Optimization. *Synthetic Metals* **1991**, 45 (3), 267–278. [https://doi.org/10.1016/0379-6779\(91\)91783-7](https://doi.org/10.1016/0379-6779(91)91783-7).
- (112) Irish, D. E.; McCarroll, B.; Young, T. F. Raman Study of Zinc Chloride Solutions. *The Journal of Chemical Physics* **1963**, 39 (12), 3436–3444. <https://doi.org/10.1063/1.1734212>.
- (113) Spiro, T. G. A Raman Study of Thallium(III) Chloride Complexes in Aqueous Solution. *Inorganic Chemistry* **1965**, 4 (5), 731–738. <https://doi.org/10.1021/ic50027a029>.
- (114) Oertel, R. P.; Plane, R. A. Raman Study of Chloride and Bromide Complexes of Bismuth(III). *Inorganic Chemistry* **1967**, 6 (11), 1960–1967. <https://doi.org/10.1021/ic50057a004>.
- (115) Molinari, N.; Mailoa, J. P.; Kozinsky, B. General Trend of a Negative Li Effective Charge in Ionic Liquid Electrolytes. *Journal of Physical Chemistry Letters* **2019**, 10 (10), 2313–2319. <https://doi.org/10.1021/acs.jpcclett.9b00798>.
- (116) Webb, M. A.; Savoie, B. M.; Wang, Z. G.; Miller, T. F. Chemically Specific Dynamic Bond Percolation Model for Ion Transport in Polymer Electrolytes. *Macromolecules* **2015**, 48 (19), 7346–7358. <https://doi.org/10.1021/acs.macromol.5b01437>.
- (117) Borodin, O.; Smith, G. D. Mechanism of Ion Transport in Amorphous Poly(Ethylene Oxide)/LiTFSI from Molecular Dynamics Simulations. *Macromolecules* **2006**, 39, 1620–1629. <https://doi.org/10.1021/ma052277v>.
- (118) Debye, P. J. W.; Huckel, E. *The Collected Papers of Peter J. W. Debye*; 1954. <https://doi.org/10.1161/01.res.2.2.185>.
- (119) Efron, B. Nonparametric Estimates of Standard Error: The Jackknife, the Bootstrap and Other Methods. *Biometrika* **1981**, 68 (3), 589–599. [https://doi.org/10.1016/0045-6535\(85\)90163-8](https://doi.org/10.1016/0045-6535(85)90163-8).
- (120) Press, W. H.; Teukolsky, S. A.; Vetterling, W. T.; Flannery, B. P. *Numerical Recipes: The Art of Scientific Computing*, 3rd ed.; Cambridge University Press, 2007.
- (121) Hiemenz, P.; Lodge, T. *Polymer Chemistry*, 2nd ed.; CRC Press, 2007.

- (122) Nitzan, A.; Rainer, M. A. Conduction in Polymers: Dynamic Disorder Transport. *J. Phys. Chem* **1994**, *98*, 1765–1775. <https://doi.org/10.1021/j100058a009>.
- (123) Druger, S. D.; Nitzan, A.; Ratner, M. A. Dynamic Bond Percolation Theory: A Microscopic Model for Diffusion in Dynamically Disordered Systems. I. Definition and One-Dimensional Case. *The Journal of Chemical Physics* **1983**, *79* (6), 3133–3142. <https://doi.org/10.1063/1.446144>.
- (124) Choo, Y.; Halat, D. M.; Villaluenga, I.; Timachova, K.; Balsara, N. P. Diffusion and Migration in Polymer Electrolytes. *Progress in Polymer Science* **2020**, *103*. <https://doi.org/10.1016/j.progpolymsci.2020.101220>.
- (125) de Gennes, P. G. Reptation of a Polymer Chain in the Presence of Fixed Obstacles. *The Journal of Chemical Physics* **1971**, *55* (2), 572–579. <https://doi.org/10.1063/1.1675789>.
- (126) Aldulaimi, N. R.; Al-Bermany, E. Tuning the Bandgap and Absorption Behaviour of the Newly-Fabricated Ultrahigh Molecular Weight Polyethylene Oxide-Polyvinyl Alcohol/Graphene Oxide Hybrid Nanocomposites. *Polymers and Polymer Composites* **2022**, *30*, 096739112211121. <https://doi.org/10.1177/09673911221112196>.
- (127) Mansfield, C. D.; Chen, T.; Ansari, M. Q.; Baird, D. G. The Rheology of Ultra-High Molecular Weight Poly(Ethylene Oxide) Dispersed in a Low Molecular Weight Carrier. *Physics of Fluids* **2022**, *34* (2). <https://doi.org/10.1063/5.0077122>.
- (128) Halat, D. M.; Snyder, R. L.; Sundararaman, S.; Choo, Y.; Gao, K. W.; Hoffman, Z. J.; Abel, B. A.; Grundy, L. S.; Galluzzo, M. D.; Gordon, M. P.; Celik, H.; Urban, J. J.; Prendergast, D.; Coates, G. W.; Balsara, N. P.; Reimer, J. A. Modifying Li⁺ and Anion Diffusivities in Polyacetal Electrolytes: A Pulsed-Field-Gradient NMR Study of Ion Self-Diffusion. *Chemistry of Materials* **2021**, *33* (13), 4915–4926. <https://doi.org/10.1021/acs.chemmater.1c00339>.
- (129) Loo, W. S.; Faraone, A.; Grundy, L. S.; Gao, K. W.; Balsara, N. P. Polymer Dynamics in Block Copolymer Electrolytes Detected by Neutron Spin Echo. *ACS Macro Letters* **2020**, *9* (5), 639–645. <https://doi.org/10.1021/acsmacrolett.0c00236>.
- (130) Singh, M.; Odusanya, O.; Wilmes, G. M.; Eitouni, H. B.; Gomez, E. D.; Patel, A. J.; Chen, V. L.; Park, M. J.; Fragouli, P.; Iatrou, H.; Hadjichristidis, N.; Cookson, D.; Balsara, N. P. Effect of Molecular Weight on the Mechanical and Electrical Properties of Block Copolymer Electrolytes. *Macromolecules* **2007**, *40* (13), 4578–4585. <https://doi.org/10.1021/ma0629541>.
- (131) Soo, P. P.; Huang, B.; Jang, Y.-I.; Chiang, Y.-M.; Sadoway, D. R.; Mayes, A. M. Rubbery Block Copolymer Electrolytes for Solid-State Rechargeable Lithium Batteries. *J Electrochem Soc* **1999**, *146* (1), 32. <https://doi.org/10.1149/1.1391560>.
- (132) Ruzette, A.-V. G.; Soo, P. P.; Sadoway, D. R.; Mayes, A. M. Melt-Formable Block Copolymer Electrolytes for Lithium Rechargeable Batteries. *Journal of The Electrochemical Society* **2002**, *148* (6), A537. <https://doi.org/10.1149/1.1368097>.

- (133) Kosonen, H.; Valkama, S.; Hartikainen, J.; Eerikäinen, H.; Torkkeli, M.; Jokela, K.; Serimaa, R.; Sundholm, F.; Brinke, G. ten; Ikkala, O. Mesomorphic Structure of Poly(Styrene)-Block-Poly(4-Vinylpyridine) with Oligo(Ethylene Oxide)Sulfonic Acid Side Chains as a Model for Molecularly Reinforced Polymer Electrolyte. *Macromolecules* **2002**, *35* (27), 10149–10154. <https://doi.org/10.1021/ma0201577>.
- (134) Trapa, P. E.; Huang, B.; Won, Y.-Y.; Sadoway, D. R.; Mayes, A. M. Block Copolymer Electrolytes Synthesized by Atom Transfer Radical Polymerization for Solid-State, Thin-Film Lithium Batteries. *Electrochemical and Solid-State Letters* **2002**, *5* (5), A85. <https://doi.org/10.1149/1.1461996>.
- (135) Cho, B.-K.; Jain, A.; Gruner, S. M.; Wiesner, U. Mesophase Structure-Mechanical and Ionic Transport Correlations in Extended Amphiphilic Dendrons. *Science (1979)* **2004**, *305*, 1598–1601. <https://doi.org/10.1126/science.1100872>.
- (136) Panday, A.; Mullin, S.; Gomez, E. D.; Wanakule, N.; Chen, V. L.; Hexemer, A.; Pople, J.; Balsara, N. P. Effect of Molecular Weight and Salt Concentration on Conductivity of Block Copolymer Electrolytes. *Macromolecules* **2009**, *42* (13), 4632–4637. <https://doi.org/10.1021/ma900451e>.
- (137) Mullin, S. A.; Stone, G. M.; Panday, A.; Balsara, N. P. Salt Diffusion Coefficients in Block Copolymer Electrolytes. *Journal of The Electrochemical Society* **2011**, *158* (6), A619. <https://doi.org/10.1149/1.3563802>.
- (138) Young, W. S.; Epps, T. H. Ionic Conductivities of Block Copolymer Electrolytes with Various Conducting Pathways: Sample Preparation and Processing Considerations. *Macromolecules* **2012**, *45* (11), 4689–4697. <https://doi.org/10.1021/ma300362f>.
- (139) Teran, A. A.; Balsara, N. P. Thermodynamics of Block Copolymers with and without Salt. *Journal of Physical Chemistry B* **2014**, *118* (1), 4–17. <https://doi.org/10.1021/jp408079z>.
- (140) Irwin, M. T.; Hickey, R. J.; Xie, S.; So, S.; Bates, F. S.; Lodge, T. P. Structure-Conductivity Relationships in Ordered and Disordered Salt-Doped Diblock Copolymer/Homopolymer Blends. *Macromolecules* **2016**, *49* (18), 6928–6939. <https://doi.org/10.1021/acs.macromol.6b01553>.
- (141) Sethi, G. K.; Jiang, X.; Chakraborty, R.; Loo, W. S.; Villaluenga, I.; Balsara, N. P. Anomalous Self-Assembly and Ion Transport in Nanostructured Organic-Inorganic Solid Electrolytes. *ACS Macro Letters* **2018**, *7* (9), 1056–1061. <https://doi.org/10.1021/acsmacrolett.8b00583>.
- (142) Li, G.; Charles, U. P. Polyhedral Oligomeric Silsesquioxane (POSS) Polymers, Copolymers, and Resin Nanocomposites. *Macromolecules Containing Metal and Metal-Like Elements: Group IVA Polymers* **2005**, *4* (3), 79–131. <https://doi.org/10.1002/0471712566.ch5>.
- (143) Matějka, L.; Strachota, A.; Pleštil, J.; Whelan, P.; Steinhart, M.; Šlouf, M. Epoxy Networks Reinforced with Polyhedral Oligomeric Silsesquioxanes (POSS). Structure and

- Morphology. *Macromolecules* **2004**, *37* (25), 9449–9456.
<https://doi.org/10.1021/ma0484577>.
- (144) Ni, Y.; Zheng, S.; Nie, K. Morphology and Thermal Properties of Inorganic-Organic Hybrids Involving Epoxy Resin and Polyhedral Oligomeric Silsesquioxanes. *Polymer (Guildf)* **2004**, *45* (16), 5557–5568. <https://doi.org/10.1016/j.polymer.2004.06.008>.
- (145) Fina, A.; Tabuani, D.; Frache, A.; Camino, G. Polypropylene-Polyhedral Oligomeric Silsesquioxanes (POSS) Nanocomposites. *Polymer (Guildf)* **2005**, *46* (19 SPEC. ISS.), 7855–7866. <https://doi.org/10.1016/j.polymer.2005.06.121>.
- (146) Pracella, M.; Chionna, D.; Fina, A.; Tabuani, D.; Frache, A.; Camino, G. Polypropylene-POSS Nanocomposites: Morphology and Crystallization Behaviour. *Macromolecular Symposia* **2006**, *234* (Figure 1), 59–67. <https://doi.org/10.1002/masy.200650209>.
- (147) Perrin, F. X.; Panaitescu, D. M.; Frone, A. N.; Radovici, C.; Nicolae, C. The Influence of Alkyl Substituents of POSS in Polyethylene Nanocomposites. *Polymer (Guildf)* **2013**, *54* (9), 2347–2354. <https://doi.org/10.1016/j.polymer.2013.02.035>.
- (148) Heeley, E. L.; Hughes, D. J.; Aziz, Y. el; Williamson, I.; Taylor, P. G.; Bassindale, A. R. Properties and Self-Assembled Packing Morphology of Long Alkyl-Chained Substituted Polyhedral Oligomeric Silsesquioxanes (POSS) Cages. *Physical Chemistry Chemical Physics* **2013**, *15* (15), 5518–5529. <https://doi.org/10.1039/c3cp44356f>.
- (149) Heeley, E. L.; Hughes, D. J.; Aziz, Y. el; Taylor, P. G.; Bassindale, A. R. Morphology and Crystallization Kinetics of Polyethylene/Long Alkyl-Chain Substituted Polyhedral Oligomeric Silsesquioxanes (POSS) Nanocomposite Blends: A SAXS/WAXS Study. *European Polymer Journal* **2014**, *51* (1), 45–56.
<https://doi.org/10.1016/j.eurpolymj.2013.11.020>.
- (150) Niemczyk, A.; Dziubek, K.; Sacher-Majewska, B.; Czaja, K.; Dutkiewicz, M.; Marciniak, B. Study of Thermal Properties of Polyethylene and Polypropylene Nanocomposites with Long Alkyl Chain-Substituted POSS Fillers. *Journal of Thermal Analysis and Calorimetry* **2016**, *125* (3), 1287–1299. <https://doi.org/10.1007/s10973-016-5497-4>.
- (151) Ueda, K.; Tanaka, K.; Chujo, Y. Synthesis of POSS Derivatives Having Dual Types of Alkyl Substituents and Their Application as a Molecular Filler for Low-Refractive and Highly Durable Materials. *Bull Chem Soc Jpn* **2017**, *90* (2), 205–209.
<https://doi.org/10.1246/bcsj.20160338>.
- (152) Miao, J.; Cui, L.; Lau, H. P.; Mather, P. T.; Zhu, L. Self-Assembly and Chain-Folding in Hybrid Coil-Coil-Cube Triblock Oligomers of Polyethylene-b-Poly(Ethylene Oxide)-b-Polyhedral Oligomeric Silsesquioxane. *Macromolecules* **2007**, *40* (15), 5460–5470.
<https://doi.org/10.1021/ma070770w>.
- (153) Yu, X.; Zhong, S.; Li, X.; Tu, Y.; Yang, S.; van Horn, R. M.; Ni, C.; Pochan, D. J.; Quirk, R. P.; Wesdemiotis, C.; Zhang, W. bin; Cheng, S. Z. D. A Giant Surfactant of Polystyrene-(Carboxylic Acid-Functionalized Polyhedral Oligomeric Silsesquioxane)

- Amphiphile with Highly Stretched Polystyrene Tails in Micellar Assemblies. *J Am Chem Soc* **2010**, *132* (47), 16741–16744. <https://doi.org/10.1021/ja1078305>.
- (154) Huang, M.; Hsu, C.-H.; Wang, J.; Mei, S.; Dong, X.; Li, Y.; Li, M.; Liu, H.; Zhang, W.; Aida, T.; Zhang, W.-B.; Yue, K.; Cheng, S. Z. D. Selective Assemblies of Giant Tetrahedra via Precisely Controlled Positional Interactions. *Science (1979)* **2015**, *348* (6233), 424–428. <https://doi.org/10.1126/science.aaa2260>.
- (155) Arges, C. G.; Kambe, Y.; Dolejsi, M.; Wu, G.; Segal-pertz, T.; Ren, J.; Cao, C.; Craig, S. W.; Nealey, P. F. Interconnected Ionic Domains Enhance Conductivity in Microphase Separated Block Copolymer Electrolytes. *Journal of Materials Chemistry A* **2017**, *5*, 5619–5629. <https://doi.org/10.1039/c6ta10838e>.
- (156) Sax, J.; Ottino, J. M. Modeling of Transport of Small Molecules in Polymer Blends: Application of Effective Medium Theory. *Polymer Engineering and Science* **1983**, *23* (3), 165–176. <https://doi.org/10.1002/pen.760230310>.
- (157) Hexemer, A.; Bras, W.; Glossinger, J.; Schaible, E.; Gann, E.; Kirian, R.; MacDowell, A.; Church, M.; Rude, B.; Padmore, H. A SAXS/WAXS/GISAXS Beamline with Multilayer Monochromator. *Journal of Physics: Conference Series* **2010**, *247*. <https://doi.org/10.1088/1742-6596/247/1/012007>.
- (158) Ilavsky, J. Nika : Software for Two-Dimensional Data Reduction . *Journal of Applied Crystallography* **2012**, *45* (2), 324–328. <https://doi.org/10.1107/s0021889812004037>.
- (159) Villaluenga, I.; Pesko, D. M.; Timachova, K.; Feng, Z.; Newman, J.; Srinivasan, V.; Balsara, N. P. Negative Stefan-Maxwell Diffusion Coefficients and Complete Electrochemical Transport Characterization of Homopolymer and Block Copolymer Electrolytes. *Journal of The Electrochemical Society* **2018**, *165* (11), A2766–A2773. <https://doi.org/10.1149/2.0641811jes>.
- (160) Schauer, N. S.; Harry, K. J.; Parkinson, D. Y.; Watanabe, H.; Balsara, N. P. Lithium Dendrite Growth in Glassy and Rubbery Nanostructured Block Copolymer Electrolytes. *Journal of The Electrochemical Society* **2014**, *162* (3), A398–A405. <https://doi.org/10.1149/2.0511503jes>.
- (161) Leibler, L. Theory of Microphase Separation in Block Copolymers. *Macromolecules* **1980**, *13* (6), 1602–1617. <https://doi.org/10.1021/ma60078a047>.
- (162) Thelen, J. L.; Teran, A. A.; Wang, X.; Garetz, B. A.; Nakamura, I.; Wang, Z. G.; Balsara, N. P. Phase Behavior of a Block Copolymer/Salt Mixture through the Order-to-Disorder Transition. *Macromolecules* **2014**, *47* (8), 2666–2673. <https://doi.org/10.1021/ma500292n>.
- (163) Shim, J.; Xie, S.; Bates, F. S.; Lodge, T. P. Effect of Ion Concentration on the Formation of Bicontinuous Microemulsions in Partially Charged Ternary Polymer Blends. *Macromolecules* **2019**, *52*, 9416–9424. <https://doi.org/10.1021/acs.macromol.9b02104>.

- (164) Flory, P. J. *Principles of Polymer Chemistry*; Cornell University Press: Ithaca, NY, 1953.
- (165) Knychala, P.; Timachova, K.; Banaszak, M.; Balsara, N. P. 50th Anniversary Perspective: Phase Behavior of Polymer Solutions and Blends. *Macromolecules* **2017**, *50* (8), 3051–3065. <https://doi.org/10.1021/acs.macromol.6b02619>.
- (166) Lohse, D. J. The Melt Compatibility of Blends of Polypropylene and Ethylene-propylene Copolymers. *Polymer Engineering & Science* **1986**, *26* (21), 1500–1509. <https://doi.org/10.1002/pen.760262106>.
- (167) Kwag, H.; Rana, D.; Cho, K.; Rhee, J.; Woo, T.; Lee, B. H.; Choe, S. Binary Blends of Metallocene Polyethylene with Conventional Polyolefins: Rheological and Morphological Properties. *Polymer Engineering and Science* **2000**, *40* (7), 1672–1681. <https://doi.org/10.1002/pen.11299>.
- (168) Wheatle, B. K.; Lynd, N. A.; Ganesan, V. Effect of Host Incompatibility and Polarity Contrast on Ion Transport in Ternary Polymer-Polymer-Salt Blend Electrolytes. *Macromolecules* **2020**, *53* (3), 875–884. <https://doi.org/10.1021/acs.macromol.9b02510>.
- (169) Loo, W. S.; Mongcopa, K. I.; Gribble, D. A.; Faraone, A. A.; Balsara, N. P. Investigating the Effect of Added Salt on the Chain Dimensions of Poly(Ethylene Oxide) through Small-Angle Neutron Scattering. *Macromolecules* **2019**, *52* (22), 8724–8732. <https://doi.org/10.1021/acs.macromol.9b01509>.
- (170) Glinka, C. J.; Barker, J. G.; Hammouda, B.; Krueger, S.; Moyer, J. J.; Orts, W. J. The 30 m Small-Angle Neutron Scattering Instruments at the National Institute of Standards and Technology. *Journal of Applied Crystallography* **1998**, *31* (3), 430–445. <https://doi.org/10.1107/S0021889897017020>.
- (171) Kline, S. R. Reduction and Analysis of SANS and USANS Data Using IGOR Pro. *Journal of Applied Crystallography* **2006**, *39* (6), 895–900. <https://doi.org/10.1107/S0021889806035059>.
- (172) Kline, S. *SANS Data Reduction Tutorial*; NIST Center for Neutron Research, 2001.
- (173) Utracki, L. A.; Wilkie, C. A. *Polymer Blends Handbook*, 2nd ed.; Springer, 2014.
- (174) Vallée, A.; Besner, S.; Prud'Homme, J. Comparative Study of Poly(Ethylene Oxide) Electrolytes Made with LiN(CF₃SO₂)₂, LiCF₃SO₃ and LiClO₄: Thermal Properties and Conductivity Behaviour. *Electrochimica Acta* **1992**, *37* (9), 1579–1583. [https://doi.org/10.1016/0013-4686\(92\)80115-3](https://doi.org/10.1016/0013-4686(92)80115-3).
- (175) Le Nest, J. F.; Gandini, A.; Cheradame, H.; Cohen-Addad, J. P. Influence of LiClO₄ on the Properties of Polyether Networks: Specific Volume and Glass Transition Temperature. *Macromolecules* **1988**, *21* (4), 1117–1120. <https://doi.org/10.1021/ma00182a044>.
- (176) Flory, P. J. Thermodynamics of High Polymer Solutions. *J. Chem. Phys.* **1942**, *46* (15), 51–61. <https://doi.org/10.1063/1.1723621>.

- (177) Huggins, M. L. Some Properties of Solutions of Long-Chain Compounds. *Journal of Physical Chemistry* **1942**, *46* (1), 151–158. <https://doi.org/10.1021/j150415a018>.
- (178) Balsara, N. P.; Fetters, L. J.; Hadjichristidis, N.; Lohse, D. J.; Han, C. C.; Graessley, W. W.; Krishnamoorti, R. Thermodynamic Interactions in Model Polyolefin Blends Obtained by Small-Angle Neutron Scattering. *Macromolecules* **1992**, *25* (23), 6137–6147. <https://doi.org/10.1021/ma00049a009>.
- (179) Dubner, W. S.; Schultz, J. M.; Wignall, G. D. Estimation of Incoherent Backgrounds in SANS Studies of Polymers. *Journal of Applied Crystallography* **1990**, *23* (6), 469–475. <https://doi.org/10.1107/S0021889890006215>.
- (180) de Gennes, P. G. Theory of X-Ray Scattering by Liquid Macromolecules with Heavy Atom Labels. *Journal de Physique* **1970**, *31* (2–3), 235–238. <https://doi.org/10.1051/jphys:01970003102-3023500>.
- (181) Hammouda, B. Random Phase Approximation for Compressible Polymer Blends. *Journal of Non-Crystalline Solids* **1994**, *172–174*, 927–931. [https://doi.org/10.1016/0022-3093\(94\)90600-9](https://doi.org/10.1016/0022-3093(94)90600-9).
- (182) Qiu, J.; Mongcopa, K. I.; Han, R.; López-Barrón, C. R.; Robertson, M. L.; Krishnamoorti, R. Thermodynamic Interactions in a Model Polydiene/Polyolefin Blend Based on 1,2-Polybutadiene. *Macromolecules* **2018**, *51* (8), 3107–3115. <https://doi.org/10.1021/acs.macromol.7b02181>.
- (183) Mark, J. E. *Physical Properties of Polymers Handbook*, 2nd ed.; Springer, 2007.
- (184) Bates, F. S.; Fredrickson, G. H. Block Copolymer Thermodynamics: Theory And Experiment. *Annual Review of Physical Chemistry* **1990**, *41* (1), 525–557. <https://doi.org/10.1146/annurev.physchem.41.1.525>.
- (185) Wang, Z. G. Effects of Ion Solvation on the Miscibility of Binary Polymer Blends. *Journal of Physical Chemistry B* **2008**, *112* (50), 16205–16213. <https://doi.org/10.1021/jp806897t>.
- (186) Nakamura, I.; Balsara, N. P.; Wang, Z. G. Thermodynamics of Ion-Containing Polymer Blends and Block Copolymers. *Physical Review Letters* **2011**, *107* (19), 1–5. <https://doi.org/10.1103/PhysRevLett.107.198301>.
- (187) Young, W. S.; Epps, T. H. Salt Doping in PEO-Containing Block Copolymers: Counterion and Concentration Effects. *Macromolecules* **2009**, *42* (7), 2672–2678. <https://doi.org/10.1021/ma802799p>.
- (188) Naidu, S.; Ahn, H.; Gong, J.; Kim, B.; Ryu, D. Y. Phase Behavior and Ionic Conductivity of Lithium Perchlorate-Doped Polystyrene-*b*-Poly(2-Vinylpyridine) Copolymer. *Macromolecules* **2011**, *44* (15), 6085–6093. <https://doi.org/10.1021/ma200429v>.

- (189) Huang, J.; Tong, Z. Z.; Zhou, B.; Xu, J. T.; Fan, Z. Q. Salt-Induced Microphase Separation in Poly(ϵ -Caprolactone)-b-Poly(Ethylene Oxide) Block Copolymer. *Polymer (Guildf)* **2013**, *54* (12), 3098–3106. <https://doi.org/10.1016/j.polymer.2013.03.070>.
- (190) Hou, K. J.; Qin, J. Solvation and Entropic Regimes in Ion-Containing Block Copolymers. *Macromolecules* **2018**, *51*, 7463–7475. <https://doi.org/10.1021/acs.macromol.8b01616>.
- (191) Morris, M. A.; Sung, S. H.; Ketkar, P. M.; Dura, J. A.; Nieuwendaal, R. C.; Epps, T. H. Enhanced Conductivity via Homopolymer-Rich Pathways in Block Polymer-Blended Electrolytes. *Macromolecules* **2019**, *52* (24), 9682–9692. <https://doi.org/10.1021/acs.macromol.9b01879>.
- (192) Jung, H.-G.; Hassoun, J.; Park, J.-B.; Sun, Y.-K.; Scrosati, B. An Improved High-Performance Lithium-Air Battery. *Nature Chemistry* **2012**, *4*, 579–585. <https://doi.org/10.1038/nchem.1376>.
- (193) Nasybulin, E.; Xu, W.; Engelhard, M. H.; Nie, Z.; Burton, S. D.; Cosimbescu, L.; Gross, M. E.; Zhang, J. Effects of Electrolyte Salts on the Performance Li-O₂ Batteries. *Journal of Physical Chemistry B* **2013**, *117*, 2635–2645. <https://doi.org/10.1021/jp311114u>.
- (194) Jache, B.; Binder, J. O.; Abe, T.; Adelhelm, P. A Comparative Study on the Impact of Different Glymes and Their Derivatives as Electrolyte Solvents for Graphite Co-Intercalation Electrodes in Lithium-Ion and Sodium-Ion Batteries. *Physical Chemistry Chemical Physics* **2016**, *18*, 14299–14316. <https://doi.org/10.1039/c6cp00651e>.
- (195) Fetters, L. J.; Lohse, D. J.; Milner, S. T.; Graessley, W. W. Packing Length Influence in Linear Polymer Melts on the Entanglement, Critical, and Reptation Molecular Weights. *Macromolecules* **1999**, *32*, 6847–6851. <https://doi.org/10.1021/ma990620o>.
- (196) Tsuchida, E.; Ohno, H.; Tsunemi, K.; Kobayashi, N. Lithium Ionic Conduction in Poly(Methacrylic Acid)-Poly(Ethylene Oxide) Complex Containing Lithium Perchlorate. *Solid State Ionics* **1983**, *11*, 227–233. [https://doi.org/10.1016/0167-2738\(83\)90028-0](https://doi.org/10.1016/0167-2738(83)90028-0).
- (197) Abraham, K. M.; Alamgir, M.; Reynolds, R. K. Polyphosphazene-Poly(Olefin Oxide) Mixed Polymer Electrolytes. *J. Electrochem. Soc.* **1989**, *136* (12), 3576–3582. <https://doi.org/10.1149/1.2096512>.
- (198) Orihara, K.; Yonekura, H. Nonlinear Effects on the Ionic Conductivity of Poly(Ethylene Oxide)/Lithium Perchlorate Complexes Caused by the Blending of Poly(Vinyl Acetate). *J. Macromol. Sci., Part A: Pure Appl. Chem.* **1990**, *27*, 1217–1223. <https://doi.org/10.1080/00222339009349687>.
- (199) Li, J.; Mintz, E. A.; Khan, I. M. Poly(Ethylene Oxide)/(Poly(2-Vinylpyridine)/Lithium Perchlorate Blends. New Materials for Solid Polymer Electrolytes. *Chem. Mater.* **1992**, *4* (6), 1131–1134. <https://doi.org/10.1021/cm00024a002>.

- (200) Acosta, J. L.; Morales, E. Structural, Morphological and Electrical Characterization of Polymer Electrolytes Based on PEO/PPO Blends. *Solid State Ionics* **1996**, *85*, 85–90. [https://doi.org/10.1016/0167-2738\(96\)00045-8](https://doi.org/10.1016/0167-2738(96)00045-8).
- (201) Kim, D.; Park, J.; Rhee, H. Conductivity and Thermal Studies of Solid Polymer Electrolytes Prepared by Blending Poly(Ethylene Oxide), Poly(Oligo[Oxyethylene]Oxysebacoyl) and Lithium Perchlorate. *Solid State Ionics* **1996**, *83*, 49–56. [https://doi.org/10.1016/0167-2738\(95\)00238-3](https://doi.org/10.1016/0167-2738(95)00238-3).
- (202) Jacob, M. M. E.; Prabaharan, S. R. S.; Radhakrishna, S. Effect of PEO Addition on the Electrolytic and Thermal Properties of PVDF-LiClO₄ Polymer Electrolytes. *Solid State Ionics* **1997**, *104*, 267–276. [https://doi.org/10.1016/S0167-2738\(97\)00422-0](https://doi.org/10.1016/S0167-2738(97)00422-0).
- (203) Rocco, A. M.; da Fonseca, C. P.; Pereira, R. P. A Polymeric Solid Electrolyte Based on a Binary Blend of Poly(Ethylene Oxide), Poly(Methyl Vinyl Ether-Maleic Acid) and LiClO₄. *Polymer (Guildf)* **2002**, *43* (13), 3601–3609. [https://doi.org/10.1016/S0032-3861\(02\)00173-8](https://doi.org/10.1016/S0032-3861(02)00173-8).
- (204) Rocco, A. M.; de Assis Carias, A.; Pereira, R. P. Polymer Electrolytes Based on a Ternary Miscible Blend of Poly(Ethylene Oxide), Poly(Bisphenol A-Co-Epichlorohydrin) and Poly(Vinyl Ethyl Ether). *Polymer (Guildf)* **2010**, *51* (22), 5151–5164. <https://doi.org/10.1016/j.polymer.2010.08.050>.
- (205) Correia, D. M.; Costa, C. M.; Nunes-Pereira, J.; Silva, M. M.; Botelho, G.; Ribelles, J.; Lanceros-Mendez, S. Physicochemical Properties of Poly(Vinylidene Fluoride-Trifluoroethylene)/Poly(Ethylene Oxide) Blend Membranes for Lithium Ion Battery Applications: Influence of Poly(Ethylene Oxide) Molecular Weight. *Solid State Ionics* **2014**, *268*, 54–67. <https://doi.org/10.1016/j.ssi.2014.09.029>.
- (206) Ito, H.; Russell, T. P.; Wignall, G. D. Interactions in Mixtures of Poly(Ethylene Oxide) and Poly(Methyl Methacrylate). *Macromolecules* **1987**, *20* (9), 2213–2220. <https://doi.org/10.1021/ma00175a028>.
- (207) Yeh, C.; Hou, T.; Chen, H.; Yeh, L.; Chiu, F.-C.; Muller, A. J.; Hadjichristidis, N. Lower Critical Ordering Transition of Poly(Ethylene Oxide)-Block-Poly(2-Vinylpyridine). *Macromolecules* **2011**, *44*, 440–443. <https://doi.org/10.1021/ma102322w>.
- (208) Zhang, J.; Yang, J.; Dong, T.; Zhang, M.; Chai, J.; Dong, S.; Wu, T.; Zhou, X.; Cui, G. Aliphatic Polycarbonate-Based Solid-State Polymer Electrolytes for Advanced Lithium Batteries: Advances and Perspective. *Small* **2018**, *14* (36), 1–16. <https://doi.org/10.1002/sml.201800821>.
- (209) Pesko, D. M.; Webb, M. A.; Jung, Y.; Zheng, Q.; Miller, T. F.; Coates, W.; Balsara, N. P. Universal Relationship between Conductivity and Solvation-Site Connectivity in Ether-Based Polymer Electrolytes. *Macromolecules* **2016**, *49*, 5244–5255. <https://doi.org/10.1021/acs.macromol.6b00851>.

- (210) Wood, K. N.; Noked, M.; Dasgupta, N. P. Lithium Metal Anodes: Toward an Improved Understanding of Coupled Morphological, Electrochemical, and Mechanical Behavior. *ACS Energy Letters*. American Chemical Society March 10, 2017, pp 664–672. <https://doi.org/10.1021/acseenergylett.6b00650>.
- (211) Trahey, L.; Brushett, F. R.; Balsara, N. P.; Ceder, G.; Cheng, L.; Chiang, Y. M.; Hahn, N. T.; Ingram, B. J.; Minter, S. D.; Moore, J. S.; Mueller, K. T.; Nazar, L. F.; Persson, K. A.; Siegel, D. J.; Xu, K.; Zavadil, K. R.; Srinivasan, V.; Crabtree, G. W. Energy Storage Emerging: A Perspective from the Joint Center for Energy Storage Research. *Proc Natl Acad Sci U S A* **2020**, *117* (23), 12550–12557. <https://doi.org/10.1073/pnas.1821672117>.
- (212) Brandell, D.; Mindemark, J.; Hernandez, G. *Polymer-Based Solid State Batteries*; De Gruyter, 2021.
- (213) Jones, S. D.; Nguyen, H.; Richardson, P. M.; Chen, Y. Q.; Wyckoff, K. E.; Hawker, C. J.; Clément, R. J.; Fredrickson, G. H.; Segalman, R. A. Design of Polymeric Zwitterionic Solid Electrolytes with Superionic Lithium Transport. *ACS Central Science* **2022**, *8* (2), 169–175. <https://doi.org/10.1021/acscentsci.1c01260>.
- (214) Porcarelli, L.; Gerbaldi, C.; Bella, F.; Nair, J. R. Super Soft All-Ethylene Oxide Polymer Electrolyte for Safe All-Solid Lithium Batteries. *Scientific Reports* **2016**, *6*. <https://doi.org/10.1038/srep19892>.
- (215) Zhang, W.; Nie, J.; Li, F.; Wang, Z. L.; Sun, C. A Durable and Safe Solid-State Lithium Battery with a Hybrid Electrolyte Membrane. *Nano Energy* **2018**, *45*, 413–419. <https://doi.org/10.1016/j.nanoen.2018.01.028>.
- (216) Dahbi, M.; Ghamouss, F.; Tran-Van, F.; Lemordant, D.; Anouti, M. Comparative Study of EC/DMC LiTFSI and LiPF₆ Electrolytes for Electrochemical Storage. *Journal of Power Sources* **2011**, *196* (22), 9743–9750. <https://doi.org/10.1016/j.jpowsour.2011.07.071>.
- (217) Snyder, R. L.; Choo, Y.; Gao, K. W.; Halat, D. M.; Abel, B. A.; Sundararaman, S.; Prendergast, D.; Reimer, J. A.; Balsara, N. P.; Coates, G. W. Improved Li⁺ Transport in Polyacetal Electrolytes: Conductivity and Current Fraction in a Series of Polymers. *ACS Energy Letters* **2021**, *6* (5), 1886–1891. <https://doi.org/10.1021/acseenergylett.1c00594>.
- (218) Yu, X.-Y.; Xiao, M.; Shuang-Jin, W.; Qi-Qiang, Z.; Yue-Zhong, M. Fabrication and Characterization of Peo/Ppc Polymer Electrolyte for Lithium-Ion Battery. *Journal of Applied Polymer Science* **2010**, *115* (5), 2718–2722. <https://doi.org/10.1002/app.29915>.
- (219) Caradant, L.; Verdier, N.; Foran, G.; Lepage, D.; Prébé, A.; Aymé-Perrot, D.; Dollé, M. Extrusion of Polymer Blend Electrolytes for Solid-State Lithium Batteries: A Study of Polar Functional Groups. *ACS Applied Polymer Materials* **2021**, *3* (12), 6694–6704. <https://doi.org/10.1021/acsapm.1c01466>.
- (220) Heller, W. T.; Cuneo, M.; Debeer-Schmitt, L.; Do, C.; He, L.; Heroux, L.; Littrell, K.; Pingali, S. V.; Qian, S.; Stanley, C.; Urban, V. S.; Wu, B.; Bras, W. The Suite of Small-Angle Neutron Scattering Instruments at Oak Ridge National Laboratory. *Journal of*

- Applied Crystallography* **2018**, *51* (2), 242–248.
<https://doi.org/10.1107/S1600576718001231>.
- (221) Heller, W. T.; Hetrick, J.; Bilheux, J.; Calvo, J. M. B.; Chen, W.-R.; DeBeer-Schmitt, L.; Do, C.; Doucet, M.; Fitzsimmons, M. R.; Godoy, W. F.; Granroth, G. E.; Hahn, S.; He, L.; Islam, F.; Lin, J.; Littrell, K. C.; McDonnell, M.; McGaha, J.; Peterson, P. F.; Pingali, S. V.; Qian, S.; Savici, A. T.; Shang, Y.; Stanley, C. B.; Urban, V. S.; Whitfield, R. E.; Zhang, C.; Zhou, W.; Billings, J. J.; Cuneo, M. J.; Leal, R. M. F.; Wang, T.; Wu, B. Drtsans: The Data Reduction Toolkit for Small-Angle Neutron Scattering at Oak Ridge National Laboratory. *SoftwareX* **2022**, *19*, 101101.
<https://doi.org/10.1016/j.softx.2022.101101>.
- (222) Nakamura, I.; Wang, Z. G. Thermodynamics of Salt-Doped Block Copolymers. *ACS Macro Letters* **2014**, *3* (8), 708–711. <https://doi.org/10.1021/mz500301z>.
- (223) Ziya Akcasu, A.; Tombakoglu, M. Dynamics of Copolymer and Homopolymer Mixtures in Bulk and in Solution via the Random Phase Approximation. *Macromolecules* **1990**, *23* (2), 607–612. <https://doi.org/10.1021/ma00204a038>.
- (224) Higgins, J. S.; Benoit, H. C. *Polymers and Neutron Scattering*; 1997.
- (225) Donnan, F. G. Theorie Der Membrangleichgewichte Und Membranpotentiale Bei Vorhandensein von Nicht Dialysierenden Elektrolyten. Ein Beitrag Zur Physikalisch-Chemischen Physiologie. *Zeitschrift fur elektrochemie* **1911**, *17* (10), 572–581.
<https://doi.org/10.1002/bbpc.19110171405>.
- (226) Donnan, F. G. The Theory of Membrane Equilibria. *Chem. Rev.* **1924**, *1*, 73–90.
<https://doi.org/10.1021/cr60001a003>.
- (227) Donnan, F. G. Theory of Membrane Equilibria and Membrane Potentials in the Presence of Non-Dialysing Electrolytes. A Contribution to Physical-Chemical Physiology. *Journal of Membrane Science* **1995**, *100* (1), 45–55. [https://doi.org/10.1016/0376-7388\(94\)00297-C](https://doi.org/10.1016/0376-7388(94)00297-C).
- (228) Katchalsky, A.; Kedem, O. Thermodynamics of Flow Processes in Biological Systems. *Biophysical Journal* **1962**, *2* (2), 53–78. [https://doi.org/10.1016/s0006-3495\(62\)86948-3](https://doi.org/10.1016/s0006-3495(62)86948-3).
- (229) Bansil, R.; Stanley, E.; Thomas LaMont, J. Mucin Biophysics. *Annual Review of Physiology* **1995**, *57* (February), 635–657.
<https://doi.org/10.1146/annurev.ph.57.030195.003223>.
- (230) Preska Steinberg, A.; Wang, Z. G.; Ismagilov, R. F. Food Polyelectrolytes Compress the Colonic Mucus Hydrogel by a Donnan Mechanism. *Biomacromolecules* **2019**, *20* (7), 2675–2683. <https://doi.org/10.1021/acs.biomac.9b00442>.
- (231) Mussel, M.; Basser, P. J.; Horkay, F. Ion-Induced Volume Transition in Gels and Its Role in Biology. *Gels* **2021**, *7* (1), 1–17. <https://doi.org/10.3390/GELS7010020>.

- (232) Yewdall, N. A.; André, A. A. M.; Lu, T.; Spruijt, E. Coacervates as Models of Membraneless Organelles. *Current Opinion in Colloid and Interface Science* **2021**, *52*, 101416. <https://doi.org/10.1016/j.cocis.2020.101416>.
- (233) Helfferich, F. *Ion Exchange*; McGraw-Hill: New York, 1962.
- (234) Schlenoff, J. B.; Yang, M.; Digby, Z. A.; Wang, Q. Ion Content of Polyelectrolyte Complex Coacervates and the Donnan Equilibrium. *Macromolecules* **2019**, *52* (23), 9149–9159. <https://doi.org/10.1021/acs.macromol.9b01755>.
- (235) Gehrke, S. H. Kinetics of Gel Volume Change and Its Interaction with Solutes, University of Minnesota, 1986.
- (236) Skouri, R.; Schosseler, F.; Munch, J. P.; Candau, S. J. Swelling and Elastic Properties of Polyelectrolyte Gels. *Macromolecules* **1995**, *28* (1), 197–210. <https://doi.org/10.1021/ma00105a026>.
- (237) Geise, G. M.; Falcon, L. P.; Freeman, B. D.; Paul, D. R. Sodium Chloride Sorption in Sulfonated Polymers for Membrane Applications. *Journal of Membrane Science* **2012**, *423–424*, 195–208. <https://doi.org/10.1016/j.memsci.2012.08.014>.
- (238) Doi, M. *Soft Matter Physics*; Oxford University Press: New York, 2013.
- (239) Flory, P. J.; Rehner, J. Statistical Mechanics of Cross-Linked Polymer Networks I. Rubberlike Elasticity. *The Journal of Chemical Physics* **1943**, *11* (11), 512–520. <https://doi.org/10.1063/1.1723791>.
- (240) Yu, X.; Jiang, X.; Seidler, M. E.; Shah, N. J.; Gao, K. W.; Chakraborty, S.; Villaluenga, I.; Balsara, N. P. Nanostructured Ionic Separator Formed by Block Copolymer Self-Assembly: A Gateway for Alleviating Concentration Polarization in Batteries. *Macromolecules* **2022**, *55* (7), 2787–2796. <https://doi.org/10.1021/acs.macromol.2c00193>.
- (241) Flory, P. J. Thermodynamics of High Polymer Solutions. *J. Chem. Phys.* **1941**, *9*, 660. <https://doi.org/10.1063/1.1750971>.
- (242) Katchalsky, A.; Michaeli, I. Polyelectrolyte Gels in Salt Solutions. *Journal of Polymer Science* **1955**, *15* (79), 69–86. <https://doi.org/10.1002/pol.1955.120157906>.
- (243) Khokhlov, A. R.; Dormidontova, E. E. Self-Organization in Ion-Containing Polymer Systems. *Phys.-Usp.* **1997**, *40* (2), 109–124. <https://doi.org/10.1070/PU1997v040n02ABEH000191>.
- (244) Rička, J.; Tanaka, T. Swelling of Ionic Gels: Quantitative Performance of the Donnan Theory. *Macromolecules* **1984**, *17* (12), 2916–2921. <https://doi.org/10.1021/ma00142a081>.
- (245) Jeon, C. H.; Makhaeva, E. E.; Khokhlov, A. R. Swelling Behavior of Polyelectrolyte Gels in the Presence of Salts. *Macromolecular Chemistry and Physics* **1998**, *199* (12), 2665–

2670. [https://doi.org/10.1002/\(SICI\)1521-3935\(19981201\)199:12<2665::AID-MACP2665>3.0.CO;2-6](https://doi.org/10.1002/(SICI)1521-3935(19981201)199:12<2665::AID-MACP2665>3.0.CO;2-6).
- (246) Manning, G. S. Polyelectrolytes. *Annu. Rev. Phys. Chem.* **1972**, *23*, 117–140. <https://doi.org/10.1146/annurev.pc.23.100172.001001>.
- (247) Manning, G. S. Limiting Laws and Counterion Condensation in Polyelectrolyte Solutions II. Self-Diffusion of the Small Ions. *The Journal of Chemical Physics* **1969**, *51* (3), 934–938. <https://doi.org/10.1063/1.1672158>.
- (248) Vis, M.; Peters, V. F. D.; Tromp, R. H.; Ern , B. H. Donnan Potentials in Aqueous Phase-Separated Polymer Mixtures. *Langmuir* **2014**, *30* (20), 5755–5762. <https://doi.org/10.1021/la501068e>.
- (249) Khokhlov, A. R.; Starodubtzev, S. G.; Vasilevskaya, V. V. *Conformational Transitions in Polymer Gels: Theory and Experiment*; 1993; Vol. 109. https://doi.org/10.1007/3-540-56791-7_3.
- (250) Kramarenko, E. Y.; Philippova, O. E.; Khokhlov, A. R. Polyelectrolyte Networks as Highly Sensitive Polymers. *Polymer Science - Series C* **2006**, *48* (1), 1–20. <https://doi.org/10.1134/S1811238206010012>.
- (251) Khokhlov, A. R.; Kramarenko, E. Y.; Makhaeva, E. E.; Starodubtzev, S. G. Collapse of Polyelectrolyte Networks Induced by Their Interaction with an Oppositely Charged Surfactant. Theory. *Macromolecular Theory and Simulations* **1992**, *1* (3), 105–118. <https://doi.org/10.1002/mats.1992.040010301>.
- (252) Yin, D. W.; Olvera De La Cruz, M.; De Pablo, J. J. Swelling and Collapse of Polyelectrolyte Gels in Equilibrium with Monovalent and Divalent Electrolyte Solutions. *Journal of Chemical Physics* **2009**, *131* (19). <https://doi.org/10.1063/1.3264950>.
- (253) Kamcev, J.; Paul, D. R.; Freeman, B. D. Ion Activity Coefficients in Ion Exchange Polymers: Applicability of Manning’s Counterion Condensation Theory. *Macromolecules* **2015**, *48* (21), 8011–8024. <https://doi.org/10.1021/acs.macromol.5b01654>.
- (254) Kamcev, J.; Galizia, M.; Benedetti, F. M.; Jang, E. S.; Paul, D. R.; Freeman, B. D.; Manning, G. S. Partitioning of Mobile Ions between Ion Exchange Polymers and Aqueous Salt Solutions: Importance of Counter-Ion Condensation. *Physical Chemistry Chemical Physics* **2016**, *18* (8), 6021–6031. <https://doi.org/10.1039/c5cp06747b>.
- (255) Kamcev, J.; Paul, D. R.; Manning, G. S.; Freeman, B. D. Predicting Salt Permeability Coefficients in Highly Swollen, Highly Charged Ion Exchange Membranes. *ACS Applied Materials and Interfaces* **2017**, *9* (4), 4044–4056. <https://doi.org/10.1021/acsami.6b14902>.
- (256) Kamcev, J.; Paul, D. R.; Freeman, B. D. Effect of Fixed Charge Group Concentration on Equilibrium Ion Sorption in Ion Exchange Membranes. *Journal of Materials Chemistry A* **2017**, *5* (9), 4638–4650. <https://doi.org/10.1039/c6ta07954g>.

- (257) Kamcev, J.; Paul, D. R.; Freeman, B. D. Equilibrium Ion Partitioning between Aqueous Salt Solutions and Inhomogeneous Ion Exchange Membranes. *Desalination* **2018**, *446* (May), 31–41. <https://doi.org/10.1016/j.desal.2018.08.018>.
- (258) Yu, C. J.; Ri, U. S.; Ri, G. C.; Kim, J. S. Revealing the Formation and Electrochemical Properties of Bis(Trifluoromethanesulfonyl)Imide Intercalated Graphite with First-Principles Calculations. *Physical Chemistry Chemical Physics* **2018**, *20* (20), 14124–14132. <https://doi.org/10.1039/c8cp01468j>.
- (259) Marcus, Y. The Standard Partial Molar Volumes of Ions in Solution. Part 4. Ionic Volumes in Water at 0–100 °C. *Journal of Physical Chemistry B* **2009**, *113*, 10285–10291. <https://doi.org/10.1021/jp9027244>.
- (260) Thompson, S. D.; Newman, J. Differential Diffusion Coefficients of Sodium Polysulfide Melts. *Journal of The Electrochemical Society* **1989**, *136* (11), 3362–3369. <https://doi.org/10.1149/1.2096451>.

11 Appendices

11.1 Additional Discussion on Electrochemical Experiments and Data Analysis

11.1.1 Resistance Measurements and Fitting

Many of the electrochemical experiments in this thesis utilize impedance spectroscopy to measure resistances within the electrolyte. For example, measuring the ionic conductivity requires knowledge of the bulk resistance of the electrolyte. To do this, one can utilize either a blocking or non-blocking electrode setup. In the case of a blocking electrode setup, the polymer electrolyte is placed between two blocking electrodes such as stainless steel. Ac impedance spectroscopy can then be run via potentiostat over a 0.1-10⁶ Hz frequency range at an amplitude of 80 mV. The resulting Nyquist plot will yield a single semicircle with a touch down point (see Figure 5.21a). The bulk resistance can be easily calculated as that touch down point (which is a local minima). In the case of a non-blocking electrode setup, the polymer electrolyte is sandwiched between two lithium electrodes. This lithium-polymer-lithium stack will have two resistances of interest: the bulk resistance of the electrolyte itself, and an interfacial resistance from the electrolyte-lithium interface. This will manifest itself in a Nyquist plot as two semicircles (see Figure 5.21b).

In both cases, one can use EC-Lab's built in "Analysis" > "Electrochemical Impedance Spectroscopy" > "Z Fit" program to manually fit the Nyquist data to an equivalent circuit. A detailed description of the equivalent circuit is beyond the scope of this Appendix. For a typical blocking electrode setup, the equivalent circuit can be seen in Figure 11.1a, where we have an inductor (L_1) in series with a resistor (R_1) and the bulk resistor (R_b) and bulk constant phase element (Q_b) in parallel. L_1 and R_1 represents the inductance and resistance of the potentiostat cables, respectively. The bulk resistance is the parameter of interest. For a typical non-blocking electrode setup, the equivalent circuit can be seen in Figure 11.1b, where in addition to the elements found in the blocking electrode setup, we have elements representing interfacial components.

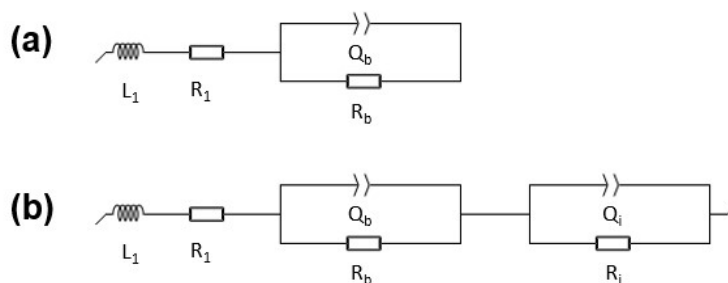


Figure 11.1. Equivalent circuits for (a) blocking electrode and (b) non-blocking electrode setups. L_1 and R_1 represents the inductance and resistance of the potentiostat cable respectively, R_b and R_i represent the bulk and interfacial resistance, and Q_b and Q_i represent the constant phase elements of the bulk and interface.

It is illustrative to understand how EC-Lab's "Z Fit" algorithm works. "Z Fit" seeks to find the best fit of the data by minimizing the following function:

$$F(f) = \frac{\sum(\Delta Z_r^2 + \Delta Z_i^2)}{\sum(|Z|^2)}, \quad (11.1)$$

where $\Delta Z_r = Z_r(\text{fit}) - Z_r(\text{data})$, $\Delta Z_i = Z_i(\text{fit}) - Z_i(\text{data})$, Z is the impedance and the subscripts i and r denote imaginary and real components respectively, and f is the frequency. A high throughput analysis for impedance data files can be done through implementation of EC-Lab's "Z Fit" via a separate programming language such as Python or MATLAB. Sample code for implementing a more automated (*i.e.* not having to manually fit in EC-Labs) procedure is provided below. The freely available function `fminsearchbnd.m()` must be downloaded, and the following functions must be written:

```
function [p, fval, exitflag, output] = curvefit( pinit, circuit, ...
                                              freq, ZrZi, ...
                                              lb, ub, options)
% Minimization function via fminsearchbnd()
parameters = pinit;
[p, fval, exitflag, output] = fminsearchbnd(@distance, parameters, lb, ub,
options);

% nested function
function dist = distance(parameters)

predicted_ZrZi = feval(circuit, parameters, freq);

% minimize sum(differences^2)/sum(|Z|^2)
dist = sum( sum((predicted_ZrZi - ZrZi).^2,2) ./ sum(ZrZi.^2,2) );
end

end
```

```
function [Rb, Ri, chi2_min] = transference_resistance( PEIS_file )

% Kevin Gao
% last edited 6/4/18
%
% INPUTS:
% [ PEIS_file ]      String; .txt file with PEIS file exported via EC-Labs:
%                   = 3 columns: 1)freq 2)Re 3)Im
%                   e.g. '10mV_02_PEIS_C01.txt'
% OUTPUTS:
% [ Rb ]            Bulk resistance (ohms)
% [ Ri ]            Interfacial resistance (ohms)
% [ chi2_min ]      Chi^2/|Z|^2 value (a measure of fit error)
%
% Calculates resistances for a Li-Li symmetric cell PEIS data up to a
% user selected point, with the following Z impedance circuit:
% [R1] + [L1] + [Q2/R2] + [Q3/R3], assuming [R1] = 0.1 ohm
```

```

%
% If not getting accurate fits, may need to change BOUNDS or INITIAL GUESS
% Can also change tolerance and stopping criterion via options

% get data from PEIS .txt file
fid = fopen(PEIS_file);

data = textscan(fid, '%f %f %f', 'HeaderLines', 1);
Hz_data = data{1};
Re_data = data{2};
Im_data = data{3};
fclose(fid);

% plot PEIS data
figure()
plot(Re_data, Im_data, 'bo')
xlabel('Re (ohm)')
ylabel('-Im (ohm)')

%%%%% NEEDS BETTER CRITERIA FOR AUTOMATION %%%%%
% find minimum after initial low frequencies
half = round(length(Im_data)/2);
[y_possible_min, index_possible_min] = min(abs(Im_data(half:end)));
% arbitrarily selected n=5 points around the minimum
n = 5;
index_bound_min = half + index_possible_min - n;
if index_bound_min <= 0
    index_bound_min = 1;
elseif index_bound_min
end %if
index_bound_max = half + index_possible_min + n;
if index_bound_max > length(Im_data)
    index_bound_max = length(Im_data);
end %if
%%%%% NEEDS BETTER CRITERIA FOR AUTOMATION %%%%%

% Z impedance circuit for [L1] + [R1] + [Q2/R2] + [Q3/R3]
% where [R1] = 0.1 ohm, [L1] = x(7)
% [Q2] = x(1), [R2] = x(2), a2 = x(5)
% [Q3] = x(3), [R3] = x(4), a3 = x(6)
fun = @(x,xdata) [ real(0.1 + (1i*xdata*2*pi)*x(7) + ...
    x(2)./(x(2).*x(1).*(1i.*xdata*2*pi).^x(5) + 1) + ...
    x(4)./(x(4).*x(3).*(1i.*xdata*2*pi).^x(6) + 1)), ...
    ...
    -imag(0.1 + (1i*xdata*2*pi)*x(7) + ...
    x(2)./(x(2).*x(1).*(1i.*xdata*2*pi).^x(5) + 1) + ...
    x(4)./(x(4).*x(3).*(1i.*xdata*2*pi).^x(6) + 1))];

p_set = zeros(index_bound_max-index_bound_min+1,7);
chi2_set = zeros(index_bound_max-index_bound_min+1,1);
for j = 1:(index_bound_max - index_bound_min)+1
    X = Re_data(1:index_bound_min+j-1);
    Y = Im_data(1:index_bound_min+j-1);
    W = Hz_data(1:index_bound_min+j-1);

```

```

%%%%% BOUNDS %%%%%
LB = [0 0 0 0 0 0];
UB = [10^-4 max(X) 10^-4 max(X) 1 1 10^-8];
%%%%% INITIAL GUESS %%%%%
x0 = [10^-10 max(X)/2 10^-10 max(X)/2 1 1 0];

ZrZi = [X, Y]; % real and imaginary Z
options = optimset('MaxFunEvals', 10*10^4, 'MaxIter', 10*10^4, ...
                  'TolFun', 1e-12, 'TolX', 1e-12);

% fit data to circuit model
[p,fval,exitflag,output] = curvefit(x0,fun,W,ZrZi,UB,options);

chi2_set(j) = fval; % store chi^2/|Z|^2 value
p_set(j,:) = p; % store parameters

end %for

% choose best chi^2/|Z|^2 i.e. best fit
[chi2_min,i_min] = min(chi2_set);

% store optimal chi^2/|Z|^2 value and optimal parameters
p_final = p_set(i_min,:);

% Resistance values; separate bulk and interfacial
if abs(p_final(5)-1) < abs(p_final(6)-1)
    Rb = p_final(2); % bulk
    Ri = p_final(4); % interface
else
    Rb = p_final(4); % bulk
    Ri = p_final(2); % interface
end %if

% check fit
W_array = logspace(log10(Hz_data(end))-1, log10(Hz_data(1))+1,100);
fitR_array = zeros(100,2); % initialize
for j = 1:length(W_array)
    fitR_array(j,:) = fun(p_final, W_array(j));
end %for

% graphically check fit
figure()
plot(Re_data, Im_data, 'bo')
xlabel('Re (ohm)')
ylabel('-Im (ohm)')
hold on

% show data points chosen for fit
plot(Re_data(1:index_bound_min+i_min-1), ...
     Im_data(1:index_bound_min+i_min-1), 'bx')
% show fit
plot(fitR_array(:,1), fitR_array(:,2),'--r','LineWidth', 1.5)
xlabel('Re (ohm)')
ylabel('-Im (ohm)')
legend(strcat('R_b = ', num2str(Rb)), ...

```



```

    strcat('R_i = ', num2str(Ri)), ...
    strcat('\chi^2 = ', num2str(chi2_min))

filename_str = strcat(PEIS_file(1:end-4), '_resistance_fit.jpg');
saveas(gcf, filename_str)
hold off

% show chi^2/|Z| error and calculated parameters
fprintf('\chi^2/|Z|^2 = %f\t [L1] = %E\n', chi2_min, p_final(7))
fprintf('[Q2] = %E\t [R2] = %f\t [a2] = %f\n', p_final(1), p_final(2),
p_final(5));
fprintf('[Q3] = %E\t [R3] = %f\t [a3] = %f\n', p_final(3), p_final(4),
p_final(6));

end

```

Note that the initial conditions for the fitting algorithm are very important for obtaining good accuracy in the fit. If the fit is not good, it is recommended to try adjusting initial conditions and examining the data carefully for artifacts and experimental suitability.

11.1.2 Restricted Diffusion Measurements and Analysis

For more detailed information on the restricted diffusion method, refer to ref. ⁹⁰ and ref. ²⁶⁰. A simplified analysis is presented here for a binary electrolyte. For example, in PEO/LiTFSI there is a cation and anion. Our system is a lithium-electrolyte-lithium cell. During polarization of the cell, a concentration gradient will develop and reach some steady-state concentration profile. We are interested in the relaxation of this concentration gradient. Example concentration profile curves are shown over time t (see Figure 11.2). We define an axis in the direction between the electrodes as x .

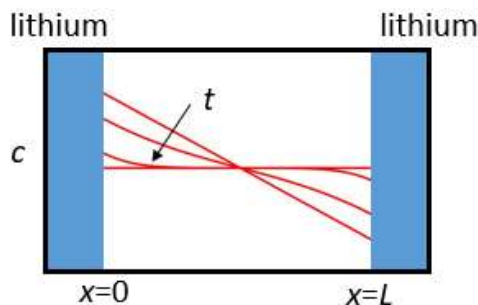


Figure 11.2. Example concentration profiles showing relaxation of concentration profiles, c , over time, t , in a lithium-electrolyte-lithium symmetric cell. The length across the electrolyte is given by L .

We begin with Fick's 2nd Law:

$$\frac{dc}{dt} = D \frac{d^2c}{dx^2}, \quad (11.2)$$

where c is the concentration, t is time, D is the salt diffusion coefficient. The boundary conditions are as follows:

$$\frac{dc}{dx} = 0 \text{ at } x = 0 \text{ and } x = L, \quad (11.3)$$

$$c(t = \infty) = c_{\infty}. \quad (11.4)$$

The first two boundary conditions are the no-flux condition at either electrode, and the third condition implies that at a long enough time (*i.e.* steady-state), there is a uniform concentration. The electrolyte velocity is assumed to be zero here. The solution to equation 11.2 is a Fourier series of the form:

$$c = c_{\infty} + \sum_{n=1}^{\infty} A_n \exp\left(-\frac{n^2\pi^2Dt}{L^2}\right) \cos\left(\frac{n\pi x}{L}\right), \quad (11.5)$$

and A_n is a coefficient dependent on the initial concentration profile in the cell. At long time, the higher order terms of equation 11.5 become negligible compared to the first term:

$$c = c_{\infty} + A_1 \exp\left(-\frac{\pi^2Dt}{L^2}\right) \cos\left(\frac{\pi x}{L}\right). \quad (11.6)$$

Then the difference in concentration at the ends of the cell in the electrolyte is given by the following:

$$\Delta c = c_{x=0} - c_{x=L} = A_1 \exp\left(-\frac{\pi^2Dt}{L^2}\right), \quad (11.7)$$

and a plot of $\ln(\Delta c)$ vs. t is linear at long time. Restricted diffusion in concentrated solution follows similar logic, and the resulting equation relating concentration difference has the same form as equation 11.7. A more detailed description can be found in ref. ⁹⁰.

We utilize the fact that $\ln(\Delta c)$ vs. t is linear at long time to calculate the salt diffusion coefficient, D . How can long time be defined? We first define a dimensionless time:

$$\alpha = \frac{Dt}{L^2}. \quad (11.8)$$

In Figure 11.3a we show several possible steady-state concentration profiles in the electrolyte after polarization. These concentration profiles serve as the initial condition for equation 11.2, and different solutions will emerge. Using these initial conditions, along with the boundary conditions given by equations 11.3 and 11.4, we can solve the partial differential equation. In Figure 11.3b,

we show the difference in concentration between the opposite ends of the electrolyte plotted against dimensionless time, α , on a semi log scale. These solutions and plots were generated using MATLAB's `pdepe()` partial differential equation solver. It is evident that at longer times, we have a linear plot of Δc on the semi log scale.

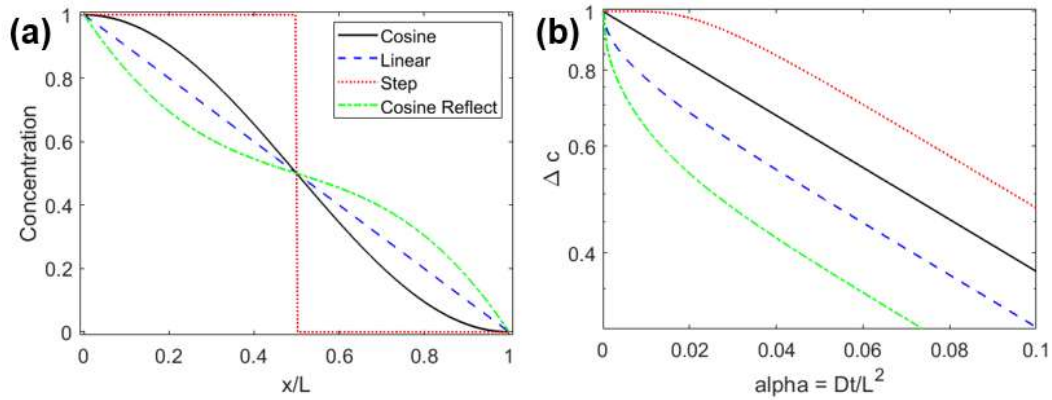


Figure 11.3. Initial concentration profiles across the electrolyte and the resulting change in concentration difference across the electrolyte over dimensionless time. (a) Several initial steady-state concentration profiles (cosine, linear, step, cosine reflected) across the electrolyte are shown, with concentration plotted against position (x/L). (b) The difference in concentration between the electrolyte at $x = 0$ and $x = L$ plotted against dimensionless time α on a semi log scale for the different initial steady-state concentration profiles shown in (a). This plot is generated from solutions to equation 11.2 given boundary conditions 11.3 and 11.4 with initial conditions given by (a).

To quantify the linearity of $\ln(\Delta c)$ vs α , we take the semi log slope from $\alpha = [a, 0.2]$ and use that in an exponential fit to the concentration relaxation solutions to qualitatively check for linearity of semi-log y-axis vs x-axis, where $\alpha = a$ is the time denoted as meeting “long time.” In Figure 11.4 we show how linear the data for $\ln(\Delta c)$ vs α after different amounts of time ($\alpha = 0.01, 0.03, 0.05$) for the different initial conditions given in Figure 11.3a. In other words, we are checking at what α value is “long time” reached. Qualitatively, it appears that $\alpha = 0.01$ is not sufficient time for linearity to be achieved, while $\alpha = 0.03$ and $\alpha = 0.05$ show a much greater linear relationship.

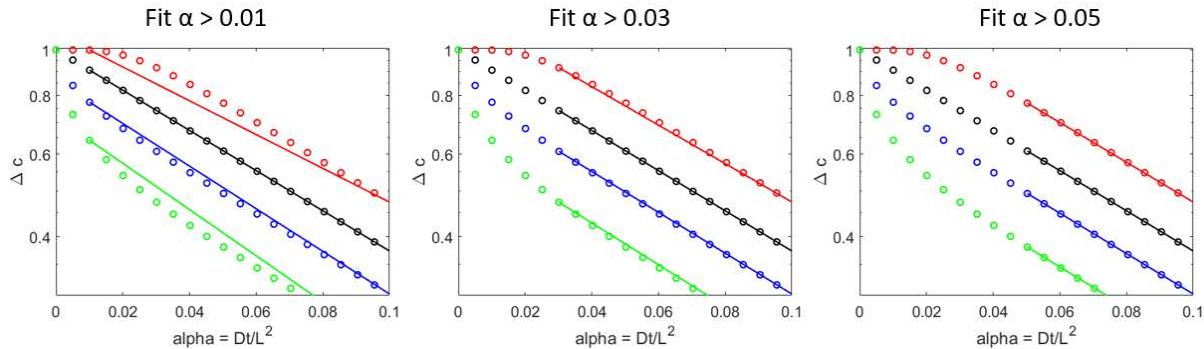


Figure 11.4. Qualitatively comparing the linearity of $\ln(\Delta c)$ vs. dimensionless time after fitting from long time of $\alpha = 0.01, 0.03, \text{ and } 0.05$. The data points represent the solutions to equation 11.2 for the different

initial conditions given in Figure 11.3 (red: step, black: cosine, blue: linear, green: cosine reflected). Note the y-axis is on a log scale.

We can quantify how linear the data is by taking the residuals of the linear fit to the data. In Figure 11.5 we plot the residuals against the α value at which we fit the concentration data. It is evident that at $\alpha = 0.03$, we have a very high R^2 value for all steady-state concentration profile relaxations ($R^2 > 0.995$). Thus, we conclude that $\alpha = 0.03$ is sufficiently “long time” for restricted diffusion calculations.

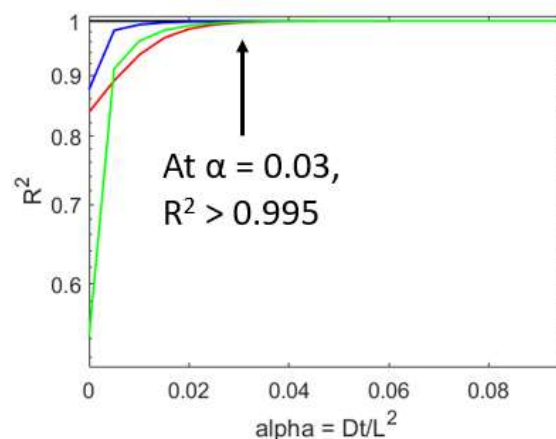


Figure 11.5. The residuals for the linear fit, R^2 , plotted against the different “long time” values of α at which the data is first fit to a linear relationship, for different initial steady-state concentration profiles (red: step, black: cosine, blue: linear, green: cosine reflected) relaxing in restricted diffusion. We see that for all initial conditions of different steady-state concentration profiles, we have very high linearity for $\alpha = 0.03$.

We now discuss the implementation of the restricted diffusion experiment in lithium-polymer-lithium cells. The first step is to apply a current density or potential difference across the cell, recording the potential or current response respectively. Once a steady-state value is reached (typically 2-4 hours for a 500 μm thick PEO/LiTFSI electrolyte), then shut off the applied potential or current and let the concentration gradient relax over time in open circuit voltage. The potential must be measured at this time. The data can then be fit to the exponential given in equation 11.7 to calculate D . We use the following equation to fit the potential data:

$$V = A_1 + A_2 \exp\left(\frac{-\pi^2 Dt}{L^2}\right), \quad (11.9)$$

where V is the measured potential, A_1 and A_2 are constants, D is the salt diffusion coefficient, and L is the thickness of the electrolyte. A_1 is the result of possible small potential drops across the cell even at uniform concentration that could be the result of minor temperature gradients or instrument artifact. The V vs t data is thus fit to equation 11.9 with three unknown parameters (A_1 , A_2 and D ; L is known). In Figure 11.6a we show an example of the potential relaxation over time and the fit of the data from $\alpha > 0.03$ onward. Because the real-world data is given in dimensional time, and the dimensionless time requires knowledge of the salt diffusion coefficient (see equation 11.8), the

data must be iteratively fit starting from different times. For more details, refer to ref. ⁸⁰. An example procedure for fitting V vs t data is outlined below:

1. Fit equation 11.9 to V data from $t = 0$ to $t = t_{\max}$ where t_{\max} is a time at which the concentration is uniform (*i.e.* steady-state is reached, around 120-150 min in Figure 11.6a). A value for D will be obtained, and α can be computed from equation 11.8.
2. Fit equation 11.9 to V data from $t = t_{\text{previous}} + t_{\text{increment}}$ to $t = t_{\max}$, where t_{previous} is the last minimum bound for the times when the data is fit and $t_{\text{increment}}$ is a small step value. A new value for D will be obtained and α can again be computed from equation 11.8.
3. Repeat step 2 until $\alpha > 0.03$ is achieved (or $\alpha > 0.05$ if desired).

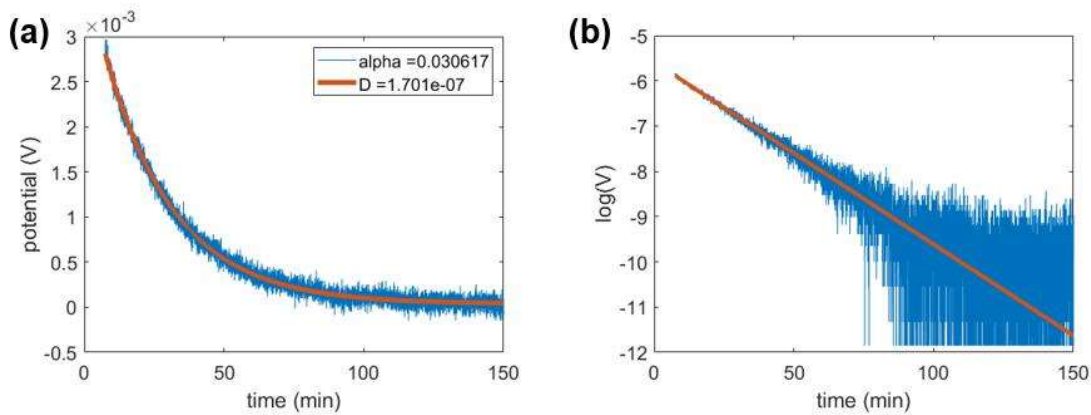


Figure 11.6. Potential over time showing relaxation of concentration gradient in a lithium-electrolyte-lithium cell. (a) Potential vs. time and fit of data to equation 11.9. (b) Log of potential vs time showing the linearity of data over time.

In Figure 11.6b we show the log of potential plotted against time. It is possible to extract a salt diffusion coefficient D from the slope of the data (see equations 11.7 and 11.9), however, notice that the $\log(V)$ data becomes quite large and negative as the potential relaxes to 0. This leads to greater error in the slope and requires careful selection of the upper bound of the time to fit the potential data to. However, fitting the data to equation 11.9 has no such problem.